

**PABLO ALEJANDRO CORREA SALDARRIAGA**

**SEVERE-TO-MILD WEAR TRANSITION DURING RUNNING-IN OF DIFFERENT  
STEEL-ON-STEEL TRIBOSYSTEMS IN BALL-ON-DISC DRY SLIDING  
RECIPROCATING TESTS**

São Paulo

(2018)

**PABLO ALEJANDRO CORREA SALDARRIAGA**

**SEVERE-TO-MILD WEAR TRANSITION DURING RUNNING-IN OF DIFFERENT  
STEEL-ON-STEEL TRIBOSYSTEMS IN BALL-ON-DISC DRY SLIDING  
RECIPROCATING TESTS**

Thesis submitted to the University of São  
Paulo for the degree of Doctor of Science

Area:  
Mechanical engineering - Design and  
manufacturing

Supervisor: Prof<sup>a</sup>. Dr<sup>a</sup>. Izabel Fernanda  
Machado

São Paulo  
(2018)

Este exemplar foi revisado e corrigido em relação à versão original, sob responsabilidade única do autor e com a anuência de seu orientador.

São Paulo, \_\_\_\_\_ de \_\_\_\_\_ de \_\_\_\_\_

Assinatura do autor: \_\_\_\_\_

Assinatura do orientador: \_\_\_\_\_

#### Catálogo-na-publicação

Correa, Pablo Alejandro  
SEVERE-TO-MILD WEAR TRANSITION DURING RUNNING-IN OF  
DIFFERENT STEEL-ON-STEEL TRIBOSYSTEMS IN BALL-ON-DISC DRY  
SLIDING RECIPROCATING TESTS / P. A. Correa -- versão corr. -- São Paulo,  
2018.

159 p.

Tese (Doutorado) - Escola Politécnica da Universidade de São Paulo.  
Departamento de Engenharia Mecânica.

1.Dry sliding wear 2.Friction 3.Hardness 4.Ball-on-disc 5.nominal contact  
pressure I.Universidade de São Paulo. Escola Politécnica. Departamento de  
Engenharia Mecânica II.t.

*to Tomás*

## ABSTRACT

The main motivation of this doctoral thesis is to extend the current knowledge about the tribological behavior of a precipitation-hardenable (PH) austenitic stainless steel (SAE XEV-F or DIN 1.4882), used for manufacturing exhaust valves for internal combustion engines in passenger cars. For this purpose, dry sliding laboratory tests were carried out using this steel and other steels, mainly austenitic and martensitic, used as model materials for the comparative characterization of wear and friction. Experimental tests were conducted using an SRV@4 tribometer in a ball-on-disc configuration with reciprocating movement, in which the discs were the samples and the balls the counter-bodies. Four kinds of steels were tested: *a)* AISI 310, *b)* SAE XEV-F, *c)* AISI H13, and *d)* Nitrided SAE XEV-F. The ball was made of AISI 52100 bearing steel. The tests were conducted at room temperature and fixed conditions of time (sliding distance) (up to 73.2 m), load (100 N), frequency (10 Hz) and stroke (2mm). Wear was evaluated by means of mass loss in the disc and the ball, and post examination of the worn surfaces. Post examination was conducted using scanning electron microscopy (SEM), coherence correlation interferometry (CCI), and X-Ray diffraction (XRD). Wear debris resulting from tribological interaction were also investigated using SEM and XRD. Additionally, the friction coefficient was measured. High speed filming and interrupted tests were also performed at specific sliding distances. This work reports a severe-to-mild wear transition occurring during the first stage of tribological interaction (*running-in*) and its relation to the load distribution variation at the interface throughout the tribological tests. The wear transition was observed in different steel-on-steel tribosystems in ball-on-disc contact configuration and occurred due to the combined effects of two factors: *a)* the contact pressure reduction, due to the increase of nominal contact area caused by wear; and *b)* subsurface strain hardening (when relevant). The pressure/distance variation was determined experimentally and modeled empirically. Subsurface strain hardening was observable (and measurable) mainly the austenitic steels. Significant differences in wear (and friction) were observed between homogeneous (monophasic) steels and the heterogeneous (multiphasic) SAE XEV-F valve steel. Wear in the homogeneous steels presented an inverse correlation with hardness. Wear on the AISI 310 presented non-linear wear rates for a significant portion of the test. Wear on the SAE XEV-F valve steel was pronounced (even in the mild regime) due to a combined effect of two factors: *a)* formation of hard debris, which induced an abrasive component to wear by relative sliding, and *b)* subsurface NbC fracture, which markedly affected the material removal due to plastic deformation in the surrounding matrix. Wear of the nitrided SAE XEV-F steel was lower than that of the non-nitrided samples by nearly two orders of magnitude. The benefits of nitriding in the SAE XEV-F were two-fold: *a)* an increased surface hardness, and *b)* the prevention of NbC fracture and detachment, which results in even higher wear resistance.

**Keywords:** Dry Sliding wear; Friction; Hardness; Ball-on-disc; Nominal contact area; Running-in; Wear transition.

## RESUMO

A principal motivação desta tese é ampliar o conhecimento atual sobre o comportamento tribológico de um aço inoxidável austenítico endurecível por precipitação (PH), o SAE XEV-F (ou DIN 1.4882), utilizado para a fabricação de válvulas de exaustão de motores de combustão interna para carros de passageiros. Para este propósito, foram realizados ensaios laboratoriais de deslizamento a seco usando este aço e outros, principalmente aços austeníticos e martensíticos, usados como materiais modelo para a caracterização comparativa do desgaste e do atrito. Os ensaios experimentais foram conduzidos usando um tribômetro SRV®4 em uma configuração esfera-disco com movimento alternado, em que os discos foram as amostras e as esferas são os contracorpos. Foram ensaiados quatro tipos de aços: *a)* AISI 310, *b)* SAE XEV-F, *c)* AISI H13, e *d)* SAE XEV-F nitretado. A esfera era feita de aço para rolamento AISI 52100. Os ensaios foram realizados a temperatura ambiente e usando condições fixas de tempo (distância total percorrida até 73.2 m), carga normal (100 N), frequência (10 Hz) e amplitude da oscilação (2 mm). O desgaste foi avaliado por meio de perda de massa, tanto do disco quanto da esfera, e exame das superfícies desgastadas utilizando microscopia eletrônica de varredura (MEV), interferometria de correlação de coerência (ICC) e difração de raios-X (DRX). Os debris de desgaste resultantes da interação tribológica também foram investigados usando MEV e DRX. Adicionalmente, a evolução do coeficiente de atrito foi analisada. Também foram realizadas filmagens de alta velocidade e ensaios interrompidos em tempos de deslizamento específicos. Este trabalho reporta uma transição de desgaste severo para moderado que ocorre durante a primeira fase da interação tribológica (*running-in*) e sua relação com a variação da carga na interface durante os ensaios tribológicos. A transição de desgaste foi observada em diferentes tribo-sistemas de aço-contra-aço na configuração esfera-plano e ocorreu principalmente por efeitos combinados de dois fatores: *a)* a redução da pressão de contato, devida ao aumento da área nominal causada pelo desgaste; e *b)* o encruamento subsuperficial (quando relevante). A variação pressão/distância foi determinada experimentalmente e modelada empiricamente. Encruamento por deformação subsuperficial foi observável (e medível) principalmente nos aços austeníticos. Foram observadas diferenças significativas no desgaste (e atrito) entre os aços homogêneos (monofásicos) e o aço de válvula SAE XEV-F, heterogêneo (multifásico). O desgaste nos aços homogêneos apresentou uma correlação inversa com a dureza. O desgaste no aço válvula SAE XEV-F foi pronunciado (mesmo no regime de desgaste moderado) devido a um efeito combinado de dois fatores: *a)* a formação de *debris* duros, o que induziu uma componente abrasiva ao desgaste por deslizamento relativo, e *b)* a fratura subsuperficial do NbC, o que afetou significativamente a remoção de material devida à deformação plástica da matriz. O desgaste do aço nitretado SAE XEV-F foi menor que o das amostras não tratadas em quase duas ordens de grandeza. Os benefícios da nitretação no aço válvula SAE XEV-F foram dois: *a)* o aumento da dureza da superfície, e *b)* a prevenção da fratura e desprendimento de NbC, o que resulta em uma resistência de desgaste ainda maior.

**Palavras-chave:** Deslizamento a seco; Desgaste; Atrito; Dureza; Esfera-disco; Área nominal de contato; *Running-in*; transição de desgaste.

## ACKNOWLEDGEMENTS

---

Several people, companies and organizations made this doctoral work come to a successful conclusion. I would like to thank:

My supervisor professor Izabel Fernanda Machado, for introducing me to scientific research in engineering, and for the careful revisions of this manuscript.

My co-advisor professor Roberto Martins de Souza, for his friendship and valuable conversations on sliding wear.

The people and companies involved in this thesis: to Dr. Alexandre Farina from Villares Metals S.A (Brazil) for providing the SAE XEV-F steel, and to Danilo Assad Ludewigs from HEF-Durferit (Brazil) for his friendship, and for providing the nitriding treatments of the samples used in this thesis.

The *triboflex consortium*, for providing the infrastructure for the development of important research projects related to internal combustion engines in passenger cars, such as the present doctoral thesis.

To the CAPES and FAPESP (Brazilian research agencies), and to COLCIENCIAS (Colombian department of science and technology administration), for their financial support

My colleagues and friends of the Surface Phenomena Laboratory (LFS-EPUSP): Dr. Tiago Cousseau, Dr. Paulo Machado, Ms.C. Juan Ignacio Pereira, Dr. Luiz Alberto Franco, M.Sc. Iramar Tertuliano, M.Sc. Michael Cano, Dr. Newton Fukumasu, Dr. Francisco Profito, Dr. Juan Marcelo Rojas, Dr. Alexander Zuleta, M.Sc. Sebastian Acero, Ms.C. Leonardo Villabón, Eng. Marcos Ara, Eng. Guido Boidi, M.Sc. Felipe Carneiro, M.Sc. Marco Aurelio Mendes, Dr. Eleir Bortoleto, Dr. Vanessa Seriacopi, M.Sc. Ana Julia Tertuliano, M.Sc. Arnaldo Lima, Eng. Cassiano Ferreira; and to the administrative and technical staff who supported the development of this thesis: Silene Carneiro, Sidney Carneiro, Raphael Oliveira, Rafael Almeida, Rodney Santos, Carlos Ramirez.

My parents, for their love, patience, encouragement and understanding; to my sister for her loving support; to my son, for providing me a glimpse into the future. Finally, to my friends inside/outside the academic world who accompanied me and gave me strength.

São Paulo, June 2018

Pablo Correa

## STATEMENT OF ORIGINALITY

---

This thesis is submitted for a doctoral degree at the University of São Paulo (Brazil). The research reported was conducted under the supervision of Professor Dr. Izabel Fernanda Machado in the Mechanical Engineering post-graduation program (PPGEM) of the Department of Mechatronics and Mechanical Systems Engineering at the University of São Paulo, between September 2013 and June 2018.

I the author declare that this manuscript is original, and confirm that I have given due consideration to the protection of intellectual property associated with this work and that there are no impediments to publication, including the timing of publication, with respect to intellectual property. In so doing I confirm that I have followed the regulations of our institutions concerning intellectual property.

I declare that neither this, nor any substantially similar work has been or is being submitted for any degree or diploma or other qualification at any other university or institution. I confirm that the manuscript has been read and approved by my supervisor and that there are no other persons who satisfied the criteria for authorship but are not listed.

I wish to confirm that there are no known conflicts of interest associated with this publication and there has been no significant financial support for this work that could have influenced its outcome.

Some part of the work has been published, or submitted for publication, as follows:

- P.A. CORREA, R.M. SOUZA, I.F. MACHADO. Tribological behavior of different steels under dry sliding: effects of hardness. Presented at the Leeds-Lyon international tribology symposium. Lyon, France (2017).
- P.A. CORREA, R.M. SOUZA, I.F. MACHADO. Comparative tribological behavior of nitrided and non-nitrided SAE XEV-F valve steel in dry sliding. Presented and Published in the Proceedings of the SAE conference on Mobility. Sao Paulo, Brazil (2017). Paper No. 2017-36-0221.

São Paulo, June 2018

Pablo Correa

## SUMMARY

<b>LIST OF FIGURES .....</b>	<b>10</b>
<b>LIST OF EQUATIONS .....</b>	<b>16</b>
<b>LIST OF SYMBOLS.....</b>	<b>16</b>
<b>LIST OF ABBREVIATIONS .....</b>	<b>17</b>
<b>1 INTRODUCTION .....</b>	<b>18</b>
1.1 MOTIVATION .....	18
1.2 DELIMITATIONS .....	21
1.3 THESIS OUTLINE .....	21
<b>2 LITERATURE REVIEW .....</b>	<b>23</b>
2.1 VALVE STEELS IN INTERNAL COMBUSTION ENGINES FOR PASSENGER CARS .....	23
<i>Exhaust valve steel SAE XEV-F .....</i>	23
<i>Tribological testing .....</i>	26
<i>Contact configuration in model laboratory tests.....</i>	28
<i>Ball-on-disc (BoD) dry sliding reciprocating tests .....</i>	30
<i>Variation of the nominal contact pressure in ball-on-disc sliding tests .....</i>	32
2.2 DRY SLIDING TRIBOLOGY OF STEELS .....	34
<i>Dry sliding of steels .....</i>	34
<i>Hardness and the Archard wear model .....</i>	35
<i>The wear coefficient.....</i>	35
<i>Wear transitions in steels .....</i>	37
<i>Wear transitions in nitrided steels .....</i>	41
<i>Subsurface deformation.....</i>	43
<i>Effect of second phases in sliding wear of alloys .....</i>	45
<i>Friction in sliding wear.....</i>	46
<b>3 OBJECTIVE .....</b>	<b>49</b>
3.1 GENERAL OBJECTIVE.....	49
3.2 SPECIFIC OBJECTIVES.....	49
<b>4 MATERIALS AND METHODS .....</b>	<b>50</b>
4.1 MATERIALS .....	50
4.2 TRIBOLOGICAL TESTS.....	52
4.3 CHARACTERIZATION .....	54
<b>5 RESULTS AND DISCUSSION .....</b>	<b>59</b>
5.1 MATERIALS .....	59
<i>Microstructure .....</i>	59
<i>Hardness.....</i>	68
<i>Nitrided layer (treated SAE XEV-F valve steel) .....</i>	69
<i>Subsurface hardness .....</i>	71
<i>Topography .....</i>	72
<i>Contact pressures under static loading.....</i>	74
5.2 FRICTION.....	77
<i>Friction coefficient (<math>\mu</math>).....</i>	77
5.3 WEAR.....	80
5.3.1 MASS LOSS EVOLUTION .....	81
<i>Evolution of wear (mass loss) during interrupted tests .....</i>	81
<i>Wear quantification (metrics) .....</i>	84
5.3.2 SEVERE-TO-MILD WEAR TRANSITION (running-in evaluation).....	88
<i>High-speed filming (In-situ observation) .....</i>	88
<i>Severe-to-mild wear transition in-situ observation and hypothesis.....</i>	90

<i>Further evidence of the severe-to-mild wear transition in the selected steel-on-steel tribosystems - wear mechanisms</i> .....	90
<b>5.3.3 DETAILED ANALYSIS OF THE WEAR SCARS AT THE FINAL STAGE OF TRIBOLOGICAL TESTS</b> .....	<b>103</b>
<i>Wear mechanisms of the discs</i> .....	103
<i>Nominal contact area and tribofilm formation</i> .....	118
<i>Wear of the balls - wear mechanisms, nominal contact area and tribofilm transfer</i> .....	120
<i>Ball penetration</i> .....	122
<i>3D analysis of the wear scars</i> .....	124
<i>Subsurface deformation and strain hardening of the discs</i> .....	128
<b>5.4 FURTHER DISCUSSION</b> .....	<b>136</b>
<i>Mechanism of the severe-to-mild wear transition during running-in in BoD dry sliding tests in the selected steel-on-steel tribosystems</i> .....	136
<i>Evolution of nominal contact pressure</i> .....	139
<i>Empirical model for the pressure/distance variation in BoD dry sliding tests</i> .....	142
<i>Threshold of nominal contact pressure for the severe-to-mild wear transition</i> .....	144
<b>6 CONCLUSIONS</b> .....	<b>147</b>
6.1 SUMMARY .....	147
6.2 CONTRIBUTIONS .....	148
6.3 FUTURE WORK SUGGESTIONS.....	149
<b>7 REFERENCES</b> .....	<b>150</b>

## LIST OF FIGURES

Figure 1.1. V6, 24-valve, double overhead camshaft (DOHC) engine.....	19
Figure 1.2. Detail of the sealing systems of the combustion chamber and the valvetrain mechanism in a DOHC engine.....	20
Figure 1.3. Valvetrain in a DOHC engine. ....	20
Figure 2.1. Engine valve (a) and flowchart of the conventional exhaust-valve making process (b). ....	24
Figure 2.2. Classification of different types of tribological testing. ....	27
Figure 2.3. Schematic view of conformal (a) and non-conformal (b) type of contacts, along with the associated stress distribution at the interface.....	29
Figure 2.4. Wear scars on AISI 304 after 10E5 cycles at a load of 11.5 N and an oscillation frequency of 100 Hz: (a) partial stick contact conditions (oscillating amplitude of 4 $\mu\text{m}$ ); (b) gross slip contact conditions (oscillating amplitude of 16 $\mu\text{m}$ ). ....	31
Figure 2.5. Schematic representation of the worn volume during reciprocating tests. ....	31
Figure 2.6. Variation of the nominal contact pressure with sliding distance during dry wear tests of various materials. ....	33
Figure 2.7. The variation of wear rate with load (contact pressure) for a 0.5% plain carbon steel pin sliding at 1 m s <sup>-1</sup> in air against tool steel in a pin-on-ring test. ....	38
Figure 2.8. Schematic diagram of the distribution of severity of plastic deformation beneath a worn metal surface in a severe wear regime. (Adapted from Rice, Nowotny and Wayne, in Rhee, Ruff and Ludema. ASME, Wear of materials (1981) pp. 47-52) ....	44
Figure 2.9. Types of two-phase microstructures. Aggregated microstructure (a), and dispersed microstructure (b).....	45
Figure 4.1. Schematic description of the studied tribosystems.....	52
Figure 4.2. Detail of the ball-on-disc contact configuration in an SRV®4 tribometer. The surface of the disc was polished to a mirror finish. ....	53
Figure 4.3. High-speed filming equipment setup. ....	57
Figure 5.1. Microstructure of the AISI 310 steel (SEM/BSE - 200x mag.).....	59
Figure 5.2. Detail of the austenitic microstructure of the AISI 310 steel. (SEM/SE - 1000x mag.) ....	60
Figure 5.3. X-Ray diffraction pattern of the AISI 310 austenitic stainless steel.....	60
Figure 5.4. SEM analysis of precipitate clusters in the AISI 310 austenitic stainless steel. BSE image (a), and EDS maps of: iron (b), chromium (c), and nickel (d). (1000x mag.) ....	61
Figure 5.5. Microstructure of the SAE XEV-F valve steel (SEM/BSE - 500x).....	62
Figure 5.6. X-Ray pattern of the SAE XEV-F valve steel.....	63
Figure 5.7. SEM analysis of precipitates in SAE XEV-F valve steel. BSE image (a), and EDS map of niobium (b). (200x mag.) ....	63
Figure 5.8. Detail of submicrometer precipitates in the SAE XEV-F valve steel. (SEM/SE - 1000x mag.) ....	64
Figure 5.9. Microstructure of the AISI H13 tool steel. (SEM/BSE - 500x mag.).....	65
Figure 5.10. X-Ray pattern of the AISI H13 tool steel.....	65
Figure 5.11. Detail of submicrometer precipitates in the AISI H13 too steel (SEM/SE - 5000x mag.).....	66

Figure 5.12. Microstructure of the AISI 52100 ball bearing steel. (SEM/SE - 1000x mag.) .....	66
Figure 5.13. Detail of submicrometer precipitates in the AISI 52100 ball bearing steel (SEM/SE - 5000x mag.) .....	67
Figure 5.14. Multiscale hardness characterization of bulk materials and other phases. ....	68
Figure 5.15. SEM analysis of the resulting nitrided layer on the SAE XEV-F valve steel (top view of the sample): <i>a</i> ) backscattered electrons image (BSE); and <i>b</i> ) corresponding niobium EDS map.(500x mag.).....	69
Figure 5.16. XRD patterns of the nitrided layer resulting after nitriding of the SAE XEV-F valve steel. ....	70
Figure 5.17. SEM/SE image of a cross section of the nitrided layer on the SAE XEV-F valve steel. ....	71
Figure 5.18. Subsurface nanohardness profiling of the polished discs (before wear). ....	72
Figure 5.19. 3D view of the polished surfaces of the AISI 310 austenitic SS. (representative of the AISI H13 and AISI 52100 steels). (Field of View - FoV: 50 x 50 $\mu$ m). ....	73
Figure 5.20. 3D view of the polished surfaces of the SAE XEV-F valve steel. (FoV: 50 x 50 $\mu$ m). ....	73
Figure 5.21. 3D view of the resulting topography after nitriding the polished surface of the SAE XEV-F. (FoV: 50 x 50 $\mu$ m). ....	74
Figure 5.22. Mean contact pressure (PM) as a function of static vertical load in a BoD contact as predicted by the model of Hertz for a 10 mm diameter steel ball against a steel flat. ....	75
Figure 5.23. 3D view of indentations on the austenitic samples after static loading with 100 N: <i>a</i> ) AISI 310, and <i>b</i> ) SAE XEV-F. (FoV: 850 x 850 $\mu$ m). ....	76
Figure 5.24. Friction coefficient during tests. Each curve was obtained as a point-to-point average of 4 repetitions (for each tribosystem).....	78
Figure 5.25. Detail of friction coefficient during running-in.....	79
Figure 5.26. Friction coefficient after running-in ( $s > 12$ m). ....	80
Figure 5.27. Evolution of the mass loss of the discs.....	82
Figure 5.28. Evolution of the mass loss of the discs during the first 3 m sliding.....	82
Figure 5.29. Mass loss at $s = 73.2$ m: <i>a</i> ) discs, and <i>b</i> ) balls.....	84
Figure 5.30. Detail of contact for the SAE XEV-F / AISI 52100 tribosystem after wear at different sliding distances ( $s$ ): <i>a</i> ) 0 m, <i>b</i> ) 9.6 m, and <i>c</i> ) 73.2 m.....	89
Figure 5.31. Wear scar on the AISI 310 steel disc at $s = 2.4$ m (1 min) (SEM/BSE - 25x mag.) .....	91
Figure 5.32. Detail of wear mechanisms on the wear scar on the AISI 310 steel at $s = 2.4$ m (1 min) (SEM/BSE - 500x mag.) .....	92
Figure 5.33. Severe wear in the AISI 310 steel discs after 2.4 m (1 min). <i>a</i> ) Subsurface deformation (500x mag.), and <i>b</i> ) metallic debris formation (1000x mag.). (SEM/SE). ....	92
Figure 5.34. Metallic debris formation under severe wear in the AISI 310 steel discs after 2.4 m (1 min) (1000x mag.). (SEM/SE) .....	93
Figure 5.35. Wear scar on the ball tested against the AISI 310 steel disc at $s = 2.4$ m (1 min) (SEM/BSE - 25x mag.).....	93
Figure 5.36. EDS analysis of the wear mechanisms in the ball tested against the AISI 310 steel at $s = 2.4$ m (1 min): chromium ( <i>a</i> ), and oxygen ( <i>b</i> ). (1000x mag.). ....	94

Figure 5.37. Development of tribofilm in the AISI 310 tribosystem at 9.6 m (4 min). (SEM/BSE - 25x mag.) .....	94
Figure 5.38. Development of tribofilm in the AISI 310 tribosystem at 73.2 m (30.5 min). (SEM/BSE - 25x mag.) .....	95
Figure 5.39. Wear scar on the SAE XEV-F steel after 2.4 m (1 min). (SEM/BSE - 25x mag.) .....	95
Figure 5.40. Detail of wear the wear mechanisms on the SAE XEV-F steel after 2.4 m (1 min) (SEM/BSE - 1000x mag.) .....	96
Figure 5.41. Subsurface deformation due to severe metallic wear in the SAE XEV-F steel after 2.4 m (1 min). (SEM/BSE - 500x mag.) .....	97
Figure 5.42. Wear scar on the AISI 52100 steel ball tested against the SAE XEV-F valve steel at $s = 2.4$ m. (SEM/BSE - 25x mag.) .....	97
Figure 5.43. EDS analysis of the wear mechanisms in the ball tested against the SAE XEV-F steel: SEM/BSE detail (a), and chromium (b). (1000x mag.) .....	98
Figure 5.44. Wear debris of the SAE XEV-F steel. (SEM/SE - 500x mag.) .....	98
Figure 5.45. EDS analysis of the wear debris produced from the SAE XEV-F steel: .....	99
Figure 5.46. Evolution of the wear scar for the SAE XEV-F steel discs: 9.6 m (4 min). (SEM/BSE - 25x mag.) .....	99
Figure 5.47. Evolution of the wear scar for the SAE XEV-F steel discs: 73.2 m (30.5 min). (SEM/BSE - 25x mag.) .....	100
Figure 5.48. Wear scar on the AISI H13 steel at $s = 0.4$ m (10 s) (SEM/BSE - 25x mag.) .....	100
Figure 5.49. Evolution of the wear scar for the AISI H13 steel: a) 2.4 m (1 min), and b) 73.2 m (30.5 min). (SEM/BSE - 25x mag.) .....	101
Figure 5.50. Evolution of the wear scar for the AISI H13 steel: a) 2.4 m (1 min), and b) 73.2 m .....	102
Figure 5.51. Wear scar in the nitrided SAE XEV-F valve steel after 0.4 m (10 s). (SEM/SE - 25x mag.) .....	102
Figure 5.52. Detail of the wear mechanisms in the nitrided SAE XEV-F valve steel after 0.4 m sliding (SEM/BSE - 1000x mag.) .....	103
Figure 5.53. Wear scar on the AISI 310 steel disc (SEM/SE - 25x mag.) .....	104
Figure 5.54. SEM/BSE image of the wear scar on the AISI 310 steel disc (25x mag.) .....	105
Figure 5.55. Wear mechanisms in the wear scar on the AISI 310 steel disc (SEM/BSE - 1000x mag.) .....	105
Figure 5.56. SEM/EDS analysis of the tribofilm in the wear scar of the AISI 310 austenitic stainless steel. EDS maps of: oxygen (a), and iron (b). (1000x mag.) .....	106
Figure 5.57. SEM/EDS analysis of the tribofilm in the wear scar of the AISI 310 austenitic stainless steel. EDS maps of: chromium (a), and nickel (b). (1000x mag.) .....	106
Figure 5.58. Wear debris of the AISI 310 steel (SEM/BSE - 100x mag.) .....	107
Figure 5.59. XRD patterns of the wear debris of AISI 310 steel. ....	108
Figure 5.60. Wear scar on the SAE XEV-F valve steel (SEM/BSE - 25x mag.) .....	109
Figure 5.61. Detail image of the wear scar on the SAE XEV-F valve steel disc (SEM/BSE - 1000x mag.) .....	110
Figure 5.62. Oxygen EDS map on the highlighted region of the wear scar on the SAE XEV-F valve steel disc (1000x mag.) .....	110
Figure 5.63. Niobium EDS map on the highlighted region of the wear scar on the SAE XEV-F valve steel disc (1000x mag.) .....	111
Figure 5.64. Wear debris of the SAE XEV-F steel (SEM/BSE - 100x mag.) .....	111

Figure 5.65. XRD patterns of the wear debris of SAE XEV-F steel. ....	112
Figure 5.66. SEM/BSE image of the wear scar on the AISI H13 steel (25x mag.). .	113
Figure 5.67. SEM analysis of the highlighted region (white rectangle) of the wear scar on the AISI H13 steel. Detail BSE image (a), and corresponding oxygen EDS map (b). (200x mag.). ....	113
Figure 5.68. Wear debris of the AISI H13 steel (SEM/BSE - 100x mag.) .....	114
Figure 5.69. XRD pattern of the wear debris of AISI H13 steel. ....	115
Figure 5.70. SEM/BSE image of the wear scar on the nitrided SAE XEV-F valve steel (25x mag.). ....	115
Figure 5.71. SEM/SE image of the wear scar on the nitrided SAE XEV-F valve steel (25x mag.). ....	116
Figure 5.72. Detail of wear mechanisms in the wear scars on the nitrided SAE XEV-F disc. ....	116
Figure 5.73. EDS maps of wear mechanisms in the nitrided SAE XEV-F disc: .....	117
Figure 5.74. EDS maps of wear mechanisms in the nitrided SAE XEV-F disc: .....	117
Figure 5.75. Niobium EDS maps of wear mechanisms in the nitrided SAE XEV-F disc (500x mag.). ....	118
Figure 5.76. Comparative (projected) nominal area and tribofilm distribution in the steel discs: .....	119
Figure 5.77. SEM/BSE images of wear scars on the AISI 52100 steel balls tested against: a) AISI 310, b) SAE XEV-F, c) AISI H13, and d) Nitrided SAE XEV-F. ....	121
Figure 5.78. SEM analysis of material transfer from the SAE XEV-F steel to the AISI 52100 ball. SEM/BSE image (a), and niobium EDS map (b). ....	121
Figure 5.79. Maximum depth of the wear scars of the discs. ....	122
Figure 5.80. Schematic representation of the wear scar on the disc and the ball. ....	123
Figure 5.81. 3D analysis of the wear scar on the AISI 310 steel at a 73.2 sliding distance: a) view of the wear scar (FoV = 5500x3500 $\mu\text{m}$ ), and b) profile a-a. ....	124
Figure 5.82. 3D analysis of the wear scar on the AISI 310 steel at a 73.2 sliding distance: a) view of the wear scar (FoV = 5500x3500 $\mu\text{m}$ ), and b) profile a-a. ....	125
Figure 5.83. 3D analysis of the wear scar on the AISI 52100 steel ball tested AISI 310 steel at a. ....	125
Figure 5.84. 3D analysis of the wear scar on the AISI H13 steel at a 73.2 sliding distance: a) view of the wear scar (FoV = 5000x2500 $\mu\text{m}$ ), and b) profile a-a. ....	126
Figure 5.85. 3D analysis of the wear scar on the AISI 52100 steel ball tested AISI H13 steel at a 73.2 sliding distance: a) view of the wear scar (FoV = 3000x3000 $\mu\text{m}$ ), and b) profile b-b. ....	127
Figure 5.86. Schematic representation of the horizontal force measurement of the SRV apparatus as a function of ball penetration. ....	128
Figure 5.87. Subsurface deformation of the AISI 310 steel. (SEM/SE images - cross sections of the wear scars - 1000x). ....	129
Figure 5.88. Subsurface deformation of the SAE XEV-F steel. (SEM/BSE images - cross sections of the wear scars - 1000x). ....	130
Figure 5.89. Detail of NbC fracture occurring in the subsurface region of the untreated SAE XEV-F valve steel. (SEM/BSE - 2000x mag.). ....	130
Figure 5.90. Subsurface deformation of the AISI H13 steel. (SEM/SE images - cross sections of the wear scars - 1000x). ....	131
Figure 5.91. Subsurface deformation of the nitrided SAE XEV-F steel. (SEM/SE images - cross section of the wear scar - 1000x). ....	132
Figure 5.92. Cross sections of a nitrided SAE XEV-F surface after 93.2 m, showing (occasional) subsurface fracture. ....	133

Figure 5.93. Comparative subsurface hardness profile at a 73.2 m sliding distance (cross-section). strain hardening (nanoindentation 5 mN). .....	134
Figure 5.94. Evolution of nominal contact area. ....	139
Figure 5.95. Estimated evolution of nominal contact pressure. ....	141
Figure 5.96. Evolution of nominal contact pressure during running-in.....	144
Figure 5.97. Correlation between friction coefficient, mass loss and mean contact pressure during running-in. ....	145

## LIST OF TABLES

Table 2.1. Nominal chemical composition of exhaust valve Fe-based Austenitic Alloys.	23
Table 2.2. Comparative mean contact pressures in tribological testing of steels	29
Table 2.3. Values of curve fitting constants $\beta$ and $k$ from the model of Ajayi and Erck (2001).	34
Table 2.4. Values of the dimensionless wear coefficient for various steels sliding against tool steel (unless otherwise stated) in dry sliding Pin-on-Ring in air.	36
Table 2.5. Summary of wear results for the untreated EN41B steel in Kato et. al. (1994)	41
Table 2.6. Summary of wear results for the gas nitrided EN41B steel in Kato et. al. (1994)	42
Table 4.1. Nominal chemical composition of the tested steels.	50
Table 4.2. Heat treatments performed on the sample steels.	51
Table 4.3. Parameters for tribological tests.	53
Table 4.4. Characterization techniques.	54
Table 4.5. Technical specifications of the equipment.	55
Table 5.1. Overestimation % of nanohardness measurements with respect to micro and macrohardness.	69
Table 5.2. Comparative Indentation depth (critical, Hertzian and measured).	77
Table 5.3. Mean (arithmetic) friction coefficient after running-in ( $s > 12$ m).	80
Table 5.4. Regression functions of mass loss of the discs between 25 and 73.2 m sliding.	83
Table 5.5. Comparative wear metrics for the studied materials.	86
Table 5.6. Running-in (Comparative wear metrics).	88
Table 5.7. Steady-state (Comparative wear metrics).	88
Table 5.8. Phase identification in the wear debris	120
Table 5.9. Change in HR (HDISC/HBALL) after 73.2 m slid.	135
Table 5.10. Evolution of nominal contact area (numeric values).	139
Table 5.11. Percentage increase of nominal contact area between distance points.	140
Table 5.12. Estimated evolution of nominal contact pressure.	141
Table 5.13. Percentage decrease of nominal contact pressure between distance points.	142
Table 5.14. Regression functions of the nominal (mean) contact pressure between 25 and 73.2 m sliding.	142
Table 5.15. Best-fit curves of data from the evolution of nominal contact pressure.	143
Table 5.16. Nominal contact pressure ranges for tribo-oxidation in the studied tribosystems.	145

## LIST OF EQUATIONS

(Equation 1)	.....	34
(Equation 2)	.....	35
(Equation 3)	.....	47
(Equation 4)	.....	76

## LIST OF SYMBOLS

$\mu$	Friction coefficient
$\varepsilon$	Epsilon Martensite
$\alpha'$	Alpha Martensite

## LIST OF ABBREVIATIONS

GHGs	Greenhouse Gases
NAMAs	Nationally Appropriate Mitigation Action plans
LFS	Surface Phenomena Laboratory
EPUSP	Escola Politécnica of the University of São Paulo
ICEs	Internal Combustion Engines
DOHC	Double overhead camshaft engine
VS	Valve/interfacial-media/Seat-insert sealing system of an ICE.
SAE	Society of Automotive Engineers
AISI	American Iron and Steel Institute
NbC	Niobium Carbide
IGSCC	Intergranular Stress Corrosion Cracking
PH	Precipitation hardening heat treatment
SS	Stainless Steels
SIMT	Strain-Induced Martensite Transformation
FEDZ	Friction Energy Dissipation Zone
SEM	Scanning Electron Microscope
SE	Secondary electrons detector of the SEM
BSE	Backscattered electrons detector of the SEM
CCI	Coherence Correlation Interferometry
FoV	Field of View of a CCI image
CL	Compound Layer of the N-layer
DL	Diffusion Layer of the N-layer
SRV®	Translatory Oscillation Apparatus (tribometer)
BoD	Ball-on-Disc type of contact
PoD	Pin-on-Disc type of contact
HR	Hardness Ratio ( $H_{\text{DISC}}/H_{\text{BALL}}$ )
SSWR	System-Specific Wear Rate

# 1 INTRODUCTION

## 1.1 MOTIVATION

Earth's climate change, and its associated negative effects, is a serious issue for humankind. Human activities increase the atmospheric concentrations of greenhouse gases (GHGs) and cause additional warming of both the surface and the atmosphere of planet Earth (UNITED NATIONS, 1992). This problem must be addressed rapidly. In this sense, global governmental efforts are focused on two strategies: *a*) the development of renewable energy technologies (e.g. solar, wind and hydraulic power), and *b*) plans for mitigation of impacts linked to combustion of fossil fuels, that is, contingency measures.

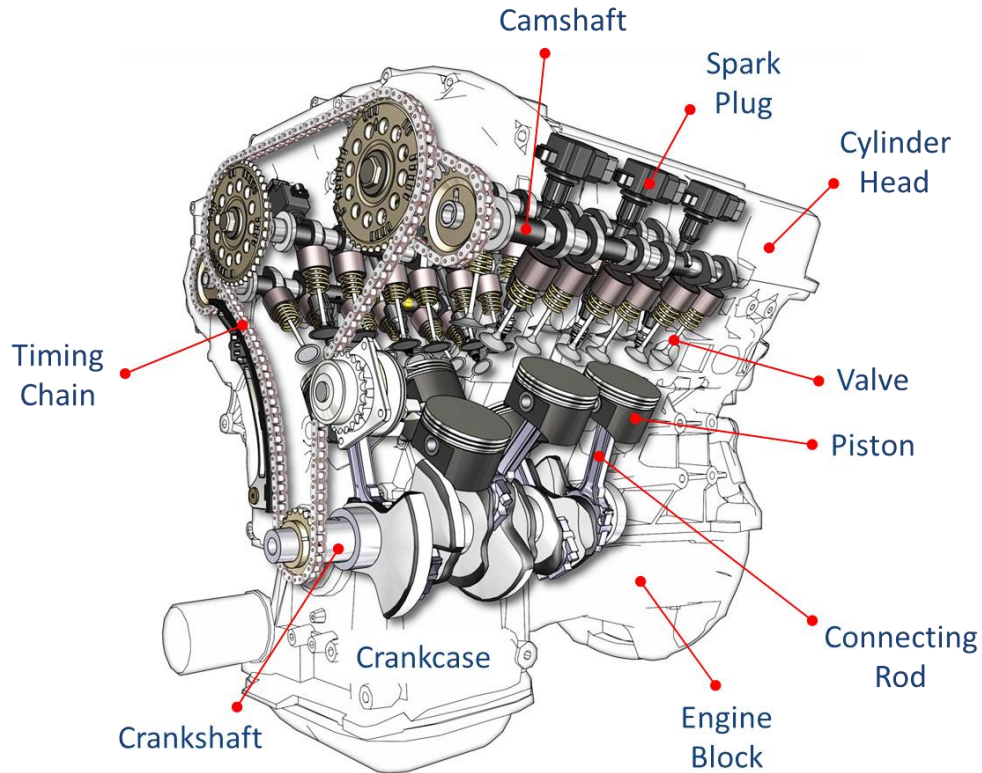
The automotive industry is one of the most important economic segments in the world involved with the production and distribution of motor vehicles (powered by Internal Combustion Engines - ICEs) (see Figure 1.1). However, the low overall efficiency of this type of engines is critical for pollutant emissions. The Nationally Appropriate Mitigation Action plans (NAMAs) are policies established by some countries to address the pollutant emission problem in a measurable, reportable and verifiable manner (UNITED NATIONS, 1992; PRESIDÊNCIA DA REPÚBLICA FEDERATIVA DO BRASIL, 2009; PRESIDÊNCIA DA REPÚBLICA FEDERATIVA DO BRASIL, 2010). In this regard, Brazilian government committed in 2010 to achieve between 36.1% and 38.9% reduction in projected emissions GHGs by 2020 (PRESIDÊNCIA DA REPÚBLICA FEDERATIVA DO BRASIL, 2009; PRESIDÊNCIA DA REPÚBLICA FEDERATIVA DO BRASIL, 2010). Contributing to this national initiative, the *Triboflex Consortium*<sup>1</sup> summoned important lubricant, auto-part and car manufacturers of the global market and important universities of the country under the leadership of the Surface Phenomena Laboratory (LFS-EPUSP), with one major objective: to improve the understanding of the tribological phenomena in the sealing systems of the combustion chamber in Internal Combustion Engines (ICEs) in passenger cars. The research presented in this thesis is one of several contributions obtained as results of the Triboflex consortium. The research conducted in this work is related to tribological behavior of materials that can be used to manufacture valves.

---

<sup>1</sup> Tribological challenges in flex-fuel engines. FAPESP process No. 2009/54891-2. São Paulo. Brazil.

The steel tribological behavior was characterized at room temperature and dry conditions, which are severe contact conditions in terms of contact pressure. Nevertheless, not all the selected test parameters are similar to the operating variables in an engine. The main limitations will be properly defined in the following section.

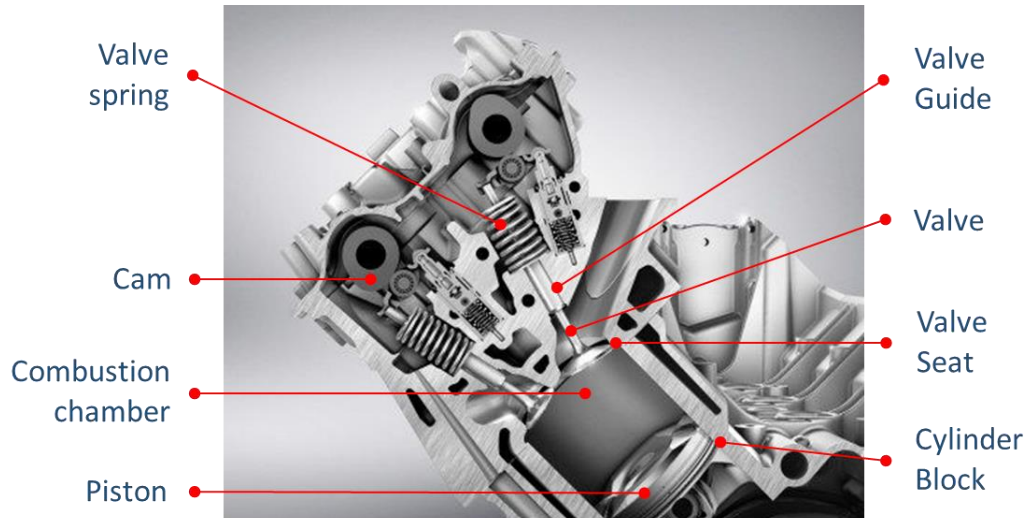
Figure 1.1. V6, 24-valve, double overhead camshaft (DOHC) engine.



The proper sealing of the combustion chamber of ICEs impacts largely on their overall efficiency (WANG; 2007). There are two sealing systems in the combustion chamber of a conventional ICE (see Figure 1.2): a) the valve/interfacial-media/seat-insert (VS system), a reciprocating dry (micro) sliding system, and b) the ring(s)/liquid-lubricant/liner, a reciprocating lubricated sliding system. This research deals with the former.

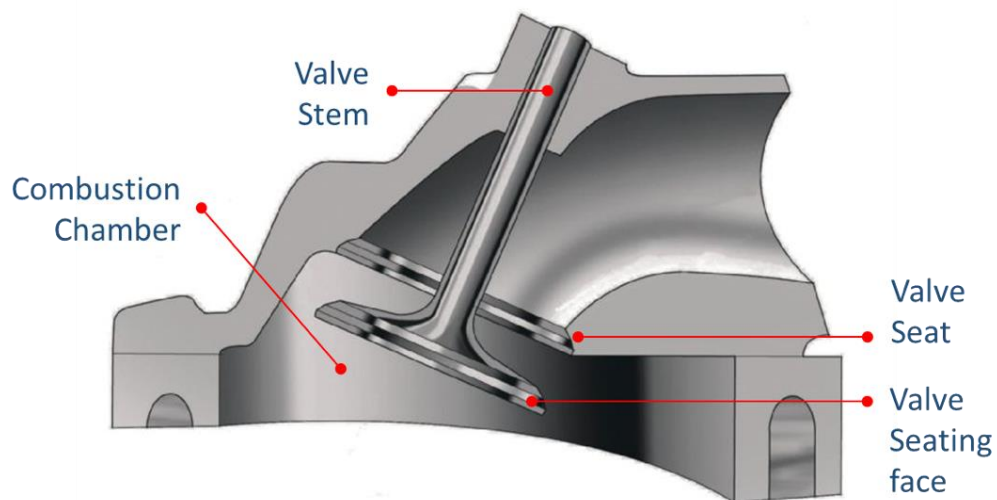
Surface damage of the valve (valve wear), causes the valve/seat (VS) system (see Figure 1.3) to lose its sealing function. Whether by progressive wear (recession) or by catastrophic damage (e.g. guttering or torching), valve wear will inevitably cause drastic compression losses. This results in equally drastic reductions in power and to greater fuel consumption and pollutant emissions (WANG, 2007; HOLMBERG; ANDERSSON; ERDEMIR, 2012).

Figure 1.2. Detail of the sealing systems of the combustion chamber and the valvetrain mechanism in a DOHC engine.



Additionally, friction (energy dissipation) is another problem during operation of mechanical systems, such as the mechanisms composing the ICE. Frictional losses in the valvetrain mechanism rank second, after those of the crankshaft (HOLMBERG; ANDERSSON; ERDEMIR, 2012). This energy is mainly lost in the cam/follower interface. Consuming a great portion of the fuel energy, friction in engines contributes to increasing pollutant emissions in a global scale. Understanding wear and frictional performance of valve steels can allow the increase of the durability of valves, resulting in overall performance improvements in ICEs.

Figure 1.3. Valvetrain in a DOHC engine.



One of the main motivations of this work is to improve the current knowledge about wear and frictional response of a selected austenitic stainless steel (SAE XEV-F or DIN 1.4882), widely used for exhaust valve manufacturing in ICEs for passenger cars. For this purpose, dry sliding tests were performed on the SAE XEV-F valve steel and other steels (mainly austenitic and martensitic) considered suitable for comparison.

## 1.2 DELIMITATIONS

Experimental laboratory material tests do not reproduce completely the operating conditions of the modeled system, in this case, the VS system. The main limitations of this study are related to temperature, counterbody materials and environment. The high temperatures resulting from valve operation, around 850 °C according to Wang (2007), were not reproduced in this study. Instead, room temperature tests were conducted in order to isolate the mechanical effects and frictional heating occurring under the specified operating parameters (load, and oscillation amplitude and frequency). The room temperature results can serve as the basis for analyzing ball-on-disc dry sliding tests in high-temperature conditions. An actual exhaust valve material was tested, along other model steels, against a hard ball bearing steel. The results obtained here can serve as basis for analyzing further studies on the effect of using actual seat materials. The tests were conducted in air with humidity monitoring. The results obtained here can serve as basis for analyzing tribological tests involving combustion products (reaction gases and particulate matter).

## 1.3 THESIS OUTLINE

The first section of chapter two introduces the fundamentals of steels for exhaust valve manufacturing in internal combustion engines for passenger cars. The selected valve steel is reviewed in this section, along with the central aspects of tribological testing (specifically ball-on-disc material tribological tests). The second section of chapter two reviews the central aspects related to dry sliding tribological behavior of different steels. Chapter three states the main objective of this thesis and the specific objectives proposed for its development. Chapter four presents the methodological aspects of the thesis. The main results of this thesis are presented in Chapter five and

divided in four sections. The first section presents the results of the material characterization before tribological tests. The second section presents the friction coefficient analysis. The third section presents the wear results and the fourth section presents the closing discussion. In chapter six are presented the conclusions, contributions and suggestions for future work and, finally, chapter seven presents the references used in this work.

## 2 LITERATURE REVIEW

### 2.1 VALVE STEELS IN INTERNAL COMBUSTION ENGINES FOR PASSENGER CARS

Valves are manufactured from metallic alloys based on iron, nickel and cobalt. While martensitic steels are usually used for manufacturing of intake valves, because of their lower operation temperatures, high temperatures in exhaust valves require the use of austenitic alloys and superalloys (e.g. Inconel) (WANG, 2007). Among exhaust valve alloys, austenitic stainless steels (austenitic SS) are the least expensive option. The good corrosion properties of austenitic SS are due to the combined effects of chromium, nickel and manganese. Additionally, nickel and manganese are also responsible for austenite presence at room temperature. Higher strengths, at elevated temperatures, are obtained by means of precipitation hardening heat treatment enabled usually by nitrogen as an alloying element. Hence, the precipitation hardening austenitic stainless steels (Table 2.1) are the most widely used alloys for exhaust valves (WANG, 2007). SAE XEV-F exhaust valve steel is an austenitic stainless steel (austenitic SS), based on SAE EV-8 steel and alloyed with tungsten, niobium, and tantalum (or a combination of them).

Table 2.1. Nominal chemical composition of exhaust valve Fe-based Austenitic Alloys.

SAE	C	Mn	Si	Cr	Ni	W	Fe	Other
EV-4	0.20	1.25	1.0	21.0	11.5	-	Bal.	N:0.20
EV-8	0.53	9.0	<0.25	21.0	4.0	-	Bal.	N:0.43
EV-12	0.55	8.5	<0.25	21.0	2.1	-	Bal.	N:0.30
EV-16	0.33	2.5	<0.75	23.0	8.0	<0.5	Bal.	N:0.30, Mo<0.5
XEV-F	0.50	9.0	<0.45	21.0	4.5	2.2	Bal.	N:0.50, Nb+Ta: 2.20

Adapted from (WANG Y, 2007).

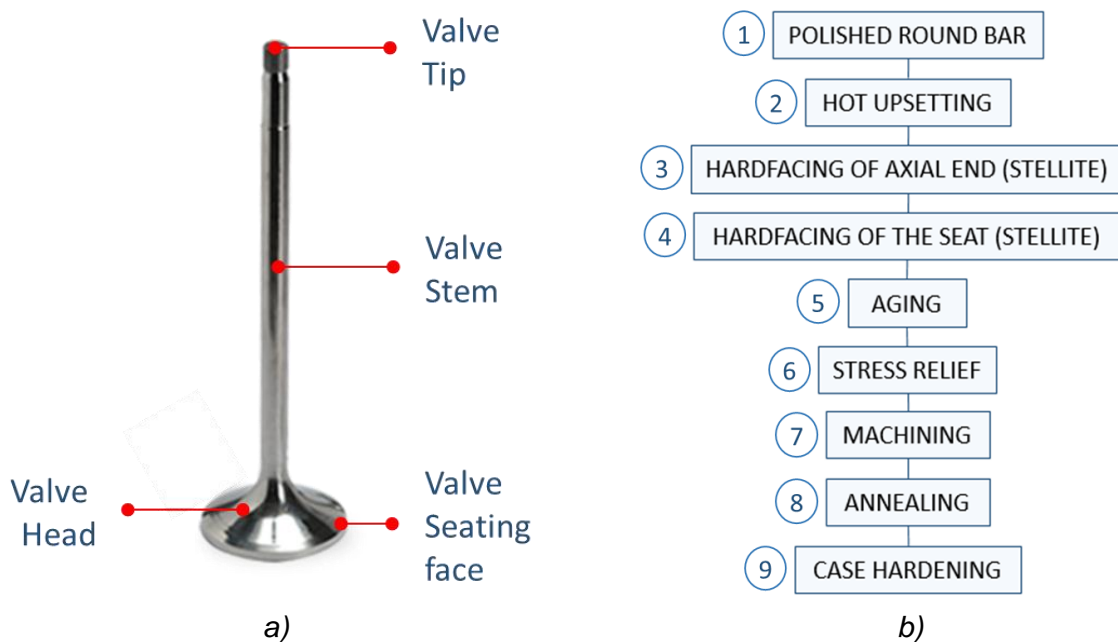
#### *Exhaust valve steel SAE XEV-F*

The SAE XEV-F steel is widely used for manufacturing exhaust valves in internal combustion engines for passenger cars (WANG Y, 2007), as a less expensive alternative to nickel alloys (WANG, 2007; OKETANI et. al., 2000). Addition of niobium to SAE XEV-F austenitic steel favors the precipitation of NbC having two different orders of magnitude in precipitates size (from micrometer to nanometer). The

precipitation of the micro-scale NbC inhibits the grain-boundary chromium carbide -  $\text{Cr}_{23}\text{C}_6$ - precipitation, therefore avoiding Intergranular Stress Corrosion Cracking (IGSCC) occurrence (OKETANI et. al., 2000; SHIRZADI; JACKSON, 2014). The well-dispersed nanoscale precipitates are obtained by means of a precipitation hardening (PH) heat treatment, and their function is to hinder the movement of dislocations (SHIRZADI; JACKSON, 2014). For this reason, the PH austenitic SS have enhanced mechanical properties (e.g. hardness) when compared to more common grades like AISI 304 (WANG, 2007).

When compared to martensitic steels (e.g inlet valves), austenitic microstructures such as that of stainless steels (e.g. SAE XEV-F) and Ni-alloys (e.g. Inconel) usually present low wear resistance. To solve this problem, case hardening thermo-chemical processes such as nitriding are widely used in the exhaust valve production process (WANG, 2007; OKETANI et. al., 2000). Figure 2.1 shows a typical engine valve and a flowchart of the conventional production process of exhaust valve steels. From a tribological point of view, Stellite welding is conducted at early stages of production (steps 3 and 4), usually at the tip of the valve (the axial end) and occasionally to protect the seating face from excessive wear. Case hardening thermo-chemical surface treatments are conducted at the final stage of production for providing wear resistance to the entire valve, namely: the tip, the stem and the seating face.

Figure 2.1. Engine valve (a) and flowchart of the conventional exhaust-valve making process (b).



Adapted from (OKETANI et. al., 2000).

Nitriding is a thermo-chemical process by means of which nitrogen atoms diffuse into the surface of a metal or metallic alloy (e.g. steel) (OKETANI et. al., 2000; HASHMI, 2014; SHIH; HUANG; CHEN, 2011; LUO; ZHAO, 2013; MINGOLO; TSCHIPTSCHIN; PINEDO, 2006). Nitrogen diffusion on surface creates a hard case, consisting of a hardened layer with varied characteristics, depending on several factors like: microstructure of the base metal, type of nitriding process (salt bath, gas or plasma), and time/temperature specifications. Austenitic SS are difficult to nitride because the  $\text{Cr}_2\text{O}_3$  passive film serves as a barrier for nitrogen diffusion: case thicknesses usually range between 2 and 50  $\mu\text{m}$  (SHIH; HUANG; CHEN, 2011; LUO; ZHAO, 2013). The microstructure of this hardened layer is usually a nitrogen-supersaturated austenite, frequently defined as expanded austenite (MINGOLO; TSCHIPTSCHIN; PINEDO, 2006). Expanded austenite has a homogeneous face-centered tetragonal crystal structure with enhanced hardness (HV~800) and better corrosion resistance than the stainless steel matrix (SHIH; HUANG; CHEN, 2011; LUO; ZHAO, 2013). Additionally, for heat treatment temperatures above 460°C, this hard case in austenitic SS may exhibit the formation of an outer *white layer*, consisting of a nitride-network (mainly Fe and Cr) (SHIH; HUANG; CHEN, 2011; LUO; ZHAO, 2013) with superior hardness due to precipitation strengthening at the surface (HV~1200) (SHIH; HUANG; CHEN, 2011; LUO; ZHAO, 2013).

The SAE XEV-F valve steel presents precipitates in an austenitic matrix. Hence, this steel presents a two-phase aggregate microstructure or heterogeneous (DIETER, 1988). Precipitation causes this steel to present improved bulk properties (e.g. creep resistance) and mechanical resistance (both at low and high temperatures). Nevertheless, the tribological behavior of SAE XEV-F valve steel has not been explored. Both with and without the surface nitriding treatment, the role of NbC precipitates still needs to be clarified. No studies have been found by the author on SAE XEV-F valve steel tribological response in the context dry sliding. In contrast, several investigations have been carried out on various homogeneous (monophasic) austenitic SS (e.g. AISI series 301, 304, 316 and 310) (DUMBLETON; DOUTHETT, 1977; HSU; AHN; RIGNEY, 1980; YANG; NAYLOR; RIGNEY, 1985; FARGAS; ROA; MATEO, 2016; FARIAS et. al., 2007) that can be regarded as model steels for understanding SAE XEV-F valve steel tribology tests. Several investigations have also been performed to understand the comparative tribological performance of nitrided and non-nitrided austenitic SS (LUO; ZHAO, 2013; MINGOLO; TSCHIPTSCHIN; PINEDO,

2006). It has already been highlighted that nitrided surfaces have superior wear resistance than the untreated steels. However, while the technology of nitriding has allowed some degree of wear control of the surfaces of the valves, there are still controversies around the wear processes involved. Some authors (LUO; ZHAO, 2013) mention that wear mechanisms of nitrided samples are mainly abrasive, in contrast with the more adhesive nature of wear of the untreated steel samples. Iron oxides may form resulting from the nitriding treatment (SHIH; HUANG; CHEN, 2011) and they should also be expected after tribological tests due to tribo-oxidative processes. Additionally, martensitic steels are often used for the manufacturing of intake valves in ICEs for passenger cars, and they are usually classified as homogeneous (monophasic). Therefore, they can be considered a suitable model material with intermediate hardness between the austenitic steels and the nitrided surfaces. The next sections describe the central tribological aspects related to this thesis.

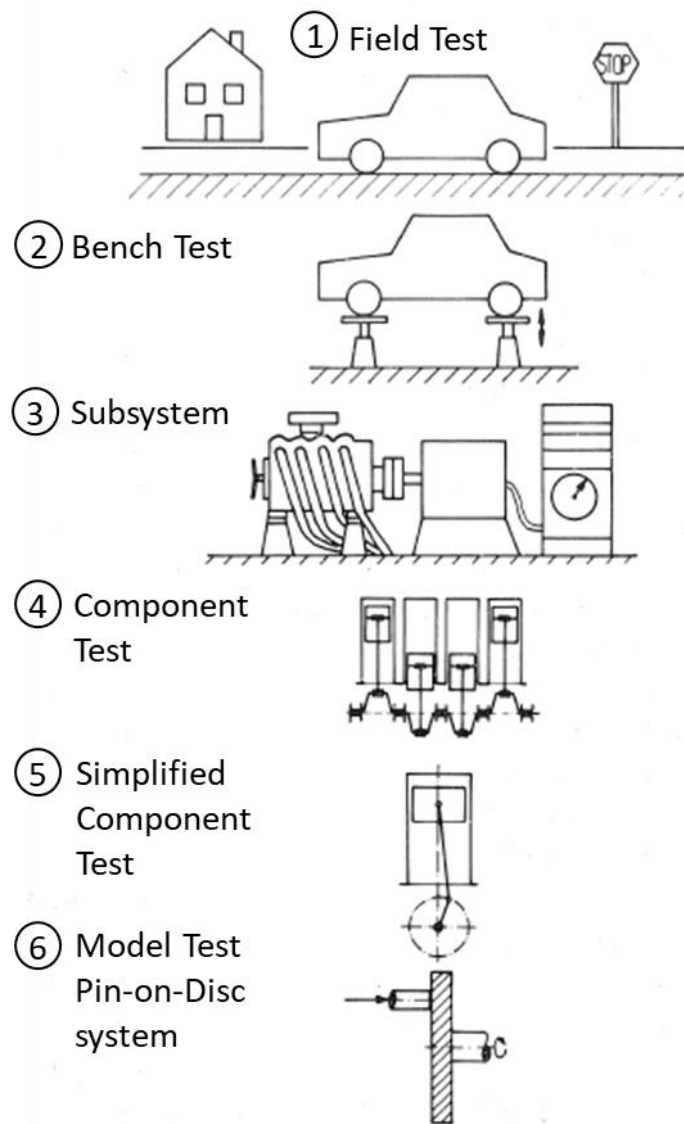
### *Tribological testing*

The selection of the appropriate type of experiment is commonly a matter of discussion (JIMBERT et. al., 2015). Model laboratory tests (See Figure 2.2) are commonly used for testing the tribological behavior of materials (or lubricants) under extreme conditions (ZUM GAHR, 1987). However, laboratory tests usually do not reproduce 100% the actual field-test operation conditions of the component it is intended to evaluate, due to simplifications of environment parameters or operating variables (ZUM GAHR, 1987). Additionally, variations up to 57% in wear volume measurements can be found between different laboratory tests, carried out under similar load and speed conditions (RUFF, 1989). In this sense, laboratory tests of materials are a good measure of the relative wear behavior *only if* the laboratory and field tests present the same: loading conditions, tribosystem structure (solid body, counter-body, interfacial element and environment), and predominating wear mechanisms (ZUM GAHR, 1987; TYLCZAK et. al., 1999; JIMBERT et. al., 2015).

There are great differences between the operation conditions of the VS system in an ICE and the laboratory tests usually used to reproduce them. On one hand, due to the high operating temperatures in the combustion chamber of an ICE (~800°C in ICE for passenger cars (WANG, 2007)), most lubricants evaporate or lose its function. The absence of effective lubricant at the interface causes the VS system to operate in

dry conditions. On the other hand, velocities during contact of the valve and the seat are controlled by an appropriate design of the profile of the cam and the spring. This condition reduces the impact component of wear (WANG, 2007) and makes sliding wear the predominant phenomena. Hence, it is viable to characterize valve and valve-seat materials in dry sliding laboratory tests (both in ambient and high temperature tests). This is supported by the fact that similar wear mechanisms have been found both in valves tested in the field and laboratory dry sliding tests of valve steels (ZULETA, 2016).

Figure 2.2. Classification of different types of tribological testing.



Source (ZUM GAHR, 1987).

Effects of variables such as combustion products are difficult to reproduce in model laboratory test. Nevertheless, in a recent study (ZULETA, 2016) similar wear mechanisms were found between valve wear field tests and dry sliding model (laboratory) tests using a Translatory Oscillation Apparatus (SRV®) in a ball-on-disc non-conformal type of contact. Hence, an SRV testing machine was used in this work to investigate dry sliding wear in a selected exhaust valve steel and other model steels. A characterization of the surface and subsurface conditions during a tribological event is needed: changes in microstructure and surface chemical composition of both the test specimens and wear *debris* are expected to occur (RIGNEY, 2000). Additionally, the evolution of certain variables of the tribosystem can be described by means of interrupted tests (different sliding distances) and using, when possible, both in-situ and post-test analysis techniques (RIGNEY, 2000).

#### *Contact configuration in model laboratory tests*

Two common contact configurations for the evaluation of wear in materials are the Pin-on-Disc (PoD) (Figure 2.3a) and the Ball-on-Disc (BoD) (Figure 2.3b). The differences between the corresponding contact pressure distributions are schematically shown. In PoD configuration, initial contact occurs over an extended nominal contact area, while in BoD tests occurs at a point. As can be seen, the associated contact pressures of these two types of contact differ in distribution and in magnitude. Conformal type of contact like in PoD tests results in a contact pressure distribution that is nearly uniform throughout the totality of the nominal contact area (with some slight concentration at the edges of contact). Non-conformal contact like in PoD tests result in a non-uniform (parabolic) contact pressure distribution. Under similar geometric dimensions of the pin and the ball, the magnitudes of the contact pressures caused by a defined load in BoD configurations are higher (both mean and maximum values) than those found in PoD.

Due to those differences in contact pressure, Ball-on-Disc dry sliding testing of materials represents a more severe type of testing when compared to Pin-on-Disc tests. Jimbert et. al. (2015) performed comparative pin-on-disc and ball-on-disc tests in three different martensitic tool steels (AISI D2, AISI A8, and AISI H13). Under the same load (nominal contact pressure) conditions, BoD tests showed wear rates that were between two and six times higher than in PoD tests. In that sense, results

obtained by both types of tribological tests should be discussed separately, or at least compared carefully.

Figure 2.3. Schematic view of conformal (a) and non-conformal (b) type of contacts, along with the associated stress distribution at the interface.

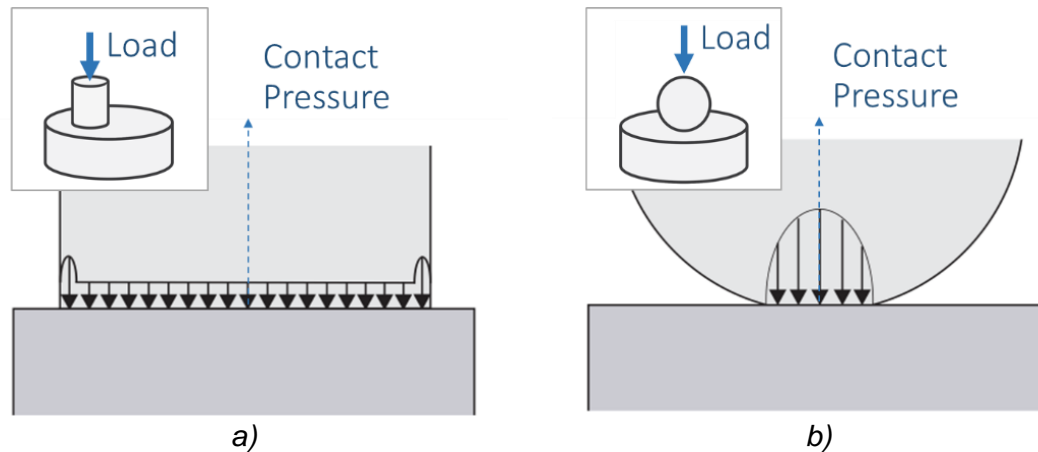


Table 2.2 shows the mean contact pressures and type of contact of some recent works on dry sliding of steels. Great differences in the mean nominal contact pressure of the works can be observed, which compromises their quantitative and qualitative comparison.

Table 2.2. Comparative mean contact pressures in tribological testing of steels (Pin-on-Disc vs Ball-on-disc)

Author	Year	steel	type of test	Mean Contact Pressure [MPa]
ZULETA	2016	AISI 52100/ AISI H13	BoD	770-2650
FARGAS; ROA; MATEO	2016	WC/ AISI 301L	BoD	880
AJAYI; ERCK	2001	AISI 52100 (self-mated), AISI M50 (self-mated)	BoD	75.4 - 198
JIMBERT et. al.	2015	AISI D2 AISI A8 AISI H13	BoD	2660
			PoD	3.5
VIÁFARA; SINATORA	2011	AISI 4140/ AISI H13	PoD	1.86
FARIAS et. al.	2007	AISI 304 (self-mated), AISI 316 (self-mated),	PoD	0.12 - 0.40

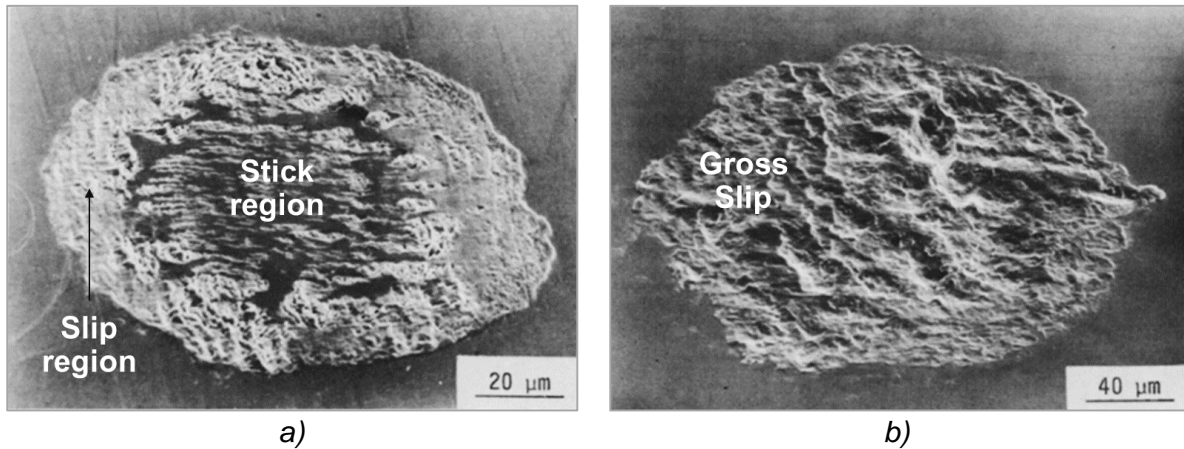
### *Ball-on-disc (BoD) dry sliding reciprocating tests*

Modeling (predicting) the amount of worn material (wear volume) is usually conducted in relation to the duration of contact (sliding distance). Hence, a common measure of wear is the volume of material removed per unit sliding distance or *wear rate*. Ball-on-Disc tribological tests are convenient for two reasons (AJAYI; ERCK, 2001), namely: ease of alignment and absence of edge loading (see Figure 2.3). The ASTM G133-05 standard (2005) provides a method for testing and measuring the sliding wear of materials using a linear, reciprocating ball-on-flat geometry. The wear volume of both sample and counterbody are the principal quantities to be determined. Nevertheless, wear volume only (not wear rate) is reported because there is no reason to assume that wear occurs at a constant rate throughout the test (ASTM G133-05, 2005). In metal contacts, it can be expected that both specimens show signs of wear, and that the amount of wear experienced by each body depends on its geometry and hardness. However, in most systems, the softer material wears out at a faster rate (HUTCHINGS, 1992; AJAYI; ERCK, 2001).

During reciprocating tests, an oscillatory movement is imposed between the two solid surfaces in contact. Under ball-on-disc contact configuration and depending on the operation conditions, relative movement between the surfaces can occur in three ways (HUTCHINGS, 1992): *a*) no slip, *b*) partial-slip, and *c*) gross slip. For a fixed normal load, there is a critical value of amplitude of oscillation for which a transition occurs from fretting (Figure 2.4a) to gross slip (Figure 2.4b). The critical value depends on the contact pressure, the oscillating frequency (mean sliding speed), and material properties (hardness). The amplitude of motion in fretting appears to be between 2 and 20  $\mu\text{m}$  in many cases (WATERHOUSE, 1979). Values greater than  $\sim 300 \mu\text{m}$  result in gross slip (HUTCHINGS, 1992).

Reciprocating sliding tests can operate under gross slip conditions at the interface. The following conditions characterize gross slip (WATERHOUSE, 1979): *a*) there is little entrapment of debris and no restriction of access of the environment at the interface, and *b*) there is a tendency of the surface material to be removed before any fatigue cracks that nucleated from cyclic loading propagate to the surface. This inhibits the failure of the surface of the tested materials. In this sense, a set of tests designed to evaluate sliding wear resistance must guarantee to be operating in gross slip conditions.

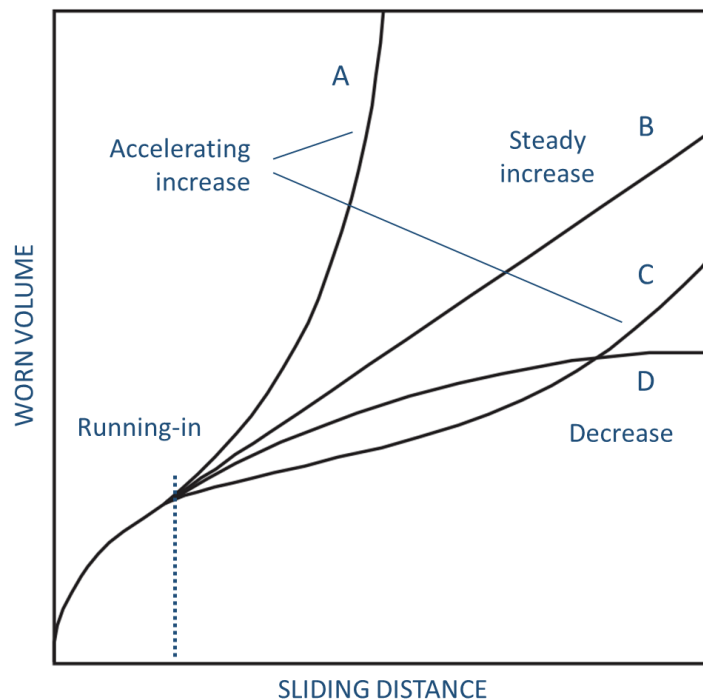
Figure 2.4. Wear scars on AISI 304 after  $10E5$  cycles at a load of 11.5 N and an oscillation frequency of 100 Hz: (a) partial stick contact conditions (oscillating amplitude of  $4\ \mu\text{m}$ ); (b) gross slip contact conditions (oscillating amplitude of  $16\ \mu\text{m}$ ).



Adapted from (BRYGGMAN: SÖDERBERG, 1986).

Additionally, during laboratory tests of steels (metallic materials in general), there is often an initial stage of severe wear in which metal-to-metal contact occurs (Figure 2.5). Plastic deformation and adhesion are the predominant wear mechanisms and the debris produced during this stage are metallic (WATERHOUSE, 1979, HUTCHINGS, 1992).

Figure 2.5. Schematic representation of the worn volume during reciprocating tests.



Adapted from (WATERHOUSE, 1979)

The running-in stage (Figure 2.5) can be followed either by a steady (curve B) or a decreasing (curve D) wear volume. The decrease in the wear after the initial stage is due to transient interfacial behavior like asperity deformation or tribofilm formation (HUTCHINGS, 1992).

In the context of laboratorial material testing, the running-in stage can be understood as the changes in friction and/or wear which occur before a tribosystem reaches steady state after start-up. Nevertheless, steady-state is formally defined as “the condition of a given tribosystem wherein the average kinetic friction coefficient, wear rate, and/or other specified parameters have reached and maintained a relatively *constant* level” (BLAU, 1991). The wear rate (the change in mass loss in time) is not one of such parameters as can be seen in Figure 2.5. Curve B, for instance, presents a steady increase in wear (a linear wear rate).

The sliding velocity is known for affecting the rate of frictional heating and, therefore, interfacial temperatures, which in turn influence the mechanical properties of the materials at their surface, and the thermally activated chemical processes at the interface. Nevertheless, under reciprocating sliding conditions the sliding velocity is highly variable along the oscillation amplitude (stroke) and there are several direction inversions during each cycle. As indicated in Hutchings (1992), the wear rate in reciprocating dry sliding tests under gross slip conditions is independent of the oscillation amplitude.

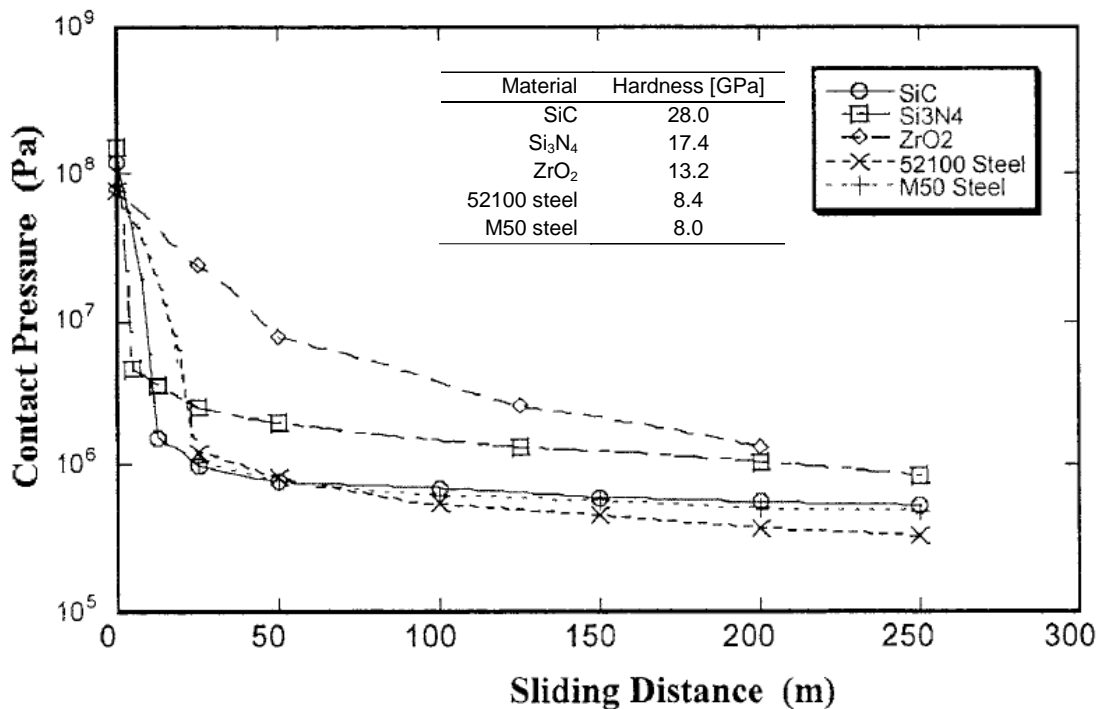
In some materials, a subsequent increase in wear volume may be observed (curves A or C). Accelerating wear is typical in metals with low hardness which develop hard wear debris (metallic or oxidized), which in turn contribute to wear by abrasion. Materials showing linear wear (curve B) are susceptible of being characterized by a unique wear rate (if one neglects the variations of wear rate occurring during the initial stages of wear). Wear rates are a common measure of the severity of wear and they allow the comparison of tests.

#### *Variation of the nominal contact pressure in ball-on-disc sliding tests*

In any contact, load transmission is always achieved through a finite area: macroscopically the nominal contact area and, at the micro- and nano- scales, the real contact area. In ball-on-disc (BoD) tribological tests, the nominal point contact area increases due to the wear of one or both bodies in contact. Consequently, the nominal

contact pressure (see Hertzian Contact Pressure in [ASTM G133-05, 2005](#)) reduces, in as much as orders of magnitude ([AJAYI; ERCK, 2001](#)). Changes in load (nominal contact pressure) are known for inducing transitions from severe adhesive mechanisms to mild tribo-oxidation during dry sliding wear ([WELSH, 1965](#)). To accurately model wear in BoD tests requires knowledge of the pressure/distance (time) variation ([AJAYI; ERCK, 2001](#)). Knowledge of this relation allows a better estimation of the contact stresses and interfacial temperatures during different stages of sliding, which leads to: a) an improved understanding of changes in wear mechanisms, b) a refined prediction of wear and other tribological phenomena that may occur, and c) a better correlation of sliding-wear data with component performance. [Figure 2.6](#) shows the variation of nominal contact pressure as a function of sliding distance as determined by Ajayi and Erck (2001) for several materials in self-mated conditions, under dry sliding and solid and liquid lubrication.

[Figure 2.6](#). Variation of the nominal contact pressure with sliding distance during dry wear tests of various materials.



Adapted from ([AJAYI; ERCK, 2001](#)).

One important observation is that, independently of the tested material, the most important reduction of the nominal contact pressure occurs during the first ~50 m of sliding. This initial reduction is followed by a more gradual decrease and tend to reach

a nearly steady value. In all cases, the nominal contact pressure varied with the sliding distance according to an inverse power relation, found empirically to be:

$$P_N = \beta \cdot P_M \cdot d^{-k} \quad (\text{Equation 1})$$

Where  $P_N$  is the “instantaneous” nominal contact pressure expressed in Pascals,  $\beta$  and  $k$  are constants,  $P_M$  is the initial mean Hertzian contact pressure, and  $d$  is the sliding distance. The values of constants  $\beta$  and  $k$  for some (martensitic) steel-on-steel dry sliding tests are shown in Table 2.3.

Table 2.3. Values of curve fitting constants  $\beta$  and  $k$  from the model of Ajayi and Erck (2001).

Material pair	$\beta$	$k$
AISI 52100 steel (self-mated)	0.099	0.568
AISI M50 steel (self-mated)	0.0386	0.331

Another important observation is that during ball-on-disc tribological tests, hardness is related to the pressure/distance variation, as can be seen from Figure 2.6. The harder silicon carbide (SiC) presented a less pronounced contact pressure reduction than the (comparatively) softer materials such as steels (AISI 52100 and AISI M50). In this sense, ball-on-disc configuration tests should consider the relationship between hardness and the variation of nominal contact pressure.

## 2.2 DRY SLIDING TRIBOLOGY OF STEELS

This chapter presents the fundamental aspects of the dry sliding tribology of steels. Relevant tribological aspects are discussed in the context of austenitic stainless steels (with and without surface nitriding) and martensitic steels as model materials for understanding valve steel wear and friction.

### *Dry sliding of steels*

Under dry sliding conditions, the behavior of the tribosystem is more material dependent than in lubricated conditions. The main interest lies in understanding the structural and chemical changes that take place at the surface and the region underneath it (RIGNEY, 2000). Mechanical stresses and interfacial temperature are

two main factors controlling the predominance of wear mechanisms (HUTCHINGS, 1992). Wear processes in dry sliding of steels involve phenomena such as plastic deformation and adhesion (both at the macro and the asperity scales), and are related to phase transformations, oxidation, delamination (occasionally), and thermo-mechanical mixing of wear products (*debris*) at the interface.

#### *Hardness and the Archard wear model*

The most common sliding wear model is that of Archard (ARCHARD, 1953), a linear wear equation relating the resulting wear volume ( $V$ ) to the normal load ( $L$ ), the distance slid ( $s$ ), the hardness ( $H$ ) of the softer of the materials in the tribo-pair, and a wear coefficient ( $k$ ).

$$V = kLs/H \quad \text{(Equation 2)}$$

Hardness is the only material property that is accounted for in the Archard wear equation, which implies that all other material properties, and the effects of other phenomena (e.g. subsurface strain hardening), must be accounted for in the wear coefficient ( $k$ ). In this sense, the wear coefficient constitutes a viable way for characterizing and comparing tribological systems.

#### *The wear coefficient*

During metal-to-metal contact in dry sliding, adhesion is thought to play a fundamental role, both in wear and wear debris formation and in frictional behavior. In this sense, the adhesive wear model (first proposed by Archard) provides a widely accepted explanation of material removal. According to this model, the wear particles are formed from the (ductile) fracture of a portion of adhesive junctions among the interacting asperities. At every moment during a test, the normal load is supported, globally by the nominal contact area, and locally by the (plastically deforming) asperities which compose the real contact area. The total amount of wear per unit sliding distance corresponds to all asperity interactions that result in worn particles. The wear coefficient ( $k$ ) represents the number of interacting asperities where conditions are such that material is torn, forming wear debris.

It is common to term the wear coefficient as an “adhesive” wear coefficient (RABINOWICZ, 1981). Nevertheless, under specific conditions, dry sliding is also known for developing interfacial media that would prevent (or diminish) adhesion (HUTCHINGS, 1992; BHUSHAN, 2013) which creates confusion around the stages and mechanisms present during wear. The neglect of the properties of the oxides by focusing exclusively in compatibility (adhesion) can lead to great uncertainty in the determination of the wear coefficient during oxidative sliding wear (RABINOWICZ, 1981).

The concept of metallurgical compatibility (closely related to the concept of chemical affinity) is central for adhesion related arguments. Compatibility, defined as the degree of intrinsic attraction of the atoms of the contacting metals with each other (RABINOWICZ, 1981), correlates directly with the degree of adhesive interaction (as long as there is no other interfacial media inhibiting this interaction). Wear between compatible and incompatible materials are significantly different. Self-mated metals present the highest degree of compatibility and, therefore, show the highest associated wear coefficients (often associated with welding and seizure of metal-to-metal contact). Incompatible pairs, on the other hand, result in much lower wear coefficients (BHUSHAN, 2013). Table 2.4 shows typical values of the dimensionless wear coefficient for steel-on-steel tribosystems in conformal type of contact.

Table 2.4. Values of the dimensionless wear coefficient for various steels sliding against tool steel (unless otherwise stated) in dry sliding Pin-on-Ring in air.

Material	Dimensionless wear coefficient
Mild steel (against mild steel)	7.0E-3
Hard tool steel	1.3E-4
Ferritic stainless steel	1.7E-7

Source: (ARCHARD; HIRST, 1956)

### *Tribo-oxidative sliding wear*

Oxidative wear (tribo-oxidation) is known as mild wear (QUINN, 1962; QUINN; SULLIVAN; ROWSON, 1984) because the observed wear rates are substantially lower than in severe metallic wear. During mild oxidative wear, a portion of the metallic wear debris generated by mechanical processes during metal-to-metal contact remain at the

sliding interface. Those particles are modified further (e.g. crushed into finer particles, compacted and agglomerated into large debris). Insufficient heat dissipation favors the increase of interfacial temperatures that lead to oxidized debris particles, which further agglomerate together and get reattached to either of the contacting surfaces. During tribo-oxidation, the metal surfaces slide against each other separated by the interfacial layer (frequently denominated third body or tribofilm), consequently reducing metal-to-metal contact. The tribofilm may be distributed through the nominal contact area or in some regions of it and may stay in place or be removed by subsequent sliding.

Tribo-oxidation during dry sliding of steels depends on the relation between chemical composition of the steel (and the counterbody), on the dominant contact pressure and interfacial temperature conditions, and on the ambient conditions such as temperature or oxygen partial pressure. For instance, interfacial tribo-films have been characterized in varied steel-on-steel dry sliding tests and they are usually found to have less than 2  $\mu\text{m}$  in thickness and to consist mainly of three iron oxides: hematite ( $\text{Fe}_2\text{O}_3$ ), magnetite ( $\text{Fe}_3\text{O}_4$ ) and wüstite ( $\text{FeO}$ ) (HSU; AHN; RIGNEY, 1980; YANG; NAYLOR; RIGNEY, 1985; FARGAS; ROA; MATEO, 2016; FARIAS et. al., 2007). When the thickness of the oxide layer surpasses a critical value, the fracture of this layer results in wear debris with sizes between 0.01 and 1  $\mu\text{m}$ , mainly oxides (HUTCHINGS, 1992).

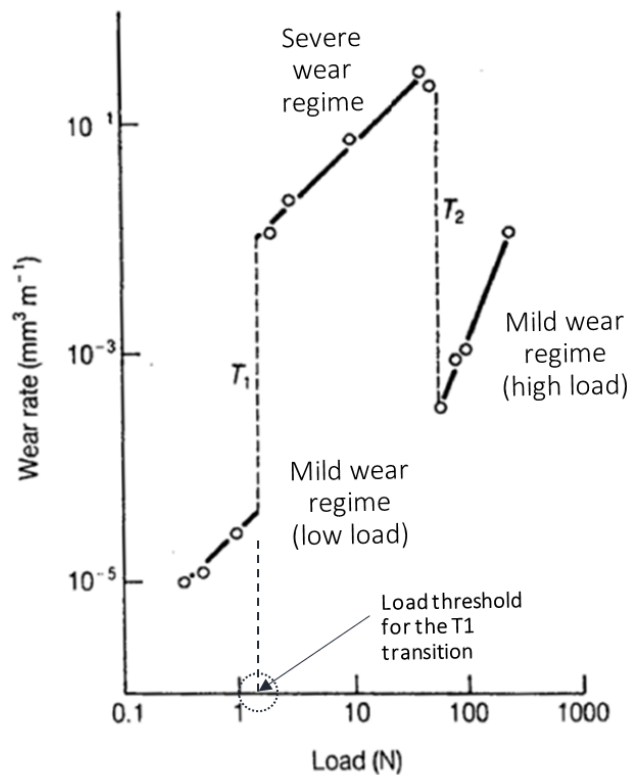
Wear by fatigue is rare in dry sliding tests (BURWELL; STRANG, 1951). Nevertheless, there exists a *delamination theory of wear* (SUH, 1973, 1977; SUH et. al., 1974) in which the wear mechanisms correspond to the growth of sub-superficial crack that convey at the surface forming wear debris.

### *Wear transitions in steels*

According to the Archard model (Equation 2), the measured worn volumes usually vary in direct proportion with the total sliding distance and the applied load. Nevertheless, abrupt changes in wear rates have been observed at specific values of load (WELSH, 1965). Such transitions are the result on the complex interactions between the mechanical, thermal, and chemical behaviors of the materials at the surface and subsurface regions. They occur when two competing processes balance: a) the rate of exposure of a fresh metal surface caused by plastic deformation and adhesion, and b) the rate of oxidation of that surface by the surrounding atmosphere

(HUTCHINGS, 1992). Figure 2.7 shows the transitions in wear regimes during dry sliding testing of steels, as observed by Welsh, (1965).

Figure 2.7. The variation of wear rate with load (contact pressure) for a 0.5% plain carbon steel pin sliding at  $1 \text{ m s}^{-1}$  in air against tool steel in a pin-on-ring test.



Adapted from (WELSH, 1965)

In this graphic, the wear rate is expressed as a function of the load (which corresponds to contact pressure), and the sliding speed is constant and unidirectional. As can be observed, there are two well-defined wear regimes: one mild regime with low associated wear rates and one severe regime for which wear rates are higher in as much as three orders of magnitude. The mild wear regime is characterized by fine oxidized debris and the occurrence of tribo-oxidation at the worn surface, while severe wear is characterized by larger metallic wear debris and the occurrence of adhesion at the interface. Additionally, it was observed by Welsh (1965) that in conformal contact, a change from one wear regime to the other occurred at well-defined values of contact pressure (threshold value). The transition from mild to severe wear (for instance)

occurs when increasing nominal contact pressure up to a well-defined value (the  $T_1$  load threshold in [Figure 2.7](#)).

Several works related to sliding wear and its related wear mechanisms and transitions have been conducted to understand the relative contributions of phenomena such as: plastic deformation and adhesion, tribo-oxidation, subsurface strain hardening, third body transformations ([HIRST, 1956](#); [HIRST](#); [LANCASTER, 1956](#); [LANCASTER, 1957](#); [WELSH, 1957, 1965](#); [HIRST](#); [LANCASTER, 1960](#); [IWABUCHI](#); [HORI](#); [KUBOSAWA, 1988](#); [JIANG](#); [STOTT](#); [STACK 1998](#); [GOTO](#); [AMAMOTO, 2003, 2006](#); [HIRATSUKA](#); [GOTO, 2000](#); [HIRATSUKA](#); [MURAMOTO, 2005](#); [KATO, 1990, 2003, 2007](#); [KATO](#); [KOMAI, 2007](#); [VIÁFARA](#); [SINATORA, 2012](#)).

In 1930, Fink ([1930](#)) published one of the first works indicating the tendency of rubbing solids to react with the environment (e.g. tribo-oxidation in steels), which corresponds to the mechanical/chemical effects of dry sliding. Latter, Rosenberg and Jordan ([1935](#)) showed the potential role of the formed oxide films as protective interfacial media. Since 1936, much work was performed by Bowden and coworkers in England ([BOWDEN](#); [RIDLER, 1936](#); [BOWDEN](#); [TABOR, 1939](#); [BOWDEN](#); [MOORE](#); [TABOR, 1943](#)), and other researchers in the USSR ([DEMKIN, 1953](#); [SHVETZOVA, 1962](#)). The following facts were established ([BAHADUR, 1978](#)): a) the contact occurs at discrete points, the real contact area, which is smaller than the nominal contact area and has a non-uniform stress distribution; b) The interaction between surfaces is both molecular (adhesion) and mechanical (plastic deformation); and c) flash temperatures can reach the melting point of the contacting bodies. Burwell and Strang ([1952](#)) studied plastic deformation and adhesion during sliding wear. They indicated during metallic contact, the amount of material transferred was roughly proportional to the load (contact pressure). This is because the main effect of increasing load is to increase the size and number of adhered (welded) junctions or true contact areas, which results in larger wear particles. They observed that for severe metallic contact, a contact stress of approximately one third of the hardness of the softer steel can be expected to be critical to the metal wear process. They also commented that in highly stressed contacts, the severity of plastic deformation tends to extend into the subsurface region. Archard and Hirst ([1956](#)) observed the two predominant wear mechanisms and state that, for any type of mechanism, once equilibrium surface conditions are established the wear rate is independent of the apparent area of contact. They proposed this observation as a general law of wear, and hence not restricted to a particular wear

mechanism. This implies that during steady-state the wear rate is directly proportional to the load (contact pressure); as long as no changes are induced in the wear mechanism. Hirst and Lancaster (1956) conducted a series of dry sliding tests on a brass-on-steel tribosystems. They studied the effect of load and hardness on the severe-to-mild wear transition and suggested that the generation of a protective surface film is an essential part of the running-in process in machinery. They confirmed the validity of the Archard wear model for severe wear and that, at constant temperature and contact pressure, wear is proportional to the load. They confirmed the results of Burwell and Strang (1952) and showed that the wear rate is independent of the nominal contact area, provided that an equilibrium surface condition is first attained, there is also a linear relationship between the wear volume and the sliding distance. They also studied the effect of speed (LANCASTER, 1957) and temperature (HIRST; LANCASTER, 1960) finding that both speed and temperature favor the formation of a protective tribofilm. Welsh (1957, 1965) studied changes in wear mechanisms of steels, and discussed the role of hardness, sliding speed and load (frictional heating) in such wear transitions. Sullivan and Hodgson (1988) studied severe-to-mild transitions and indicated the increase in thickness on the strain hardened subsurface layer with load and speed. The work developed by Godet (1984) and by Berthier et al. (1988) showed that wear also depends on debris formation and debris ejection and argued that less conforming geometries (e.g. Ball-on-disc configurations) more easily eject the debris from the interface than conforming ones. In this sense, the contact behavior in BoD tests is less dependent on third body accommodation. More recently, wear transitions have been studied on steels, and aspects such as strain hardening and third body transformation have been discussed by: Iwabuchi, Hori and Kubosawa (1988); Jiang, Stott and Stack (1998); Goto and Amamoto (2003, 2006); Hiratsuka and Goto (2000); Hiratsuka and Muramoto (2005); Kato (1990, 2003,2007); and Kato and Komai (2007). Czichos (1977, 1978) has proposed a systems analysis approach for wear studies. Wear being a function of the operating variables, the elements of the system and their properties, and the wear mechanisms (BAHADUR, 1978), and depending on the interplay of the various effects and influencing factors. Ashby et al. (LIM; ASHBY, 1987) classified the unlubricated sliding wear of steel by means of the wear maps, into seven elementary mechanisms of material removal. Such maps show that there are well-defined boundaries between

wear regimes, that is, small changes in contact pressure and/or sliding speed may result in a transition between different wear mechanisms.

### *Wear transitions in nitrided steels*

In 1998, Kato and coworkers (KATO et. al., 1994) conducted a comparative study of the tribological behavior (pin on disc tests) of an untreated ferritic steel (C 0.4wt.%, Cr 1.6wt.%) with the gas nitrided conditions. Both samples were tested in unidirectional dry sliding against a martensitic disc (C 1.0wt.%, Cr 1.4wt.%) - the counterbody. Nitriding in the treated samples was conducted in a gas atmosphere (NH<sub>3</sub>) at 520°C for 80 hours. The nitrided layer was constituted by a 30 µm thick compound layer (ε-Fe<sub>3</sub>N) and a rather large diffusion layer (~700 µm thick). Hardness values of the pins were 260HV for the untreated condition, and 1150HV0.3 for the nitrided pins. The hardness of the disc was 700HV. The (uniform) nominal contact pressures were varied between 0.6 and 63.7 MPa and the (constant) sliding speeds between 0.2 and 5 m/s. The summary of their results is presented in Table 2.5 for the untreated steel and in Table 2.6 for the gas nitrided steel.

Table 2.5. Summary of wear results for the untreated EN41B steel in Kato et. al. (1994)

Untreated EN41B steel			
Wear regime	Mild	Severe	Extremely-severe
Type of wear curve <sup>2</sup>	A, B	C, D	E
Wear rate [mg/m]	1e-4 to 1e-2	1e-2 to 1e-1	1 to 10
PIN (CYLINDER)	Smooth surface No plastic deformation Patchy oxides	Rough surface Plastic deformation "White etched" layer	Heavy plastic deformation
DISC	Smooth surface Patchy oxides	Rough surface	Transferred particles ("white-etched")
Wear debris	Fine (~1 µm) Oxidized (Fe <sub>2</sub> O <sub>3</sub> , Fe <sub>3</sub> O <sub>4</sub> )	Medium (~50 µm)	Large (1 mm)

A running-in behavior (<250 m) was observed in the untreated EN41B steel at low contact pressures (1.3 - 3.2 MPa) - high wear rates followed by a decrease to a lower constant value. No (significant) plastic deformation was observed in the surface

<sup>2</sup> Type A The wear rate is very low and constant throughout the duration of the test.  
 Type B High initial wear rate, followed by a decrease to a lower constant.  
 Type C The wear rate Increases as the sliding distance increases.  
 Type D The wear rate is high and constant Throughout the duration of the test.  
 Type E The wear rate is very high throughout the duration of the tests, which is fairly short

of the mild wear specimens. In contrast, heavy plastic deformation in the subsurface layer was evidenced ( $\sim 200 \mu\text{m}$  deep). Several wear transitions were observed with increasing load: a)  $T_1$  transition (at 6.4 MPa): from a low-load-mild wear ( $3\text{e-}3 \text{ mg/m}$ ) to a severe -plastic/adhesive- wear ( $3\text{-}8 \text{ e-}2 \text{ mg/m}$ ), b) a  $T_2$  transition (at 25.5 MPa): from a severe wear to a high-load-mild wear ( $2\text{e-}2 \text{ mg/m}$ ), and c) a  $T_S$  transition (at 38.2 MPa): from severe wear to extremely-severe ( $4 \text{ mg/m}$ ).

Table 2.6. Summary of wear results for the gas nitrided EN41B steel in Kato et. al. (1994)

Gas nitrided EN41B steel		
Wear regime	Mild	Severe
Type of wear curve	A, B	C
Wear rate [mg/m]	$1\text{e-}4$ to $1\text{e-}2$	$1\text{e-}2$ to $1\text{e-}1$
PIN (CYLINDER)	Smooth surface No plastic deformation	Rough surface Plastic deformation "White etched" layer
DISC	Smooth surface Patchy oxides	Transferred particles ("white-etched")
Wear debris	Very fine ( $\sim 0.5 \mu\text{m}$ ) Oxidized ( $\text{Fe}_2\text{O}_3$ , $\text{Fe}_3\text{O}_4$ )	Large ( $\sim 200 \mu\text{m}$ ) Metallic (Fe) Oxidized (FeO)

On the other hand, the running-in behavior ( $< 500 \text{ m}$ ) in the gas nitrided EN41B steel was observed at low contact pressures (1.3 - 3.2 MPa). No extremely-severe wear regime was observed in the gas nitrided steel, which exhibited mild wear over the whole load and speeds ranges investigated. Nitriding reduced the wear rate in the low-load-mild wear regime ( $L < L_{T1}$ ) from  $3\text{e-}3 \text{ mg/m}$  (untreated) to  $1.6\text{e-}4 \text{ mg/m}$ . Gas nitriding reduced the wear rates in the severe wear regime ( $L_{T1} < L < L_{T2}$ ) from  $3\text{-}8 \text{ e-}2 \text{ mg/m}$  (untreated) by one ( $1\text{e-}3 \text{ mg/m}$ ) or two orders of magnitude ( $1\text{e-}4 \text{ mg/m}$ ). Nitriding also reduced the wear rate by a factor of four in the high-load-mild wear ( $L > L_{T2}$ ), from  $2\text{e-}2 \text{ mg/m}$  to  $5\text{e-}3 \text{ mg/m}$ . Gas nitriding increased the  $T_1$  transition (nominal) contact pressure from 0.6 MPa to 19.1 MPa, leading to a wider mild wear regime. The authors argue that "the wear behavior of the gas nitrided pin was controlled mainly by the diffusion layer" because "the thickness of the compound layer was *only*  $30 \mu\text{m}$ ", and "this layer was worn away quickly" (KATO et. al., 1994). Nevertheless, there was no evidence of the wear-off of the compound layer.

Finally, based on the characteristics of the wear debris, wear maps were produced (for both untreated and gas nitrided steels), to indicate the dominant regimes of the wear mechanisms as a function of nominal contact pressure and sliding speed.

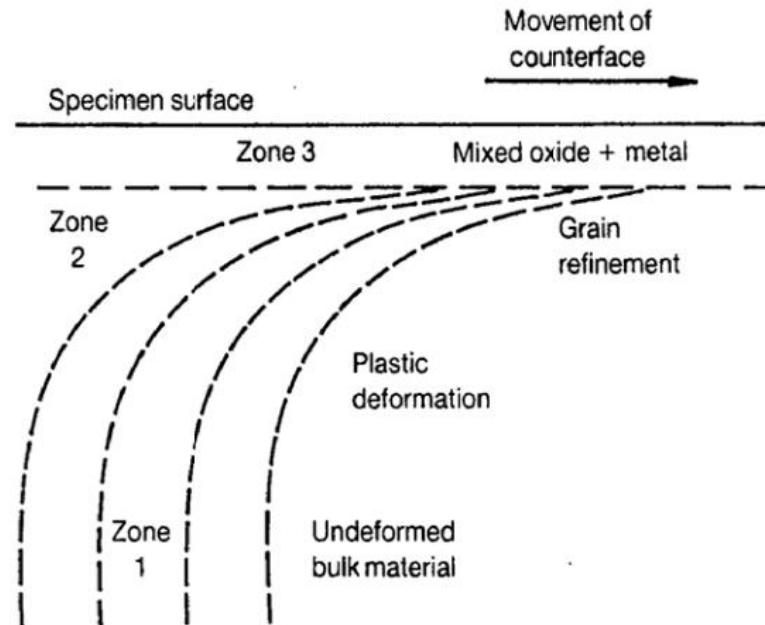
They concluded that gas nitriding did not only reduce the wear rate of the steel, but also expanded the mild wear region toward higher loads and sliding speeds.

### *Subsurface deformation*

The role of hardness as a central variable affecting the sliding behavior of steel tribosystems in dry sliding conditions has been reviewed (RIGNEY, 1994). Variations in hardness affect the tribological behavior of the steels of the tribosystem and can cause wear transitions (VIÁFARA; SINATORA, 2012). Local variations of hardness are produced during the sliding of metals in both surfaces in contact due to the large plastic strains at the sliding interface and large strain gradients in the near-surface material. The severe shear conditions cause plastic deformations on the subsurface regions resulting in strain hardening of the surfaces, which can have several consequences. On one hand, they cause the removal of metallic debris by means of mechanical mechanisms like the breakage of adhesive junctions, the formation of grooves and scratches due to plastic deformations of surfaces, and the nucleation and propagation of surface and subsurface cracks and voids. On the other hand, they create refined deformation subsurface layers which affect the relative overall hardness of the contacting bodies (WELSH, 1965; RIGNEY, 1997; HEILMANN et. al., 1983). Figure 2.8 shows how the shear strain increases towards the surface, as illustrated in Hutchings (1992): Zone 1 corresponds to the undeformed bulk material; Zone 2 contains plastically deformed material with plastic shear strains increasing towards the surface; and next to the free surface, Zone 3 is grain refined (sub-micrometer), and can contain both material transferred from the counterface and oxides (mechanically mixed layer).

The development of the deformation substructures is accompanied by changes in hardness, that is, subsurface strain hardening (HIRATSUKA; GOTO, 2000). Strain hardening of the subsurface region reduces further plastic deformation of the surfaces, hindering adhesive mechanisms that cause further material transfer (STACHOWIAK; BATCHELOR, 2005; HIRATSUKA; GOTO, 2000). In this sense, hardness is a central variable controlling transitions to mild wear, both from the point of view of the bulk materials (VIÁFARA; SINATORA, 2011) and of the surface region (HIRATSUKA; GOTO, 2000; DUMBLETON; DOUTHETT, 1977; HSU; AHN; RIGNEY, 1980; YANG; NAYLOR; RIGNEY, 1985; FARGAS; ROA; MATEO, 2016; FARIAS et. al., 2007).

Figure 2.8. Schematic diagram of the distribution of severity of plastic deformation beneath a worn metal surface in a severe wear regime. (Adapted from Rice, Nowotny and Wayne, in Rhee, Ruff and Ludema. ASME, Wear of materials (1981) pp. 47-52)



Source: (HUTCHINGS, 1992).

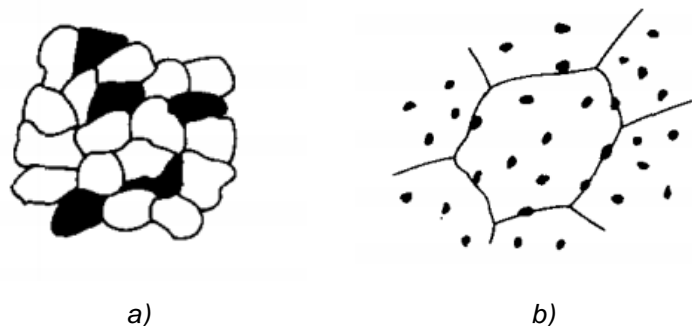
It must be noted that additional effects are relevant in the transformation and development of the subsurface layer. For instance, austenitic steels are known to have: low hardness and mechanical resistance on one hand, and high ductility and strain hardening tendency on the other. These aspects of mechanical behavior influence the intensity (and extension) of strain hardening which is closely related to the austenite stability of the steel, that is, a consequence of the alloying elements. Austenite in the austenitic SS with low Cr and high Ni, Mn, N and Cu are more stable and, therefore, have differentiated strain hardening properties (HSU; AHN; RIGNEY, 1980; YANG; NAYLOR; RIGNEY, 1985). Intense strain hardening of the subsurface region is known to be related to the strain-induced martensite transformation (SIMT) of austenite (DUMBLETON; DOUTHETT, 1977; HSU; AHN; RIGNEY, 1980; YANG; NAYLOR; RIGNEY, 1985; FARGAS; ROA; MATEO, 2016; FARIAS et. al., 2007). Different grades of austenitic SS form different amounts of martensite ( $\epsilon$  and  $\alpha'$ ), depending on austenite stability and on how large the deformation imposed (affected material volume): macroscopic deformations (e.g. forming processes) or microscopic deformations (tribological surface interactions) (DUMBLETON; DOUTHETT, 1977; HSU; AHN; RIGNEY, 1980; FARIAS et. al., 2007). The amount of martensite existing

before dry sliding, called pre-existing martensite (FARGAS; ROA; MATEO, 2016), affects the posterior amount of martensite formed as a consequence of wear-induced deformation of the subsurface. The role of SIMT has been widely discussed. Some authors suggest that it increases wear resistance, by increasing the overall hardness of the deformed layer and hence the surface load-carrying capacity (DUMBLETON; DOUTHETT, 1977; HSU; AHN; RIGNEY, 1980). Other authors argue that it is detrimental for wear resistance, because it can induce a transition to a more severe and fragile wear mechanism (delamination). The hard wear particles entering the interface can act as abrasive media (HSU; AHN; RIGNEY, 1980; YANG; NAYLOR; RIGNEY, 1985; FARGAS; ROA; MATEO, 2016). That is, high amounts of martensite (whether preexisting or due to sliding) would cause high wear, when compared to the annealed condition of the steel.

*Effect of second phases in sliding wear of alloys*

Second hard phases can precipitate in the matrix of steel (and other alloys) during heat treatments. This kind of steels are called multiphase alloys or aggregates (DIETER, 1988). The different microstructures that may be encountered can be classified in two major types: Aggregated structure and dispersed structure (See Figure 2.9).

Figure 2.9. Types of two-phase microstructures. Aggregated microstructure (a), and dispersed microstructure (b).



Source: (DIETER, 1988).

Figure 2.9a shows the aggregated type of two-phase structure. The size of the second-phase particles is of the order of the grain size of the matrix. The other general type of structure is called dispersed two-phase structure, in which each particle is

surrounded by a matrix of a single orientation (grain). The size of the second phase is much finer for the dispersed structure and may extend down to submicroscopic dimensions. The mechanical strength (and wear resistance) of such two-phase alloys depends on different parameters of the second phases such as shape, size, quantity or volume fraction, and distribution. Localized internal stresses arise from the presence of second-phase particles in a continuous matrix phase and may result in the modified mechanical behavior of the continuous phase (DIETER, 1988).

Parameters (properties) related to both matrix and second phases such as strength, ductility, and strain-hardening behavior can strongly influence the mechanical behavior of such type of alloys (heterogeneous), along with the crystallographic fit between the phases, and the interfacial energy and interfacial bonding between them (DIETER, 1988; ZUM GAHR, 1998).

Hard reinforcing phases can reduce wear by abrasive particles (e.g. strain hardened wear debris) if the *mean free path* between the second phase particles is smaller than the abrasive particle. However, large phases weakly bonded to the matrix can be detached and can lead to further fracture and detachment at the interface (ZUM GAHR, 1998). Under mild operating conditions abrasive wear decreases with increasing volume fraction of the reinforcing phase. Under severe conditions with fracturing and detachment of the reinforcing phase, wear can increase.

### *Friction in sliding wear*

Friction is the resistance to movement experienced by a body in contact and moving over another (HUTCHINGS, 1992; BLAU, 2009). This resistance to movement is characterized by a force (the friction force) that is intrinsically related to the phenomena responsible for frictional dissipation between the sliding bodies, occurring at the interface and in the region near that interface (RIGNEY; HIRTH, 1979). The basis for the understanding of the dependence of frictional resistance on the systems variables (load, speed and area of contact) were set by the works of Leonardo da Vinci (1452-1519), Guillaume Amontons (1663), and Charles-Augustin de Coulomb (1736-1806) (BURWELL; STRANG, 1952). Their contributions are known as the laws of friction.

The frictional dissipation in a system is most frequently characterized via the *friction coefficient* ( $\mu$ ), which is the constant of proportionality between the friction force (F) and the normal load (L):

$$\mu = F/L \quad (\text{Equation 3})$$

In metals sliding in air, the friction coefficient is often constant for a wide range of loads and sliding speeds. (HUTCHINGS, 1992). Nevertheless, under different regimes of wear (severe/mild) different friction coefficients are expected. According to the classic theory of friction (BOWDEN; TABOR, 1956) the mechanisms responsible for friction during (metallic) dry sliding are plastic deformation and adhesion. Nevertheless, Amontons had already indicated that also elastic deformation of asperities during sliding was fundamental to friction. Adhesion is also related to material transfer, which occurs when the adhesive forces at the junctions are stronger than the cohesive strength of the softer of the two materials. In this sense, adhesion (and junction growth) is more predominant among very soft and ductile metals (HUTCHINGS, 1992). During oxidative wear, plastic deformation and adhesion occur on the interfacial film rather than in the bulk. Hence, it is expected that frictional energy be transformed in a different manner during this type of wear.

In addition, friction is not only a superficial phenomenon, but also it is associated to a volume. The subsurface deformation resulting from the tribological interaction (e.g. the plastically deformed layers) is an important consideration (RIGNEY AND HIRT, 1979). In this sense, it is also important to differentiate between the stored and the dissipated fractions of the frictional energy. As reviewed by Viáfara (2010), friction is related to: heat, creation of new surfaces (wear), and to the deformation of the surface and subsurface regions. Other conditions must be considered in cases where there are wear particles at the interface

It is necessary to analyze the dissipative frictional processes in relation to the operation of a predominating wear mechanism during sliding wear for the computation of representative parameters of a particular tribosystem (e.g.  $k$ ). However, the relation between friction and wear is a complex one, which is revealed by the great number of wear models and the difficulty in predicting the evolution of wear with friction coefficient (BURWELL; STRANG, 1952). There are different manners in which the frictional energy is transformed. Other than that, while all asperity contacts contribute to friction

only a very small fraction of contacts result in wear. Thus, while friction is dominated by the contact events that occur without damage, wear is dominated by the (small) chance that a particular contact event results in rupture (i.e. the wear coefficient). In this sense, high friction does not necessarily traduce in catastrophic wear ([SCHNURMANN, 1962](#)), as long as the dissipated energy is spent in other processes different of wear.

### 3 OBJECTIVE

#### 3.1 GENERAL OBJECTIVE

To investigate the changes occurring during the running-in of four different steel-on-steel tribosystems and their relation to hardness and the variation in nominal contact pressure during dry sliding tests in ball-on-disc reciprocating contacts.

#### 3.2 SPECIFIC OBJECTIVES

- To perform a set of tribological tests in four different steel-on-steel tribosystems with different hardness and microstructural features to investigate the changes occurring during the running-in period and to evaluate the consequences of these changes on the overall tribological performance of each system.
- To evaluate the subsurface deformation and tribo-oxidation of the selected tribosystems under the specified testing parameters during the running-in stage of interaction.
- To characterize the tribological behavior of the SAE XEV-F valve steel with and without nitriding and to discuss its technological implications.

## 4 MATERIALS AND METHODS

### 4.1 MATERIALS

Four tribosystems were used for this study. Two of the tribosystems are composed of the SAE XEV-F valve steel, provided by [Villares Metals S.A.](#) (Brazil). This alloy is a precipitation hardening austenitic stainless steel (PH austeniticSS). The precipitates range in sizes from submicrometer to 50  $\mu\text{m}$ . One tribosystem corresponds to the untreated steel while the other is salt-bath nitrided, as commonly performed in exhaust valves. The other two tribosystems, considered as reference materials, are composed of an austenitic stainless steel (AISI 310) and a martensitic high-speed steel (AISI H13). The balls (i.e. counter-bodies) were made of AISI 52100, a martensitic ball bearing steel. The nominal chemical compositions of the disc and ball steels are presented in [Table 4.1](#).

[Table 4.1](#). Nominal chemical composition of the tested steels<sup>3</sup>.

El.	AISI 310	SAE XEV-F	AISI H13	AISI 52100
<b>C</b>	< 0.25	0.50	0.40	1.00
<b>Cr</b>	25.00	21.00	5.00	1.40
<b>Mn</b>	< 2.00	9.00	0.35	0.35
<b>Ni</b>	21.00	4.00	-	-
<b>Nb</b>	-	2.20	-	-
<b>W</b>	-	1.20	-	-
<b>N</b>	-	1.00	-	-
<b>Mo</b>	-	-	1.40	-
<b>V</b>	-	-	1.00	-
<b>Fe</b>	Bal. (~50.60)	Bal. (~60.65)	Bal. (~90.85)	Bal. (~96.95)

The diameter of the balls was 10 mm. For the preparation of the discs, round bars of each steel having diameter of 25.4 mm were first turned to a diameter of 24 mm and then cut into discs of ~11 mm in height. Cutting was conducted using electrical

<sup>3</sup> The nominal chemical composition of the SAE XEV-F valve steel was provided by the manufacturer. The nominal chemical compositions of the AISI 310, AISI H13 and AISI 52100 steel were obtained from the matweb database (see <http://www.matweb.com/>).

discharge machining (EDM). This height was later reduced to 9 mm for subsequent finishing processes (grinding) until reaching the final height ( $7.9\pm 0.1$  mm).

Heat treatment of the SAE XEV-F valve steel discs was conducted according to the specifications of the manufacturer, as shown in [Table 4.2](#). The other steels were treated according to usual practices. Uniform treating conditions (temperature, atmosphere, pressure) were maintained between batches of the samples to ensure that no important variations occurred between the microstructures of the tested samples.

[Table 4.2](#). Heat treatments performed on the sample steels.

Sample	Heat treatment
<b>AISI 310</b>	Solubilized for 1 h (Heated between 1050 and 1100 °C for 1 h, cooling in water/air)
<b>SAE XEV-F</b>	Solubilized for 1 h (Heated between 1050 and 1100 °C for 1 h, cooling in water/air) + Precipitation hardening (15 h at 815 °C) in a controlled argon atmosphere and air cooling.
<b>AISI H13</b>	Quenched in air from 1050 °C + Two tempering stages at 550 °C in a controlled argon atmosphere and air cooling.

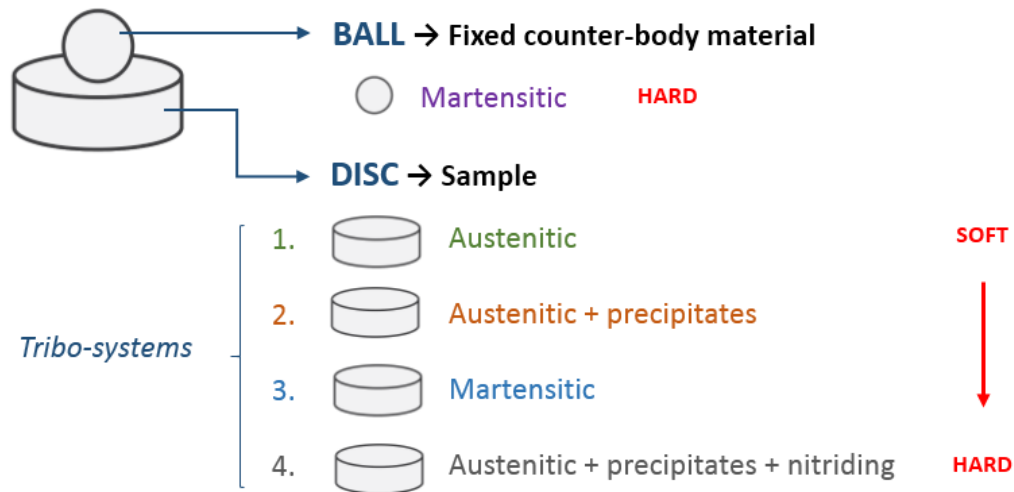
The different heat treatments and chemical compositions lead to different hardness and particular microstructural characteristics in each of the sample steels. In this sense, four tribosystems with different hardness were tested in the present study. The schematic description of the studied tribosystems is shown in [Figure 4.1](#).

After heat treatment, surface finishing of the discs was conducted. In order to ensure parallelism, both sides of the discs were ground in a tangential machine using synthetic cutting fluid and a 254 mm diameter grinding wheel (reference:  $\phi 10''$ AA60) made of white aluminum oxide. A final grinding pass was performed with a shallow cutting depth (0.1 mm) to avoid burns and other surface finishing defects that may influence the tribological behavior. At the final stage of surface finishing, mirror polishing was conducted using a final pass in a suspension of abrasives with an average particle size of 1  $\mu\text{m}$ .

The nitrided discs were obtained through the ARCOR® process, provided by [HEF-Durferit](#) (Brazil). This thermochemical surface treatment consisted of the

immersion of a portion of the polished SAE XEV-F valve steel discs in a salt bath, composed of carbonates and cyanates, for 50 min at 530 °C. Before nitriding the discs were cleaned employing detergent and then pre-heated in air for 15 - 30 min at 300 - 400 °C.

Figure 4.1. Schematic description of the studied tribosystems.



## 4.2 TRIBOLOGICAL TESTS

Tribological tests were conducted using an SRV®4 tribometer manufactured by Optimol Instruments. Figure 4.2 shows a detailed view of the ball-on-disc contact configuration.

In this type of tribometer, one ball and one disc are placed in the test chamber and loaded against each other. Then the ball is oscillated with respect to the disc for tribological interaction. During this interaction, friction coefficient and other variables (e.g. relative humidity and chamber temperature) are continuously recorded. The controlled variables in this equipment are: load, frequency, stroke, and temperature of the lower support structure called the block. The tests were conducted in dry sliding conditions and the measured values of relative humidity of air varied between 40 and 55%. Four (4) repetitions were conducted for each experimental condition. The selected parameters for testing are presented in Table 4.3. These parameters were selected based on the operational limits of the SRV equipment.

Figure 4.2. Detail of the ball-on-disc contact configuration in an SRV@4 tribometer. The surface of the disc was polished to a mirror finish.

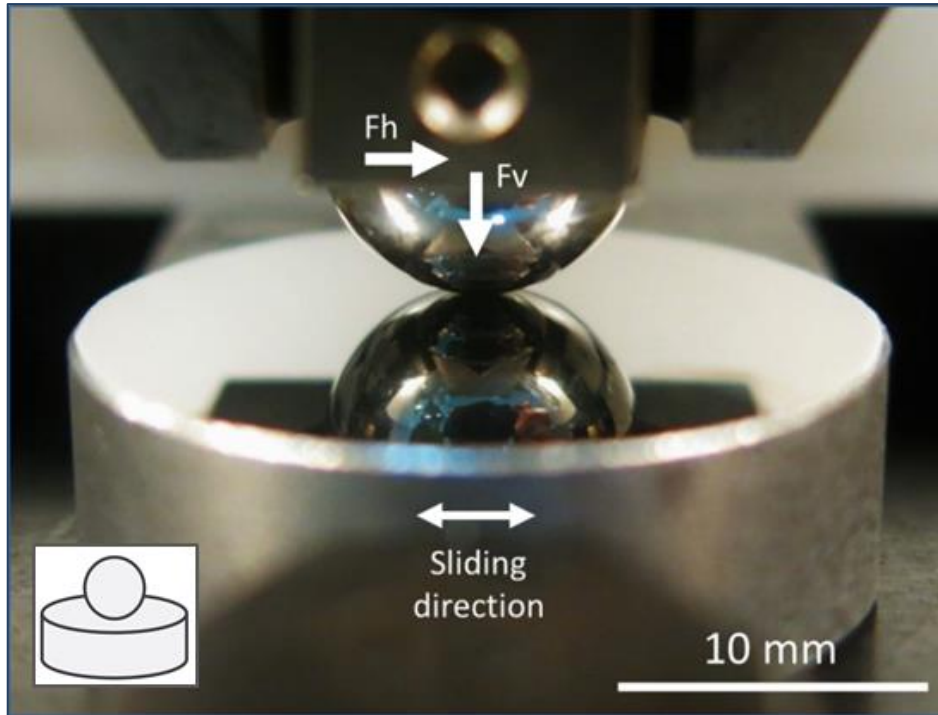


Table 4.3. Parameters for tribological tests.

Parameter	Value
Temperature	Room
Testing time [min / s]	30.5 / 1830
Sliding distance [m]	73.2
Load [N]	100
Hertz contact pressure <sup>4</sup> (max. / mean <sup>5</sup> ) [GPa]	2.18/1.45
Frequency [Hz]	10
Stroke [mm]	2
Linear Speed (max. / mean) [m/s]	0.13/0.08

Test Method ASTM G 133, Procedure A (2005) provides the general outlines for linearly reciprocating ball-on-flat sliding wear laboratory testing. The tests performed in this work are not in full compliance with the provisions of the ASTM method, because: the normal force in these tests was 100 N, instead of 25 N; the stroke length was 2 mm, instead of 10 mm; the oscillating frequency was 10 Hz instead of 5 Hz; and the fact that the wear volume was controlled by means of mass losses and not

<sup>4</sup> Hertz contact parameters were determined for a steel ball of 10 mm in diameter against a flat steel. For practical purposes, a Young's modulus of 200 GPa and a Poisson's ratio of 0.29 was used for both materials.

<sup>5</sup> Arithmetic mean over the nominal area

geometrically as prescribed by the standard. All other provisions of Test Method G 133 have been followed. The differences between the values specified by the ASTM method and the ones selected present work are due to equipment limitations and other considerations related to ease of wear characterization.

### 4.3 CHARACTERIZATION

The samples (materials and surfaces) were characterized before and after wear (resulting from tribological tests). The process was also monitored by means of the friction coefficient and high-speed filming. Several other techniques were used for characterization. [Table 4.4](#) shows a summary of the characterization techniques. The technical specifications of the equipment used are presented in [Table 4.5](#).

[Table 4.4](#). Characterization techniques.

CHARACTERIZATION TECHNIQUE	ANALYSIS		
	Unworn surfaces	Process (records)	Wear scars
Friction coefficient	-	X	-
High speed filming	-	X	-
SEM + EDS	X	-	X
Image Analysis	X	-	X
XRD	X	-	X
Hardness	X	-	X
CCI	X	-	X
Mass	X	-	X

#### *Sample characterization (bulk and surface)*

Before the tests, the characterization conducted on the discs were: microstructural evaluation, hardness, subsurface hardness and topography. Bulk material microstructure and hardness measurements are the reference values for assessing mechanical and microstructural alterations in the surface region. Other reference values were subsurface hardness and topography of the polished surface.

Microstructural characterization of the bulk materials and surfaces was performed via SEM with detectors of secondary electrons (SE) and backscattered electrons (BSE), aided by Energy-dispersive X-ray Spectroscopy (EDS) analysis. Surface preparation consisted on: *a*) polishing the surface to a mirror finish ( $S_a < 0.15 \mu\text{m}$ ), *b*)

cleaning with detergent, c) immersing for 10 min. in an ethanol bath assisted by ultrasound, and d) drying with compressed clean air. For the microstructural examination, chemical etching was used depending on the sample: a) Vilella etching was used for the martensitic steels (AISI 52100 and AISI H13), the samples were plunged for 10 s and b) electrolytic etching at 3 V for 90 s in oxalic acid (10%) for the austenitic steels. Phase identification was based on microscopy and supported by XRD analysis, using Cu K $\alpha$  radiation with a voltage of 45 kV and an electrical current of 40 mA. XRD measurements were conducted over an angle range of 10-110° (2 $\theta$ ) with a step size of 0.02° and nominal time per step of 150 s.

Table 4.5. Technical specifications of the equipment.

Technique	Equipment	Details
Scanning Electron Microscopy	Jeol JSM-6010 la	<ul style="list-style-type: none"> <li>- Resolution: 4 nm at 20 kv.</li> <li>- Magnification: 5x to 300.000x.</li> <li>- Field of view: up to 25.4 mm.</li> <li>- Accelerating voltage: 500 v to 20 kv.</li> <li>- Imaging modes: secondary electron (SE) and backscatter electron (BSE).</li> <li>- Integrated energy dispersive x-ray analyzer (EDS).</li> </ul>
X-Ray Diffraction	Philips X'Pert Pro pw 3040/00	<ul style="list-style-type: none"> <li>- Detectors: sealed proportional counter and X'celerator PSD.</li> <li>- X-ray source: Philips high intensity ceramic sealed tube (3kw).</li> <li>- Wavelength: cu k<math>\alpha</math> (0.15405 nm).</li> <li>- Configurations: high-resolution (hr) and powder diffraction (pd).</li> <li>- Angle (2theta): 10-135 degrees.</li> </ul>
Non-contact 3D Optical Profilometry	Taylor Hobson CCI MP	<ul style="list-style-type: none"> <li>- Spatial resolution: 1024x1024 pixel array for large FoV.</li> <li>- 0.1 Å resolution over the entire measurement range.</li> <li>- &lt;0.2 Å rms repeatability. &lt;0.1% step height repeatability.</li> </ul>
Mass measurement (Analytical Balance)	Mettler Toledo xp205	<ul style="list-style-type: none"> <li>- Resolution: 0.01 mg</li> <li>- Maximum capacity: 220 g.</li> <li>- Repeatability (test weight): 0.015 mg in 10 g.</li> </ul>
Macro hardness (Vickers)	Buehler 1600-6306	<ul style="list-style-type: none"> <li>- Pyramidal diamond indenter</li> <li>- Load: 1 to 50 kgf.</li> </ul>
Micro hardness (Vickers)	Buehler micromet 2100	<ul style="list-style-type: none"> <li>- Pyramidal diamond indenter</li> <li>- Load: 5 to 300 gf.</li> </ul>
Nano hardness (Berkovich)	Hysitron TI950	<ul style="list-style-type: none"> <li>- Berkovich diamond indenter</li> <li>- Load: 2 to 10 mN (Low load module).</li> </ul>

Hardness was measured in all bulk materials, both at macro (30 kgf) and micro (0.1 kgf) scales with a Vickers pyramidal indenter. 10 indents were performed in each case. Nanoindentation (5 mN) was performed with a Berkovich indenter for mechanical characterization of individual phases: NbC, austenite and martensite. 27 indents were performed in the matrix and 10 indents were performed in different precipitates. To convert from GPa (obtained in the Nanoindentation measurements) to HV (as displayed in [Figure 5.14](#)), one must divide by a factor of 0.009807 as mentioned by Yovanovich (2006).

Subsurface nanohardness (5 mN) profiling was performed on cross-sectional areas of the discs to determine the extension and severity of subsurface strain hardening. Before profiling, the cut discs were mounted in hard resins for edge retention, in order to minimize edge defects that may interfere with the interpretation of the results.

Topography measurements were obtained via 3D optical profilometry (CCI). A 20x magnification lens with a field of view (FoV.) of 0.841 mm<sup>2</sup> was used for the measurement of an area of 2 mm<sup>2</sup> at the testing region. The discs were cleaned and dried before topography measurements, as described in the surface preparation procedure. The Talymap software (by Taylor Hobson) was used for surface characterization.

Mass measurements of discs and balls were conducted in a precision scale. These measured values were used to compute the metrics commonly used to quantify wear.

### *Test results records*

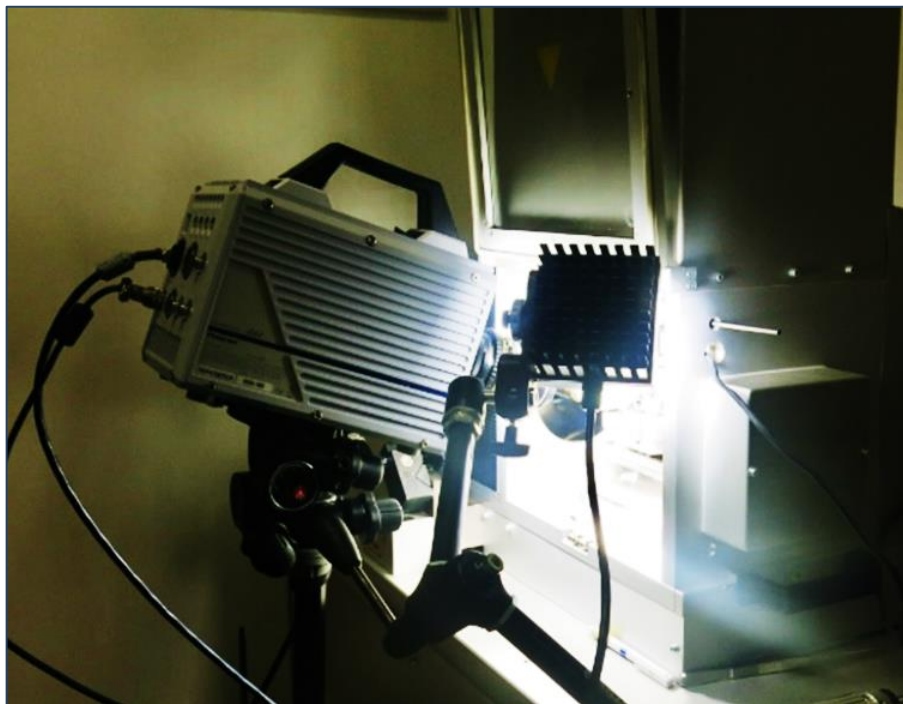
In each test, a sensor measures a real-time signal of the friction force ( $F_h$  in [Figure 4.2](#)) at a rate of 1 value every second, which is then divided by the normal load value ( $F_v$  in [Figure 4.2](#)) for obtaining the *friction coefficient* ( $\mu$ ) during the test. Monitoring the friction coefficient of a system allows to identify transitions in behavior that could be related with changes wear mechanisms.

High speed filming was performed with a *Fastcam SA4* equipment manufactured by *Photron*. The selected acquisition rate was 3000 fps (frames per second), considered adequate in relation to the oscillation frequency of test: 10 Hz (or 10 strokes

per second). Due to the high acquisition rate, intense illumination is necessary to enable acquisition. [Figure 4.3](#) presents the setup of the filming equipment.

High speed filming allowed the in-situ observation of evidence confirming certain hypotheses. Such results and friction coefficient analyzes suggested the need of performing tests interrupted at sliding distances that where selected based on the analysis of the friction coefficient. Results of such tests were analyzed by means of the characterization methodology previously described.

[Figure 4.3](#). High-speed filming equipment setup.



### *Wear characterization*

The main aspects evaluated in post examination of the worn discs and worn balls were: mass loss, nominal contact area, wear mechanisms, role of hard precipitates (in the SAE XEV-F valve steel samples), and subsurface deformation. After tribological testing and before mass loss measurements, loose debris were removed with compressed air from the surfaces of both discs and balls to avoid contamination of the sample arising from other cleansing media (e.g. alcohol bath), and to prevent the contamination of the SEM vacuum pump. The nominal area of the wear scars is an indirect measure of wear and was quantified in addition to mass loss. The wear

mechanisms were analyzed by inspection of the wear scars via SEM and EDS mapping. The subsurface deformation of the worn surfaces was evaluated by means of SEM observation of the etched cross-sections of the discs.

## 5 RESULTS AND DISCUSSION

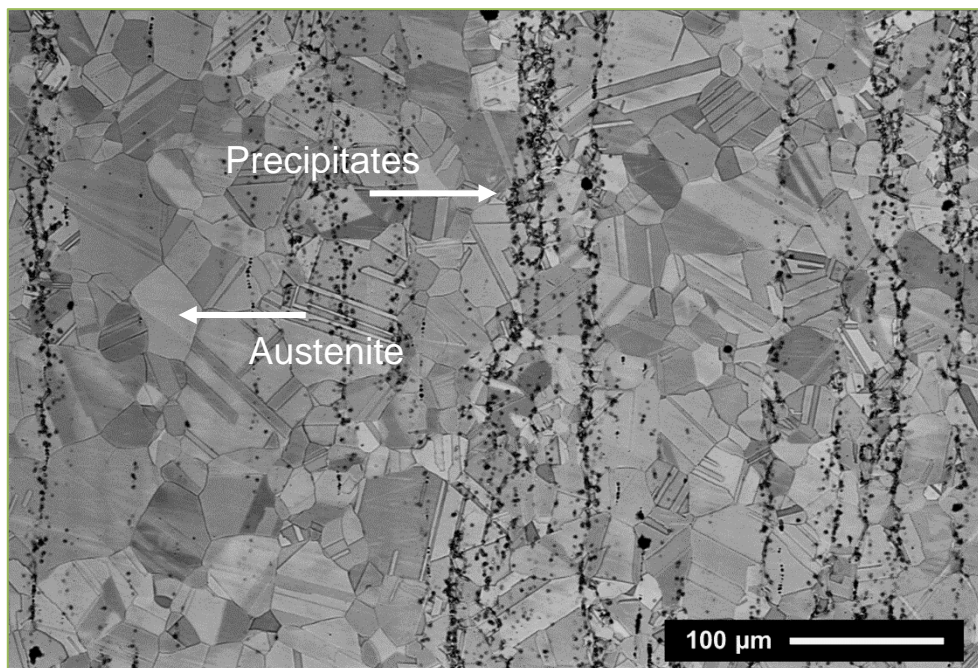
### 5.1 MATERIALS

This section presents the results of characterizations conducted in the condition before the wear tests. Microstructure, bulk hardness, subsurface hardness, and topography were evaluated for the steel surfaces, and the properties of the nitrided layer (composition, subsurface hardness and topography), for the treated disc.

#### *Microstructure*

SEM images were obtained using sensors for both secondary electrons (SE) and backscattered electrons (BSE) detection to investigate the steel microstructures. [Figure 5.1](#) shows the microstructure of the AISI 310 steel.

[Figure 5.1](#). Microstructure of the AISI 310 steel (SEM/BSE - 200x mag.).



The microstructure of the AISI 310 stainless steel shows an austenitic matrix with equiaxed grains with sizes smaller than 90  $\mu\text{m}$ . Precipitates were observed (signaled by a white arrow in [Figure 5.1](#)). [Figure 5.2](#) shows a detailed view of the microstructure of the AISI 310 steel. The precipitates are found both in the grain boundary and at the inside of some of the austenite grains (indicated by a white arrow) clustered in the

rolling direction (vertical direction in Figure 5.2). The XRD pattern of the AISI 310 steel for crystal structure identification is presented in Figure 5.3. Austenite (Reference JCPDS code: 00-031-0619) was identified as the main microstructural component. Chromium carbides of the types  $\text{Cr}_{23}\text{C}_6$  (JCPDS code: 00-035-0783) and  $\text{Cr}_7\text{C}_3$  (JCPDS code: 00-036-1482) were also detected. Some heat treatment twins can also be observed (Figure 5.2), which are commonly found in austenitic SS.

Figure 5.2. Detail of the austenitic microstructure of the AISI 310 steel. (SEM/SE - 1000x mag.)

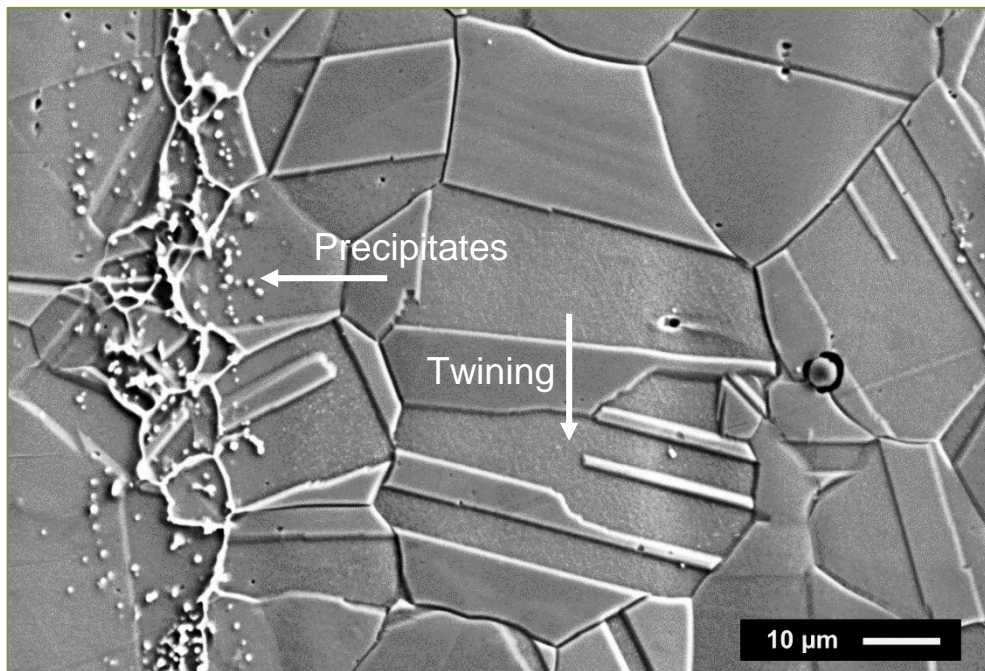
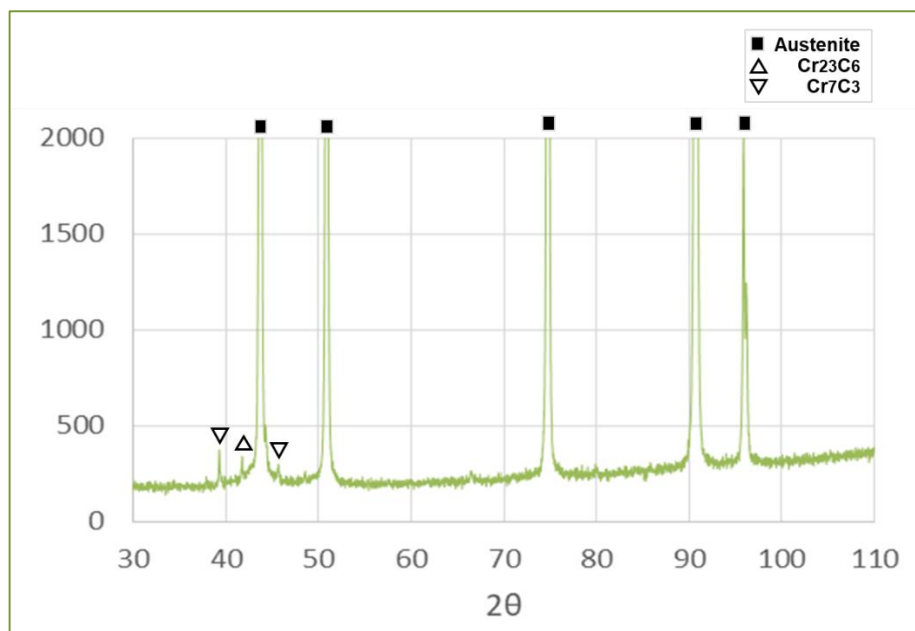
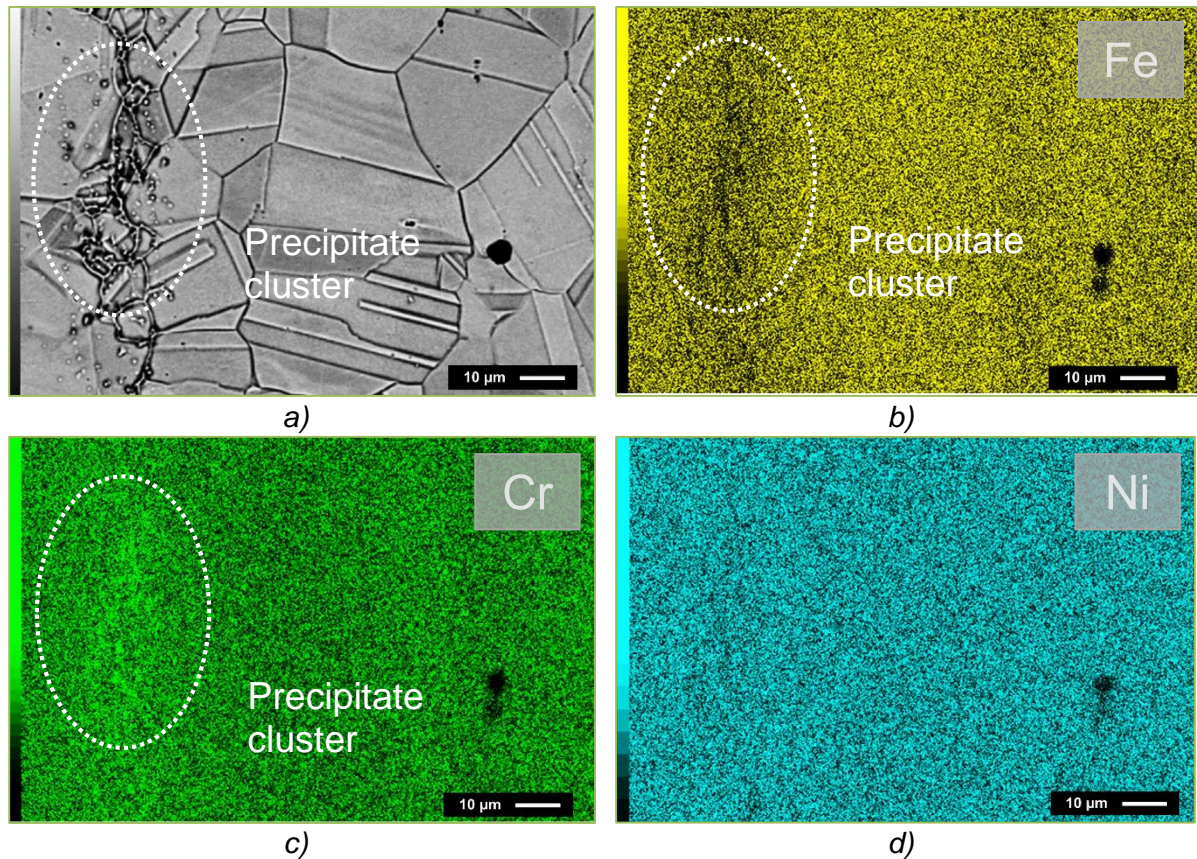


Figure 5.3. X-Ray diffraction pattern of the AISI 310 austenitic stainless steel.



Some clusters of precipitates were observed (Figure 5.2). EDS analysis (point and map) were conducted on precipitation zones to gain some insight on the nature of the observed clusters of precipitates. The results are show in Figure 5.4.

Figure 5.4. SEM analysis of precipitate clusters in the AISI 310 austenitic stainless steel. BSE image (a), and EDS maps of: iron (b), chromium (c), and nickel (d). (1000x mag.)



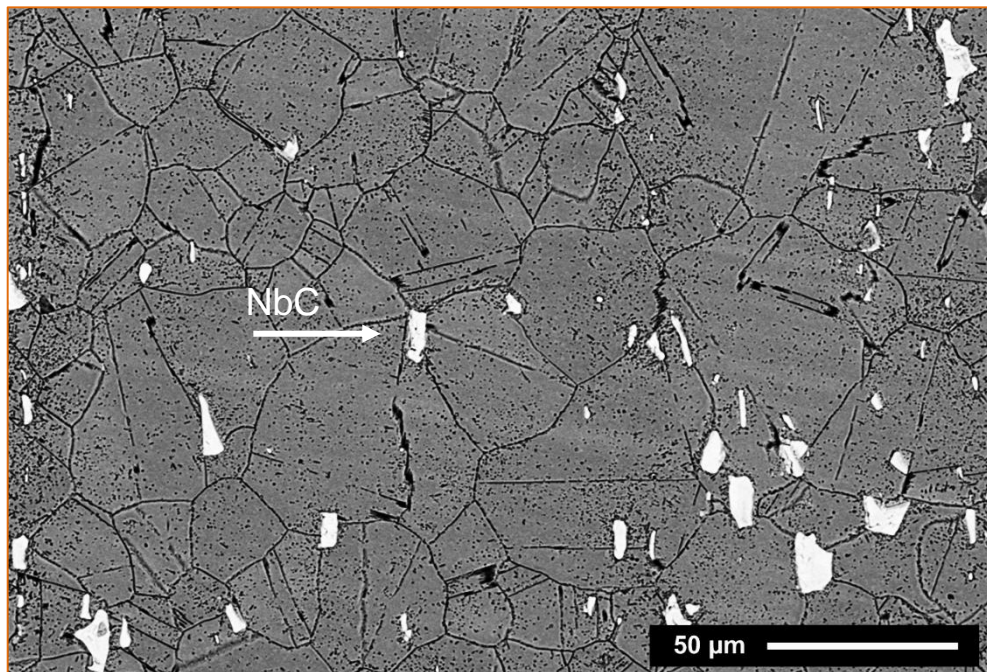
The observed precipitation clusters, highlighted in the SEM/BSE image (Figure 5.4a), appear as low concentration regions in the iron EDS map (Figure 5.4b). In contrast, the chromium EDS map (Figure 5.4c) shows high concentration regions (bright green) in the precipitation clusters, indicating chromium precipitation. However, EDS mapping is only a qualitative technique and does not allow to determine the nature of the observed precipitates. The nickel EDS did not show any preferential distribution, as can be confirmed from the noisy image in Figure 5.4d. XRD diffraction results identified the precipitates observed in Figure 5.1, Figure 5.2 and Figure 5.4, as chromium carbides ( $\text{Cr}_{23}\text{C}_6$  and  $\text{Cr}_7\text{C}_3$ ).

The hardness of the precipitates could not be measured due to their submicrometer size. Due to the submicrometer size and low volume fraction of

precipitates in the AISI 310 steel, it was considered homogeneous throughout the discussion presented in this thesis.

Figure 5.5 shows the microstructure of the SAE XEV-F valve steel. An austenitic matrix is observed, having equiaxed grains with sizes smaller than 80  $\mu\text{m}$ . Precipitates ranging in sizes between 1 and 20  $\mu\text{m}$  were also observed (white spots), and presented a random distribution in the matrix.

Figure 5.5. Microstructure of the SAE XEV-F valve steel (SEM/BSE - 500x).



Contrast in Backscattered electron SEM images emerges as a function of atomic density. The carbides contain a higher percentage of an element that has a higher atomic number than iron (probably niobium), hence showing up as a brighter region on the image. Intergranular and transgranular precipitates were predominantly observed. These precipitates were identified as niobium carbide -NbC- (JCPDS code: 00-002-1031) by XRD (Figure 5.6), which was expected for the SAE XEV-F valve steel (SHIRZADI; JACKSON, 2014). Chromium carbides ( $\text{Cr}_{23}\text{C}_6$  and  $\text{Cr}_7\text{C}_3$ ) were also identified in the XRD pattern.

An additional SEM analysis was conducted to study the precipitates in the SAE XEV-F valve steel (Figure 5.7). The niobium EDS map (Figure 5.7b) presented high intensity spots in the regions corresponding to the white precipitates observed in the BSE image (Figure 5.7a). This result confirms the identity of the precipitates and

illustrates how SEM/BSE images and Nb EDS maps can be useful in the study of the tribological role of NbC in sliding conditions.

Figure 5.6. X-Ray pattern of the SAE XEV-F valve steel.

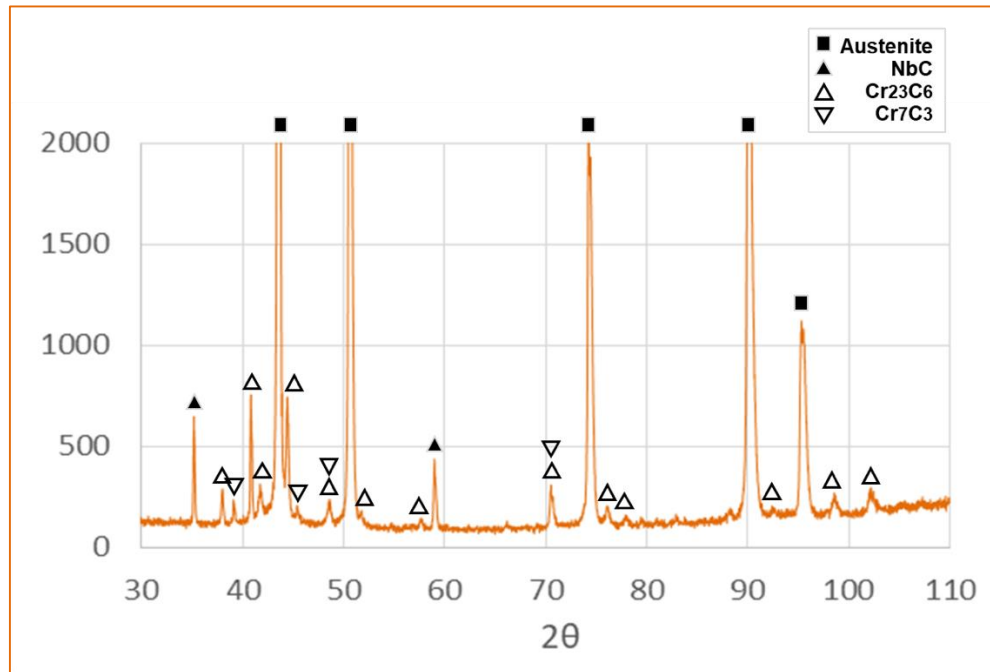
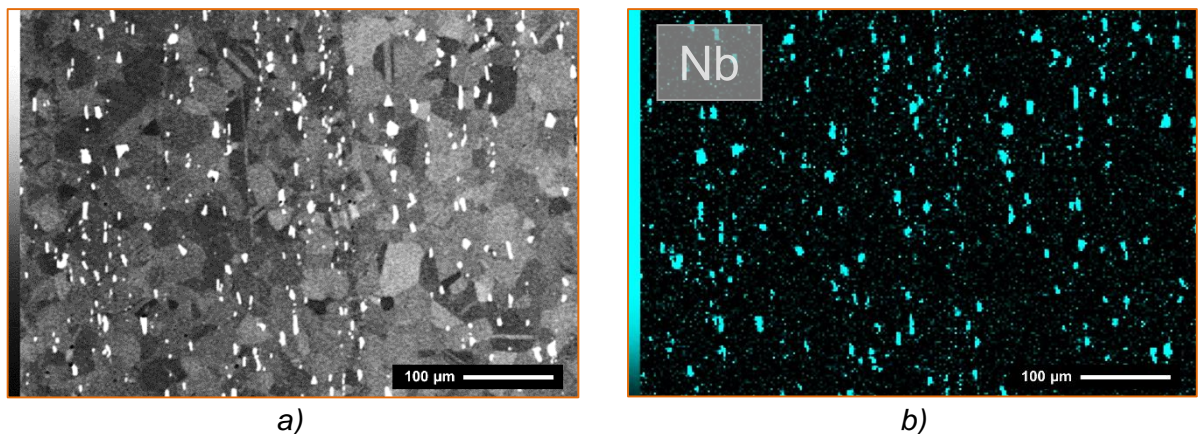


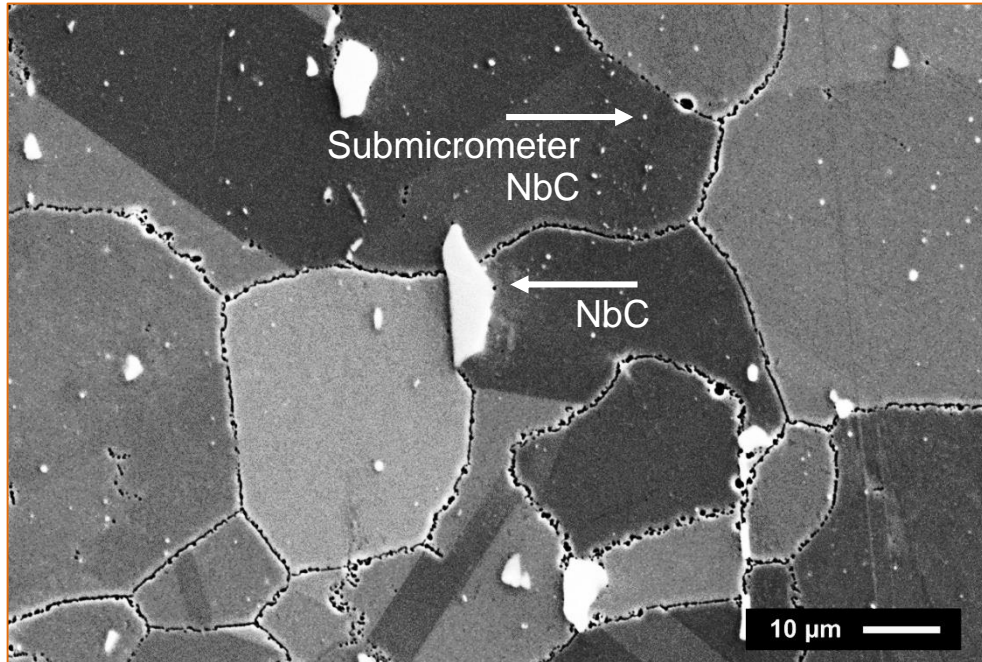
Figure 5.7. SEM analysis of precipitates in SAE XEV-F valve steel. BSE image (a), and EDS map of niobium (b). (200x mag.)



Niobium as alloying element in SAE XEV-F presents a two-fold benefit: on one hand, the Nb present as solid solution in the austenitic matrix will precipitate in submicrometer particles (mainly carbides) responsible for the precipitation strengthening of the matrix (Figure 5.8) (DIETER, 1988). On the other hand, niobium is a strong carbide forming element. Therefore, Nb above the solubility limit precipitates as carbides due to the available carbon in the steel (0.5 wt.%) inhibiting grain-boundary

chromium precipitation at treatment temperatures above 425°C (SHIRZADI; JACKSON, 2014).

Figure 5.8. Detail of submicrometer precipitates in the SAE XEV-F valve steel.  
(SEM/SE - 1000x mag.)



As mentioned, due to the presence of precipitates ( $> \sim 1 \mu\text{m}$ ), this steel can be considered as a heterogeneous material. The tribological behavior at the surface will depend on the interaction between the phases when submitted to the shear strains induced by dry sliding. Great differences between the mechanical properties of the phases in the scales evaluated can affect the interaction during tribological tests as will be presented further on.

Figure 5.9 shows the microstructure of AISI H13 tool steel. At this magnification, a homogeneous martensitic (JCPDS code: 00-044-1289) matrix is observed. Chromium carbides ( $\text{Cr}_{23}\text{C}_6$ ) were also identified in the XRD pattern (Figure 5.10).

Figure 5.9. Microstructure of the AISI H13 tool steel. (SEM/BSE - 500x mag.)

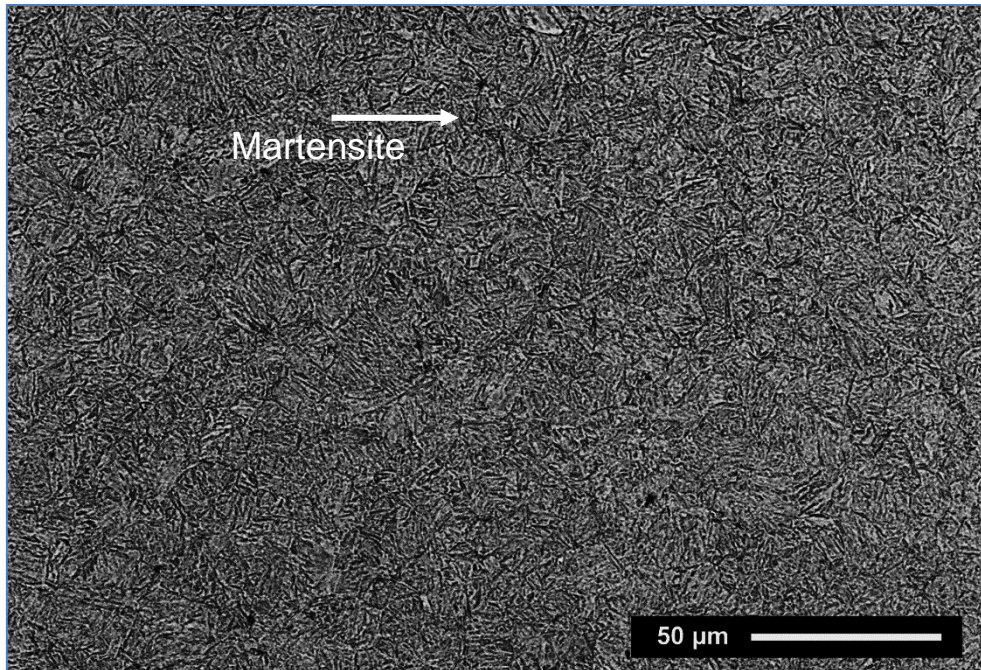
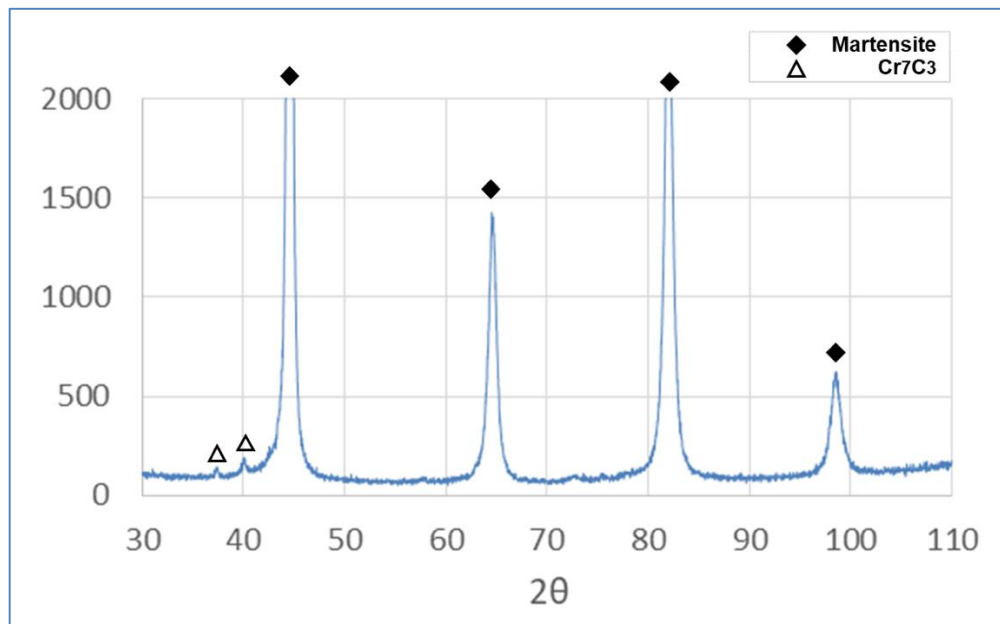


Figure 5.10. X-Ray pattern of the AISI H13 tool steel.



A detailed image of the martensitic microstructure of the AISI H13 tool steel reveals the submicrometer precipitates, better appreciated in a high magnification image such as that in (Figure 5.11).

Figure 5.11. Detail of submicrometer precipitates in the AISI H13 tool steel (SEM/SE - 5000x mag.).

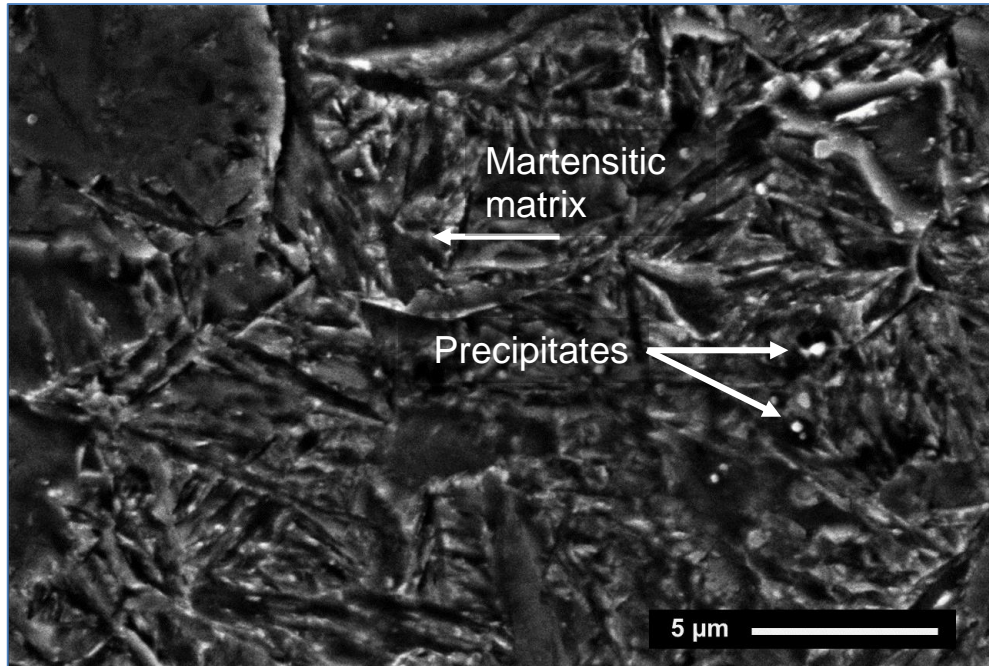


Figure 5.12 shows the microstructure of AISI 52100 bearing steel. The presence of submicrometer precipitates can be observed in the matrix. A detail of such microstructure can be seen in Figure 5.13.

Figure 5.12. Microstructure of the AISI 52100 ball bearing steel. (SEM/SE - 1000x mag.)

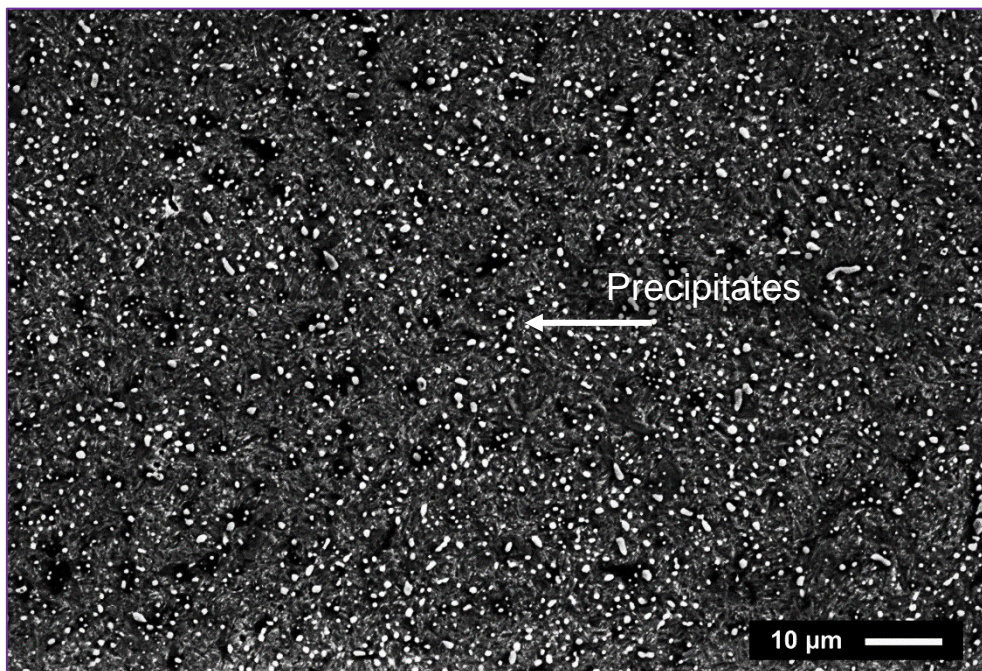
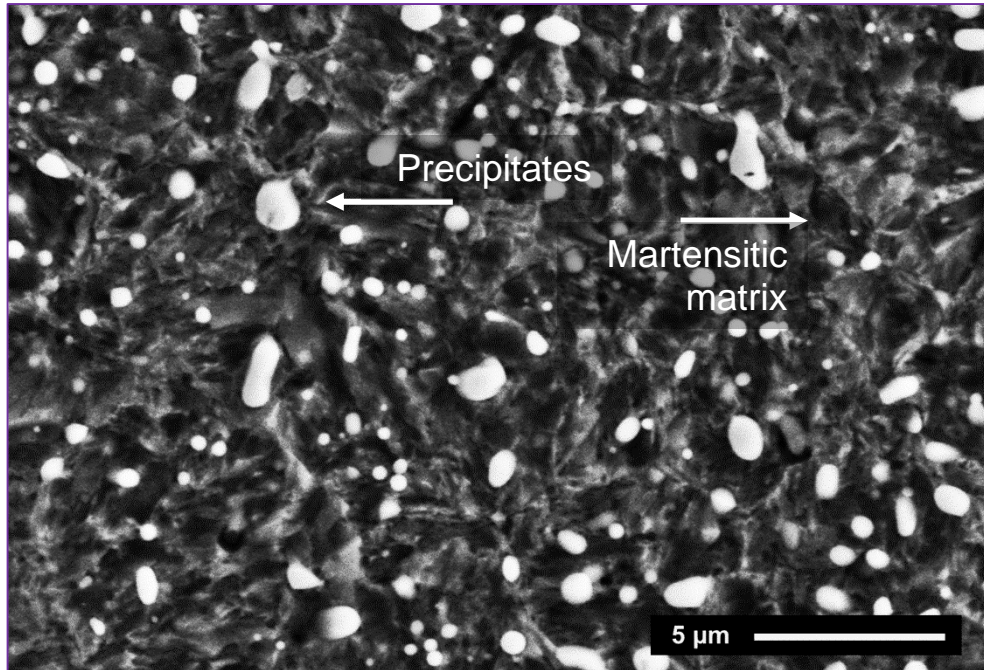


Figure 5.13. Detail of submicrometer precipitates in the AISI 52100 ball bearing steel (SEM/SE - 5000x mag.).



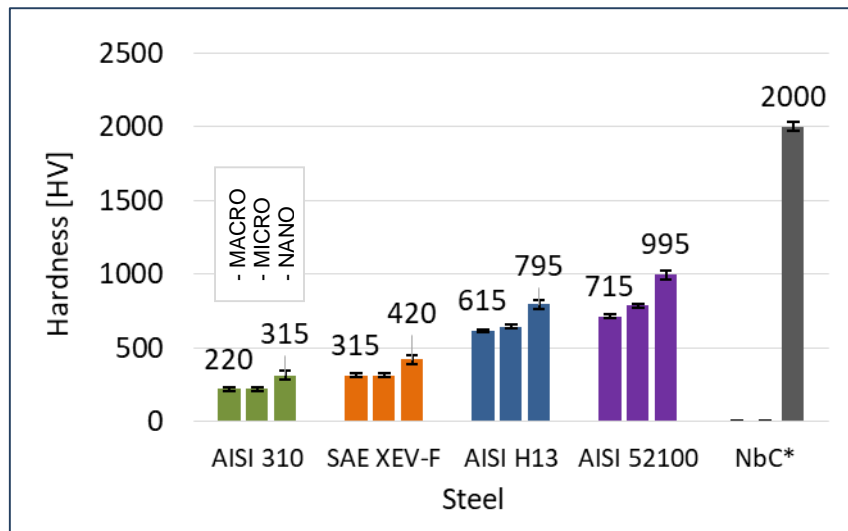
The fine precipitates observed in the refined martensitic matrix presented a spheroidal morphology and were approximately  $\sim 1 \mu\text{m}$  in size. They were identified elsewhere for the same steel as being  $(\text{Fe,Cr})_3\text{C}$  (STICKELS, 1974).

All the materials of this study presented precipitates. Nevertheless, they were different both in size and morphology. Together with their associated mechanical properties (e.g. hardness) they can influence the mechanical behavior of the surrounding steel matrix. The hardness of the precipitates in the AISI 310 was not possible to measure by means of nanoindentation due to their size (usually,  $< 1 \mu\text{m}$ ). Due to their small size, the AISI 310 austenitic stainless steel can be considered homogeneous in the microscale and will be treated as such within context of this thesis. In the same sense, the AISI H13 and AISI 52100 steels can be regarded as homogeneous steels in the microscale, due to the submicrometer size of the precipitates present in them. In contrast, a different behavior of the NbC microscale precipitates in SAE XEV-F valve steel can be expected and, therefore, this material was considered a heterogeneous (composite) steel in the context of this thesis.

## Hardness

Multi-scale hardness measurements were conducted to characterize the matrix and precipitates (when the later were larger than 1  $\mu\text{m}$ ). [Figure 5.14](#) summarizes the hardness results for the materials of the discs and the ball. From left to right: matrix of the AISI 310 stainless steel (green), SAE XEV-F valve steel (orange), matrix of the AISI H13 tool steel (blue), matrix of the AISI 52100 bearing steel (purple), and NbC precipitates in the SAE XEV-F valve steel (gray). For each steel, values for three hardness scales are presented. From left to right, they correspond to the macro (Vickers, 30 kgf), micro (Vickers, 0.1 kgf), and nanohardness (Berkovich, 5 mN).

[Figure 5.14](#). Multiscale hardness characterization of bulk materials and other phases.



The observed macro (left bar) and micro (center bar) hardness values were similar for all steels. Even for the heterogeneous SAE XEV-F valve steel, the existing volume fraction of NbC ([Figure 5.5](#)) did not result in different values for the macro and micro hardness measurements.

The hardness values measured via Nanoindentation (right bar in all steels) were always higher (i.e. overestimated) than those from macro and micro tests (left and center bars, correspondingly). The overestimation percentage is presented in [Table 5.1](#) for each steel. The higher values observed with Nanoindentation are probably due to the calculation procedures used in each technique and indentation size effects (QIAN L., LI M., ZHOU Z., YANG H., SHI X., 2005; PHARR G.M., HERBERT E.G., GAO Y., 2010). The mean (arithmetic) overestimation value (36%) should be

considered whenever nanohardness measurements are compared to microhardness values, and vice versa.

**Table 5.1.** Overestimation % of nanohardness measurements with respect to micro and macrohardness.

STEEL	MICRO/MACRO-HARDNESS (VICKERS) [5 gf]	NANO-HARDNESS (BERCOVICH) (5 mN)	OVERESTIMATION [%]
AISI 310	220	315	43
SAE XEV-F	315	420	33
AISI H13	615	795	29
AISI 52100	715	995	39

*Nitrided layer (treated SAE XEV-F valve steel)*

BSE/SEM images and EDS maps were obtained from top views of the nitrided samples (Figure 5.15). The BSE image (Figure 5.15a) indicates a pronounced topography. The NbC can be observed at the surface (white spots), meaning that nitriding does not prevent the NbC to remain visible at the surface. These carbides are randomly distributed in the surface as in the untreated SAE XEV-F valve steel. This result was confirmed by the niobium EDS map, as seen in Figure 5.15b. XRD was used to determine the composition of the nitrided layer. Figure 5.16 shows the resulting XRD patterns.

**Figure 5.15.** SEM analysis of the resulting nitrided layer on the SAE XEV-F valve steel (top view of the sample): a) backscattered electrons image (BSE); and b) corresponding niobium EDS map.(500x mag.).

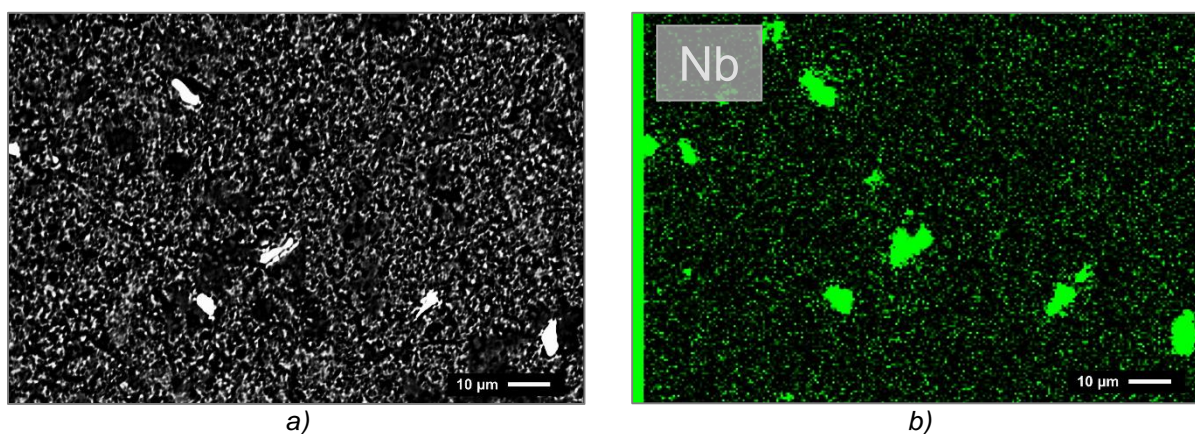
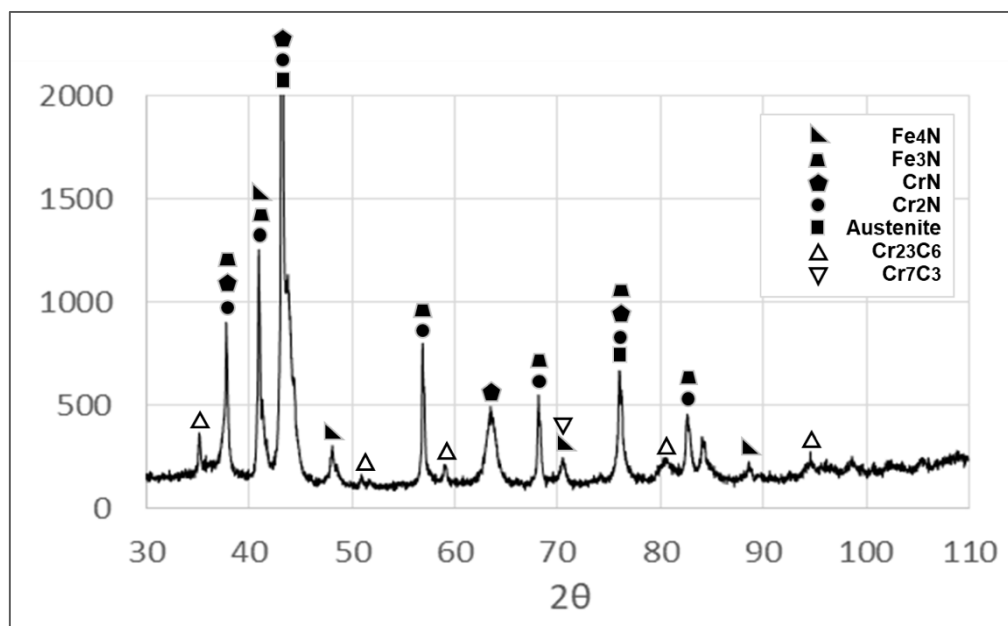


Figure 5.16. XRD patterns of the nitrided layer resulting after nitriding of the SAE XEV-F valve steel.



The XRD pattern of the nitrided layer revealed the presence of austenite and chromium nitrides<sup>6</sup> ( $\text{Cr}_2\text{N}$ ,  $\text{CrN}$ ) and iron nitrides ( $\text{Fe}_4\text{N}$ ,  $\text{Fe}_3\text{N}$ ), confirming that nitriding changes the chemical composition of the surface by a thermochemical reaction. Hence, a compound layer is expected on the hard case (SHIH; HUANG; CHEN, 2011; LUO; ZHAO, 2013). Chromium oxides ( $\text{Cr}_{23}\text{C}_6$  and  $\text{Cr}_7\text{C}_3$ ) were also identified, in accordance with other works (SHIH; HUANG; CHEN, 2011; LUO; ZHAO, 2013).

The cross-section of the nitrided surfaces was also investigated to identify the different surface layers resulting from the applied thermochemical process. Figure 5.17 shows a BSE image of the nitrided layer of the SAE XEV-F valve steel.

It can be observed that the nitrided layer is primarily composed of two layers: The compound layer (CL) and the diffusion Layer (DL). The nitriding process creates a continuous nitrogen gradient on the surface and a well-defined interface between these layers does not exist. The mean thicknesses of the CL and the DL layers were measured to be  $3.7 \pm 0.6$  and  $5.6 \pm 0.8$   $\mu\text{m}$ , respectively. The compound layer is composed by a nitride network of Iron and Chromium precipitates, and the austenite in the DL (N supersaturated) works as a hard substrate for the compound layer. Some primary NbC at the surface region can be observed in the nitrided layer.

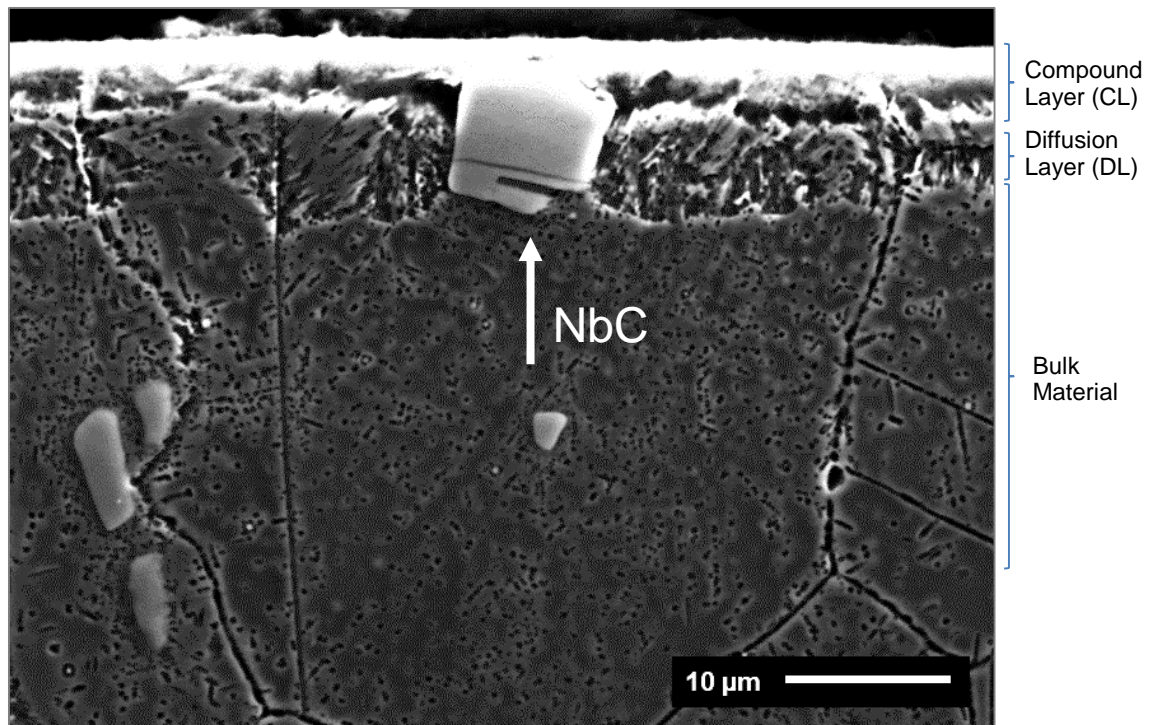
<sup>6</sup>  $\text{Cr}_2\text{N}$ , JCPDS code: 00-001-1232.

$\text{CrN}$ , JCPDS code: 00-003-1157.

$\text{Fe}_4\text{N}$ , JCPDS code: 00-001-1219.

$\text{Fe}_3\text{N}$ , JCPDS code: 00-001-1236.

Figure 5.17. SEM/SE image of a cross section of the nitrided layer on the SAE XEV-F valve steel.

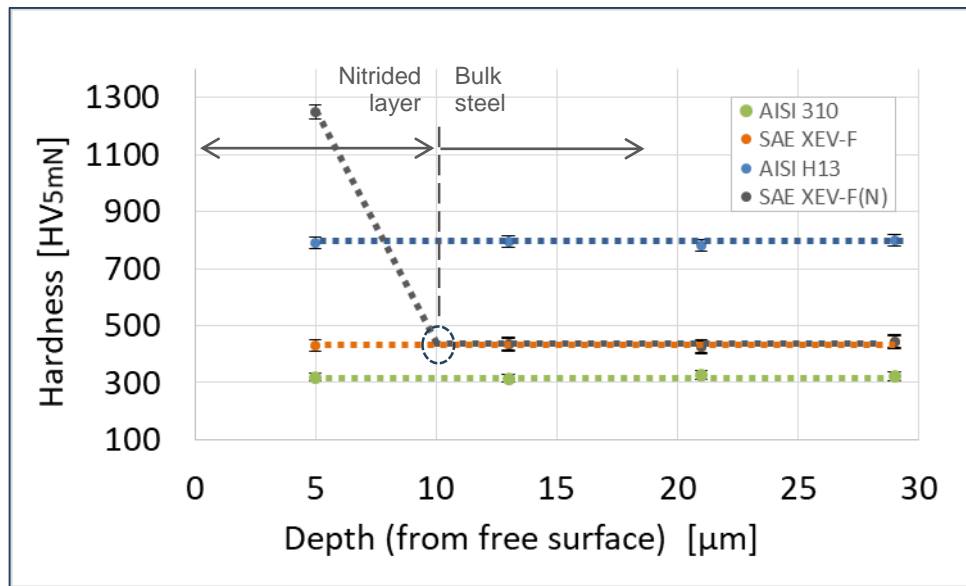


### *Subsurface hardness*

Nanohardness profiling of the subsurface region of the polished surfaces was conducted in cross-sections of the discs for measuring any strain hardening resulting from mechanical polishing processes before the tribological tests. Figure 5.18 shows the resulting hardness profiles.

As can be observed, no strain hardening was measurable in the polished steel surfaces of the studied tribosystems below 5 μm from the surface. These results indicate that the surface preparation method used in this work resulted in a negligible strain hardening before tribological tests. In the case of the SAE XEV-F valve steel, the nitriding process creates an outer case with superior hardness (as expected). The measured hardness values of the nitride layer were  $1250 \pm 20$  HV<sub>5mN</sub>.

Figure 5.18. Subsurface nanohardness profiling of the polished discs (before wear).



### Topography

3D topography measurements were conducted via CCI on the top face of the discs. Preprocessing of the obtained images from the polished surfaces consisted in filling of non-measured points (always less than 1%), surface levelling and filtering. The resulting *scale-limited surface* was obtained with the use of a *nesting index* (i.e. cut-off value,  $\lambda_c$ ) selected according to the guidelines of ISO 16610. That is, the nesting index was equivalent to  $\lambda_c = 250 \mu\text{m}$ . Surface parameters were computed from the resulting short-wave components of topography (roughness).

Figure 5.19 and Figure 5.20 show the 3D images of such surfaces for visualization. Figure 5.19 shows the representative characteristics of the polished surfaces of the AISI 310 (also representative of the considered homogeneous AISI H13 and AISI 52100 steels).

Figure 5.19. 3D view of the polished surfaces of the AISI 310 austenitic SS. (representative of the AISI H13 and AISI 52100 steels). (Field of View - FoV: 50 x 50  $\mu\text{m}$ ).

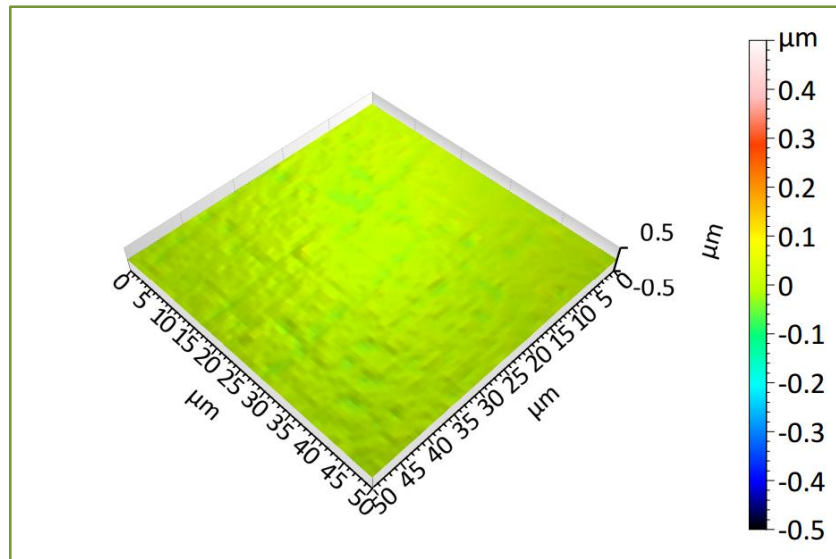


Figure 5.20 shows the characteristics of the polished SAE XEV-F valve steel topography. It can be observed that the precipitates were not polished to the same level as the surrounding austenitic matrix, due to their higher hardness. Nitriding of such surfaces results in an increase of roughness as can be observed in Figure 5.21.

Figure 5.20. 3D view of the polished surfaces of the SAE XEV-F valve steel. (FoV: 50 x 50  $\mu\text{m}$ ).

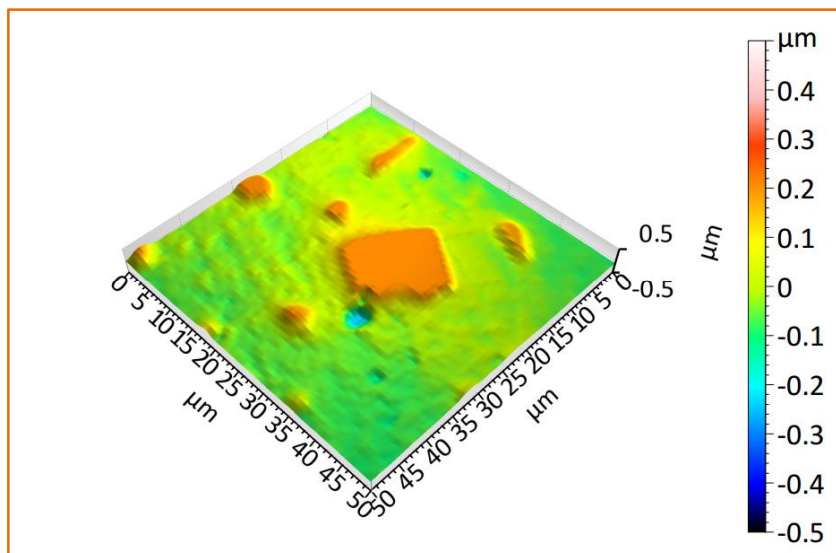
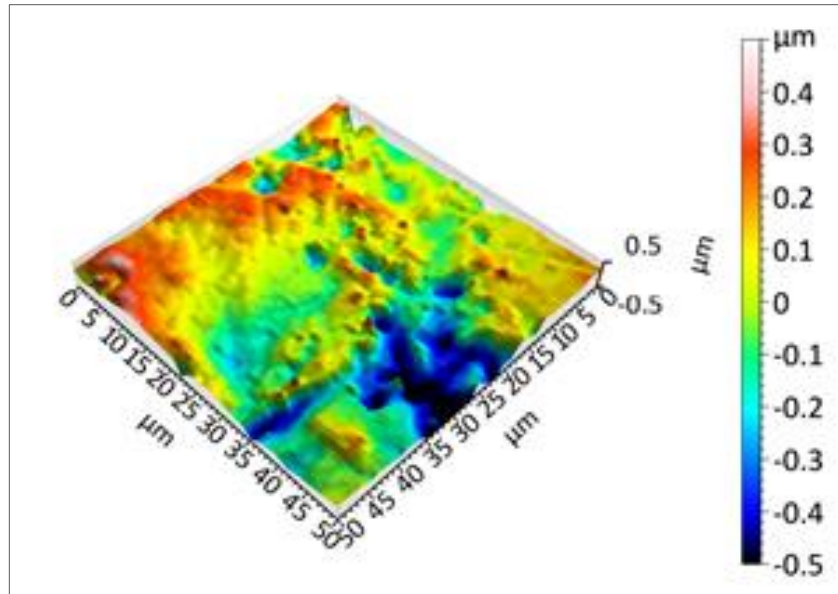


Figure 5.21. 3D view of the resulting topography after nitriding the polished surface of the SAE XEV-F. (FoV: 50 x 50  $\mu\text{m}$ ).



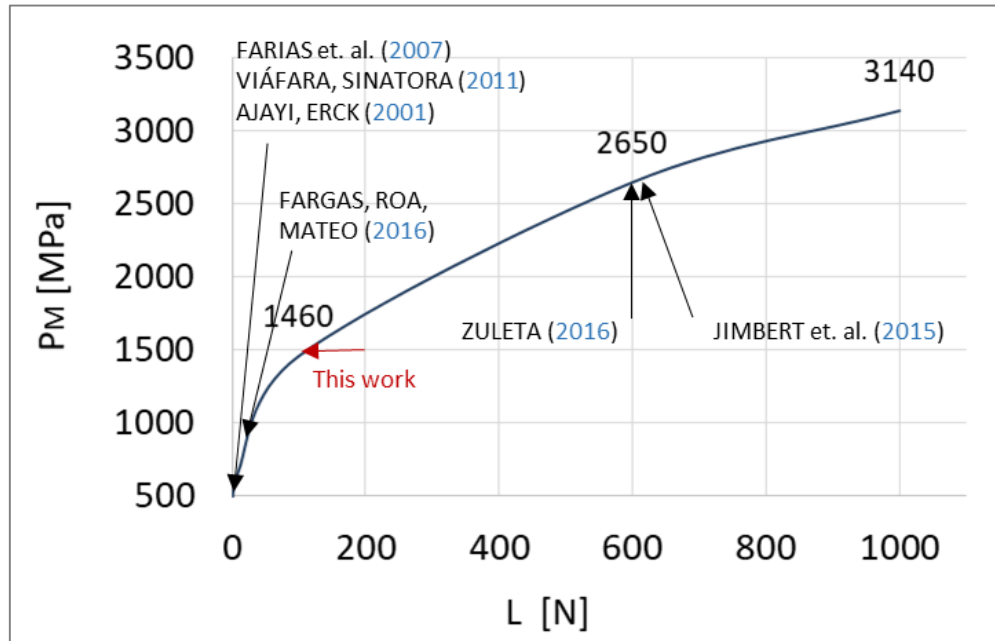
The measured roughness values were different between the heterogeneous SAE XEV-F valve steel ( $S_a = 35 \pm 6 \text{ nm}$ ) and the homogeneous steels: AISI 310 ( $S_a = 14 \pm 2 \text{ nm}$ ), AISI H13 ( $S_a = 12 \pm 2 \text{ nm}$ ) and AISI 52100 ( $S_a = 12 \pm 2 \text{ nm}$ ). Thus, it can be verified that heterogeneities in polished steel surfaces increase ( $\sim 3x$ ) the average roughness with respect to a homogeneous steel. Additionally, the roughness of the nitrided surface was  $385 \pm 11 \text{ nm}$ . That is, the nitriding process increases  $\sim 350 \text{ nm}$  the  $S_a$  value of the surface of the untreated SAE XEV-F valve steel (one order of magnitude).

#### *Contact pressures under static loading*

The elastic contact model due to Hertz is widely used for determining contact pressure, indentation and contact area, in nominal point contacts before sliding. The results of tribological tests are discussed in terms of these calculations. Nevertheless, the high contact pressures imposed by ball-on-disc configurations can surpass the yield strength of the surface of the materials and plastically deform it, even in the absence of sliding. Figure 5.22 presents the Hertz contact pressure as a function of load in a BoD configuration. The maximum values of nominal contact pressure obtained in other works under BoD and PoD configurations were also indicated for

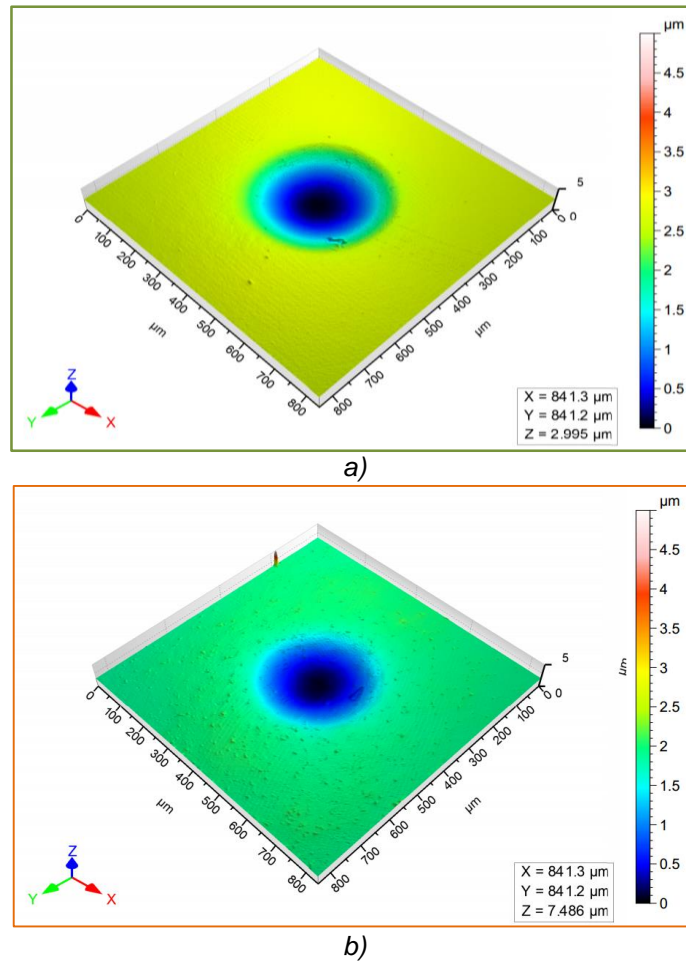
comparison purposes (see [Table 2.2](#)). It must be remembered that whenever plastic deformation occurs (indentation) the Hertz contact model is no longer valid.

**Figure 5.22.** Mean contact pressure (PM) as a function of static vertical load in a BoD contact as predicted by the model of Hertz for a 10 mm diameter steel ball against a steel flat.



When comparing the mean (arithmetic) contact pressure values of the cited works illustrated in [Figure 5.22](#), it can be readily observed that the geometric differences between BoD and PoD contacts have significant effects. Since contact pressures are an important parameter related to subsurface stresses and elastic/plastic behavior of the surfaces, it is important to analyze the extent to which the computed values using the Hertz model are valid. In this sense, a comparison between the predicted values of indentation and nominal contact area and the experimental results of static indentation are useful. For this purpose, static loading of sample and counter-body materials was performed with a 10 mm diameter ball with a 100 N load, using a 5 minute resting time. No indentations were measurable in the harder surfaces (AISI H13 and nitrided SAE XEV-F). Indentations in the austenitic steels (AISI 310 and SAE XEV-F) were measured via CCI. [Figure 5.23](#) shows the views of the resulting indentations.

Figure 5.23. 3D view of indentations on the austenitic samples after static loading with 100 N: a) AISI 310, and b) SAE XEV-F. (FoV: 850 x 850  $\mu\text{m}$ ).



It has been mentioned (ZUM GAHR, 1987) that the transition from elastic to elastoplastic behavior of a rigid ball against a deformable flat occurs when the indentation depth surpasses a critical value, given by:

$$h_{CR} = 0.89R (H/E)^2 \quad (\text{Equation 4})$$

Where R is the radius of the sphere (10 mm), H is the hardness (GPa) and E the Young's modulus of the deformable material (GPa). Table 5.2 shows the critical indentation depths for the studied tribosystems as compared to the indentation depth predicted by Hertz' model and the measured values of the static loading experimental tests. For comparison purposes the elastic modulus of the nitrided layer was assumed to be the same as that of the AISI H13 steel. It must be noted that the measured depth includes some elastic spring back of the surface material.

Table 5.2. Comparative Indentation depth (critical, Hertzian and measured).

STEEL	HARDNESS [HV]	HARDNESS [GPa]	YOUNG MODULUS [GPa]	$h_{CR}$ [ $\mu\text{m}$ ]	$h_{HERTZ}$ [ $\mu\text{m}$ ]	$h_{measured}$ [ $\mu\text{m}$ ]
AISI 310	220	2.15	200	0.51	4.65	2.62
SAE XEV-F	315	3.09	205	1.01	4.61	1.90
AISI H13	615	6.03	190	4.48	4.71	-
Nitrided SAE XEV-F	1250	12.23	190	18.44	4.71	-

It can be readily observed that under the 100 N load the Hertz' indentation value surpasses the critical indentation depth in the cases of the austenitic steels and the AISI H13 steel. As a consequence, a transition from elastic to plastic behavior is expected in these systems (even in the AISI H13 steel where the indentation was not measurable). A fair reasoning is that in such cases plastic deformation occurs due to static loading creating a plastically deformed zone that is preexistent to sliding and can affect the running-in stage. This deformed layer is expected to affect a large portion of the surface in the case of austenitic steels and a smaller portion of the surface (on the asperity level) of the AISI H13 steel. Purely elastic behavior should be expected from the surface of the nitrided SAE XEV-F valve steel.

Additionally, it should be mentioned that conditions near to those described by the Hertz model are only valid in elastic surfaces only before any sliding has occurred. Once plastic deformation takes place which creates contact conditions far from the basic assumptions of Hertz' model. Severe shear strains in the subsurface region causes strain hardening, which induces further deviations from the model.

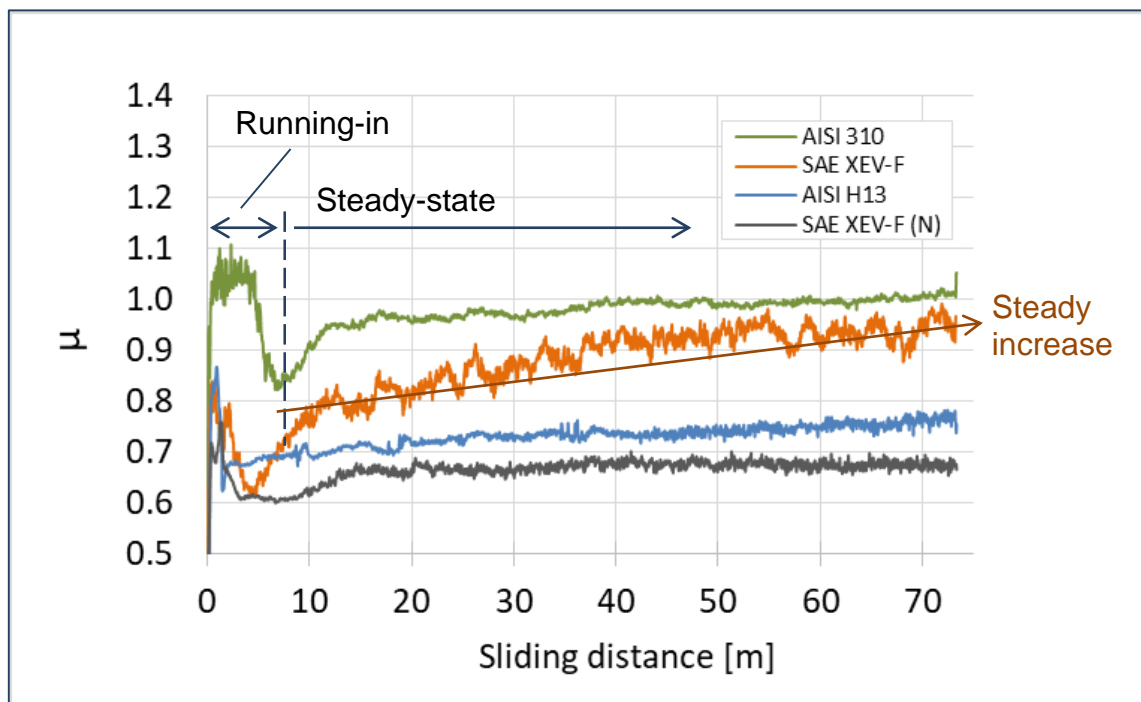
## 5.2 FRICTION

### *Friction coefficient ( $\mu$ )*

The friction coefficient was analyzed to investigate its evolution during the tests. Each curve in Figure 5.24 was constructed by computing the values of the four repetitions at a given second into the arithmetic mean. This is called a (point-to-point) average. One averaged curve was constructed for each of the four studied tribosystems. Two stages of frictional behavior are readily identified for all

tribosystems: an initial transient behavior (running-in) followed by a stage in which the friction coefficient is more stable but not constant. In this sense, the observed behavior of the friction coefficient does not follow the formal definition of *steady-state* mentioned by Blau (1991). In the context of this work, this stage presenting steady increase of the friction curves will be considered as the steady-state.

Figure 5.24. Friction coefficient during tests. Each curve was obtained as a point-to-point average of 4 repetitions (for each tribosystem).

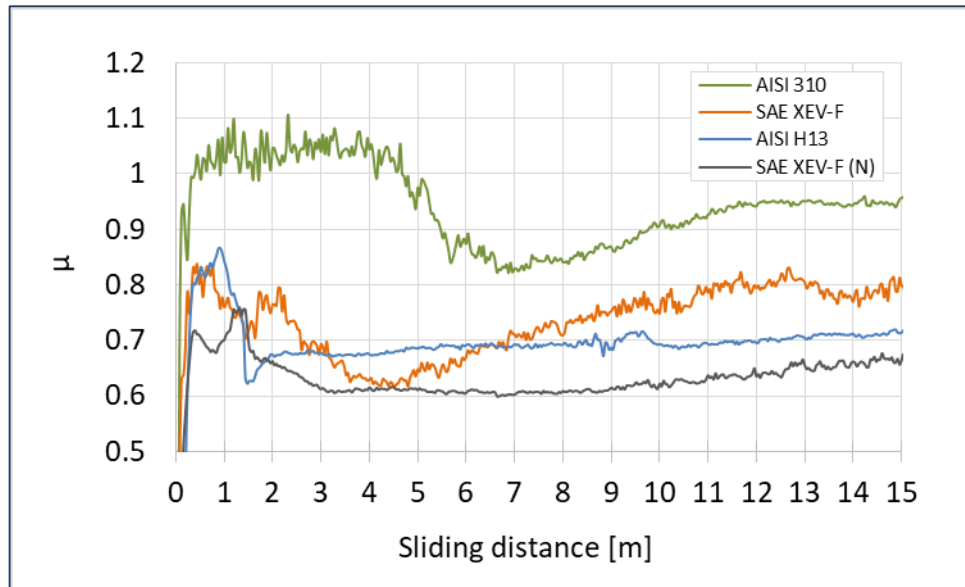


The austenitic steels stabilized after longer sliding distances ( $s \sim 12$  m), and they presented higher friction coefficient values. In contrast, the harder surfaces (AISI H13 and nitrided SAE XEV-F steels) stabilized rapidly (during the first 2 m) presenting lower friction coefficient values. There is an apparent inverse correlation between the friction coefficient and hardness. The hardest surface (nitrided SAE XEV-F) presented the lowest friction coefficient, and the softest surface (AISI 310) presented the highest friction coefficient. Indicating that harder materials present surfaces with higher load-carrying capacities.

The running in period of all systems can be better observed in Figure 5.25. The AISI 310 shows the highest friction coefficient peak ( $\mu \sim 1.0$ ) during running-in, followed by a pronounced valley ( $\mu \sim 0.85$ ) before reaching steady-state ( $\mu \sim 0.95$ ). On the other hand, the SAE XEV-F valve steel presents peak and valley values that are lower by

half. One hypothesis is that the marked differences between the austenitic steels can be related primarily to the presence of microscale NbC in the valve steel, and secondarily to its higher hardness. The peak and valley of the AISI H13 steel presented the same intensity as the valve steel but half its duration. The nitrided SAE XEV-F peak was the lowest, both in intensity and duration.

Figure 5.25. Detail of friction coefficient during running-in.

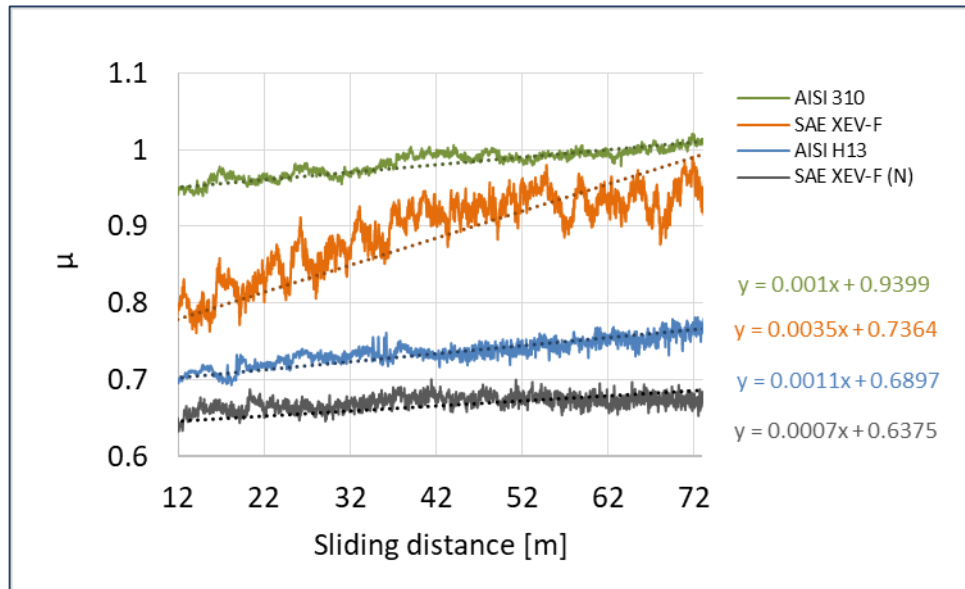


After the running-in stage a change to steady-state friction occurs (Figure 5.26). According to Rigney (1997) the following variables become stable: friction coefficient, magnitude of friction fluctuations, surface roughness, depth of deformed layer, and the composition and microstructure of near-surface material. Additionally, stabilization of the variation in nominal contact pressure should also be expected in ball-on-disc type of tests, as indicated by the results of Ajayi and Erck (2001) (see Figure 2.6).

Since a linear tendency is observed in all cases, a linear regression is suitable for describing the friction coefficient after running-in (defined based on variations in the friction coefficient), and the slope of the line for quantifying friction increase. The slopes of the linear regressions for the AISI 310 and AISI H13 steels approximately is the same ( $1e-3$ ). The slope in the SAE XEV-F valve steel was four times greater ( $4e-3$ ) while that of the nitrided SAE XEV-F was lower by an order of magnitude ( $7e-4$ ). Among all samples, the SAE XEV-F showed the most pronounced friction increase after the running-in period, which can be related to the presence of NbC in the

austenitic matrix. NbC microscale particles influenced the wear behavior as will be detailed further on.

Figure 5.26. Friction coefficient after running-in ( $s > 12$  m).



Reported values of mean friction coefficient during steady state are frequently found (Table 5.3). Nevertheless, it is evident that the mean friction coefficient is only an approximation to the friction description of the entire tribological event (Figure 5.26).

Table 5.3. Mean (arithmetic) friction coefficient after running-in ( $s > 12$  m).

STEEL	$\mu$	Standard deviation
AISI 310	1.0	0.05
SAE XEV-F	0.9	0.08
AISI H13	0.8	0.04
Nitrided SAE XEV-F	0.7	0.04

### 5.3 WEAR

This section presents the results of the characterizations after tribological tests. It is divided into three parts. The first part presents the evolution of mass loss and its correlation to friction coefficient. The second part presents the evidence of the severe-to-mild wear transition observed in the steel-on-steel tribosystems. The third part

consists of a detailed analysis of wear mechanisms at the end of the full length (73.2 m) tribological tests

In this study, the discs were selected as the sample materials (studied materials), and they presented higher mass losses than the balls. Hence, the wear of the discs was explored in the first place to determine the wear mechanisms and their predominance in the wear scar. In second place, wear of the ball were discussed to explore material transfer. The results obtained from the AISI 310 steel are usually discussed in the first place, due to their homogeneous austenitic matrix, which makes them suitable as a model material for studying the wear (and friction) behavior of the SAE XEV-F valve steel. Subsequently, these results were compared to those obtained from the heterogeneous SAE XEV-F valve steel. The AISI H13 will then be discussed as the material with intermediate hardness and finally the hardest material of the nitrided SAE XEV-F. Special attention was given to the characterization of mass loss, wear mechanisms, tribofilm formation, nominal contact area, role of hard particles, and subsurface deformation.

### 5.3.1 MASS LOSS EVOLUTION

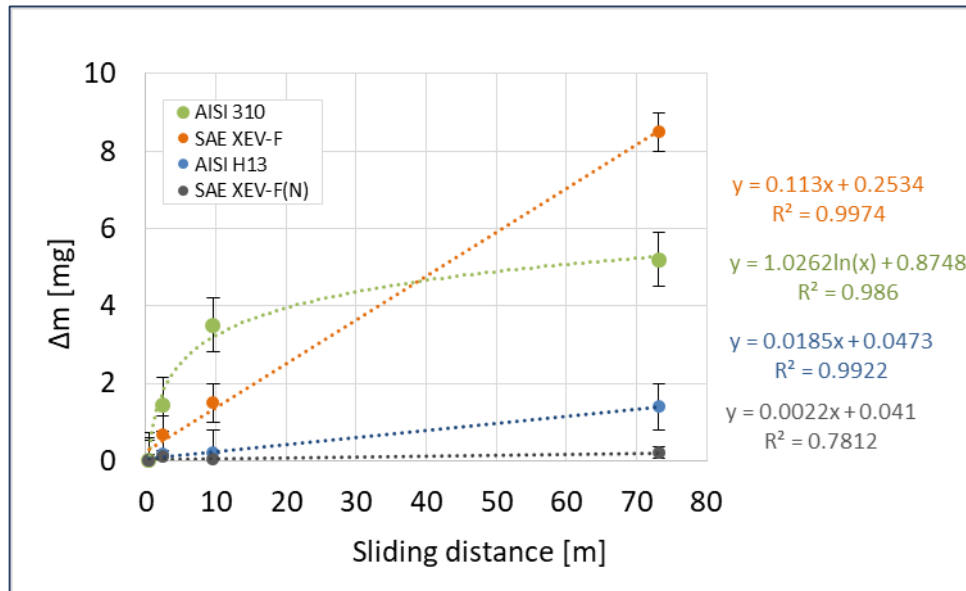
#### *Evolution of wear (mass loss) during interrupted tests*

The evolution of mass loss was determined by means of tribological tests interrupted after different sliding distances (times): 0.4 m (10 s), 2.4 m (60 s), 9.6 m (240 s) and 73.2 m (30.5 min). These distances were selected conveniently according to the variations observed in the friction coefficient (see [Figure 5.24](#)) to evaluate the running-in behavior in all tribosystems. Evolution of mass loss of the balls was not included due to two facts: on one hand, the measured values of mass loss of the balls were too small compared to those of the discs; on the other hand, the measured values have a large dispersion, and it is not reliable to infer any conclusions from them.

The evolution of mass loss of the discs is presented in [Figure 5.27](#). Good correlation coefficients were observed from the respective regressions. The mass loss evolutions (i.e. wear rates) were diverse. The AISI 310 presented a mass variation that followed an inverse power function (non-linear) with respect to sliding distance. The wear rate almost stabilized to a lower value in the steady-state stage. SAE XEV-F, AISI

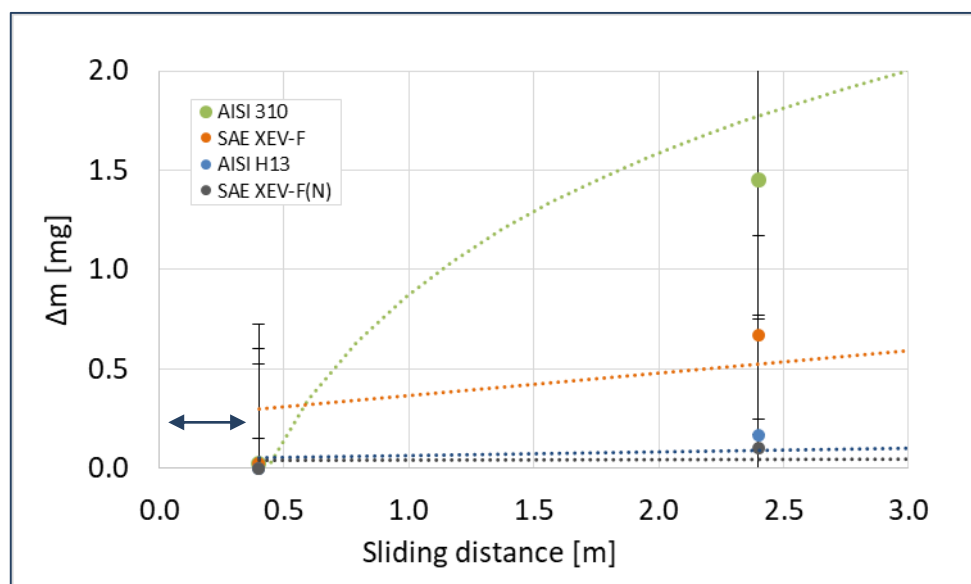
H13, and nitrided SAE XEV-F steels present a linear behavior in the evaluated sliding distances.

Figure 5.27. Evolution of the mass loss of the discs



Nevertheless, the regression line does not pass through the origin, as indicated by non-zero intercepts found from the linear regression of the corresponding set of data (Figure 5.27). This implies that there must have been nonlinearities at least at the first 0.5 m sliding (see Figure 5.28), and suggests that most important changes in nominal contact occur in this stage, which was considered the as the *running-in*.

Figure 5.28. Evolution of the mass loss of the discs during the first 3 m sliding.



In the case of the SAE XEV-F valve steel, the higher hardness impedes the rapid initial penetration of the ball, thus explaining the lower friction peak observed during the running-in (see [Figure 5.25](#)) when compared to the AISI 310 steel. A more gradual penetration (e.g. in a linear proportion) of the ball also accounts for the lower values of the friction coefficient in the early moments of the steady-state, and the stable increase observed afterwards ([Figure 5.26](#)). The stable increase of the friction coefficient in the case of the SAE XEV-F steel would therefore correspond to a stable increase in penetration of the ball, aided by subsurface stress concentration in the metallic matrix around the NbC (which facilitate material removal), and by abrasive processes caused by harder debris, containing also NbC particles or broken NbC particles. These two processes compete with the strain hardening of the matrix. Hence, the stress concentration effect in the SAE XEV-F steel does not allow the stabilization of the subsurface layer. Probably, the material in this region accumulates plastic strain at each experienced cycle, which results in a constant wear rate. Wear rates can be quantified and compared assuming that a linear regression describes the wear behavior in the steady-state by means of the slope in a linear regression obtained from the mass loss/distance plot (see [Table 5.4](#)). Nevertheless, it is important to consider that this approach assumes linearity (a constant wear rate) in the steady-state. To confirm this assumption, interrupted tests can be conducted at intermediate sliding distances. The former is outside the scope of this work, which concentrated primarily on the running-in stage.

[Table 5.4](#). Regression functions of mass loss of the discs between 25 and 73.2 m sliding.

STEEL	Regression
AISI 310	$0.027x + 3.255$
SAE XEV-F	$0.110x + 0.432$
AISI H13	$0.019x + 0.019$
Nitrided SAE XEV-F	$0.002x + 0.027$

It has been noted by Burwell and Strang ([1952](#)) that, whenever the relation between wear (mass or volume) and distance is linear for a given load (L), the wear rate (V/L) is constant and can be conveniently compared against load. As observed, this is usually the case in PoD tests after running-in. Nevertheless, the wear coefficient value must be computed separately for the running-in and steady-state stages in order to obtain reliable inferences from the obtained results. The amount of material loss due

to severe wear during running-in accounts for a great part of the wear of each system. The oxidative wear mechanisms occurring during the steady-state stage would account for a minor part of the total amount of wear during the tests (for the selected sliding distance and other operating parameters).

### *Wear quantification (metrics)*

Wear is generally reported in 'raw' values (mass loss, wear volume) or in normalized units - that imply linear relationships between the applied variables (e.g. sliding distance, load), and the resultant wear total mass or volume change, but others involve normalized or combined units that imply linear relationships between applied variables, such as load and sliding distance, and the resultant wear. (BLAU, 2015). In this section mass loss values were discussed from the point of view of the most common wear metrics.

### *Mass loss (73.2 m)*

Figure 5.29 shows the mass loss of the discs and the balls at the end of the full 73.2 m (30.5 min) tribological test.

Figure 5.29. Mass loss at  $s = 73.2$  m: a) discs, and b) balls.

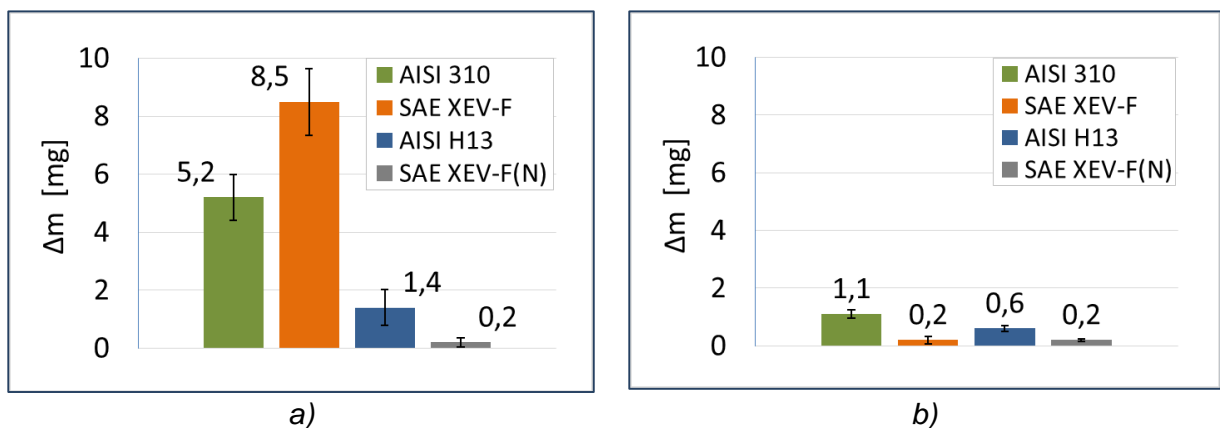


Figure 5.29a shows the wear of the discs after 73.2 m. The measured mass loss values were higher for the softer austenitic steels (AISI 310 and SAE XEV-F), with values between ~5.2 and ~8.5 mg. The harder surfaces (AISI H13 and nitrided SAE XEV-F) resulted in less wear, as expected. Mass loss was ~1.4 mg for the martensitic

steel (AISI H13) and ~0.2 mg for the nitrided SAE XEV-F valve steel. Between the austenitic steels, the SAE XEV-F valve steel presented a mass loss that was 60.5% higher than for the AISI 310 steel. This was an unexpected result given that the hardness of the SAE XEV-F valve steel was 43.2% harder than the AISI 310 steel (see [Figure 5.14](#)). This result will be further discussed.

The balls lost considerably less mass than the discs at 73.2 m ([Figure 5.29b](#)). This result was expected due to two main factors ([HUTCHINGS. 1992](#)): a) the high hardness of the balls when compared to that of the discs, and b) the large differences in stress fields on both discs and balls. The ball tested against the (untreated) SAE XEV-F valve steel presented a low wear value when compared to the ball tested against the AISI 310. This is an unexpected result given the hardness differences between these two steels. The mass loss of the balls tested against the other steels (AISI 310, AISI H13, and nitrided SAE XEV-) showed an inverse correlation with the corresponding hardness of the disc.

The SAE XEV-F steel presented the most particular behavior. The pronounced wear of the disc, and the (almost) negligible wear of the corresponding ball, are both related to the effect of hard particles (micrometer-scale NbC) at the interface and the subsurface regions next to it.

With the exception of the SAE XEV-F valve steel, the wear of the discs presented an inverse correlation to the hardness of the surface. That is, in the homogeneous steels (AISI 310, AISI H13, and nitrided SAE XEV-F) wear decreased with increasing the surface hardness. The surface of the nitrided SAE XEV-F valve steel was considered homogeneous as a result of the nitriding process due to the following facts. On one hand, the hardness differences between the NbC (~2000 HV<sub>5</sub> mN) and the compound layer (~1250 HV<sub>5</sub> mN) are lower than those between the NbC and the untreated steel (~420 HV<sub>5</sub> mN). This fact is expected to reduce the severity of plastic deformation in the subsurface layer of the nitrided discs. On the other hand, the diffusion layer supports the compound layer, which now includes hard NbC precipitates which further increase load support capacity of the surface. In contrast, the SAE XEV-F valve steel disc presented the highest mass loss, 63.5% higher than the AISI 310 steel, despite its higher hardness value (43.2% higher). This behavior is thought to be related to the role of the hard heterogeneities in the SAE XEV-F valve steel and will be further discussed in subsequent sections.

### Wear metrics

Based on the mass loss values at 73.2 m, computations were made to determine three widespread wear metrics: wear volume, wear rate (wear volume per sliding distance), specific wear rate (wear rate per unit load), and the -Archard- wear coefficient ( $k = VH/LS$ ). The method used for computation was that exposed by Bhushan (2013) and the values used for each variable and the results are listed in Table 5.5. A density of 8.0 g/cm<sup>3</sup> was used for the steels as an approximation. For comparative purposes, the density of the nitrided surface of the SAE XEV-F valve steel was assumed the same as that of the bulk material (which is only an approximation). A load of 100 N and sliding distance of 73.2 m were selected as testing parameters (as indicated in Table 4.3). According to Bhushan (2013) wear coefficients vary between 10e-8 to 10e-4 for mild wear (tribo-oxidation), characterized by oxidized metallic surfaces and the formation of fine oxidized wear debris. This result is in accordance with the predominant tribo-oxidative wear mechanisms observed in all steel-on-steel tribosystems at a 73.2 m sliding distance, with the exception of the nitrided SAE XEV-F valve steel (see Figure 5.76). Nevertheless, expecting a unique value of any wear metric to describe the complete tribological event is equivalent to assuming that the wear rate does not change during the complete tribological process.

Table 5.5. Comparative wear metrics for the studied materials.

STEEL	Hardness (H) [GPa]	Mass Loss ( $\Delta m$ ) [g]	Wear Volume (V) [mm <sup>3</sup> ]	Wear Rate (V/S) [mm <sup>3</sup> /m]	Specific Wear Rate (V/LS) [mm <sup>3</sup> /N.m]	Wear Coefficient (k) -
AISI 310	2.15	5.20e-03	0.65	0.65	6.5e-03	1.9e-04
SAE XEV-F	3.09	8.50e-03	1.06	1.06	10.6e-03	4.5e-04
AISI H13	6.03	1.40e-03	0.18	0.18	1.8e-03	1.4e-04
Nitrided SAE XEV-F	12.23	0.20e-03	0.03	0.03	0.3e-03	0.4e-04

To assume a unique value of a wear metric to describe the complete tribological event also implies that the wear rate evolves linearly with respect to sliding distance (or time), and that the wear rate (the slope in a wear volume - sliding distance plot), is constant during the test. However, it is well known that non-linear wear rates are often found in tribological tests (see Figure 2.5). The variation of the nominal contact

pressure in as much as two orders of magnitude are a major non-linearity in wear rates observed in BoD dry sliding tests.

*Wear metrics in tribological systems with non-linear wear- Interrupted tests*

The evolution of mass loss of the studied tribosystems (Figure 5.27) showed that non-linear wear rates occurring during running-in can largely affect the way in which wear is reported and interpreted. Recently, Blau (2015) has commented on the implications of wear transitions for materials selection and design. There are situations in which wear cannot be accurately represented by a linear relation, regardless of the wear metric used to describe it (e.g. the highly non-linear behavior shown by the AISI 310 steel in this work). The term *system-specific wear rate* (SSWR) was used to describe this assumed linear relation between mass loss (or wear volume) and sliding distance (or time). The SSWR is the most commonly used metric in reporting laboratory results, despite the fact that it ignores any variations in wear rate. The SSWR of this work was presented in Table 5.5.

Blau (2015) recommended the following approach for reporting sliding wear data for systems undergoing wear with different rates: *a*) to use the (standardized) system-specific wear rate (SSWR) as a pre-screening tool, and *b*) to report wear according to number of observed wear stages (e.g. different steady-states) during wear, reporting both starting and end points. This approach allows the wear of the system to be approximated to a simple linear model, such as  $V = V_1 + V_2$ , in which the total amount of wear ( $V$ ) occurs during stages 1 ( $V_1$ ) and 2 ( $V_2$ ) at different (presumed constant) wear rates. As indicated by the author, the former argument implies that the wear volume of each stage is proportional to the total frictional work done during over the sliding distance for that stage. In this way, wear can be reported in accordance with wear transitions.

Table 5.6 and Table 5.7 present the running-in and steady state wear metrics results of this work, respectively. The load and sliding distance were 100 N and 73.2 m, respectively (as indicated in Table 4.3)

Table 5.6. Running-in (Comparative wear metrics).

STEEL	Hardness (H) [GPa]	Running-in distance ( $\Delta s$ ) [m]	Mass Loss ( $\Delta m$ ) [g]	Wear Volume (V) [mm <sup>3</sup> ]	Wear Rate (V/S) [mm <sup>3</sup> /m]	Specific Wear Rate (V/LS) [mm <sup>3</sup> /N.m]	Wear Coefficient (k) -
AISI 310	2.15	9.6 0-9.6 <sup>7</sup>	3.5e-3	0.44	0.0456	4.56e-04	9.80e-04
SAE XEV-F	3.09	9.6 0-9.6	1.5e-3	1.88	0.0195	1.95e-04	6.04e-04
AISI H13	6.03	2.4 0-2.4	0.2e-3	0.25	0.0104	1.04e-04	6.28e-04
Nitrided SAE XEV-F	12.23	0.4 0-0.4	0.1e-3	0.01	0.0313	3.13e-04	3.82e-03

Table 5.7. Steady-state (Comparative wear metrics).

STEEL	Hardness (H) [GPa]	Steady-state distance ( $\Delta s$ ) [m]	Mass Loss ( $\Delta m$ ) [g]	Wear Volume (V) [mm <sup>3</sup> ]	Wear Rate (V/S) [mm <sup>3</sup> /m]	Specific Wear Rate (V/LS) [mm <sup>3</sup> /N.m]	Wear Coefficient (k) -
AISI 310	2.15	63.6 9.6-73.2	1.7e-3	0.21	0.0033	3.32e-05	7.18e-05
SAE XEV-F	3.09	63.6 9.6-73.2	7.0e-3	0.90	0.0138	1.38e-04	4.25e-04
AISI H13	6.03	70.8 2.4-73.2	1.2e-3	0.15	0.0022	2.17e-05	1.28e-04
Nitrided SAE XEV-F	12.23	72.8 0.4-73.2	0.1e-3	0.01	0.0002	1.72e-06	2.10e-05

The conjunct analysis of the friction coefficient (Figure 5.24) and mass evolution (Figure 5.27) during BoD dry sliding tribological tests evidenced clear correlations. Two stages of tribological behavior can be distinguished in in both figures: a) an initial transitional stage (running-in), characterized by a highly variable friction coefficient. This fact clearly indicates the need to characterize both stages independently. Neglecting the occurrence of such running-in processes and their implications on the resulting conditions before the steady-state is reached can lead to misinterpretation of the overall wear and friction results of laboratory BoD tests.

### 5.3.2 SEVERE-TO-MILD WEAR TRANSITION (RUNNING-IN EVALUATION)

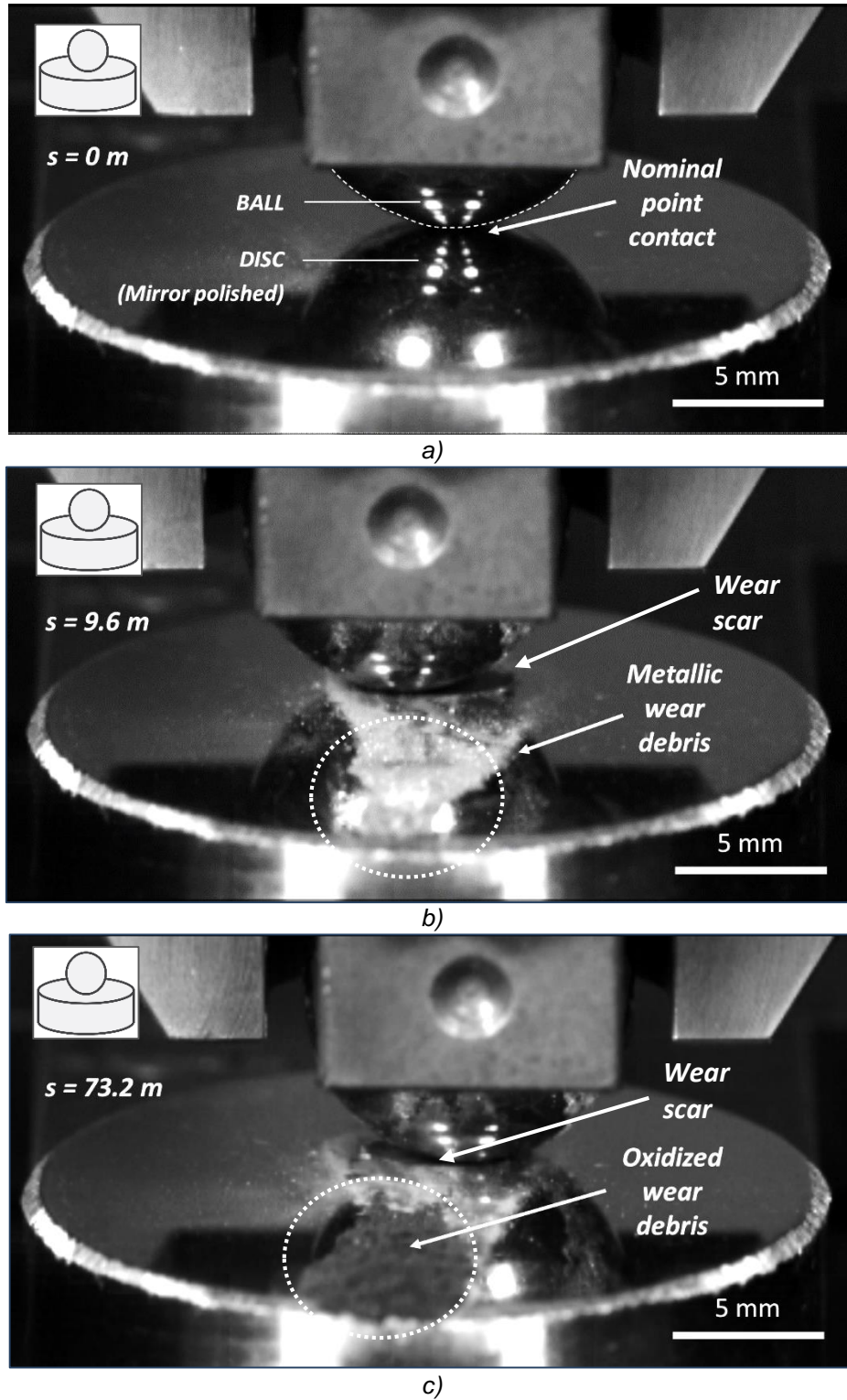
#### *High-speed filming (In-situ observation)*

High speed filming was performed to investigate visually (and in situ) the characteristics of contact and wear debris at different sliding distances, selected according to the observed transitions in friction coefficient (see Figure 5.24). Figure

<sup>7</sup> The subscripts refer to the starting and end point of each stage. The selected units of duration were the cumulative sliding distance (for each stage).

5.30 shows the evolution of contact for the SAE XEV-F valve steel tribosystem, as filmed at different sliding distances ( $s = 0$ ; 9.6 and 73.2 m).

Figure 5.30. Detail of contact for the SAE XEV-F / AISI 52100 tribosystem after wear at different sliding distances ( $s$ ): a) 0 m, b) 9.6 m, and c) 73.2 m.



At a sliding distance of 9.6 m, that is, before the running-in stage is considered finished (see [Figure 5.24](#)), a developed wear scar on the disc can be observed and the presence of metallic debris, which exit the sliding interface and accumulate on the free surface of the disc ([Figure 5.30b](#)). No oxidized debris can be observed at this sliding distance, which indicates that only severe (plastic/adhesive) mechanisms were predominantly active during running-in. After this initial stage, tribo-oxidative wear mechanisms prevail, as can be observed from the oxidized debris accumulated at the surface of the disc ([Figure 5.30c](#)). Hence, the high-speed filming results showed evidence of the occurrence of the severe-to-mild wear transition. Further evidence will be provided in the following sections.

#### *Severe-to-mild wear transition in-situ observation and hypothesis*

In-situ high speed filming of the tribological tests indicated that all the studied tribosystems (except the nitrided SAE XEV-F valve steel) underwent a transition from metallic debris particles (severe wear) to oxidized debris (mild wear). Therefore, a reasonable hypothesis is that a transition must have occurred between the initial metal-to-metal wear mechanisms (during running-in) and the following state of oxidative wear. The transition must depend on the nominal contact pressure and should occur at a well-defined threshold value, similar to the defined load (contact pressure) value for the occurrence of the mild-to-severe transition as described by Welsh (1965). Noting that in this case the transition occurred due to a continuous reduction of the contact pressure caused by wear (BoD), and in the work of Welsh the contact pressure was varied by controlling the imposed load (PoD). The evidence of the severe-to-mild wear transition in a BoD configuration occurring in the selected tribosystems, and the quantitative values of the nominal contact threshold for its occurrence, are presented in the following sections.

#### *Further evidence of the severe-to-mild wear transition in the selected steel-on-steel tribosystems - wear mechanisms*

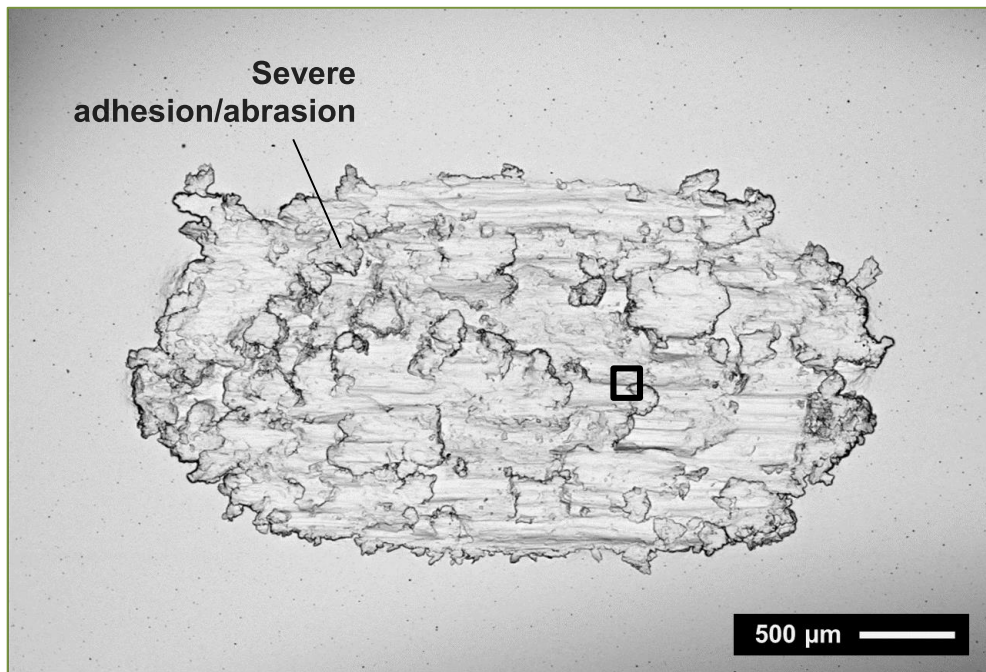
The wear mechanisms and subsurface deformation of the discs were analyzed during the interrupted tests to investigate the occurrence of the severe-to-mild wear

transition and to provide evidence and discussion of such transition, occurring during the running-in of each of the evaluated systems.

### *AISI 310 Austenitic SS*

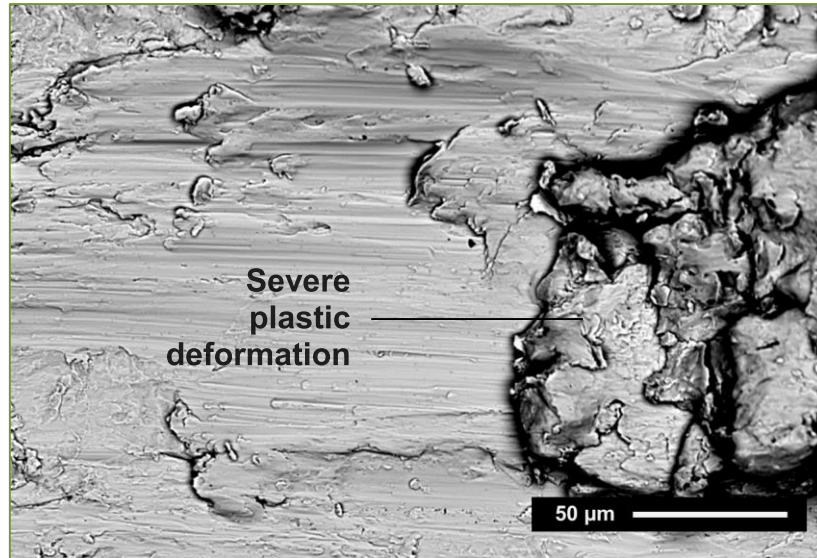
Figure 5.31 shows an SEM/SE image of the projected area of a representative wear scar on the surface of the AISI 310 discs after sliding 2.4 m (1 min). Sliding direction was horizontal.

Figure 5.31. Wear scar on the AISI 310 steel disc at  $s = 2.4$  m (1 min) (SEM/BSE - 25x mag.)



The SEM/BSE image does not show any tribofilm formation, indicating that wear occurred due to metal-to-metal contact. Plastic deformation due to severe adhesive wear can be seen (A detail of the wear mechanisms is shown in Figure 5.32). Hence, detachment of wear debris occurs by ductile fracture. Consequently, a great increase in surface roughness can be observed due to wear. The nominal (projected) area developed considerably due to severe mechanisms exclusively.

Figure 5.32. Detail of wear mechanisms on the wear scar on the AISI 310 steel at  $s = 2.4$  m (1 min)  
(SEM/BSE - 500x mag.)



The corresponding subsurface deformed layer at 2.4 m can be observed in Figure 5.33. The depth of the (developing) subsurface region extends up to  $30\ \mu\text{m}$  below the surface. A clearly defined interface separates the deformed region in the direction of the bulk and a heavily deformed region, which in turn will separate as metallic wear debris (Figure 5.33). The resulting wear debris particles present flow patterns due to plastic deformation (Figure 5.34).

Figure 5.33. Severe wear in the AISI 310 steel discs after 2.4 m (1 min). a) Subsurface deformation (500x mag.), and b) metallic debris formation (1000x mag.). (SEM/SE).

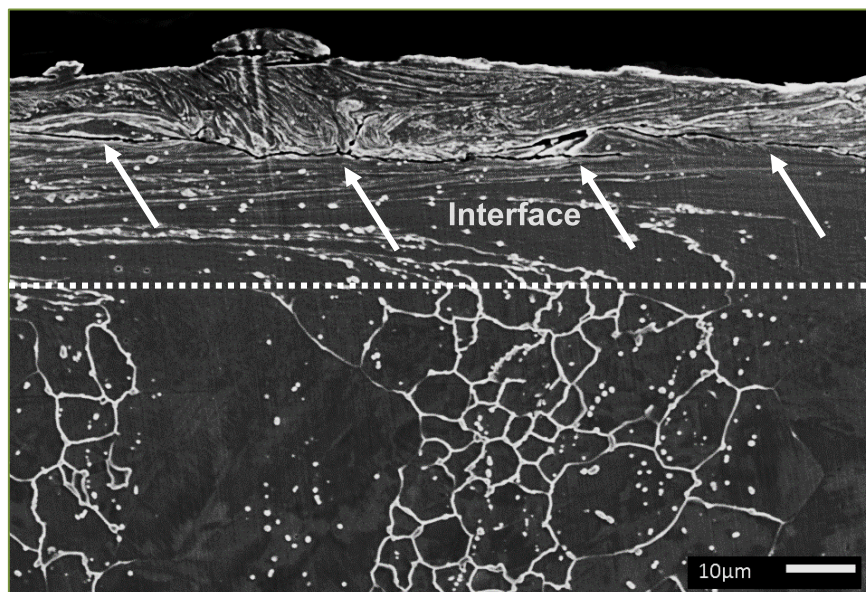
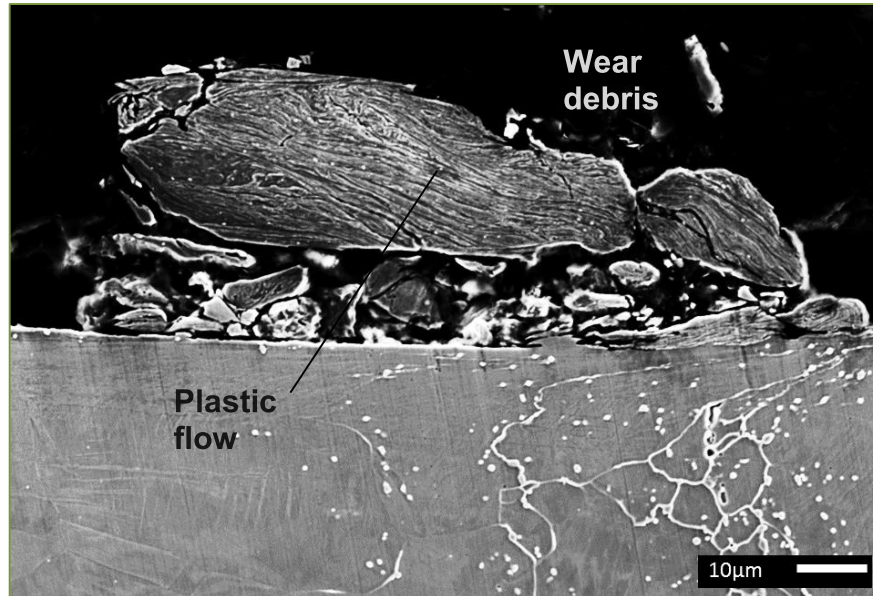


Figure 5.34. Metallic debris formation under severe wear in the AISI 310 steel discs after 2.4 m (1 min) (1000x mag.). (SEM/SE)



Metallic transfer from the disc to the ball was also observed. Figure 5.35 shows the wear scar on the ball tested against the AISI 310 steel after 2.4 m. EDS analyses conducted on the highlighted region in Figure 5.35 are shown in Figure 5.36. No tribofilm was identified at the worn surface of the ball. The transferred material appears bright in chromium map (Figure 5.36b), given that the AISI 310 steel has a greater content (25.0 wt.%) than the AISI 52100 steel (1.4 wt.%). The oxygen map (Figure 5.36b) confirms that there is negligible oxidation in the transferred metallic material.

Figure 5.35. Wear scar on the ball tested against the AISI 310 steel disc at  $s = 2.4$  m (1 min) (SEM/BSE - 25x mag.).

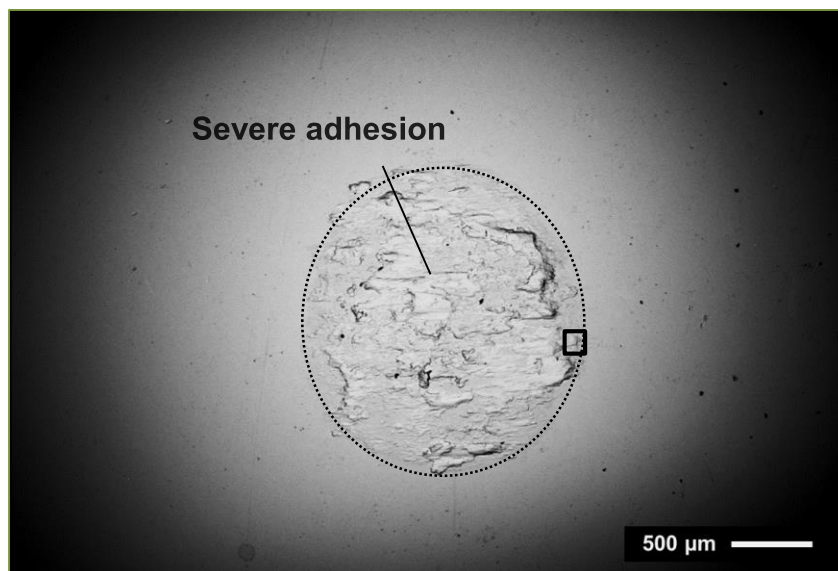
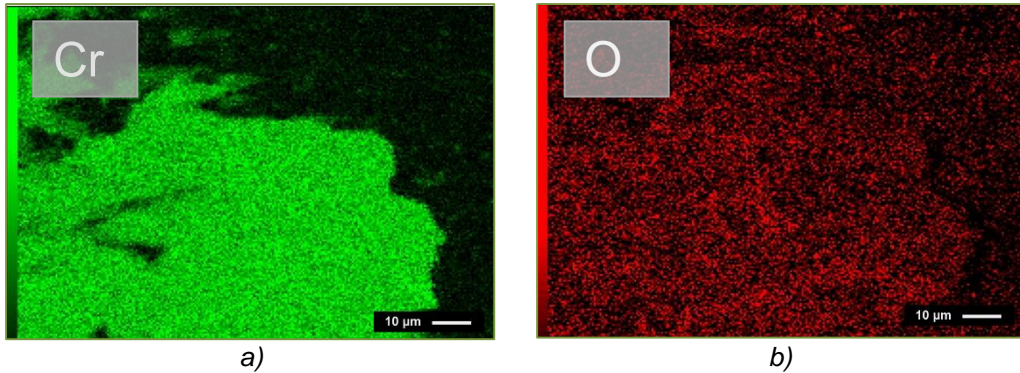


Figure 5.36. EDS analysis of the wear mechanisms in the ball tested against the AISI 310 steel at  $s = 2.4$  m (1 min): chromium (a), and oxygen (b). (1000x mag.).



Great variation in wear rates occur during the first 9.6 m (Figure 5.27), corresponding to alterations of the system from the onset of tests. Figure 5.37 shows the wear scar of the AISI 310 steel after 9.6 m. Tribofilm can be readily observed, indicating that the onset of tribo-oxidative wear mechanisms (a severe-to-mild wear transition) occurred between 0.4 and 9.6 m. At the end of the tests (73.2 m), a fully developed tribofilm can be observed (Figure 5.38).

Figure 5.37. Development of tribofilm in the AISI 310 tribosystem at 9.6 m (4 min). (SEM/BSE - 25x mag.)

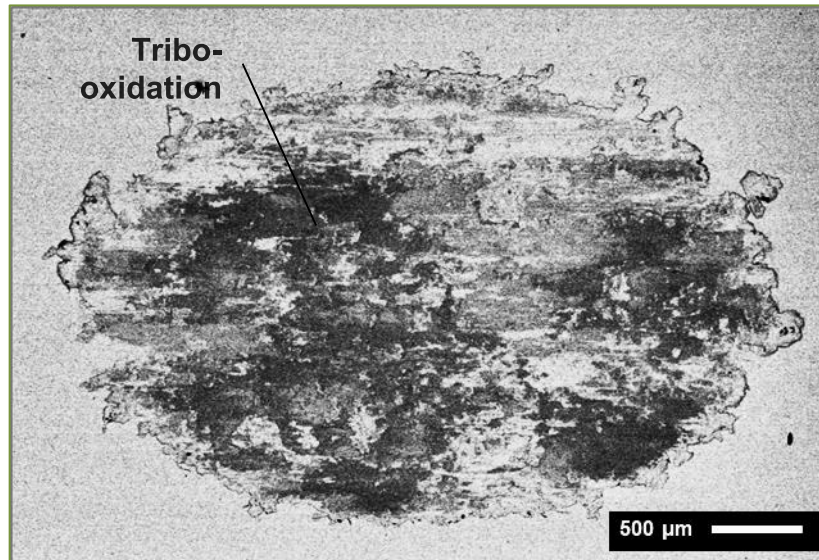
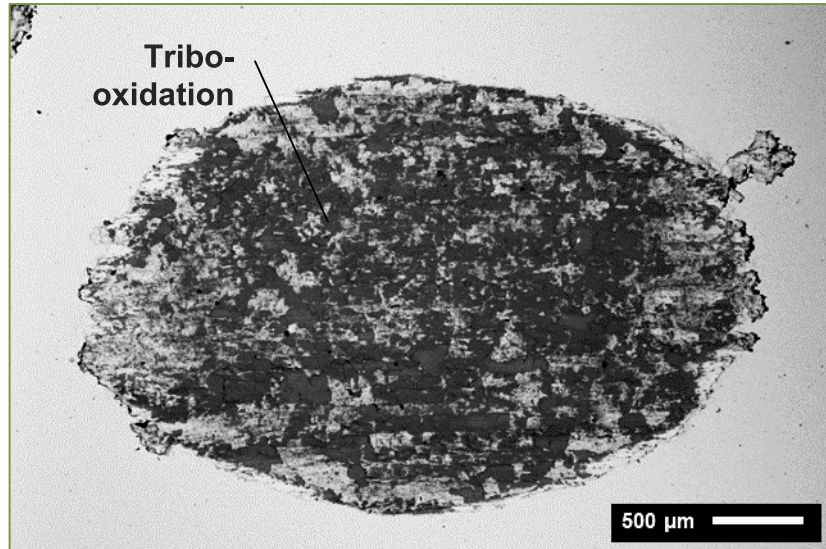


Figure 5.38. Development of tribofilm in the AISI 310 tribosystem at 73.2 m (30.5 min). (SEM/BSE - 25x mag.)



*SAE XEV-F valve steel*

A different behavior was observed for the untreated SAE XEV-F valve steel. Figure 5.39 shows the wear scar on this steel after 2.4 m. A detail of the wear mechanisms is shown in Figure 5.40.

Figure 5.39. Wear scar on the SAE XEV-F steel after 2.4 m (1 min). (SEM/BSE - 25x mag.)

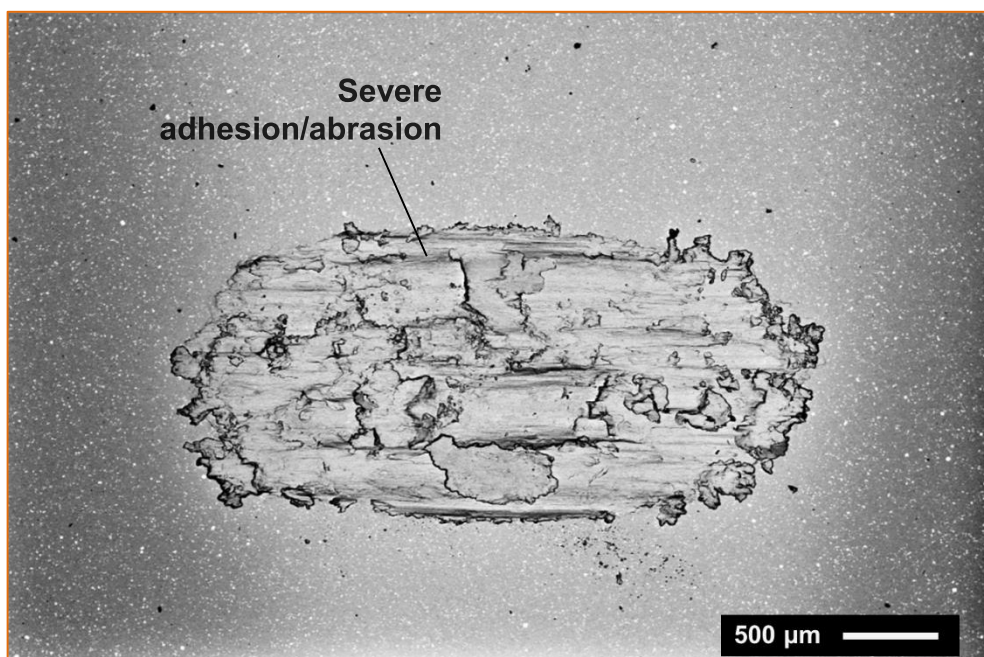
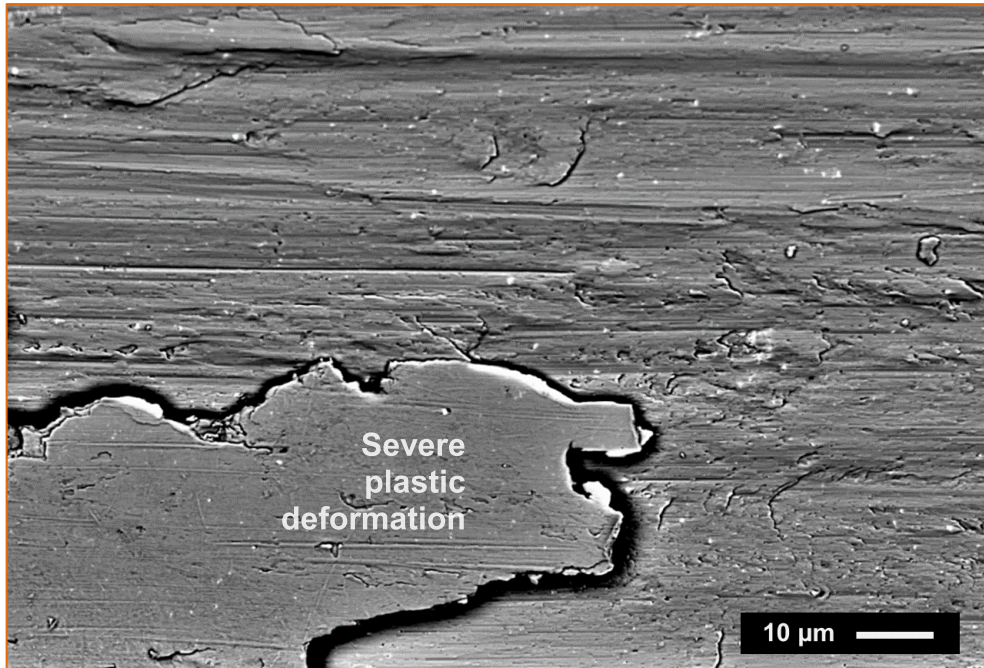


Figure 5.40. Detail of wear the wear mechanisms on the SAE XEV-F steel after 2.4 m (1 min)  
(SEM/BSE - 1000x mag.)



Wedge formation is observed, especially at the points of movement reversal. Metal-to-metal contact, adhesion, massive plastic deformation and mild abrasion can be identified (Figure 5.40). No tribofilm formation can be observed. Hence, only severe wear mechanisms were active. Ductile fracture controls wear debris generation. Surface roughness is higher when compared to the oxidized topography (see Figure 5.60). The nominal area developed considerably due exclusively to severe mechanisms. However, the wear scar observed in the SAE XEV-F steel is 25% smaller than the scar on the AISI 310 steel at the same sliding distance (Figure 5.31). Hence, ball penetration (and mass loss) was also smaller. This is due to the higher hardness of this steel, when compared to the AISI 310. The corresponding deformed layer (after 2.4 m) can be observed in Figure 5.41. The depth of the developing subsurface region extends to approximately 10 μm below the surface, the same value of depth found after 73.2 m (see Figure 5.88). Fracture of the NbC particles is readily observable, suggesting that the deformed layer in the SAE XEV-F steel developed soon after the beginning of sliding test. Further details of subsurface NbC fracture will be provided in the following sections.

Figure 5.41. Subsurface deformation due to severe metallic wear in the SAE XEV-F steel after 2.4 m (1 min). (SEM/BSE - 500x mag.)

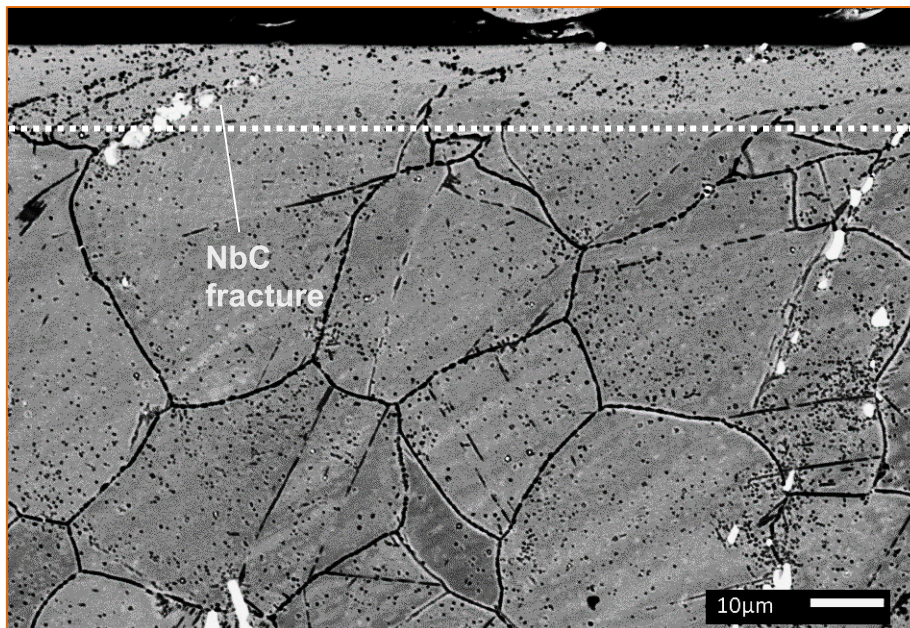


Figure 5.42 shows the wear scar on the ball tested against the SAE XEV-F steel after 2.4 m. No tribofilm was identified at the worn surface of the ball. A detailed view of the wear mechanisms is presented in (Figure 5.43a) and the corresponding chromium EDS map (Figure 5.43b) conducted on the highlighted region in Figure 5.42. The high chromium intensity confirms material transfer from the SAE XEV-F steel (Cr21 wt%) to the AISI 52100 steel (Cr1.4 wt%).

Figure 5.42. Wear scar on the AISI 52100 steel ball tested against the SAE XEV-F valve steel at  $s = 2.4$  m. (SEM/BSE - 25x mag.)

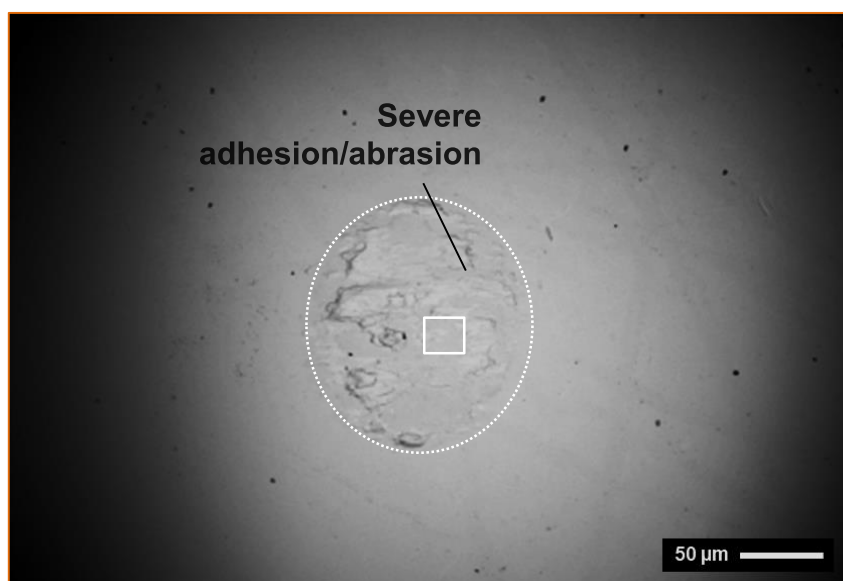
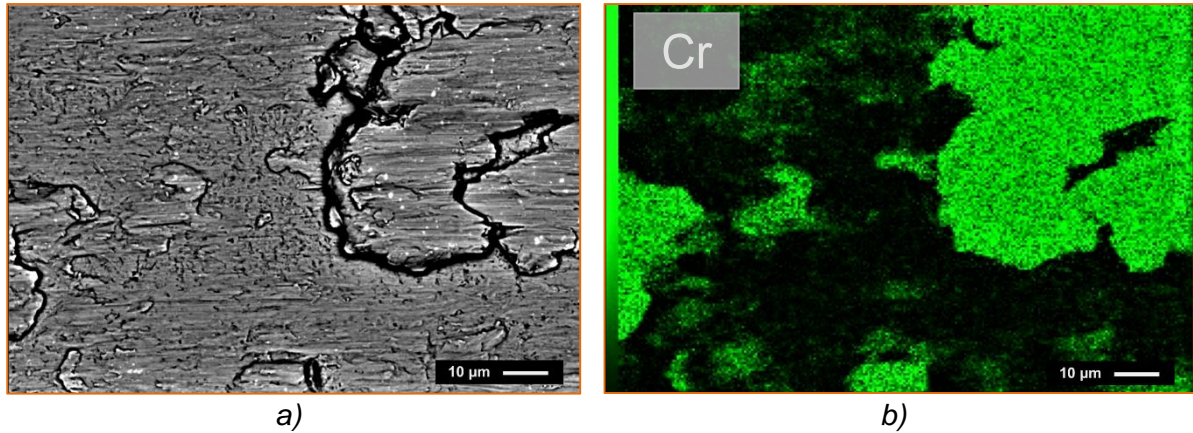
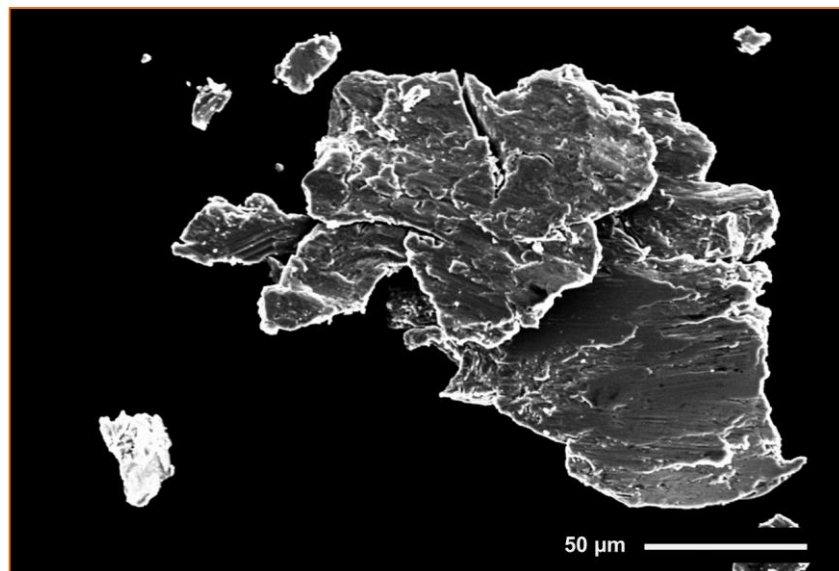


Figure 5.43. EDS analysis of the wear mechanisms in the ball tested against the SAE XEV-F steel: SEM/BSE detail (a), and chromium (b). (1000x mag.)



An EDS analysis of the wear debris of the SAE XEV-F steel produced in the severe regime was additionally conducted to inquire on the effect of NbC. An image of such wear debris is presented in Figure 5.44.

Figure 5.44. Wear debris of the SAE XEV-F steel. (SEM/SE - 500x mag.)



A region of the debris surface was selected to conduct de niobium EDS mapping. The results are shown in Figure 5.45. The presence of fractured NbC particles mechanically mixed within the (plastically deformed) austenitic matrix are readily observed. The size of the NbC particles is lower than the size of the wear debris in as much as one order of magnitude. This implies that the fractured NbC does not work as an abrasive particle itself. Instead, it contributes to increase the overall hardness of the wear particle.

Figure 5.45. EDS analysis of the wear debris produced from the SAE XEV-F steel: SEM/BSE image (a), and niobium (b). (1000x mag.)

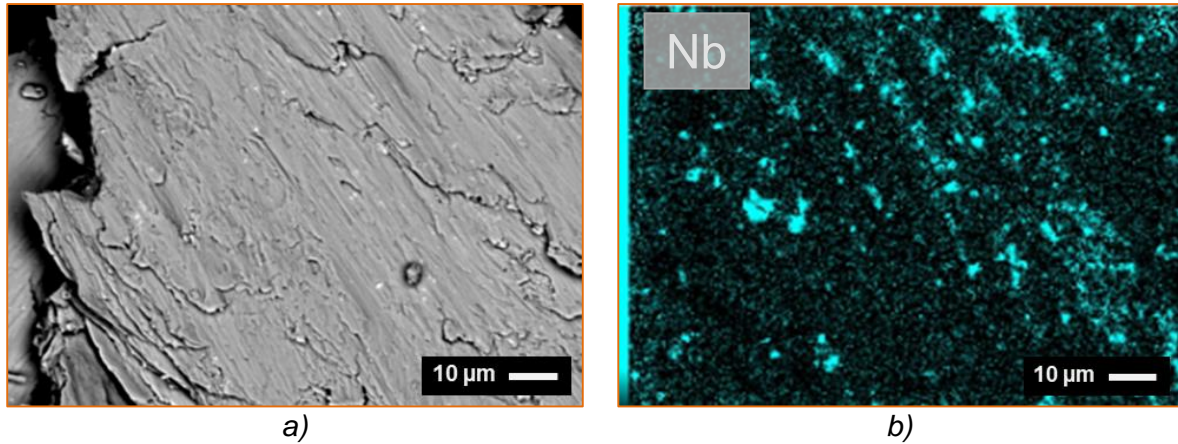


Figure 5.46a shows a typical wear scar on the SAE XEV-F steel after 9.6 m. The onset of oxidative wear mechanisms can be observed. The contact pressure reached the severe-to-mild transition threshold, despite no transition in mass loss was registered. The linear wear rate observed in this steel after 0.5 m (comparing Figure 5.46 and Figure 5.47) is due to its heterogeneous microstructure. Strain hardening of the surface competes with plastic stress concentration effects and the action of abrasive debris, hence avoiding the stabilization of the surface layer and facilitating material removal. The effective protective action of any existing tribofilm is hindered. This fact explains the stable increase in mass loss of the SAE XEV-F steel observed in Figure 5.27. Non-linear wear rates occur only in the first 0.5 m.

Figure 5.46. Evolution of the wear scar for the SAE XEV-F steel discs: 9.6 m (4 min). (SEM/BSE - 25x mag.).

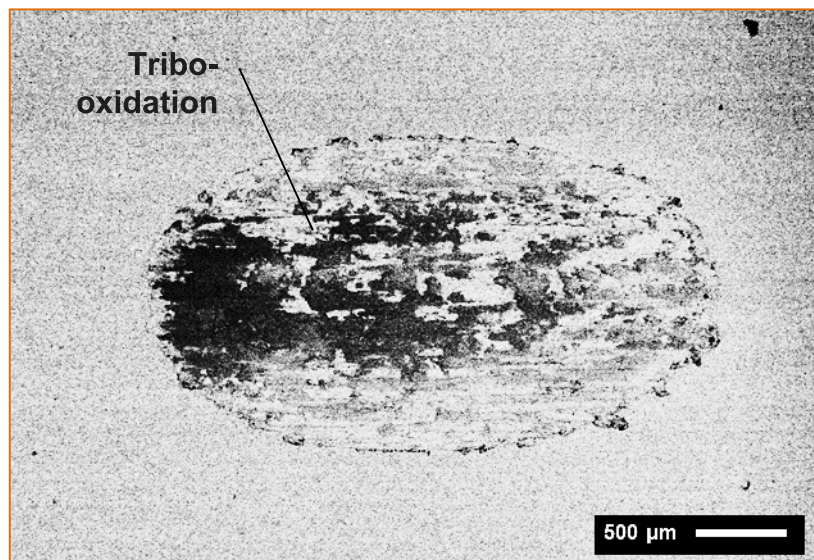
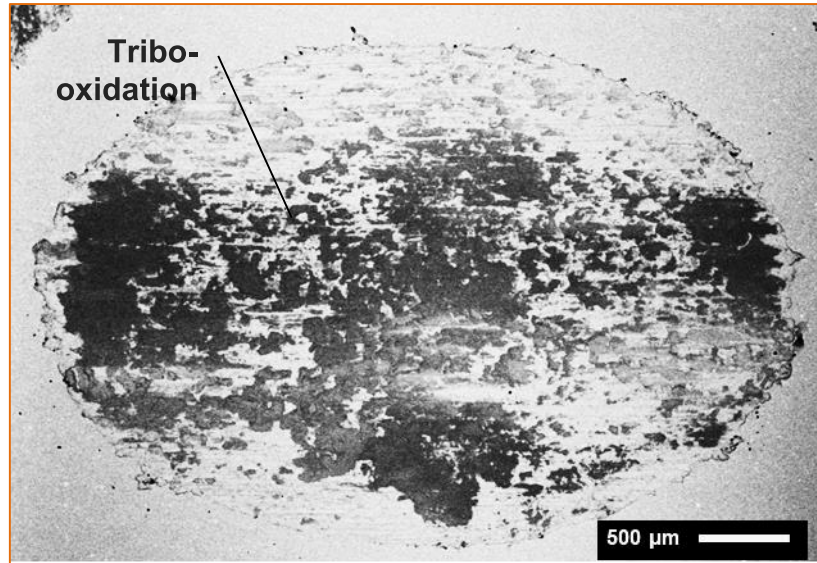


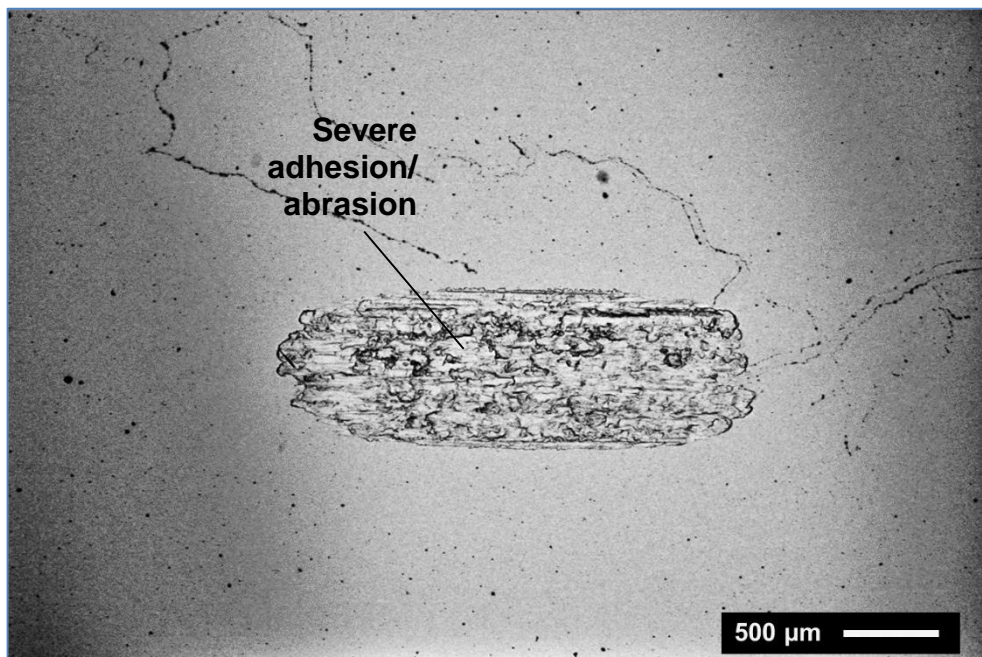
Figure 5.47. Evolution of the wear scar for the SAE XEV-F steel discs: 73.2 m (30.5 min). (SEM/BSE - 25x mag.).



*AISI H13 tool steel*

The wear scar in the AISI H13 steel at 0.4 m sliding distance is shown in Figure 5.48. The increase in nominal area is due to severe mechanisms after the first 0.4 m. No oxidative mechanisms are observed.

Figure 5.48. Wear scar on the AISI H13 steel at  $s = 0.4$  m (10 s) (SEM/BSE - 25x mag.).



Mass loss in the AISI H13 steel evolved in a linear manner (constant wear rate) after 0.4 m (see [Figure 5.28](#)), which indicates that changes in wear rates occurred only in the first 0.5 m (for the selected test parameters). In addition, subsurface plastic deformation in this steel due to sliding wear ([Figure 5.90](#)) presents a shallow depth ( $\sim 1 \mu\text{m}$ ). These two facts suggest that the severe-to-mild wear transition in the AISI H13 occurs without significant subsurface strain hardening, neither during running-in nor after. The hardness of the martensitic matrix is comparable to that of the ball (see [Figure 5.14](#)) and provides a surface with sufficient load-carrying capacity to induce the onset of tribo-oxidative mechanisms. This occurs once the contact pressure reaches a threshold value, between 0.4 m and 2.4 m ([Figure 5.49a](#)). The percentage of wear area covered by tribofilm remains (approximately) constant between 2.4 m and 73.2 m ([Figure 5.49b](#)).

[Figure 5.49](#). Evolution of the wear scar for the AISI H13 steel: a) 2.4 m (1 min), and b) 73.2 m (30.5 min). (SEM/BSE - 25x mag.)

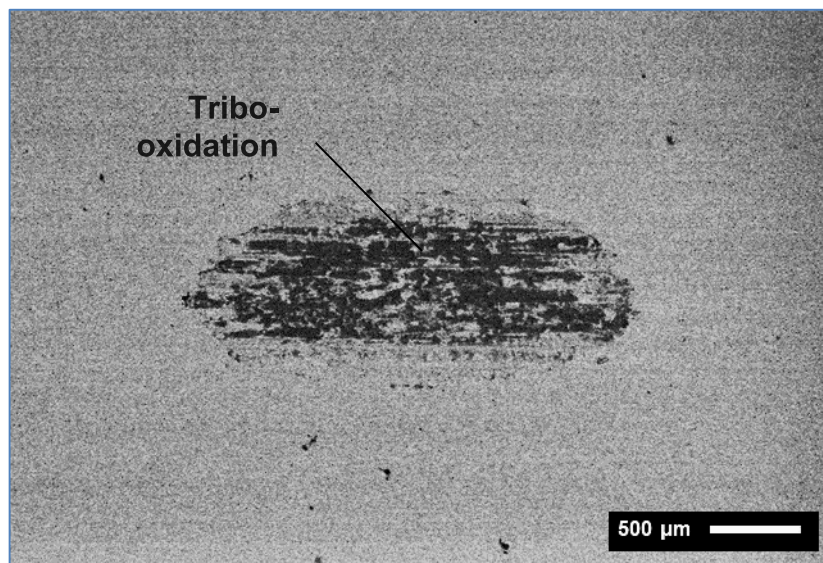
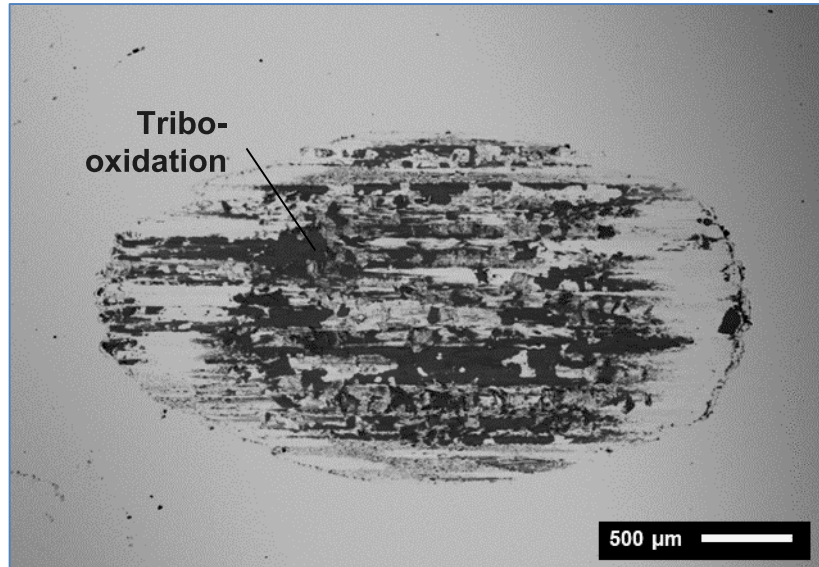


Figure 5.50. Evolution of the wear scar for the AISI H13 steel: a) 2.4 m (1 min), and b) 73.2 m (30.5 min). (SEM/BSE - 25x mag.)



*Nitrided SAE XEV-F valve steel*

Figure 5.51 shows the wear scar in the nitrided SAE XEV-F valve steel. No indication of predominant oxidation was observed, as previously discussed. Instead, mild abrasive wear mechanisms were observed, as highlighted in Figure 5.52. Hence, the evidence indicates that the severe-to-mild wear transition did not occur during running-in in this system under the specified values of test parameters.

Figure 5.51. Wear scar in the nitrided SAE XEV-F valve steel after 0.4 m (10 s). (SEM/SE - 25x mag.).

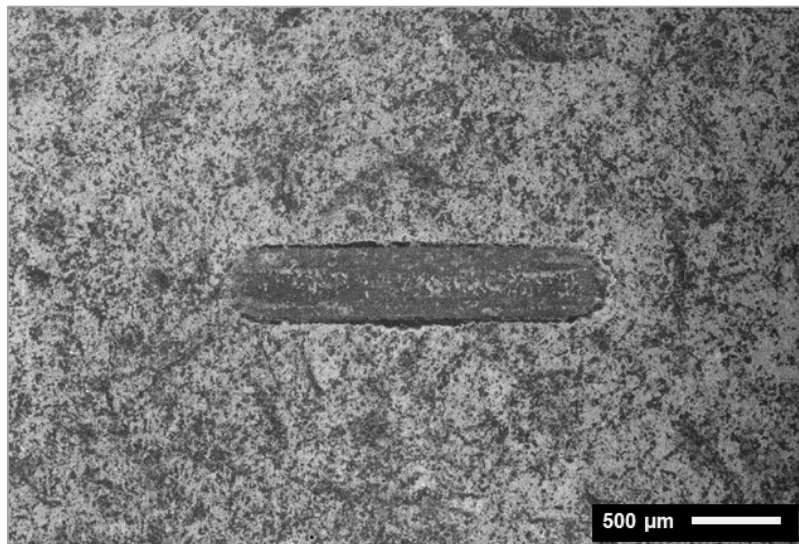
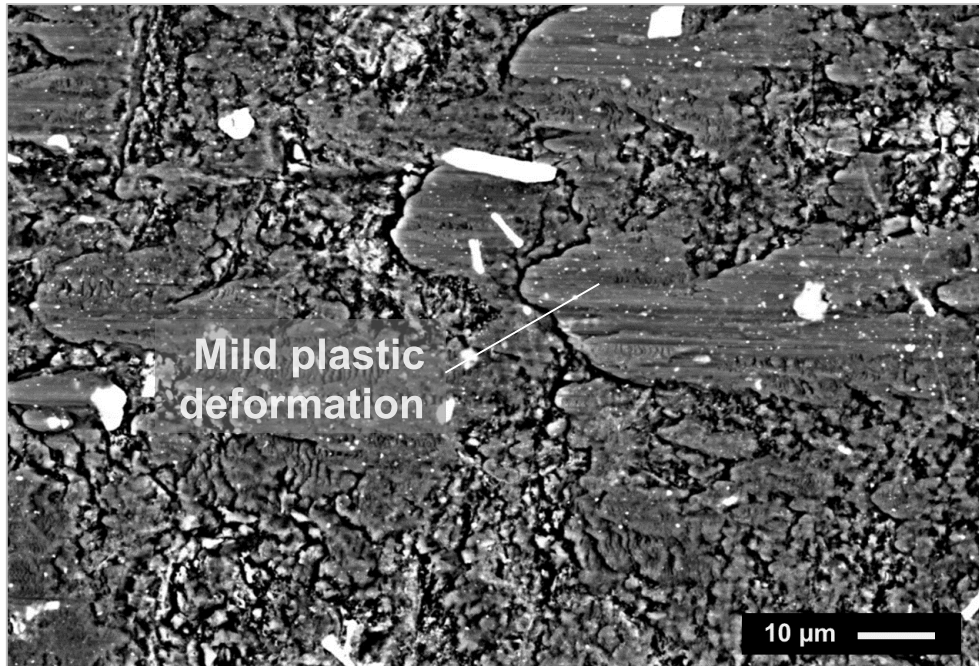


Figure 5.52. Detail of the wear mechanisms in the nitrided SAE XEV-F valve steel after 0.4 m sliding (SEM/BSE - 1000x mag.).



### 5.3.3 DETAILED ANALYSIS OF THE WEAR SCARS AT THE FINAL STAGE OF TRIBOLOGICAL TESTS

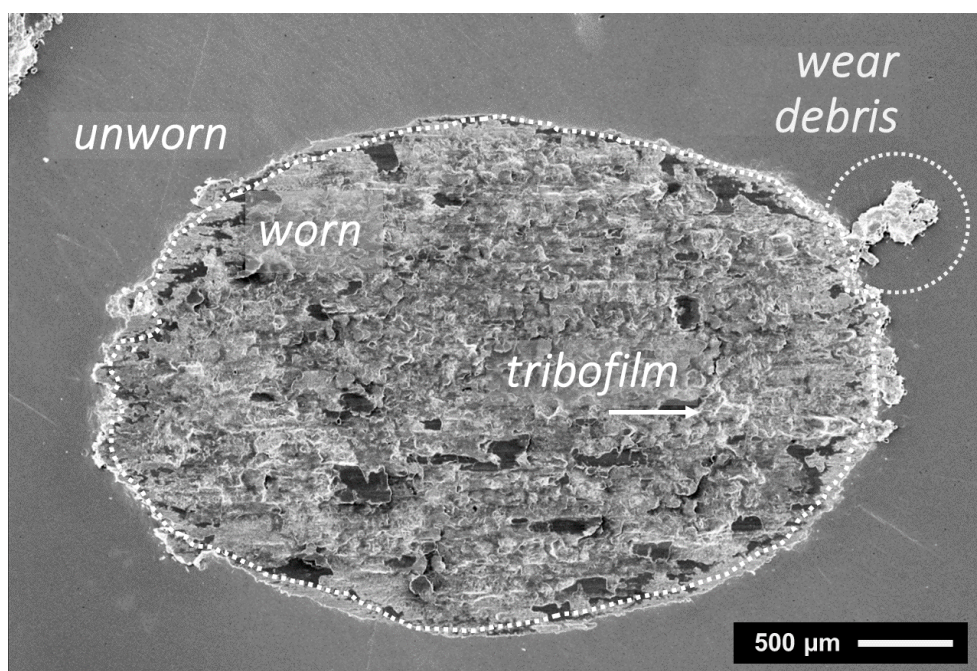
A detailed characterization of the wear scars after the full 73.2 m (30.5 min) tribological tests was conducted. The following aspects are discussed: wear mechanisms, nominal contact area, tribofilm formation and transfer, ball penetration, three-dimensional analysis of the wear scars, and subsurface deformation and strain hardening.

#### *Wear mechanisms of the discs*

Figure 5.53 shows an SEM/SE image of the projected area<sup>8</sup> of a representative wear scar on the surface of the AISI 310 discs. Sliding direction was horizontal (length of the scar).

<sup>8</sup> The value of the nominal contact area (as visualized in the SEM images of the wear marks) differs from that of the actual area of the wear scar. This aspect will be further discussed in the ball penetration section.

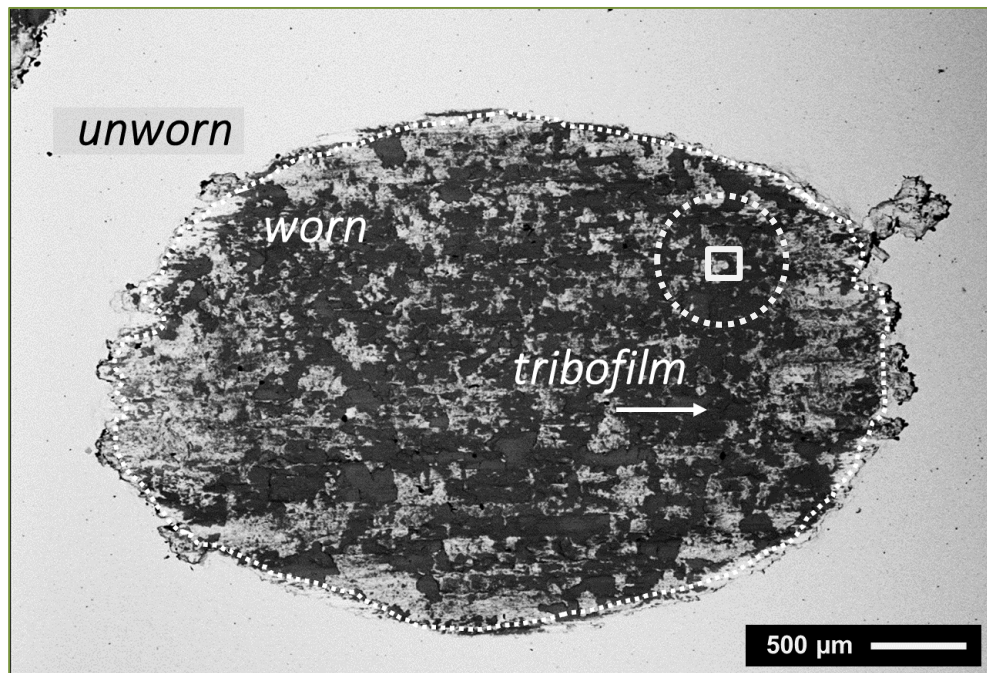
Figure 5.53. Wear scar on the AISI 310 steel disc (SEM/SE - 25x mag.).



Both debris formation (highlighted in Figure 5.53) and wedge formation can be observed at both left and right ends of the wear scar, that is, at the points of inversion of direction. This was expected due to the low hardness and high ductility of AISI 310 austenitic stainless steel. Additionally, a significant increase in surface roughness can be observed due to wear. In this sense, SEM/SE images are useful in identifying topographical and morphological features of the worn surfaces. However, they do not allow clear differentiation of tribofilm formation. In contrast, SEM/BSE images (Figure 5.54) readily show the presence of a tribofilm (dark regions) covering the wear scar. Hence, backscattered electrons images are fundamental for evaluating the tribofilm formation and were widely employed in this thesis.

Two distinct regions can be observed within the contour of the wear scars in Figure 5.54: abundant dark gray regions and (scarce) light gray regions. Since SEM/BSE images correlate with atomic number, dark gray regions indicate a tribofilm with predominance of oxygen (ROSENBERG; JORDAN, 1934; QUINN; SULLIVAN; ROWSON, 1984) as indicated by EDS analysis (see Figure 5.56a). In this sense, the widespread observation of a tribofilm indicates that, under the specified test conditions, wear of the AISI 310 steel occurs in the mild oxidative regime.

Figure 5.54. SEM/BSE image of the wear scar on the AISI 310 steel disc (25x mag.).



A detailed image of the wear mechanisms in the AISI 310 steel is shown in [Figure 5.55](#). It can be observed that the tribofilm is smeared on the metal surface reaching different levels of compaction (as highlighted in the figure). There is no evidence of abrasive mechanisms, which is an indication that the formed tribofilm performs as a protective interfacial medium.

Figure 5.55. Wear mechanisms in the wear scar on the AISI 310 steel disc (SEM/BSE - 1000x mag.).

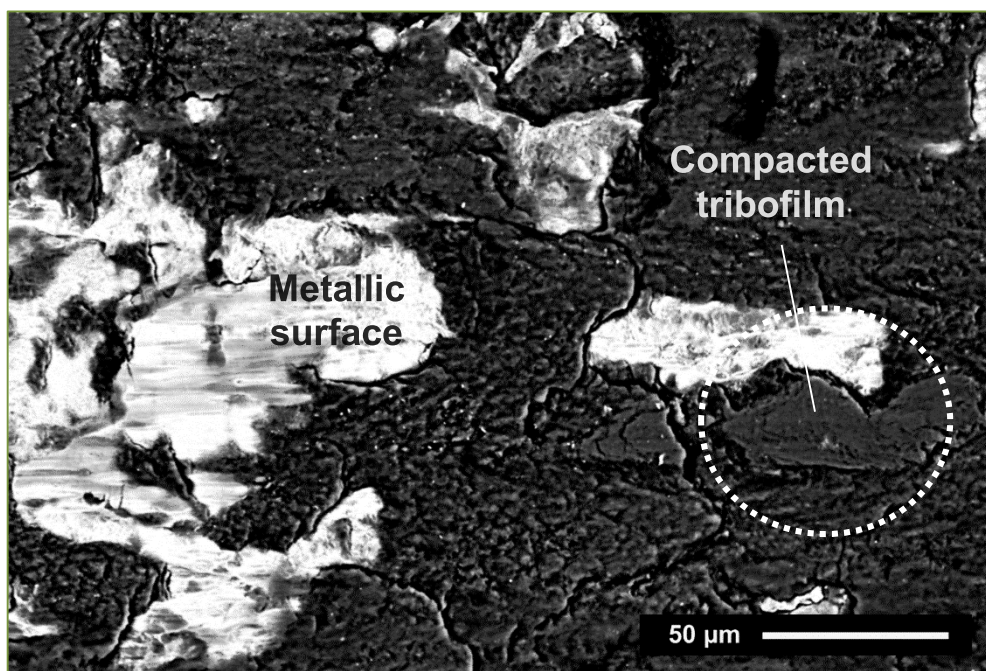
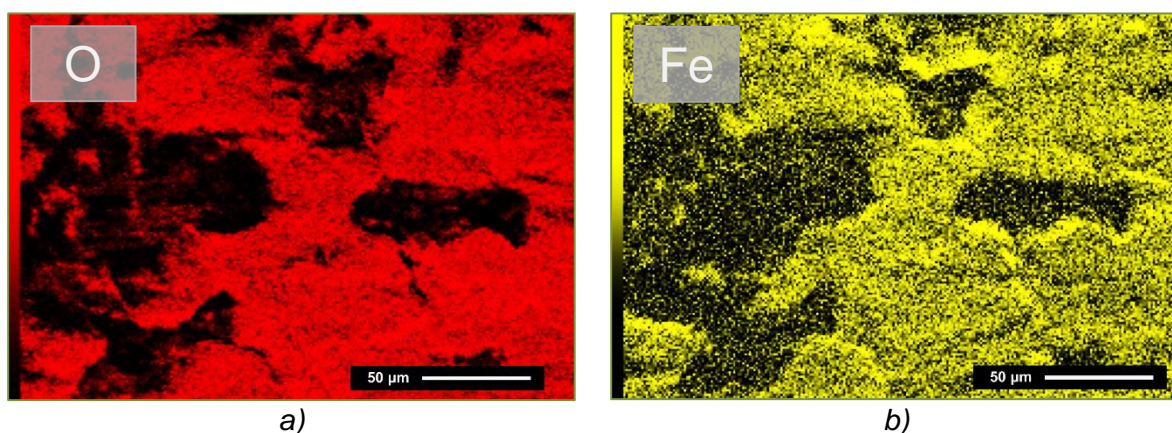


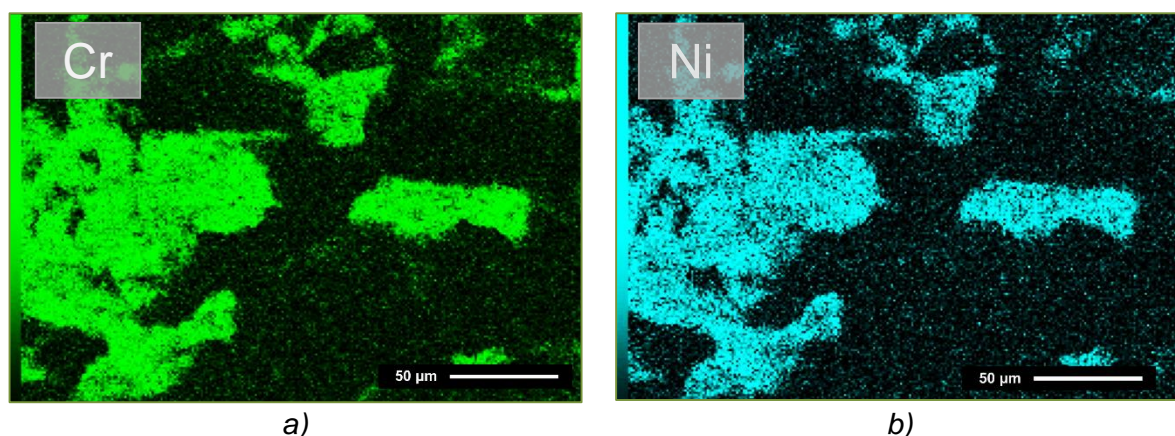
Figure 5.56 shows the EDS maps of oxygen, iron, chromium and nickel, corresponding to the region shown in the BSE image (Figure 5.55). A clear correlation can be observed between the BSE image (Figure 5.55) and the corresponding EDS maps (Figure 5.56). Oxygen (Figure 5.56a) and iron (Figure 5.56b) are found highly concentrated in the tribofilm region, suggesting that the tribofilm is composed of iron oxides.

Figure 5.56. SEM/EDS analysis of the tribofilm in the wear scar of the AISI 310 austenitic stainless steel. EDS maps of: oxygen (a), and iron (b). (1000x mag.)



The chromium (Figure 5.57a) and nickel (Figure 5.57b) concentrations in the tribofilm were low when compared to those in the metal surface indicating that there are no observable metallic debris embedded in the tribofilm.

Figure 5.57. SEM/EDS analysis of the tribofilm in the wear scar of the AISI 310 austenitic stainless steel. EDS maps of: chromium (a), and nickel (b). (1000x mag.)

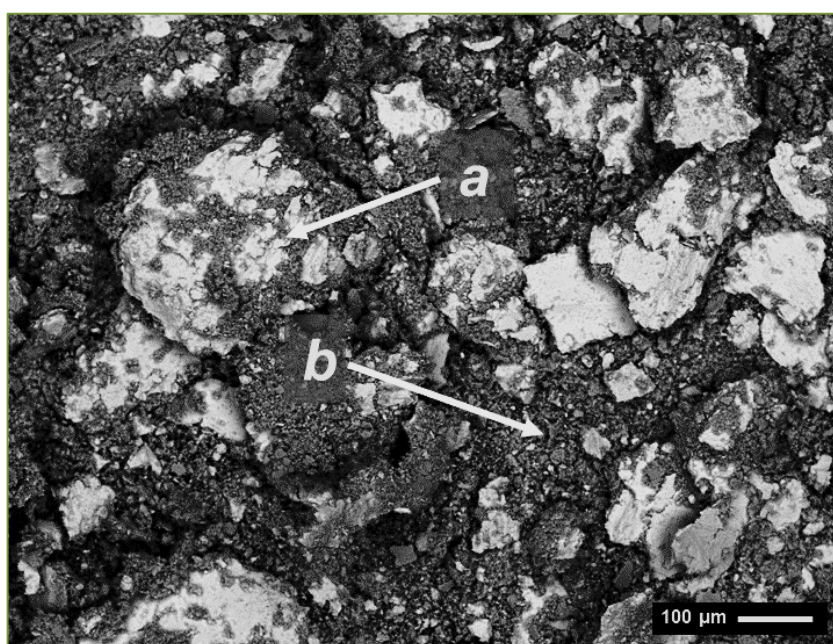


The widespread tribofilm formation occurred despite the high chromium content of this steel (25 wt.%). Chromium is an alloying element primarily added to prevent iron oxidation by means of the formation of a passivated layer (a nano-scale chromium

oxide film). Hence, the acting interfacial conditions of pressure and temperature (which are related to the competition between oxide formation and removal) hinder the formation of the passivated layer and massive iron oxidation occurs.

Most of the formed wear debris do not remain at the sliding interface, but are expelled to the outer region of the wear scar. Wear debris resulting from tribological tests were collected for analysis and examined via electron microscopy and XRD. [Figure 5.58](#) shows a SEM/BSE image of the wear debris obtained in the AISI 310 tests.

[Figure 5.58](#). Wear debris of the AISI 310 steel (SEM/BSE - 100x mag.)



As indicated before, BSE images can readily identify between metal (light grey) and oxides (dark grey). This is confirmed in [Figure 5.58](#). Wear debris were composed of large metallic particles (as big as  $\sim 500 \mu\text{m}$ ) labelled *a*; and fine oxide particles ( $\sim 10 \mu\text{m}$  max), labelled *b*. However, the samples obtained were only a portion of the total amount of debris formed. To better estimate the representative sizes of wear debris further statistical analysis could be conducted and were not in the scope of this work. XRD analysis was performed on the collected debris after the tests. The AISI 310 pattern is shown in [Figure 5.59](#). Peaks in the wear debris XRD patterns present low definition (wider peaks) and higher dispersion (background noise) when compared to those obtained from the bulk materials (compare to [Figure 5.3](#)). However, phase identification was performed via indexation. Austenite was found on the wear debris of the AISI 310 steel confirming the presence of metallic (austenitic) particles. No strain-

induced martensite was identified in the wear debris. Two iron oxides were found in the pattern: hematite<sup>9</sup> ( $\text{Fe}_2\text{O}_3$ ) and magnetite ( $\text{Fe}_3\text{O}_4$ ). No wüstite ( $\text{FeO}$ ) was detected. These two detected oxide species ( $\text{Fe}_2\text{O}_3$  and  $\text{Fe}_3\text{O}_4$ ) have been identified as the result of dry sliding of steels since 1934 (ROSENBERG; JORDAN, 1934). The iron oxides at the interface are thought to work as a protective film and are usually associated with the occurrence of mild wear (ROSENBERG; JORDAN, 1934; QUINN; SULLIVAN; ROWSON, 1984). Chromium oxide formation ( $\text{Cr}_2\text{O}_3$ ) may occur, but regarding its small volume fraction it was not identified in the XRD pattern.

Figure 5.59. XRD patterns of the wear debris of AISI 310 steel.

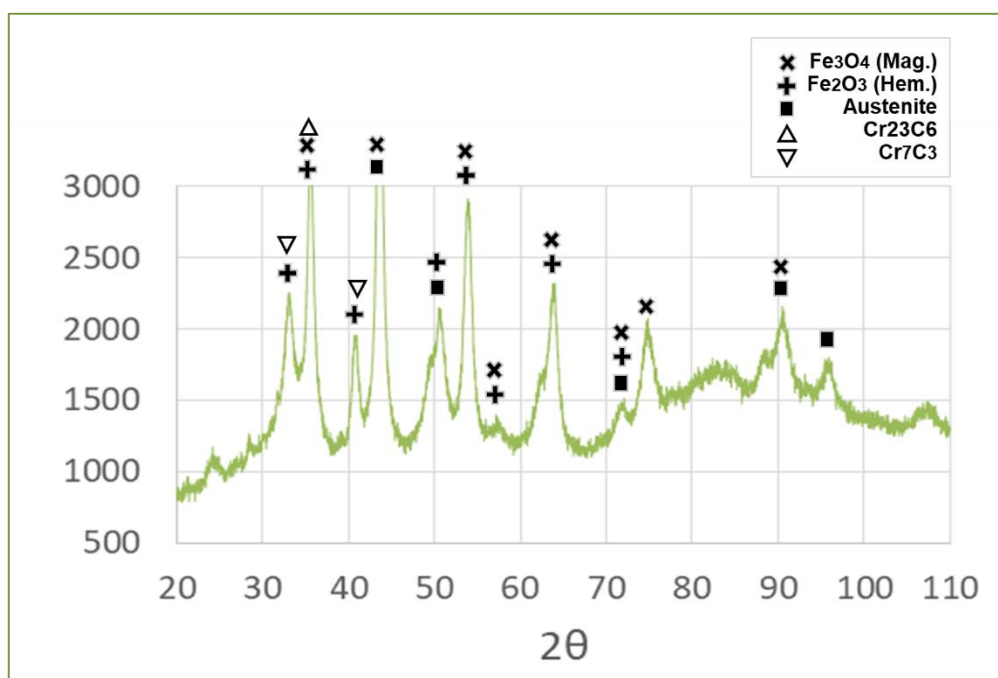


Figure 5.60 shows an SEM/BSE image of the projected area of a representative wear scar on the surface of the SAE XEV-F discs. Sliding direction was horizontal.

Tribofilm formation can be readily observed within the contour of the wear scar, but in a lesser degree than in the AISI 310 steel (Figure 5.54) despite the higher chromium content of the SAE XEV-F steel (21wt.%). As in the AISI 310 steel, the acting interfacial conditions of pressure and temperature hinder the formation of the passivated layer and massive iron oxidation occurs. The presence of a tribofilm suggests that, under the specified test conditions, wear of the SAE XEV-F steel occurs

<sup>9</sup> Hematite, JCPDS code: 00-001-1053.

Magnetite, JCPDS code: 00-001-1111.

Wüstite, JCPDS code: 00-001-1223

in the mild oxidative regime. However, since hard NbC precipitates are thought to have an important role in this steel, a detailed analysis of the wear scars was conducted to further investigate the predominant wear mechanisms.

Figure 5.60. Wear scar on the SAE XEV-F valve steel (SEM/BSE - 25x mag.).

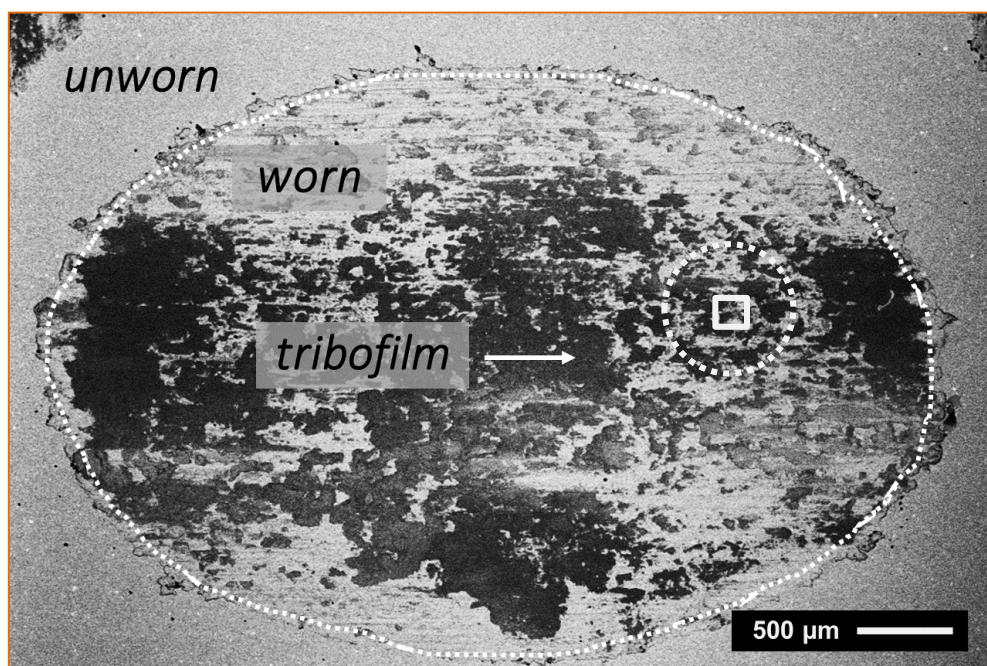


Figure 5.61 presents a detailed view of the highlighted region in Figure 5.60. Tribo-oxidative mechanisms are identified and confirmed by the oxygen EDS map (Figure 5.62).

Regarding the NbC precipitates, the corresponding niobium EDS map (Figure 5.63) shows NbC precipitates oriented parallel to the sliding direction and in sizes lower than in the unworn steel (see Figure 5.8). These results suggest that NbC fracture occurred, and the fractured precipitates detached from the matrix and were dragged along the surface together with the existing tribofilm. Since large NbC particles are not readily observed, the hypothesis of hard abrasive NbC particles increasing wear by abrasion (ZUM GAHR, 1998) is not supported by the presented evidence.

Nevertheless, the presence of hard abrasive particles was identified at the interface (as highlighted in Figure 5.61), and shown in detail in Wear debris were collected for analysis and examined via electron microscopy and XRD. Figure 5.64 shows a SEM/BSE image of the wear debris obtained in the SAE XEV-F tests. The BSE images reveal metallic particles (<100 μm) labelled *a*; and fine oxide particles

(~10  $\mu\text{m}$  max), labelled *b*. The SAE XEV-F XRD pattern is shown in [Figure 5.65](#). These particles, partially oxidized, strain hardened and with embedded NbC, cause abrasion grooves in the austenitic matrix (as indicated in [Figure 5.61](#)). This effect is probably related to the pronounced wear of the SAE XEV-F steel. The results indicate that oxidative wear in the SAE XEV-F steel does not necessarily traduce in low wear.

[Figure 5.61](#). Detail image of the wear scar on the SAE XEV-F valve steel disc (SEM/BSE - 1000x mag.).

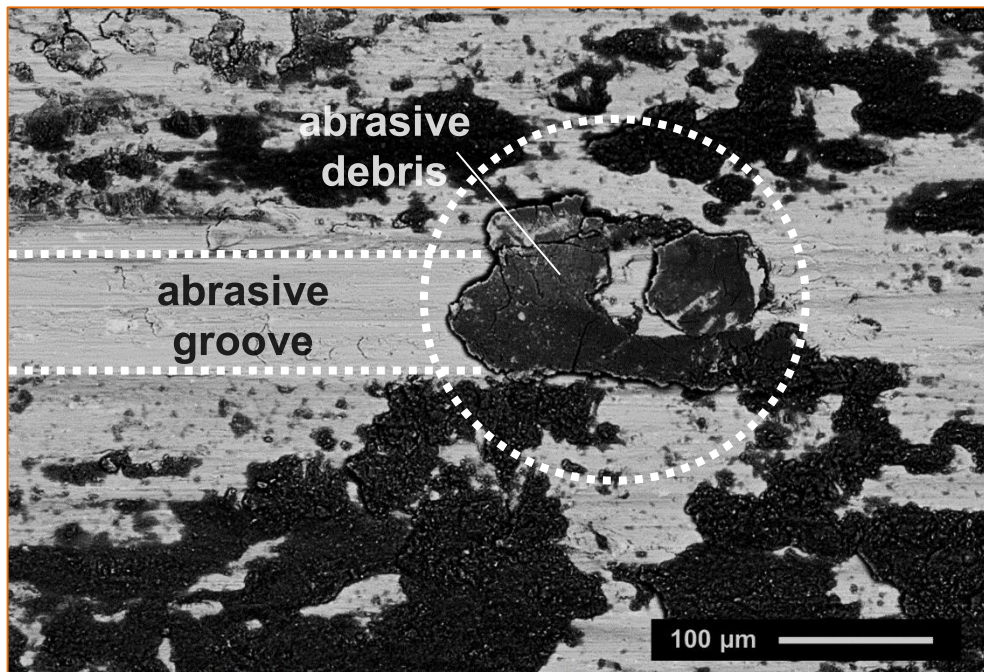


[Figure 5.62](#). Oxygen EDS map on the highlighted region of the wear scar on the SAE XEV-F valve steel disc (1000x mag.).

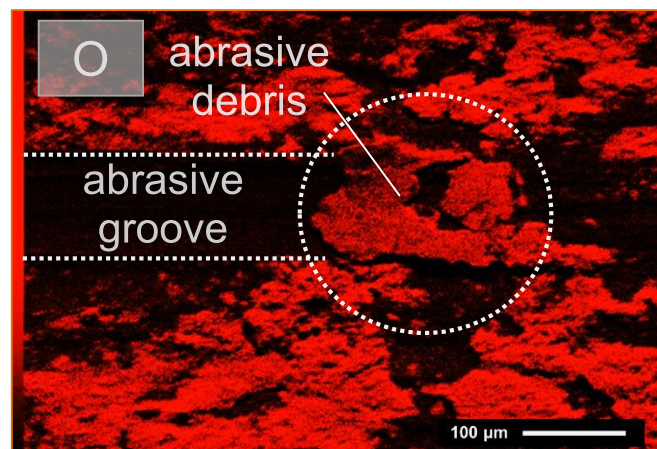
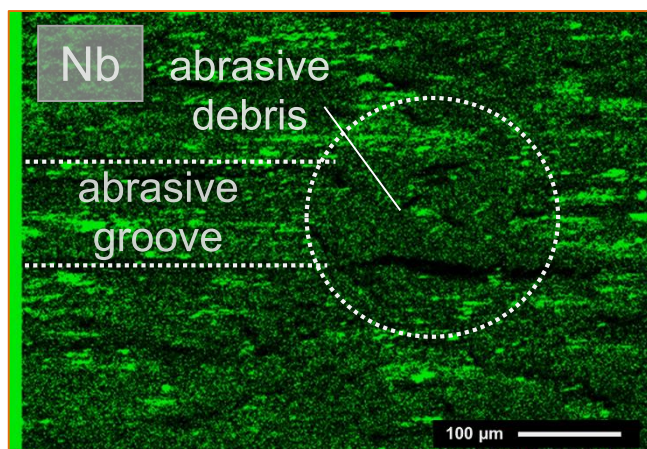


Figure 5.63. Niobium EDS map on the highlighted region of the wear scar on the SAE XEV-F valve steel disc (1000x mag.).



Wear debris were collected for analysis and examined via electron microscopy and XRD. Figure 5.64 shows a SEM/BSE image of the wear debris obtained in the SAE XEV-F tests. The BSE images reveal metallic particles (<100 μm) labelled *a*; and fine oxide particles (~10 μm max), labelled *b*. The SAE XEV-F XRD pattern is shown in Figure 5.65.

Figure 5.64. Wear debris of the SAE XEV-F steel (SEM/BSE - 100x mag.)

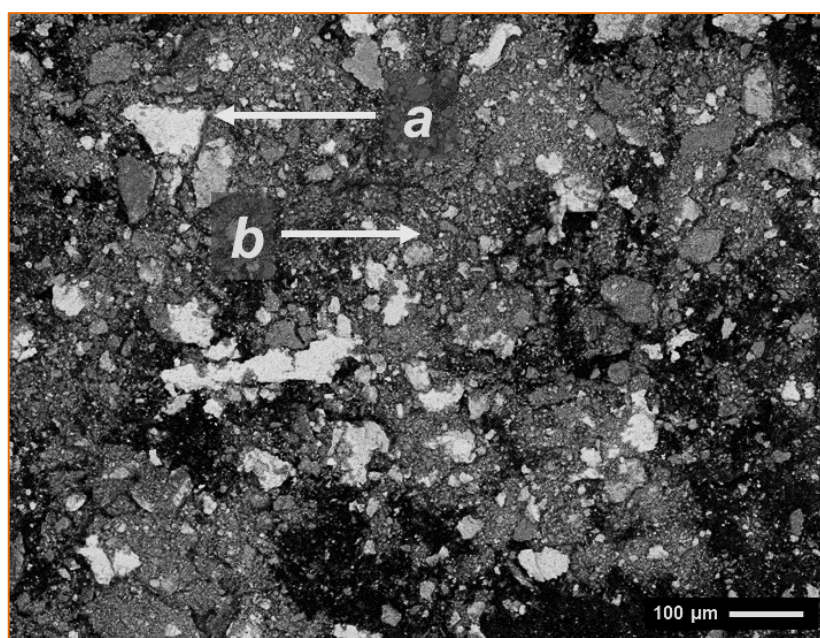
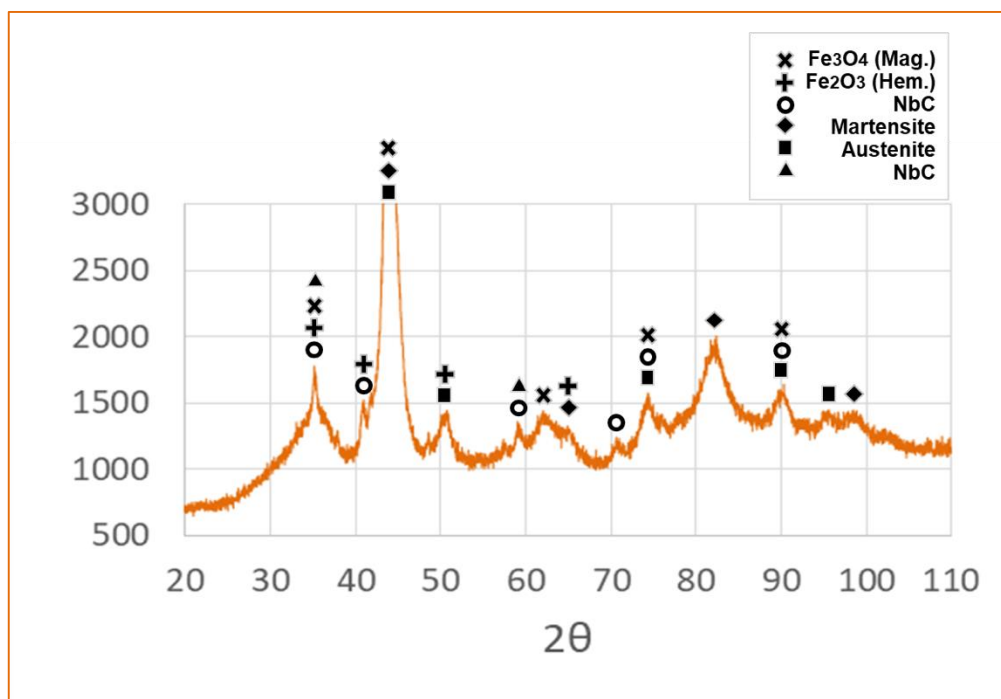


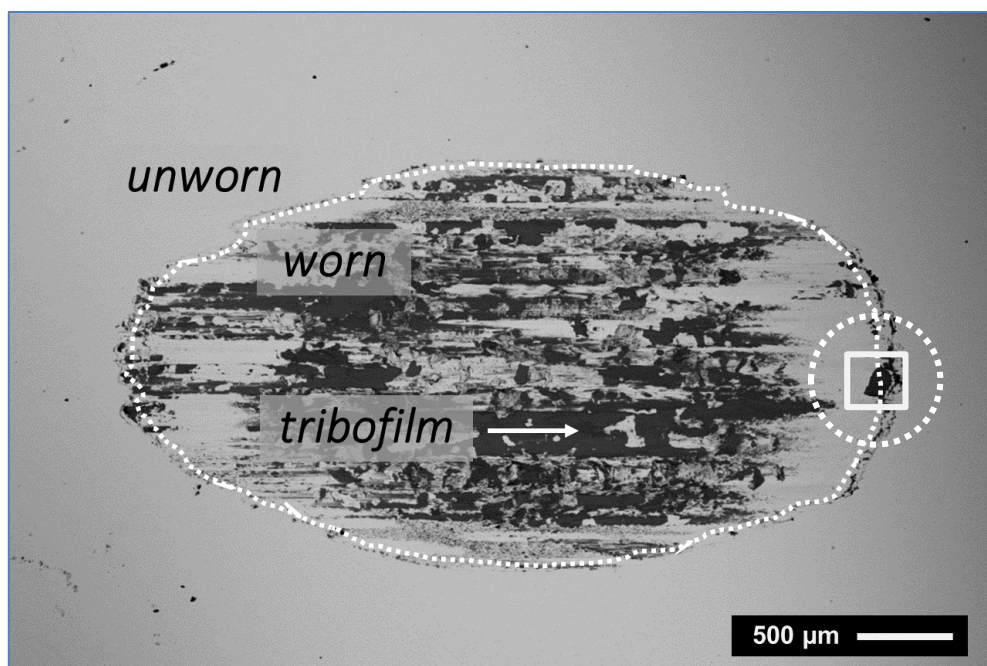
Figure 5.65. XRD patterns of the wear debris of SAE XEV-F steel.



Phase identification was performed via indexation. Austenite was found on the wear debris of the SAE XEV-F steel confirming the presence of metallic (austenitic) particles. Two iron oxides were found in the pattern: hematite ( $\text{Fe}_2\text{O}_3$ ) and magnetite ( $\text{Fe}_3\text{O}_4$ ). Martensite was also found in the wear debris of SAE XEV-F valve steel indicating that wear debris in this system also consist of a low volume fraction of strain-induced martensite. Although in low volume fraction, the martensite may increase wear by abrasive processes in this tribosystem given the lower hardness of the austenitic matrix when compared to martensite. NbC particles are also identified in the wear debris of the SAE XEV-F valve steel, indicating that precipitates were incorporated in the tribofilm during the wear debris forming process. The protective function of the iron oxides at the interface seems to compete with other wear mechanisms. This hypothesis is further explored in the subsurface deformation section.

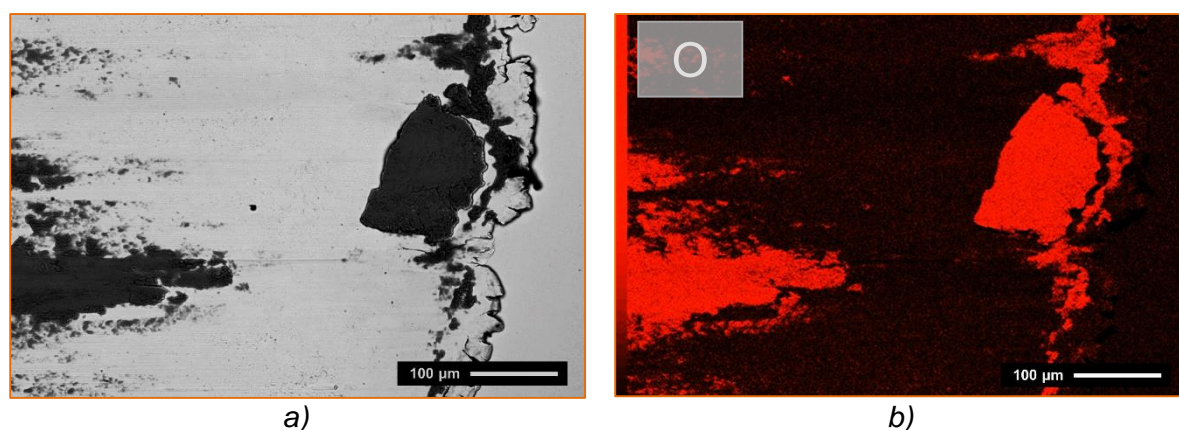
Figure 5.66 shows a SEM/BSE image of the projected area of a representative wear scar on the surface of the AISI H13 discs. Sliding direction was horizontal.

Figure 5.66. SEM/BSE image of the wear scar on the AISI H13 steel (25x mag.).



Tribofilm formation can be readily observed within the contour of the wear scar. This result was confirmed via SEM analysis of the wear scars of the discs (Figure 5.67) by the corresponding EDS maps of oxygen (Figure 5.67b). The presence of a tribofilm suggests that, under the specified test conditions, wear of the AISI H13 steel occurs in the mild oxidative regime.

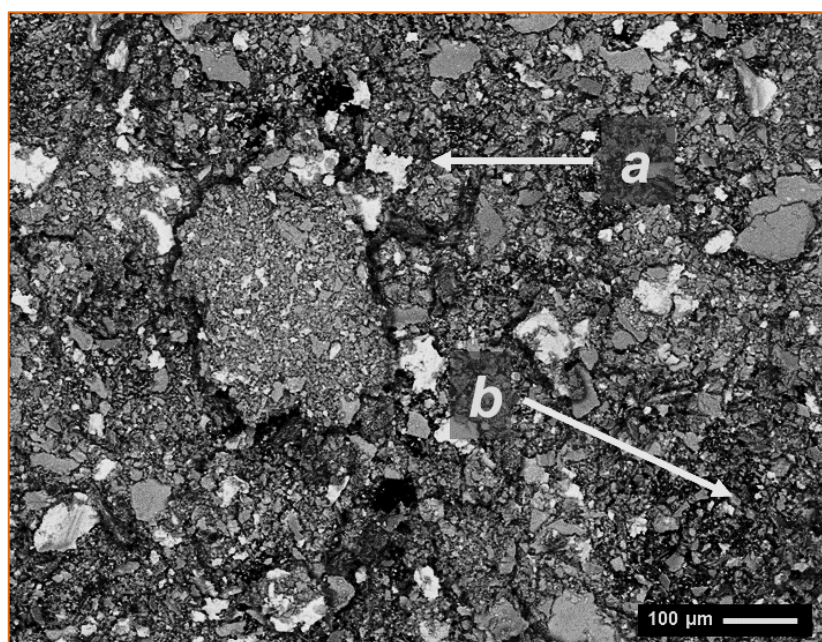
Figure 5.67. SEM analysis of the highlighted region (white rectangle) of the wear scar on the AISI H13 steel. Detail BSE image (a), and corresponding oxygen EDS map (b). (200x mag.).



Wear debris were collected for analysis and examined via electron microscopy and XRD. Figure 5.68 shows a SEM/BSE image of the wear debris obtained in the AISI H13 tests. The BSE images reveal metallic particles (<math><50\ \mu\text{m}</math>) labelled a; and fine

oxide particles (~10  $\mu\text{m}$  max), labelled *b*. Hence, an important observation is that the size of metallic debris particles presented an inverse correlation to hardness. Higher hardness values seem to generate smaller metallic debris and in a less amount. As can be observed when comparing the metallic wear particles in [Figure 5.58](#), [Figure 5.64](#) and [Figure 5.68](#). Nevertheless, further statistical analysis is required to ensure statistical representativeness of such tendency.

[Figure 5.68](#). Wear debris of the AISI H13 steel (SEM/BSE - 100x mag.)



The AISI H13 wear debris XRD pattern is shown in [Figure 5.65](#). Martensite was identified in the wear debris of the AISI H13 steel, as expected. Hence, the metallic particles observed in [Figure 5.68](#) are martensitic. Two iron oxides were identified: hematite ( $\text{Fe}_2\text{O}_3$ ) and magnetite ( $\text{Fe}_3\text{O}_4$ ). The iron oxides at the interface appeared to work as a protective film (mild wear).

[Figure 5.70](#) shows a SEM/BSE image of the projected area of a representative wear scar on the surface of the nitrided SAE XEV-F discs. Sliding direction was horizontal (length of the scar).

Figure 5.69. XRD pattern of the wear debris of AISI H13 steel.

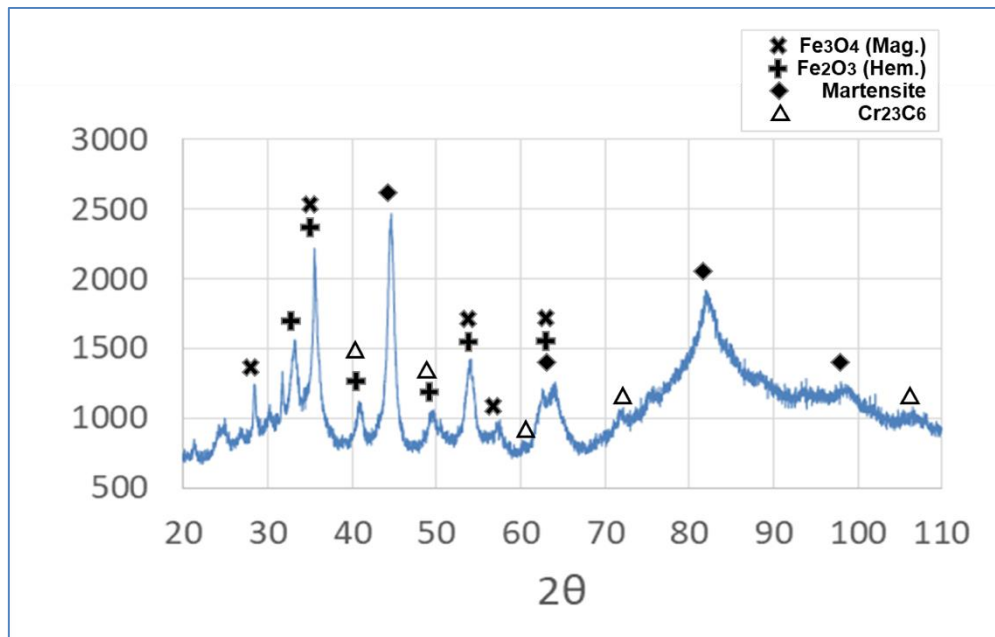
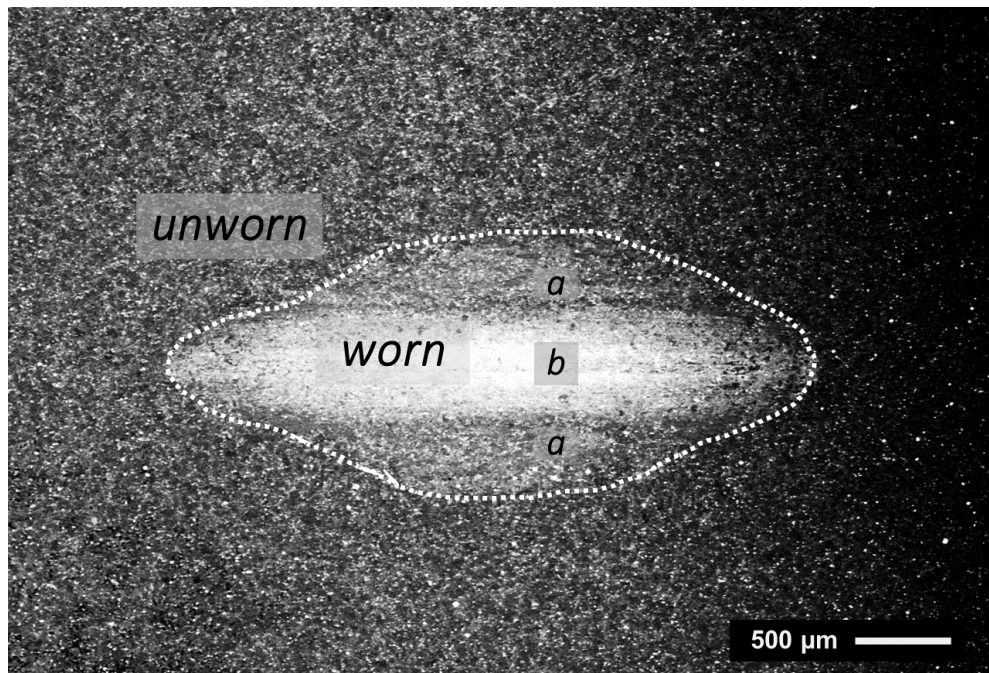


Figure 5.70. SEM/BSE image of the wear scar on the nitrided SAE XEV-F valve steel (25x mag.).



Tribofilm formation cannot be readily observed within the contour of the wear scar. Instead, three regions can be distinguished: one central (brighter) region named *b*, and two lateral (less bright) regions named *a*. Apparently, wear mechanisms in both regions (*a*) are similar, and different from mechanisms in region *b*. In this case, BSE images alone do not allow to visualize the developed tribofilm, contrary to the (untreated) steel surfaces (Figure 5.54, Figure 5.60 and Figure 5.66). Figure 5.71

shows a SEM/SE image of the wear scar on the nitrided SAE XEV-F steel. Regions *a* and *b* are readily distinguishable. Some (rare) dark spots can be observed (indicated by black arrows). A detail of the wear features occurring in the highlighted region of Figure 5.71 can be appreciated in Figure 5.72.

Figure 5.71. SEM/SE image of the wear scar on the nitrided SAE XEV-F valve steel (25x mag.).

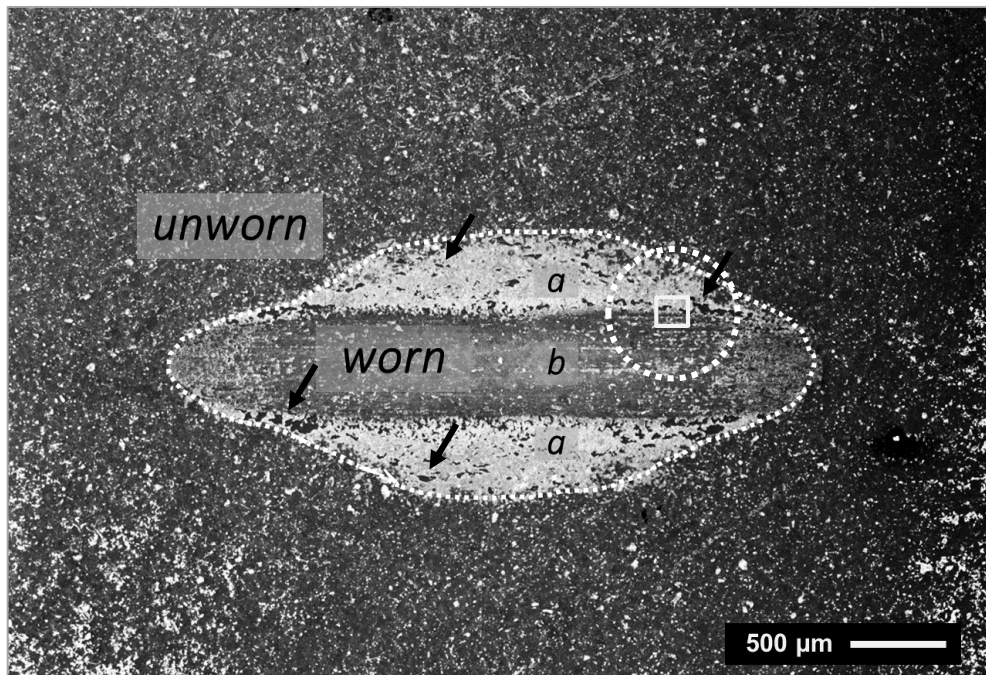
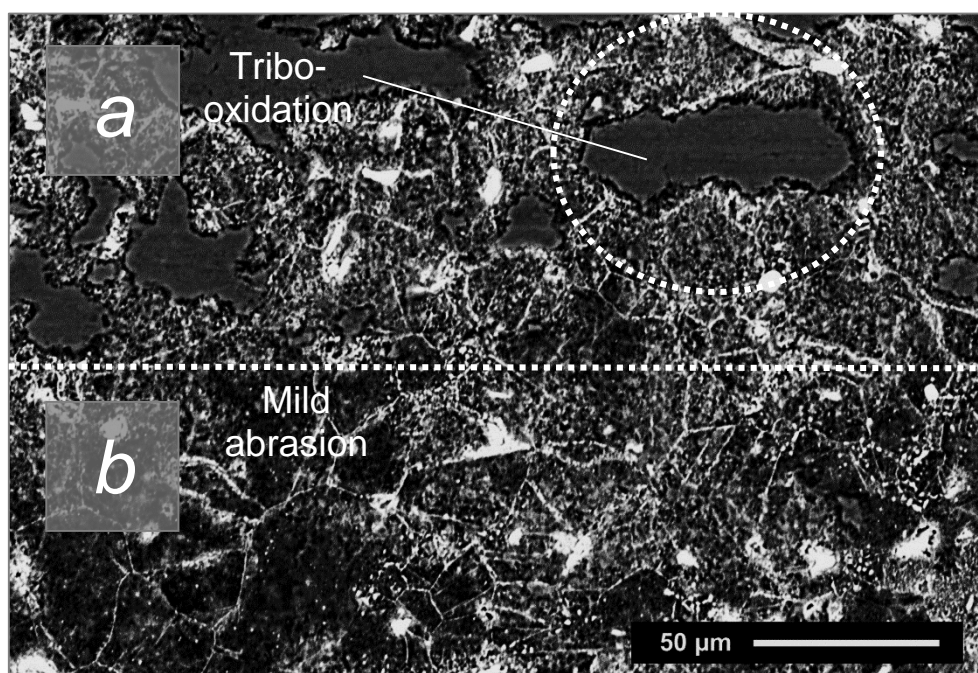
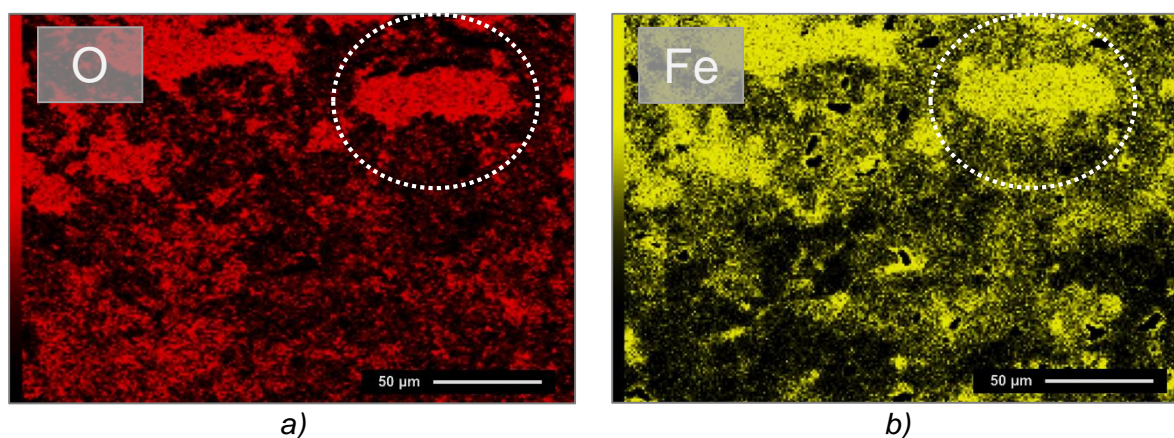


Figure 5.72. Detail of wear mechanisms in the wear scars on the nitrided SAE XEV-F disc. (SEM/SE - 500x mag.).

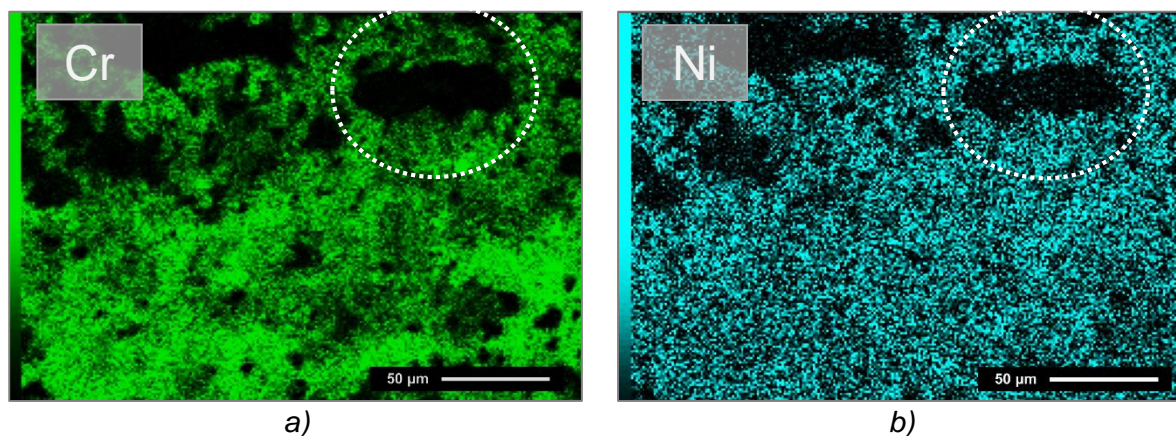


The dark spots in region *a* are compacted *islands* (highlighted in [Figure 5.72](#)), different from the surrounding nitrated surface. A SEM/EDS analysis was conducted on the worn surface of the nitrated SAE XEV-F valve steel. The maps for oxygen and iron, and chromium and nickel, are show in [Figure 5.73](#) and [Figure 5.74](#). These results are similar to those from [Figure 5.56](#) and [Figure 5.57](#), indicating that the islands correspond to iron oxides. The amount of wear debris produced in this tribosystem (~0.4 mg) was not enough to perform XRD analysis.

[Figure 5.73](#). EDS maps of wear mechanisms in the nitrated SAE XEV-F disc: oxygen (a), and iron (b). (500x mag.).



[Figure 5.74](#). EDS maps of wear mechanisms in the nitrated SAE XEV-F disc: chromium (a), and nickel (b). (500x mag.)

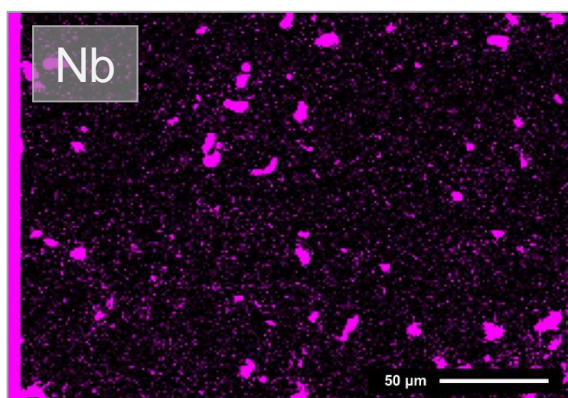


Nevertheless, tribo-oxidative mechanisms, despite present, were not predominant. Oxide islands such as those shown in [Figure 5.72](#) were scarce in the whole area of the wear scar (see dark spots in [Figure 5.71](#)). Instead, most of the areas of both *a* and *b* regions present a worn (non-oxidized) nitrated layer. Mild abrasive

mechanisms occur in these regions and constitute the predominant mechanisms. These mechanisms are expected, as previously indicated in other works on the wear of nitrided austenitic stainless steels (LUO; ZHAO. 2013).

Figure 5.75 shows the niobium EDS map corresponding to Figure 5.72. NbC precipitates are randomly distributed in the worn surface, instead of aligned in the sliding direction as in the untreated SAE XEV-F steel (see Figure 5.63). Their sizes are similar to those in the unworn surface (see Figure 5.5 and Figure 5.7) indicating that there was no fracture of the particles.

Figure 5.75. Niobium EDS maps of wear mechanisms in the nitrided SAE XEV-F disc (500x mag.).



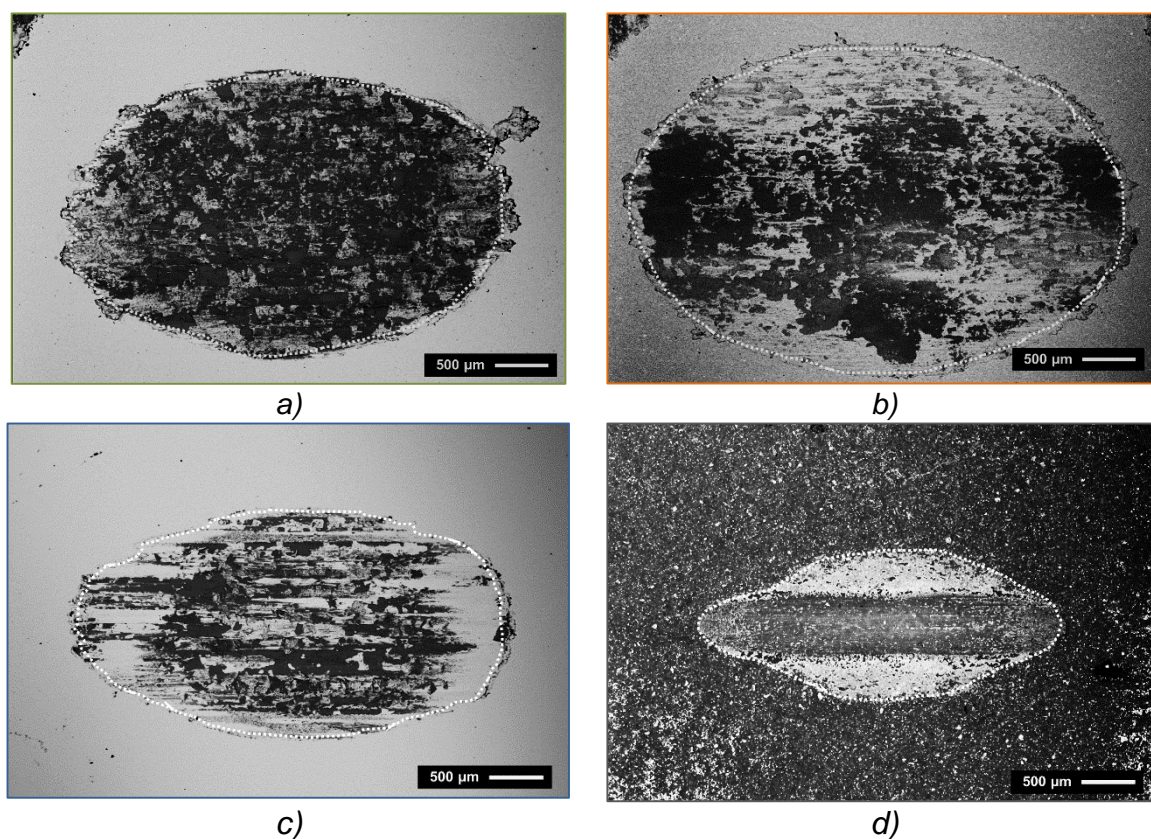
#### *Nominal contact area and tribofilm formation*

If the formed oxides did in fact worked as a protective tribofilm on the worn surface, then the spatial distribution of such film in the (projected) nominal worn area is worth being quantified. An image processing software installed in the SEM allowed the measurement of the nominal area, and the percentage of that area effectively covered by tribofilm was estimated by using the open-source image-processing software *ImageJ* (from the National Institutes of Health, USA). The wear scars in the four discs are comparatively presented in Figure 5.76.

The differences between the projected area and the actual area demand a conservative interpretation of the quantitative values obtained by SEM (i.e. projected area). This issue will be further discussed in the *ball penetration* section. The measured values of the projected nominal contact areas were:  $10.0 \pm 1.0 \text{ mm}^2$  for the AISI 310 steel (Figure 5.76a),  $11.1 \pm 0.5 \text{ mm}^2$  for the SAE XEV-F valve (Figure 5.76b),  $6.6 \pm 0.5$

mm<sup>2</sup> for the AISI H13 steel (Figure 5.76c), and  $4.3 \pm 0.7$  for the nitrided SAE XEV-F valve steel (Figure 5.76d). That is, while the values for the austenitic steels were similar, the values for the hard surfaces were smaller, both for the martensitic steel (by ~34%) and for the nitrided valve steel (by ~57%). Hence, the development of the nominal contact area correlates inversely to hardness. That is, the harder the surface of the disc, the lower the developed nominal contact area.

Figure 5.76. Comparative (projected) nominal area and tribofilm distribution in the steel discs: AISI 310 (a), SAE XEV-F (b), AISI H13 (c), and nitrided SAE XEV-F (d). (SEM - 25x mag.).



In the untreated steels, the percentages of the nominal projected area of the wear scars covered with tribofilm were: ~95% for the AISI 310 steel (Figure 5.76a), ~65% for the SAE XEV-F valve steel (Figure 5.76b), and ~70% for the AISI H13 steel (Figure 5.76c). In this sense, tribofilm formation at the surfaces of the discs is related to hardness but only in an indirect manner, and other tribo-chemical aspects seem to play a fundamental role. The tribofilm was formed in all three discs regardless of hardness or the Cr content and other alloying elements. The AISI 310 stainless steel showed higher amount of tribofilm than the SAE XEV-F (also stainless) valve steel, even if their Cr content (wt.) is similar (25wt% and 21wt.%, respectively). Another example of this

complex relation is the AISI H13 steel (Figure 5.76c), which presented comparable tribofilm formation to that of the SAE XEV-F valve steel, despite their differences in hardness and chromium content. The predominant wear mechanism in the nitrided SAE XEV-F valve steel was mild abrasion.

The results discussed in this section indicate that, in addition to hardness and chemical composition, interfacial conditions such as nominal pressure (and consequently frictional heating) control the predominant wear mechanisms. Wear was found to be predominantly tribo-oxidative in the untreated steel samples (AISI 310, SAE XEV-F and AISI H13). Table 5.8 shows a summary of the oxide species and phases found in the wear scars as determined by the XRD analysis of the wear debris.

Table 5.8. Phase identification in the wear debris

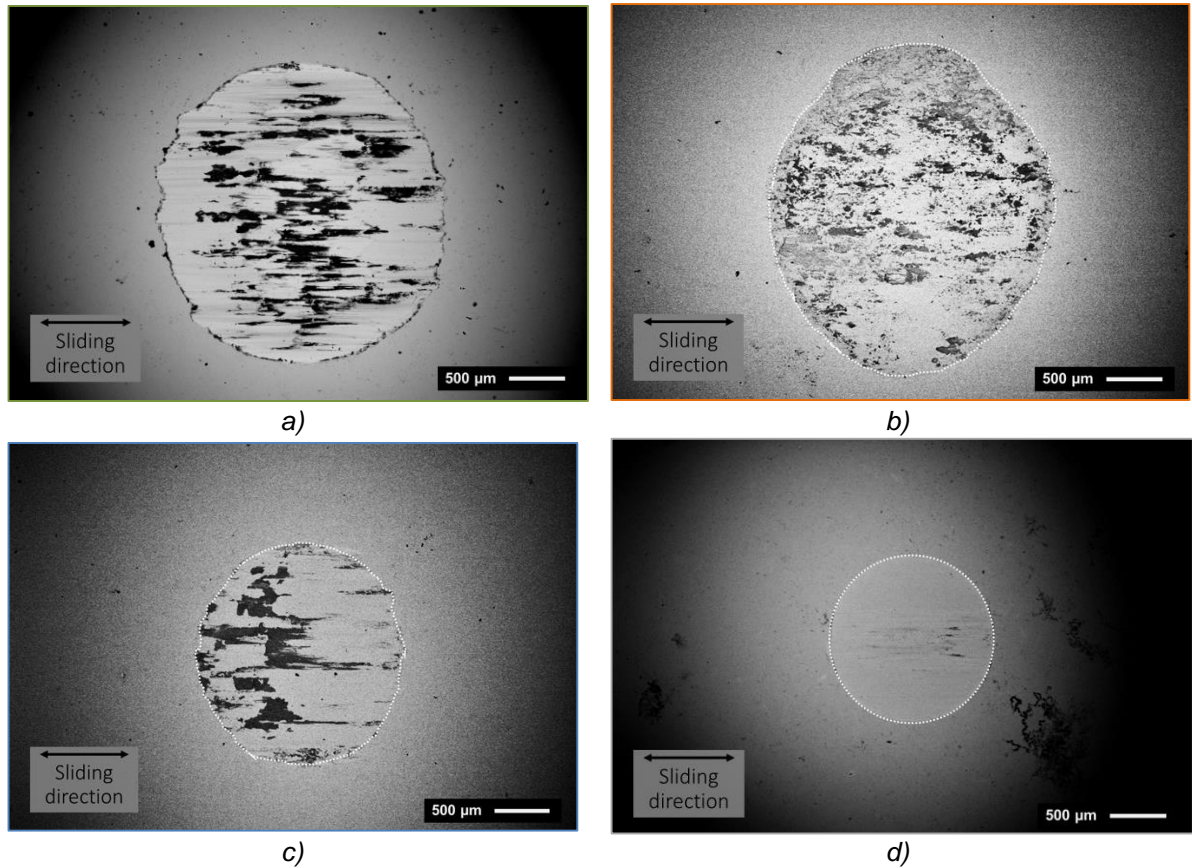
SAMPLE	MAGNETITE	HEMATITE	AUSTENITE	MARTENSITE	NbC
AISI 310	X	X	X	-	-
SAE XEV-F	X	X	X	X	X
AISI H13	X	X	-	X	-

*Wear of the balls - wear mechanisms, nominal contact area and tribofilm transfer*

Figure 5.77 shows SEM/BSE images of the wear scars on the balls. The dark regions inside the wear scars is tribofilm transferred from the surface of the disc as indicated by SEM and EDS analysis, similar to those conducted on the discs. As an example, material transfer to the ball tested against the SAE XEV-F is shown in (Figure 5.78). The EDS map of niobium indicates the presence of NbC in the transferred material.

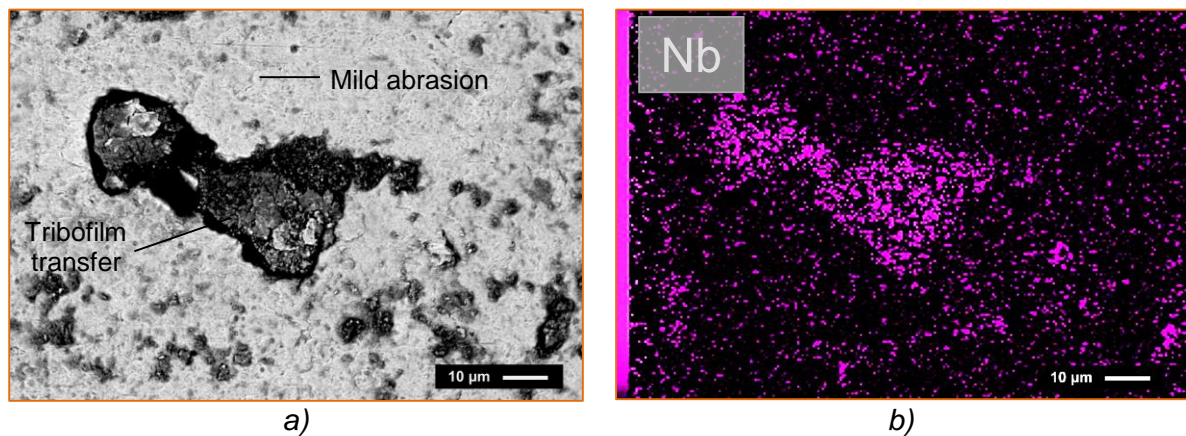
The measured values of the (projected) nominal contact area were similar for the balls tested against the austenitic steels:  $5.3 \pm 0.3 \text{ mm}^2$  for the AISI 310 and  $5.7 \pm 0.2 \text{ mm}^2$  for the SAE XEV-F; and lower for the harder surfaces:  $2.4 \pm 0.4 \text{ mm}^2$  for the AISI H13 steel and  $1.9 \pm 0.2 \text{ mm}^2$  for the nitrided SAE XEV-F valve steel. Hence, the hard surfaces on the discs displayed more load-carrying capacity than the softer steels, limiting the penetration of the ball and the growth of the nominal contact area.

Figure 5.77. SEM/BSE images of wear scars on the AISI 52100 steel balls tested against: a) AISI 310, b) SAE XEV-F, c) AISI H13, and d) Nitrided SAE XEV-F.



Mainly adhesion (tribofilm transfer) and mild abrasion were identified as the predominant wear mechanisms. There was no evidence of gross metallic particles transferred to the balls, only transfer of the developed tribofilm. The tribofilm is composed of a mixture of metals and oxides.

Figure 5.78. SEM analysis of material transfer from the SAE XEV-F steel to the AISI 52100 ball. SEM/BSE image (a), and niobium EDS map (b).

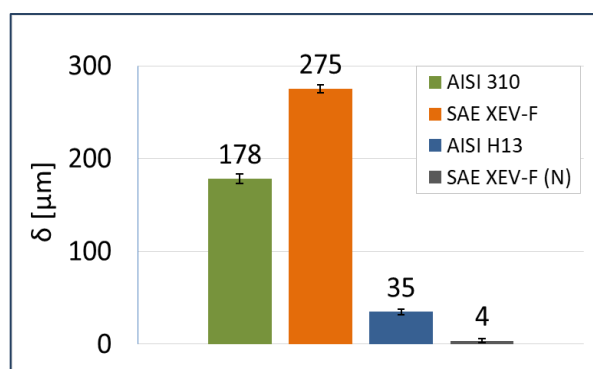


Transfer was small in all cases with respect to the nominal projected area: ~20% in the case of the balls tested against austenitic steels (Figure 5.77a and Figure 5.77b), and ~5% in the balls tested against the martensitic steel (Figure 5.77c). In the case of the ball tested against the nitrided valve steel tribofilm transfer was negligible. Tribofilm transfer is an important feature to be studied since it has been mentioned that, whenever there is deposit of wear debris at the tip of the balls, measures of mass loss are not reliable (ASTM G 133-05. 2005). Nevertheless, it must be remembered that the mass loss of the balls (Figure 5.29b) was low when compared to that of the discs (Figure 5.29a), and in no case a mass gain (i.e. a negative mass loss) was observed in the balls.

### *Ball penetration*

It has been mentioned that the value of the nominal contact area as visualized in the SEM images of the wear marks differs from that of the actual area<sup>10</sup> of the wear scar. This fact can be better understood by observing *ball penetration*. For this purpose, the maximum depth of the wear scars in the discs was measured with respect to the unworn surface via CCI and is presented in Figure 5.79.

Figure 5.79. Maximum depth of the wear scars of the discs.



The difference of about one order of magnitude between the depths observed in the soft austenitic steels and the hard martensitic and nitrided steels indicates that the wear process in the soft steels involves the penetration of the ball into the sample surface, contrary to what is observed in the harder surfaces. Between the two

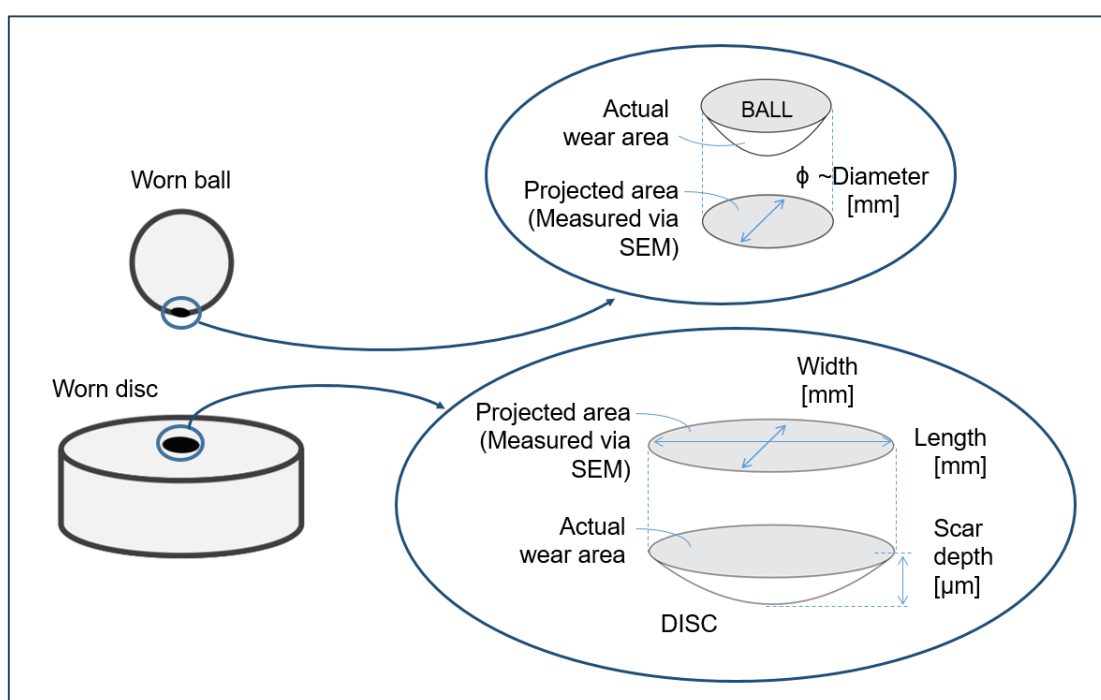
<sup>10</sup> The actual nominal area of the wear scar must not be confused with the *real* area of contact arising from asperity contacts.

austenitic steels, the SAE XEV-F valve steel presented the greater penetration depth. Accentuated wear in the SAE XEV-F valve steel is due to the presence of the hard precipitates.

Ball penetration appears to be a major factor affecting wear (and friction) in BoD tests. Apart from SAE XEV-F valve steel, penetration depends (primarily) on hardness through an inverse correlation: the higher the hardness the lower the ball penetration. Therefore, ball penetration is inversely related to wear volume and nominal contact area. Figure 5.80 shows a schematic representation of the actual and projected worn areas of the discs and the balls.

The wear of the balls (Figure 5.29b) and ball penetration (controlled by hardness of the disc) follow a similar tendency. In the homogeneous materials (AISI 310, AISI H13, and nitrided SAE XEV-F) penetration decreased with increasing the disc hardness. The penetration in the SAE XEV-F tribosystem on the other hand, was pronounced. This is due to effects involving the hard heterogeneities of the SAE XEV-F valve steel, such as subsurface NbC fracture and abrasive debris formation that lead to increased wear of the disc. The evidence of such effects is presented in the following sections. Negligible wear occurs in the corresponding ball. The nitrided SAE XEV-F system presented the lowest degree of penetration, and the mass losses of the ball and disc were equivalent

Figure 5.80. Schematic representation of the wear scar on the disc and the ball.



### 3D analysis of the wear scars

Given that the initial nominal point contact changes during the tests, 3D images of the wear scars were obtained via CCI in order to investigate the conformity of contact at the end of the test (73.2 m) in each tribosystem. Figure 5.81 and Figure 5.82 show the 3D analysis of the wear marks obtained in the AISI 310/AISI52100 tribosystem. The observed depth in the wear scar on the AISI 310 (Figure 5.81) illustrates how the nominal projected area (see Figure 5.53) is an underestimation of the actual developed area. Wedge formation can be identified at the longitudinal ends of the wear scar, that is, at the point of movement reversal (also observable in Figure 5.53). Wedge formation can be an indication of the massive plastic deformation occurring in this steel due to wear. Figure 5.82 shows a profile obtained at the point of maximum depth (line *a-a* in Figure 5.81) showing a smooth curvature of the wear scar that can be comparable to a ball. This provides evidence of ball penetration and shows that only shallow wear (very superficial) occurred in the ball. It can be observed that wedge formation is a source of uncertainty in the depth measurement since the observed value ( $\sim 200 \mu\text{m}$ ) differs slightly of that reported using the unworn surface as reference (Figure 5.79):  $\sim 178 \mu\text{m}$ .

Figure 5.81. 3D analysis of the wear scar on the AISI 310 steel at a 73.2 sliding distance: a) view of the wear scar (FoV =  $5500 \times 3500 \mu\text{m}$ ), and b) profile *a-a*.

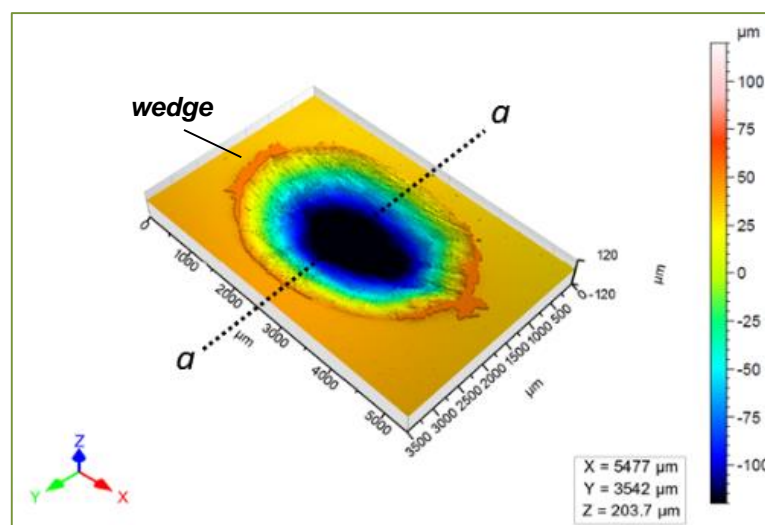


Figure 5.82. 3D analysis of the wear scar on the AISI 310 steel at a 73.2 sliding distance: a) view of the wear scar (FoV = 5500x3500  $\mu\text{m}$ ), and b) profile a-a.

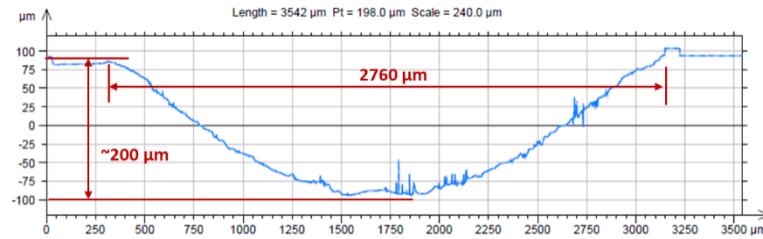


Figure 5.83b shows the profile of the ball, corresponding to line *b-b* in Figure 5.83a. It can be appreciated that the curvature of the worn profile matches the curvature of the wear scar on the disc. This is evidence that a conformal type of contact was developed between the disc and the ball due to wear from the initial non-conformal point contact.

Similar results were obtained for the SAE-XEV-F/AISI52100 tribosystem. A pronounced penetration of the ball onto the surface of the disc was observed and smooth and matching curvatures of the profiles of both the disc and the balls showed conformity of contact at the end of the test.

Figure 5.83. 3D analysis of the wear scar on the AISI 52100 steel ball tested AISI 310 steel at a 73.2 sliding distance: a) view of the wear scar (FoV = 3000x3000  $\mu\text{m}$ ), and b) profile *b-b*.

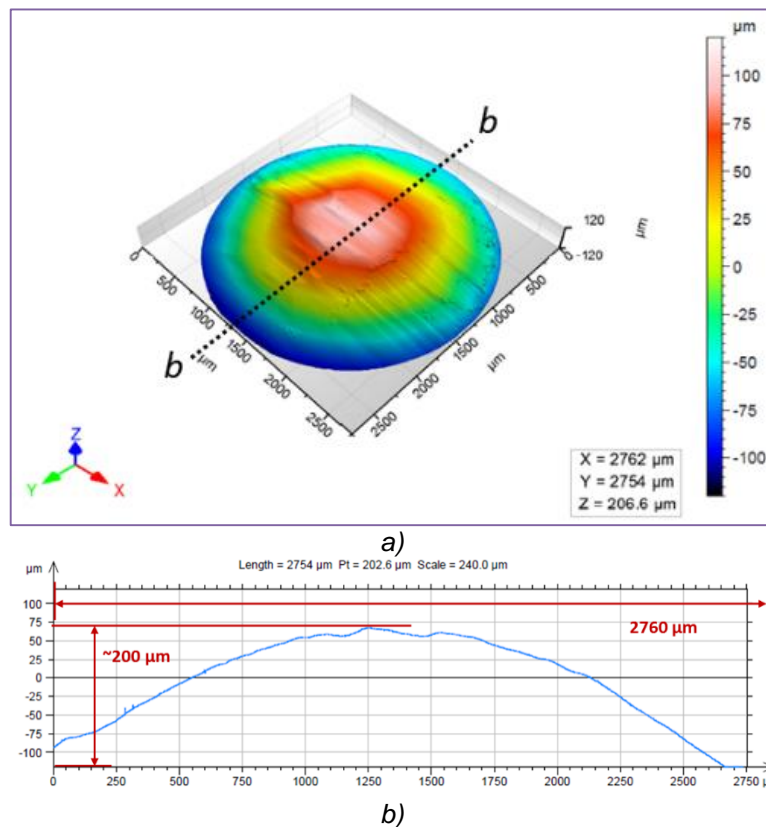
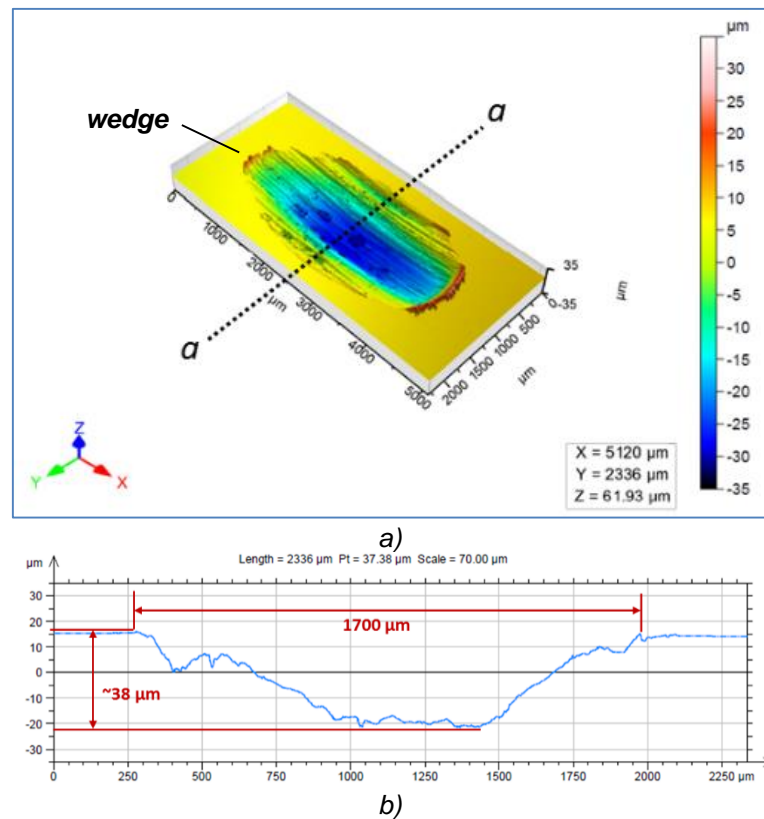


Figure 5.84 shows the 3D analysis of the wear marks obtained in the AISI H13/AISI 52100 tribosystem. In this case, the wear of the AISI H13 disc (Figure 5.84a) evidenced a shallow depth of penetration. This implies a lower underestimation of the nominal area from SEM, as compared to AISI 310 and SAE XEV-F steels. Wedge formation can also be identified at the longitudinal ends of the wear scar but the analysis of profile *a-a* (Figure 5.84b) shows that it does not represent an important source of uncertainty of the depth, since the observed value of maximum penetration corresponds to that registered in Figure 5.79.

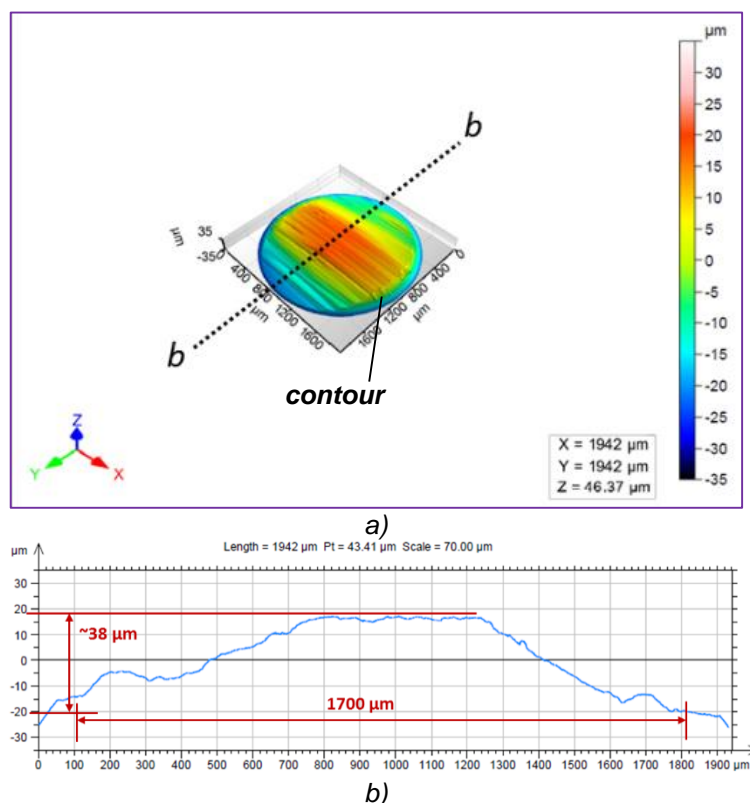
Figure 5.84. 3D analysis of the wear scar on the AISI H13 steel at a 73.2 sliding distance: a) view of the wear scar (FoV = 5000x2500  $\mu\text{m}$ ), and b) profile *a-a*.



The curvature of profile *a-a* was not smooth (Figure 5.84b). Instead, a stepped profile was observed, which does not present a unique defined curvature. This indicates that in addition to a shallow penetration of the ball into the AISI H13 disc, pronounced wear of the contacting tip of the ball occurred. This is supported by the observation of a well-defined contour on the 3D image of the wear scar of the ball (Figure 5.85a) and the characteristics of profile *b-b* (Figure 5.85b). Additionally, profile

*b-b* on the ball matches the configuration of profile *a-a* on the disc, which is evidence of the development of conformal type of contact due to wear.

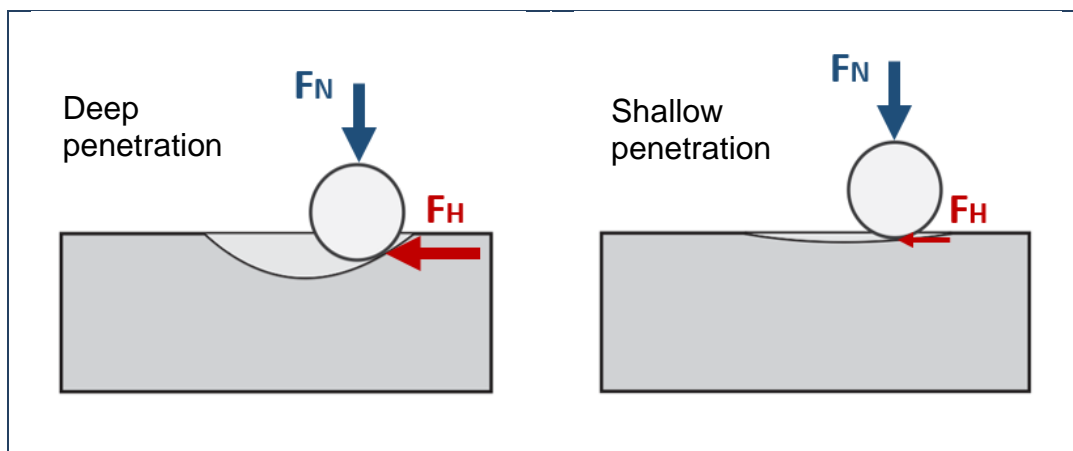
Figure 5.85. 3D analysis of the wear scar on the AISI 52100 steel ball tested AISI H13 steel at a 73.2 sliding distance: a) view of the wear scar (FoV = 3000x3000  $\mu\text{m}$ ), and b) profile *b-b*.



Similar results were obtained for the nitrided SAE-XEV-F/AISI52100 tribosystem: a shallow penetration of the ball onto the surface of the disc; pronounced wear of the tip of the ball (stepped profile); and matching profiles of both the disc and the balls showing conformity of contact at the end of the test. It should be noted that none of the balls presented a perfect flat worn surface. This fact can induce errors in wear and nominal contact pressure estimations when flat worn surfaces are assumed. This is especially critical in the case of the soft discs where there is significant ball penetration (Figure 5.79).

Ball penetration can have a significant influence on the measured values of the friction coefficient (see Figure 5.24). This fact can lead to unreal (overestimated) values of the friction coefficient by virtue of the (macroscopic) interaction between the ball and the (pronounced) wear scar on the disc. Figure 5.86 shows a schematic representation of the horizontal force measurement of the SRV, indicating how ball penetration leads to the horizontal force overestimation during measurement.

Figure 5.86. Schematic representation of the horizontal force measurement of the SRV apparatus as a function of ball penetration.

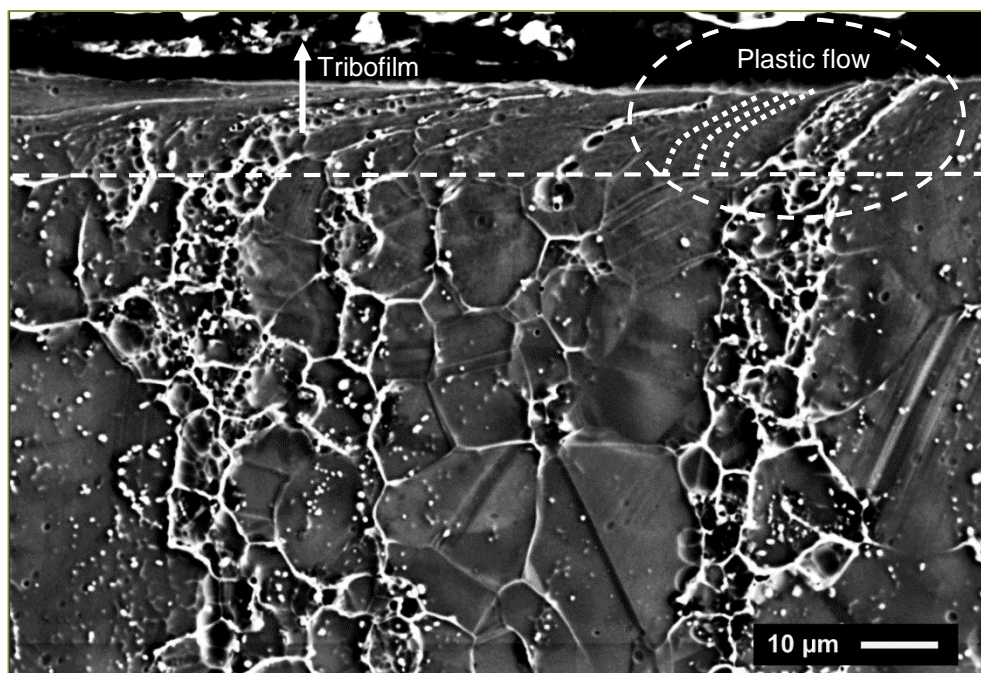


The differences in frictional behavior of the four tribosystems (Figure 5.24) are related to hardness in different manners, depending on scale. As mentioned, hardness controls ball penetration, which affects the measurement of the horizontal component of the force. In this sense, the high friction coefficient observed in the AISI 310 system would suggest a sudden ball penetration, in contrast to the SAE XEV-F steel. This fact can explain the unusual high values in the austenitic steels. In this sense, the friction coefficient values obtained in BoD tests with significant ball penetration should only be compared qualitatively (not quantitatively), since it includes effects other than the microscopic interfacial phenomena. Microscopically, differences in hardness between the existing phases can cause marked differences in tribological behavior (e.g. the SAE XEV-F steel). The effects of hardness differences on a microscopic scale on the behavior of the selected tribosystems will be commented in the following sections.

#### *Subsurface deformation and strain hardening of the discs*

Subsurface deformation was analyzed using SEM examination of cross sections of the discs to investigate variations in the hardness of the surface of the steel discs. Figure 5.87 shows a SEM/SE image of the deformed layer of the AISI 310 steel obtained from a cross section of the wear scar.

Figure 5.87. Subsurface deformation of the AISI 310 steel. (SEM/SE images - cross sections of the wear scars - 1000x).



As can be observed, there is evidence of permanent deformation as indicated by plastic flow patterns on the subsurface. Plastic deformation occurred in the subsurface region down to  $\sim 10 \pm 5 \mu\text{m}$  (as indicated by the dotted line). Despite the fairly constant depth of plastic deformation, there is no reason to think that it evolved linearly during the tests. Severe non-linearities in nominal contact pressure (and consequently shear stress) occur during the running-in process. Therefore, both the nominal contact area and the hardened layer (extension and strain hardening level) are expected to develop differently during running-in and the considered steady state. Nevertheless, evidence of plastic deformation in the AISI 310 steel suggests subsurface strain hardening and a variation of the hardness ratio ( $HR = H_{\text{DISC}}/H_{\text{BALL}}$ ) of this tribosystem. It is interesting to note that, despite the test being conducted under reciprocating movement, plastic flow patterns are oriented only in one direction (from left to right).

Figure 5.88 shows a SEM/SE image of the deformed layer of the SAE XEV-F steel obtained from a cross section of the wear scar. Evidence of permanent deformation is indicated by plastic flow patterns on the surface. Plastic deformation occurred in the subsurface region down to  $\sim 10 \pm 5 \mu\text{m}$  (as indicated by the dotted line). As in the case of the AISI 310 steel, a fairly constant depth of plastic deformation is observed. Fracture of the NbC carbides in the deformed layer can be readily appreciated and are shown in detail in Figure 5.89.

Figure 5.88. Subsurface deformation of the SAE XEV-F steel. (SEM/BSE images - cross sections of the wear scars - 1000x).

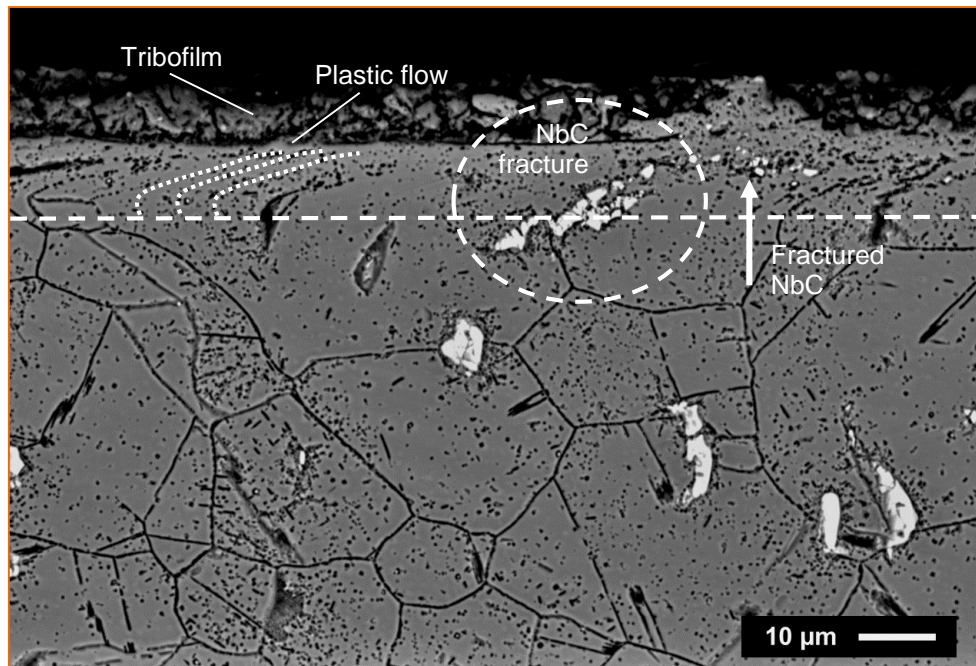
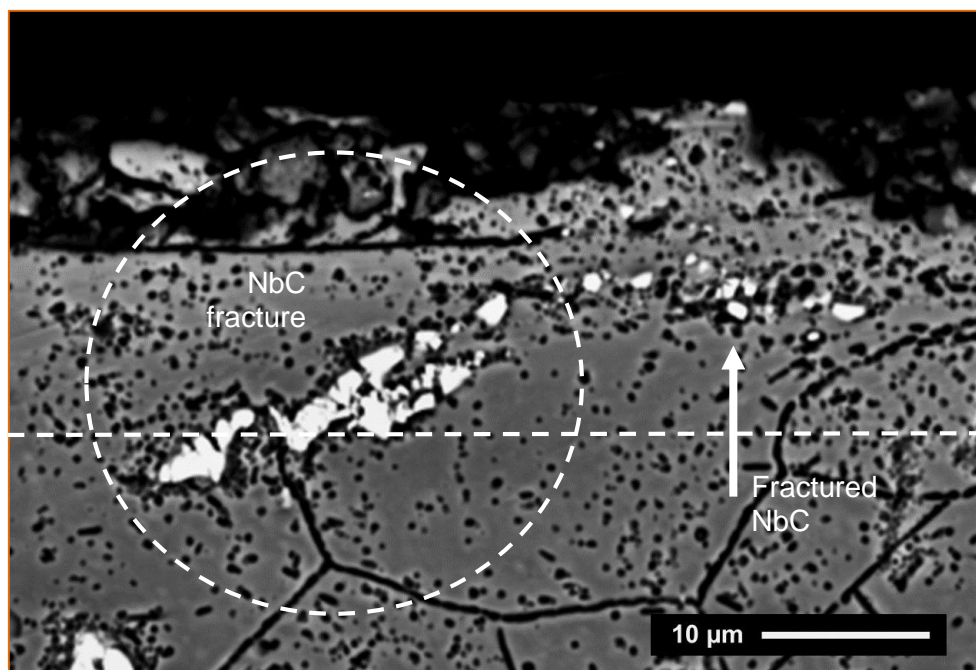


Figure 5.89. Detail of NbC fracture occurring in the subsurface region of the untreated SAE XEV-F valve steel. (SEM/BSE - 2000x mag.).



Due to the great differences between its hardness ( $\sim 315$  HV<sub>5mN</sub>) and that of the NbC ( $\sim 1470$ <sup>11</sup> HV<sub>5mN</sub>), shear stresses in the subsurface region probably caused the NbC failure. This occurred through plastic deformations in the regions surrounding the NbC, which also result in stress concentration and ductile failure of the steel matrix. Together with the formation of hard abrasive debris. Together with the formation of hard abrasive debris (Figure 5.61), subsurface fracture of the NbC contributes (partially) to the pronounced wear in the SAE XEV-F steel.

Figure 5.90 shows a SEM/SE image of the deformed layer of the AISI H13 steel obtained from a cross section of the wear scar. Plastic flow in the subsurface region was limited to  $\sim 1 \pm 2$   $\mu\text{m}$  (as indicated by the dotted line). Given the shallow depth of the deformed layer (plastic deformation occurs only at the outer surface) strain hardening is not expected to affect considerably the hardness ratio of this tribosystem.

Figure 5.90. Subsurface deformation of the AISI H13 steel. (SEM/SE images - cross sections of the wear scars - 1000x).

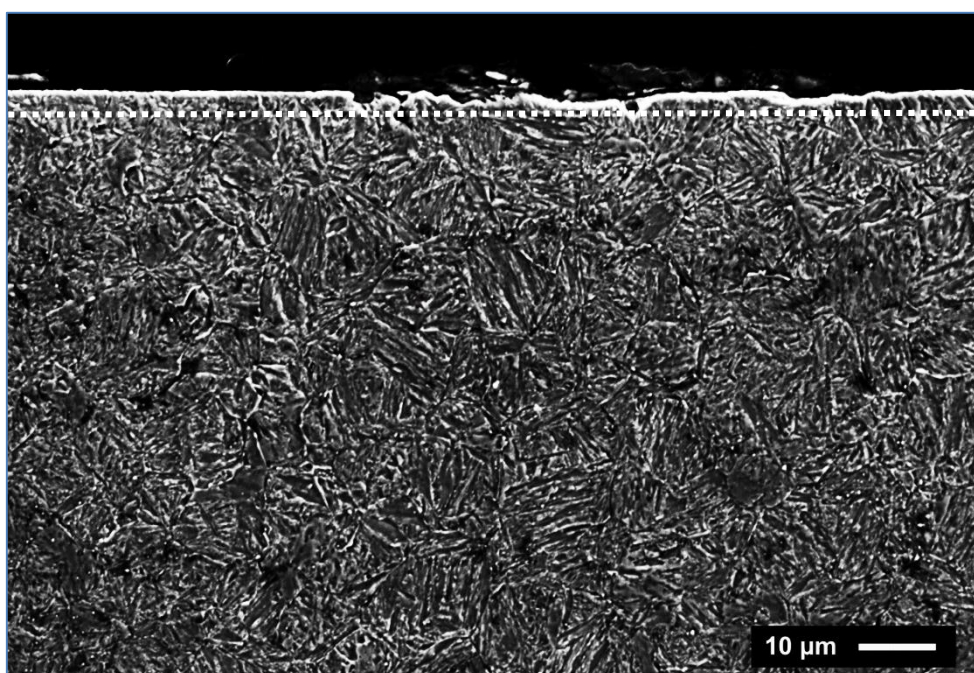


Figure 5.91 shows the subsurface region in the nitrided SAE XEV-F valve steel. Subsurface plastic deformation was not observable. As in the case of the AISI H13,

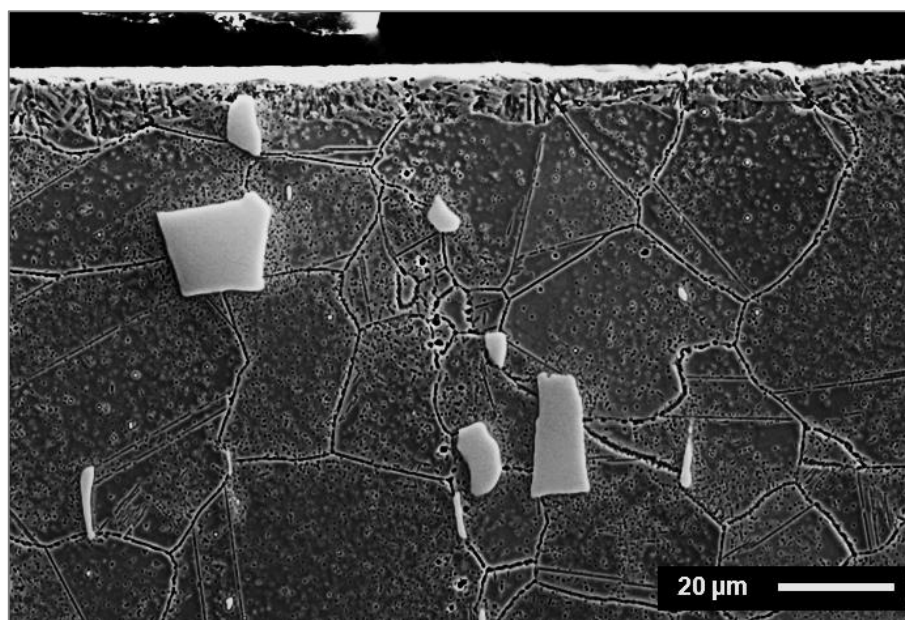
---

<sup>11</sup> Corrected based on a 36% overestimation of the 2000 HV nanohardness value of NbC reported in Figure 5.14.

strain hardening of the nitrided valve steel is not expected to affect the HR of the tribosystem.

Plastic deformation occurs only at outer surface, exclusively on the most superficial region of the compound layer (depth < 1  $\mu\text{m}$ ). The nitrided layer was never worn through (to the diffusion layer), even at the end of the test (after 73.2 m), as shown by the shallow depth ( $4\pm 0.5$   $\mu\text{m}$ ) (Figure 5.79), and the worn surfaces of the nitrided valve steel (Figure 5.71 and Figure 5.72). Mild abrasive wear mechanisms were predominant. Occasional subsurface fracture extending through the diffusion layer (and some NbC) was observed in some regions of the wear scar after 73.2 m (Figure 5.92). However, *delamination* (SUH, 1973, 1977; SUH et. al., 1974) was not a predominant wear mechanism of the nitrided SAE XEV-F valve steel under the specified values of the operational parameters (e.g. sliding distance, contact pressure, mean sliding speed). Additionally, no significant (nor predominant) subsurface fracture and detachment of NbC was observed at any of the stages of wear of the nitrided SAE XEV-F steel.

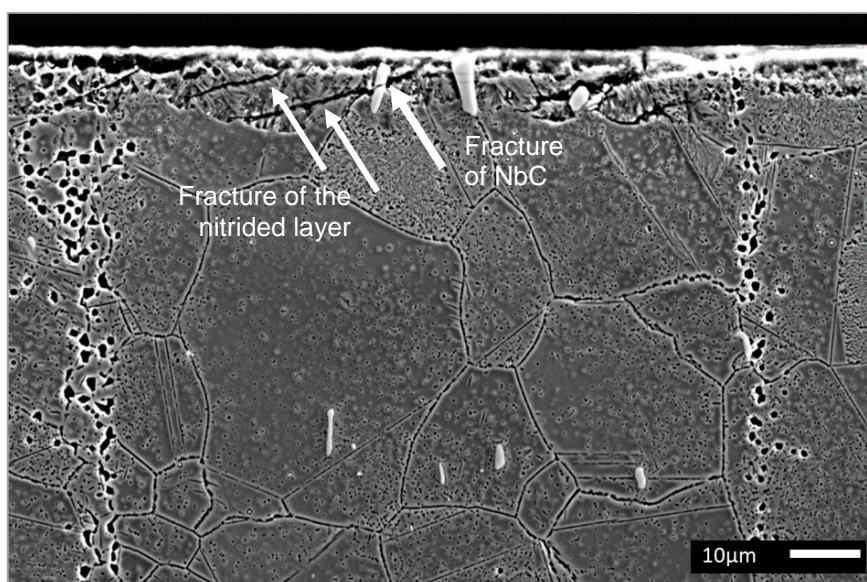
Figure 5.91. Subsurface deformation of the nitrided SAE XEV-F steel. (SEM/SE images - cross section of the wear scar - 1000x).



The wear rate was constant after the first 0.4 m (see Figure 5.28), indicating that non-linear wear rates must occur before this sliding distance. Therefore, non-linear wear rate in this system are associated exclusively with the growth of the nominal

contact area due to wear. The wear scar rapidly reached a stable size before 0.4 m. The wear mechanisms were not in accordance to other works in nitrided surfaces (see [KATO et. al., 1994](#)), in which predominantly oxidative mechanisms are responsible for mild wear. In this work, mild wear of the nitrided samples occurred through mild abrasive mechanisms. The threshold of nominal contact area for transition to steady-state behavior is readily reached ( $s < 0.5$  m) due to the high load carrying capacity of the nitrided layer; provided by the combined action of the high hardness of compound layer, and the supporting diffusion layer.

**Figure 5.92.** Cross sections of a nitrided SAE XEV-F surface after 93.2 m, showing (occasional) subsurface fracture.



The observed behavior of NbC in the worn surface of nitrided SAE XEV-F steel is evidence that the benefits from applying the nitriding process to this steel are two-fold: on one hand, the traditional increase in surface hardness, on the other, the prevention of fracture and detachment of NbC from the matrix. The latter further increases the load-carrying capacity of the surface due to the (hard) NbC in the nitrided metal that functions as a hard matrix at the surface.

### *Strain hardening*

Nanoindentation profiles allowed the quantification of strain hardening. The comparative hardness profiles of all steels at 73.2 m are shown in [Figure 5.93](#). Each

point corresponds to an average of 4 measurements. The (average) hardness ( $HV_{5mN}$ ) of the AISI 310 steel surface increased from  $321 \pm 15$  in the bulk region to  $407 \pm 18$  in the surface, causing a 27.2% strain hardening. The hardness of the SAE XEV-F steel increased from  $433 \pm 12$  in the bulk region to  $479 \pm 20$  in the subsurface, causing a 10.1% strain hardening. Strain hardening in the AISI H13 steel could not be measured via nanoindentation due to the shallow depth of the deformed layer. Hence, strain hardening of this steel was assumed negligible and no change in HR was considered. The same conclusions are drawn for the strain hardening of the subsurface region in the nitrided SAE XEV-F steel.

Figure 5.93. Comparative subsurface hardness profile at a 73.2 m sliding distance (cross-section). strain hardening (nanoindentation 5 mN).

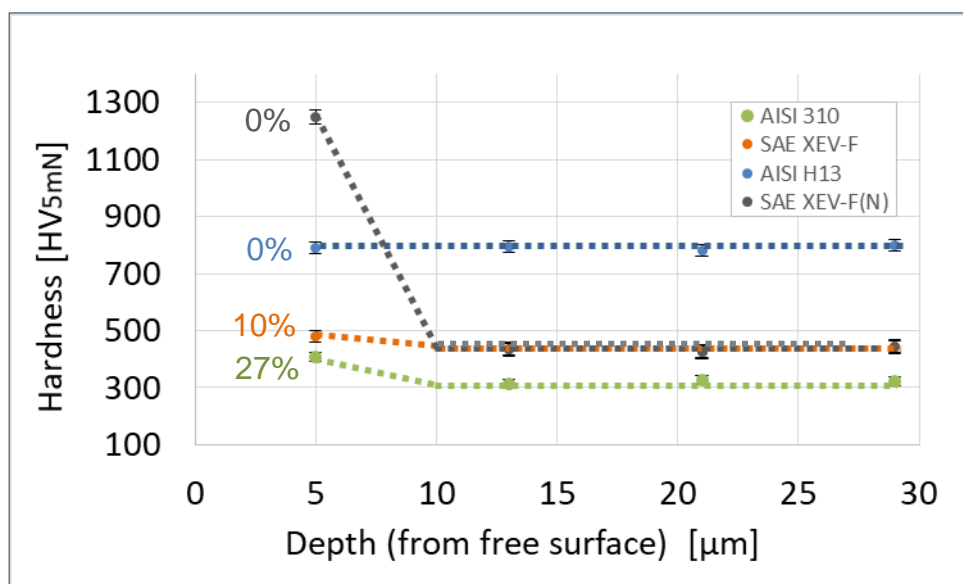


Table 5.9 shows the variation (%) in the hardness ratio (HR) of the tribosystems (measured via nanoindentation). The hardness of the ball was considered to be 995  $HV_{5mN}$  (see Figure 5.14). The hardness of the discs was that obtained as the arithmetic mean of the three bulk values for each material in Figure 5.93. The increase in HR for the austenitic materials after 73.2 m slid implicates an increase in the load-carrying capacity of the surfaces.

The discussion conducted in this section shows that, under the specified operating conditions tested in this research, subsurface deformation occurred most notably in the soft austenitic steels, and was negligible for the harder surfaces. These results indicate that the extension and severity (strain hardening) of subsurface

deformation due to wear is inversely correlated to the bulk hardness of the steel as related to microstructure.

Table 5.9. Change in HR (H<sub>DISC</sub>/H<sub>BALL</sub>) after 73.2 m slid.

STEEL	H <sub>DISC</sub>	HR <sub>0m</sub>	HR <sub>73.2m</sub>	Change [%]
AISI 310	321	0.32	0.41	28.1
SAE XEV-F	433	0.44	0.48	9.1
AISI H13	791	0.80	0.80	0
Nitrided SAE XEV-F	1250	1.26	1.26	0

The hardness differences between the existing phases in the SAE XEV-F steel caused marked differences in its tribological behavior. Stress concentration around precipitates favored fracture, which increased wear (together with the formation of hard abrasive debris). This kind of subsurface phenomena explains the high friction fluctuation observed. Hence, the role of the NbC particles during wear are two-fold: *a*) to facilitate material removal by increasing plastic deformation around precipitates by means of a *stress concentration effect*, which impedes the stabilization of the deformed layer; and *b*) to fracture and incorporate the wear debris, causing additional wear by abrasion, and increasing (gradually) the penetration of the ball. This explains the stable increase tendency of the friction coefficient in this system (see Figure 5.24).

Ball penetration (Figure 5.80) and subsurface plastic deformation are limited in the AISI H13 (~1 μm after 73.2 m sliding distance. See Figure 5.90) and is even less in the nitrided SAE XEV-F valve steel (Figure 5.91). Hence, one infers that plastic deformation occurs only at the outer surface. Therefore, friction measurement in these systems involves only the interfacial phenomenon of interest, since there is no significant effect of ball penetration. Additionally, due to the chemical alterations of the surface of the nitrided SAE XEV-F valve steel discs, they present a different mechanical structure (a hard compound layer supported by a hard nitrogen-supersaturated austenite) and a different degree of metallurgical compatibility than the other steel-on-steel systems. Thus, the adhesion component in the SAE XEV-F valve steel system should be lower. These two facts account for the differences between friction of both AISI H13 and nitrided SAE XEV-F steels (z).

As can be seen from the mass evolution (see Figure 5.27) The AISI 310 varies according to an inverse power function with respect to sliding distance. The

stabilization of the wear rate to a lower value after the running-in period can be explained in the following way: the ball penetration reaches a maximum due both to strain hardening and to the change in nominal contact pressure occurring in the system. Subsurface deformation reduces its plastic behavior creating a state of residual stress; that is, the surface does not undergo any net accumulation of plastic deformation after stabilization. The new (strain hardened) load-carrying capacity together with the nominal contact pressure induce a change to oxidative wear in the AISI 310 steel. SAE XEV-F, AISI H13, and nitrided SAE XEV-F steels present a linear behavior

#### 5.4 FURTHER DISCUSSION

This section presents several aspects related to the observed severe-to-mild wear transition during running-in and its relation to the evolution of the nominal contact pressure in BoD dry sliding tests of steel-on-steel tribosystems. The results of the pressure/distance variation (empirical model) are discussed, along with the definition of threshold values (ranges) for the occurrence of the wear transition in each tribosystem evaluated. Additionally, a discussion is provided on ball penetration and its effects on the friction coefficient measurement; and finally, wear metrics are discussed.

##### *Mechanism of the severe-to-mild wear transition during running-in in BoD dry sliding tests in the selected steel-on-steel tribosystems*

The results presented in the previous sections evidence the occurrence of a severe-to-mild wear transition in three steel-on-steel tribosystems of different hardness values and microstructural characteristics, under specific test parameters (sliding distance, load, oscillating frequency and distance). These transitions occur differently in the soft and hard surfaces due effects such as ball penetration (indentation), growth of the nominal contact area, strain hardening, and frictional heating. The following mechanism synthesizes the overall observations about the severe-to-mild wear transition reported in this work:

1. Initial metal-to-metal contact exists at the interface before relative motion. Nominal point contact causes high contact pressure conditions.
2. Once sliding starts, severe plastic/adhesive wear causes two simultaneous effects: *a)* the growth of the nominal contact area from a “point” (i.e. an infinitesimal area) to a macroscopic area, and *b)* subsurface strain hardening (when significant). Plowing and shearing of the surfaces causes large plastic strains in the subsurface region, such that the friction work is mainly due to plastic deformation (and adhesion), and the produced debris are mainly metallic. Gross metallic transfer should be expected along with gross metallic debris. The increase in area causes a drop in the nominal contact pressure. At specific interfacial conditions the combined effects of contact pressure, frictional heating and heat conduction (material), and subsurface deformation (when significant<sup>12</sup>), cause a transition from severe wear to tribo-oxidative wear.
3. After the severe-to-mild wear transition, the following variables stabilize friction coefficient, magnitude of friction fluctuations, surface roughness, depth of deformed layer, and the composition and microstructure of near-surface material. Additionally, stabilization of the nominal contact area is also expected in ball-on-disc type of tests, as indicated by Ajayi and Erck (2001). Tribo-oxidative mechanisms become predominant during the whole considered steady-state stage. Tribofilm formation and seizure is continuous producing fine wear debris. A small amount of tribofilm transfer should be expected.

Nevertheless, variables change and interact in different manners for each system during the test. In the AISI 310 soft homogeneous steel, ball penetration, contact area growth, and the development of the subsurface region, all occur suddenly during the first stages of running-in. Hardness of the discs controls penetration, which is the main variable controlling the growth of the nominal contact area. The surface layer hardens due to plastic strains up to a threshold. In this sense, strain hardening of the surface can be regarded as a precursor of tribo-oxidation in this steel. The most pronounced growth in the nominal contact area occurred in the first 15 m. The wear rate decreases dramatically during these events while tribo-oxidative mechanisms develop gradually. After the very beginning of running-in, mild wear predominates (low wear rate) and iron

---

<sup>12</sup> Only the AISI 310 and SAE XEV-F steels present significant deformation and strain hardening (26.7% and 16.1% respectively).

oxides at the interface function as a protective tribofilm. The steady-state (~constant) wear rate is reached after 20 m.

Ball penetration in the SAE XEV-F steel does not occur suddenly due to the higher matrix hardness. The SAE XEV-F presents NbC precipitates (microscale), which are much harder than the austenitic matrix and, thus can improve the overall (macroscopic) hardness of the steel. Nevertheless, since these NbC precipitates are very hard, their failure by brittle failure can be expected. Moreover, the influence of subsurface fracture of these particles in the tribological behavior is probably related to stress concentration in the austenitic matrix at the regions near microscopic NbC leading to plastic deformation and the failure the NbC. This fact leads to a local increase of the stress in the subsurface region and facilitates ductile failure in the austenitic matrix. This effect, together with the action of hard abrasive wear debris, explains the pronounced and constant wear rate of this steel at the selected sliding distances. Tribo-oxidation occurred at well-defined threshold values of contact pressure but this did not reduce the wear rate as will be discussed in the final sections. Nevertheless, the occurrence of tribo-oxidation in the SAE XEV-F steel did not guarantee a low wear rate, as can be seen in the pronounced slope of the wear rate (Figure 5.27). The growth in the nominal contact area occurred linearly (as mass loss) after the first 0.5 m. Hence, the most pronounced growth in the nominal contact area must have occurred before that.

Strain hardening was not significant in the AISI H13 steel. Therefore, the severe-to-mild wear transition in this steel was controlled primarily by the growth of the nominal contact area, and the combined effects of frictional heating and heat conduction away from the interface.

No severe-to-mild wear transition was observed in the nitrided SAE XEV-F system. Mild abrasive mechanisms were observed in the nitrided surface of this steel, due to both the structure and chemical composition of the nitrided layer. These results were in not in accordance with other works (KATO, 1994), in which oxidative mechanisms were found predominantly as a consequence of mild wear in nitrided steel surfaces.

### Evolution of nominal contact pressure

The presented evidence showed that sliding wear in BoD tests causes a drastic increase in nominal contact area, which traduces in an equally drastic decrease in nominal contact pressure. This is in accordance with other works on the subject (AJAYI; ERCK, 2001). The experimental results on the area/distance variation are presented in Figure 5.94. This variation was measured from projected areas of the wear scars of the balls in interrupted tests (see Figure 5.77). Each value of the projected area was determined from three SEM image of the corresponding wear scar, in which three measurements were conducted via an image processing software. The nominal contact area is plotted in a logarithmic scale. The corresponding values are listed in Table 5.10.

Figure 5.94. Evolution of nominal contact area.

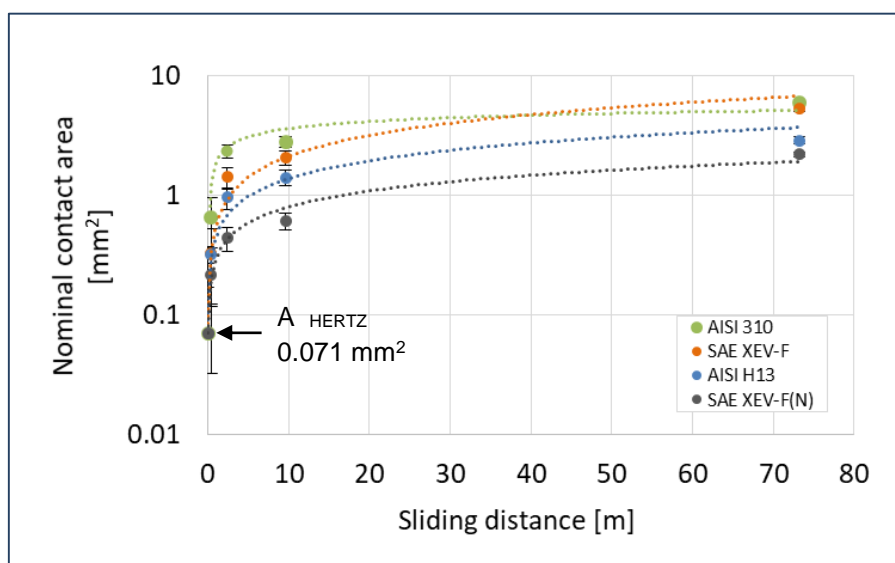


Table 5.10. Evolution of nominal contact area (numeric values).

sliding distance [m]	AISI 310 [mm <sup>2</sup> ]	SAE XEV-F [mm <sup>2</sup> ]	AISI H13 [mm <sup>2</sup> ]	Nitrided SAE XEV-F [mm <sup>2</sup> ]
0 (HERTZ)	0.071	0.071	0.071	0.071
0.4	0.664 ± 0.053	0.333 ± 0.041	0.324 ± 0.021	0.219 ± 0.011
2.4	2.351 ± 0.130	1.431 ± 0.122	0.971 ± 0.112	0.444 ± 0.092
9.6	2.811 ± 0.121	2.083 ± 0.350	1.419 ± 0.303	0.619 ± 0.293
73.2	6.035 ± 0.112	5.391 ± 0.230	2.895 ± 0.324	2.222 ± 0.305

It can be observed from [Figure 5.94](#) that the evolution of nominal contact area is described by an inverse power function. This tendency is most pronounced in the case of the AISI 310, indicating the rapid area growth during the first 0.4 m of sliding. The less pronounced area growth was observed in the nitrided SAE XEV-F steel. Changes in as much as orders of magnitude can be appreciated in all cases, mainly during the 0.0 - 0.4 m and 0.4 - 2.4 m stages of sliding. [Table 5.11](#) presents the percentage area changes in each sliding stage (between distance points in interrupted tests).

[Table 5.11](#). Percentage increase of nominal contact area between distance points.

	Distance Interval	Distance [m]	AISI 310 [%]	SAE XEV-F [%]	AISI H13 [%]	Nitrided SAE XEV-F [%]
$\Delta A$	0-0.4 m	0.4	835	369	356	208
$\Delta A$	0.4-2.4 m	2.0	254	330	200	103
$\Delta A$	2.4-9.6 m	7.2	20	46	46	39
$\Delta A$	9.6-73.2 m	63.6	115	159	104	259

During the first 0.4 m, the AISI 310 steel experienced an 835% increment in area, which is more than double than in the SAE XEV-F steel (369%). Instead, the growth percentage was comparable between the SAE XEV-F steel and the AISI H13 steel (369% and 356%, respectively). The area growth in the nitrided was around half of the percentage increase in the AISI H13 steel, that is, 208%. The changes in area registered between 0.4 and 2.4 m are also significant. The stage between 2.4 and 9.6 m presented a minor increase percentage in all samples. Changes between 9.6 and 73.2 m correspond approximately to the steady-state.

The pressure/distance plot is presented in [Figure 5.95](#). This plot was constructed by dividing the nominal load (100 N) by the projected area of the wear scars of the balls obtained from the interrupted tests. Simplifications were made, such as considering that the same elastic modulus and Poisson's ratio for the selected steels. The nominal contact pressure is plotted in a logarithmic scale. The corresponding values are listed in [Table 5.12](#).

Figure 5.95. Estimated evolution of nominal contact pressure.

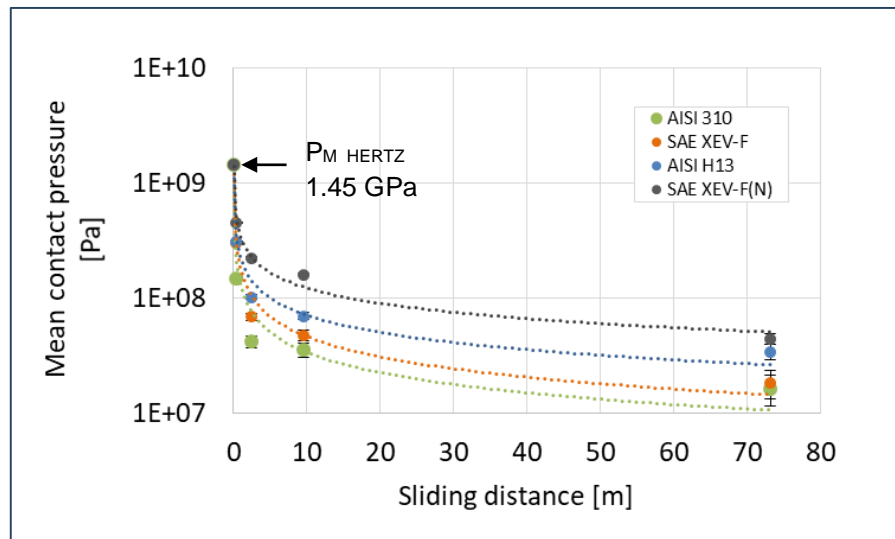


Table 5.12. Estimated evolution of nominal contact pressure.

sliding distance [m]	AISI 310 [MPa]	SAE XEV-F [MPa]	AISI H13 [MPa]	Nitrided SAE XEV-F [MPa]
0 (HERTZ)	1460.00	1460.00	1460.00	1460.00
0.4	150.50 ± 8.15	300.74 ± 30.27	308.92 ± 19.85	456.71 ± 22.78
2.4	42.54 ± 2.35	69.86 ± 5.51	102.99 ± 10.59	225.23 ± 50.18
9.6	35.57 ± 1.32	48.01 ± 7.15	70.47 ± 12.13	161.55 ± 50.11
73.2	16.57 ± 0.33	18.55 ± 0.79	34.54 ± 2.05	45.00 ± 6.91

The pressure/distance variation follows an inverse power relation, as a direct consequence of the area/distance variation (Figure 5.94). The rate of pressure variation of the systems becomes stable soon after 9.6 m, different to the 50 m stabilization observed by Ajayi and Erck (2001), probably due to the differences in the testing parameters. Changes in as much as orders of magnitude in the nominal contact pressure can be appreciated in all cases in Figure 5.95, mainly in the 0-0.4 m and 0.4-2.4m stages. This can be better observed in Table 5.13, which presents the percentage changes in pressure between distance points.

During the first 0.4 m, the AISI 310 steel experienced a 90% decrease in contact pressure, 11% less than in the SAE XEV-F and AISI H13 steels (79%). The contact pressure decrease in the nitrided SAE XEV-F steel was 10% less than in the AISI H13 steel. The changes in pressure registered between 0.4 and 2.4 m are also significant. The stage between 2.4 and 9.6 m presents the minor increase percentage in all samples. Changes between 9.6 and 73.2 m correspond (approximately) to the steady-state.

Table 5.13. Percentage decrease of nominal contact pressure between distance points.

	Distance interval	Distance [m]	AISI 310 [%]	SAE XEV-F [%]	AISI H13 [%]	Nitrided SAE XEV-F [%]
$\Delta P_M$	0-0.4 m	0.4	90	79	79	69
$\Delta P_M$	0.4-2.4 m	2.0	72	77	67	51
$\Delta P_M$	2.4-9.6 m	7.2	16	31	32	28
$\Delta P_M$	9.6-73.2 m	63.6	53	61	51	72

As the wear rates (see Table 5.4), the contact pressure variation (rate) can also be quantified and compared by means of the slope of a linear regression, remembering that this approach assumes linearity after 9.3 m. Table 5.14 shows the linear regression functions

Table 5.14. Regression functions of the nominal (mean) contact pressure between 25 and 73.2 m sliding.

STEEL	Regression
AISI 310	$0.299x + 38.443$
SAE XEV-F	$0.463x + 52.454$
AISI H13	$0.565x + 75.896$
Nitrided SAE XEV-F	$1.833x + 179.140$

#### *Empirical model for the pressure/distance variation in BoD dry sliding tests*

The results presented in the foregoing section showed a quantitative assessment of the variations in nominal contact pressure, as well as a description of the decrease percentage between distance points. The running-in stage (0 - 2.4 m) presented the higher pressure reductions. The reduction was particularly drastic in the AISI 310 steel (90%+72%) due to its lower hardness (which is an indication of its low load-carrying capacity) which allows the rapid penetration of the ball. In contrast, the high load-carrying capacity of the nitrided SAE XEV-F steel requires little contact pressure reduction to reach steady conditions (69%+51%).

The reduction of nominal contact pressure is an important factor in BoD tests in steel-on-steel tribosystems because it affects the interfacial conditions leading to a severe-to-mild wear transition. An inverse power relation was observed to describe the

pressure/distance variation (AJAYI; ERCK, 2001). Equation 1 presents such empirical model, which for discussion purposes is recalled here:

$$P_N = \beta \cdot P_M \cdot d^k$$

Where:  $P_N$ : “Instantaneous” nominal contact pressure [Pa],  
 $\beta$ : and  $k$  are variables determined empirically,  
 $P_M$ : Initial mean Hertzian contact pressure,  
 $D$ : sliding distance.

The empirical constants were found to vary in the following manner:  $\beta$  (0.0386 - 0.099) and  $k$  (0.331 - 0.568) for two steel-on-steel (martensitic-on-martensitic) tribosystems. The results of the non-linear regresions of the pressure/distance variation data of this work is presented in Table 5.15. The initial mean Hertzian contact pressure was 1.45 GPa (1.45e9 Pa).

Table 5.15. Best-fit curves of data from the evolution of nominal contact pressure.

STEEL	$f(x) = (\beta \cdot P_M) \cdot x^k$	$R^2$	$\beta$	$k$
AISI 310	$1E8x^{-0.582}$	0.9181	0.069	0.582
SAE XEV-F	$2E8x^{-0.585}$	0.9752	0.138	0.585
AISI H13	$2E8x^{-0.498}$	0.9671	0.138	0.498
Nitrided SAE XEV-F	$3E8x^{-0.442}$	0.9857	0.207	0.442

The inverse-power relation describing the instantaneous pressure ( $f(x) = \beta \cdot P_M \cdot x^k$ ) presented good values of the correlation coefficient ( $R^2$ ) in all cases, indicating a good strength (goodness of fit) of the relation. The values of  $k$  showed an inverse correlation to hardness. In contrast, the values of  $\beta$  presented a direct correlation to hardness.

Hardness ratio (HR) variation is presumed to influence the evolution of contact pressure (see Table 5.9). No significant (nor measurable) strain hardening occurs in the hard steels (AISI H13, nitrided SAE XEV-F valve steel). Hence, it was considered that there was a zero strain hardening percentage (the hardness ratio variation) during the test. On the other hand, both austenitic steels presented significant strain hardening causing an important variation of the hardness ratio of these systems: 32.3% (AISI 310) and 40.6% (SAE XEV-F). Wear evidence has shown that due to a subsurface fracture of microscale NbC particles and the abrasive action of hard debris, strain hardening of the SAE XEV-F steel did not cause a reduction in the wear rate. In

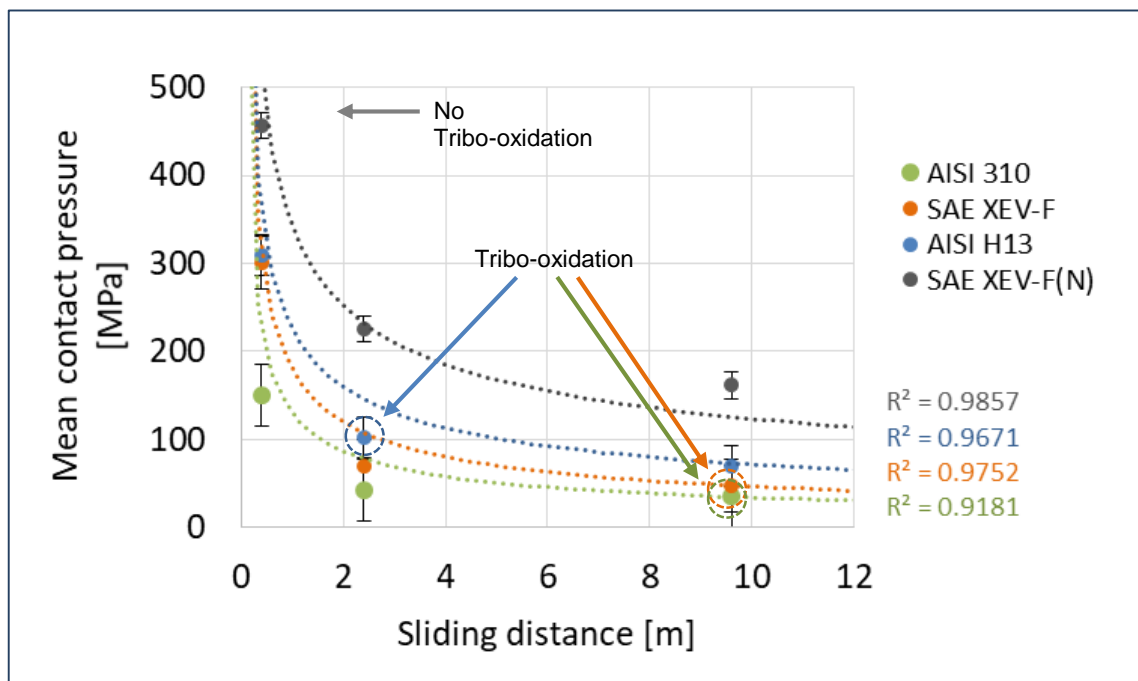
the AISI 310 steel, on the other hand, strain hardening did contribute to the decrease in the wear rate.

*Threshold of nominal contact pressure for the severe-to-mild wear transition*

The steel-on-steel tribosystems all showed evidence of a severe-to-mild wear transition occurring during running-in ( $s < 9.6$  m). Figure 5.96 shows a detailed view of the pressure/distance variation of the four tribosystems during the running-in stage. The mean contact pressure (plotted in a linear scale) was obtained by dividing the nominal load (100 N) by the projected area of the wear scar of the ball at each sliding distance.

From SEM evidence, it was noticed that the sliding distance required for tribo-oxidation was shorter for the (hard) AISI H13 steel (see Figure 5.49a) than for the austenitic steels (Figure 5.37a and Figure 5.46a). Figure 5.96 offers some context on the contact pressures related to the severe-to-mild wear transition in each system.

Figure 5.96. Evolution of nominal contact pressure during running-in



Tribo-oxidation in the AISI H13 steel occurred between 0.4 and 2.4 m, corresponding to pressure values of  $301 \pm 20$  and  $103 \pm 11$  MPa, respectively. In the AISI 310 and SAE XEV-F steels, tribo-oxidation was observed between 2.4 and 9.6 m,

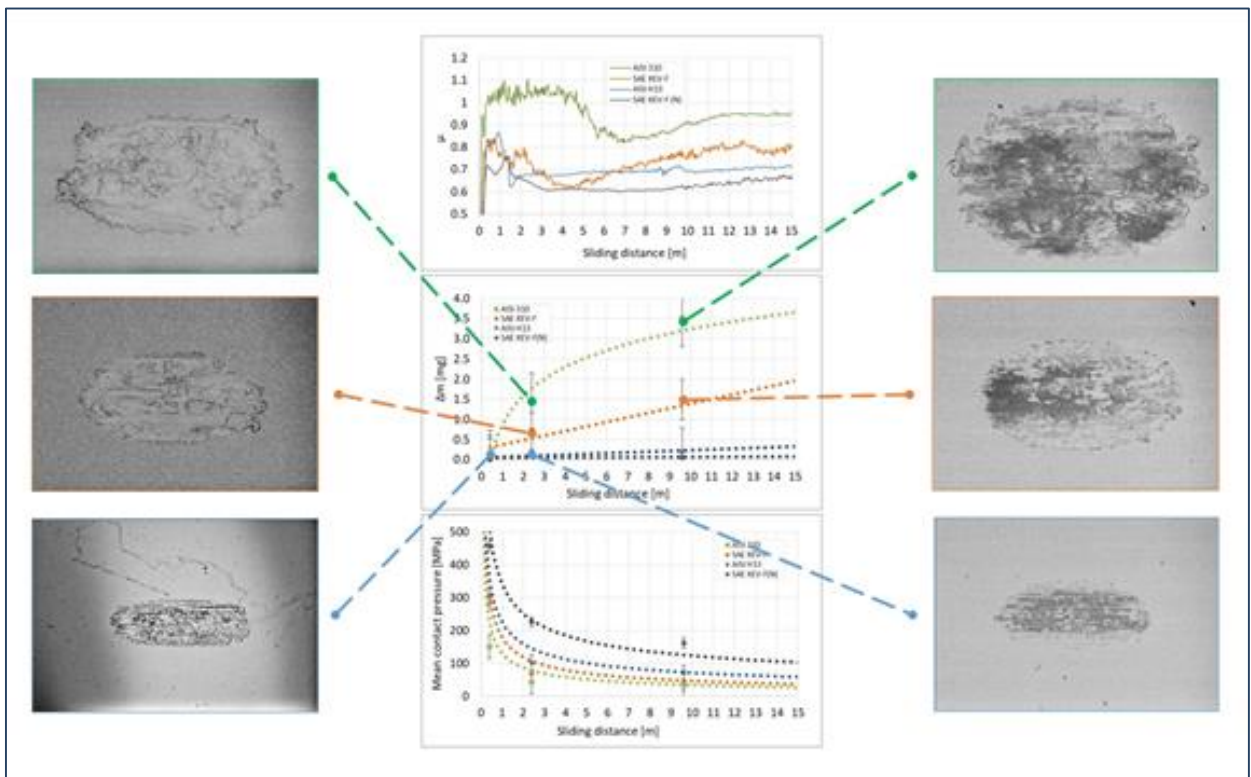
corresponding to pressure values of  $43 \pm 2$  and  $36 \pm 1$  MPa (respectively) for the AISI 310 steel, and to values of  $70 \pm 6$  and  $48 \pm 7$  MPa (respectively) for the SAE XEV-F steel. These results are summarized in Table 5.16. The lower contact pressure values correspond to a non-oxidized interface and the higher values to the oxidized one.

The conjunct analysis of the friction coefficient plot (Figure 5.24), mass evolution plot (Figure 5.27) and the pressure/distance variation during BoD dry sliding tribological tests evidenced clear correlations (see Figure 5.97).

Table 5.16. Nominal contact pressure ranges for tribo-oxidation in the studied tribosystems.

Steel	$P_M$ [MPa]	$\Delta S$ [m]
AISI 310	$36 < x < 43$	2.4 - 9.6
SAE XEV-F	$48 < x < 70$	2.4 - 9.6
AISI H13	$103 < x < 301$	0.4 - 2.4

Figure 5.97. Correlation between friction coefficient, mass loss and mean contact pressure during running-in.



Two stages of tribological behavior can be distinguished in the three plots: a) an initial transitional stage (running-in), characterized by a highly variable friction

coefficient. This fact clearly indicates the need to characterize both stages independently. Neglecting the occurrence of such running-in processes and their implications on the resulting conditions before the steady-state is reached can lead to misinterpretation of the overall wear and friction results of laboratory BoD tests. The SEM evidence of the severe-to-mild transition in wear regime is also presented in [Figure 5.97](#) in a summarized fashion for the AISI 310 austenitic SS, the SAE XEV-F valve steel (austenitic SS) and the AISI H13 tribosystems.

## 6 CONCLUSIONS

### 6.1 SUMMARY

The main conclusions of this thesis are:

- A phenomenological description of the severe-to-mild wear transition occurring during the running-in process in ball-on-disc dry sliding reciprocating tests conducted on some selected steel-on-steel tribosystems (mainly austenitic and martensitic), under specified conditions of load (100 N), frequency (10 Hz), stroke (2 mm) and room temperature. This transition was found to be predominantly due to the increase of nominal contact area (a mechanical-geometric property), which results in a reduction in nominal contact pressure. The pressure/distance variation was markedly influenced by hardness and the penetration of the ball, directly related to hardness.
- Subsurface deformation and tribo-oxidation are phenomena associated with the process leading to a severe-to-mild transition in wear. Nevertheless, their effect is highly related to nominal contact pressure. It was shown that a significant part of subsurface deformation occurs during the first stages of running-in before the severe-to-mild wear transition occur. This suggests that the subsurface features and properties stabilized before the tribo-oxidative mechanisms were fully developed, especially in the austenitic steels.
- While submicrometer-scale precipitates in the SAE XEV-F valve steel result in good high temperature bulk properties (e.g creep resistance), the micro-scale precipitates led to a poor wear and frictional performance. This was due to two reasons: on one hand, the great differences in mechanical properties (e.g. hardness) between the NbC and the austenitic matrix, which led to stress concentration effects around precipitates imposed by the large shear strains resulting from sliding. The stress/strain concentration caused fracture of the NbC, which contributed to further plastic subsurface deformation and material removal. The condition described causes great frictional losses that tend to increase steadily in time. On the other hand, the fractured NbC entered and mixed with the third body additionally contributing to the abrasive component of wear. Nitriding of the SAE XEV-F reduced wear in friction in two ways: the conventional case

hardening of the outer surface of the soft austenitic matrix, and by hindering the strain concentration effect due to plastic deformation, which impedes fracture and detachment of the NbC, due to hardening of the surrounding steel matrix.

## 6.2 CONTRIBUTIONS

The main contributions of this thesis are:

- From a fundamental perspective, this thesis provides a phenomenological description of the severe-to-mild wear transition occurring at room temperature during running-in of ball-on-disc dry sliding reciprocating tests for some selected steel-on-steel tribosystems with different hardness values. A varied behavior was observed which was found to be correlated to microstructural features and mechanical properties of the phases.
- From a technological perspective, the tribological behavior of the SAE XEV-F exhaust valve steel, and the traditional surface treatment for valve wear improvement (nitriding) were studied. The ways in which surface performance benefits of such processes were described based on the observed wear mechanisms. Further studies on Stellite surfaces using the methodology proposed in this work could provide important information useful in the optimization of the valve manufacturing process (see [Figure 2.1](#)). If the tribological performance of Stellite is not significantly different from that of the nitrided valve steels (both in ambient and high temperatures), Stellite deposition in the face of the valve could be avoided, that is, nitriding of the Stellite surface can be a redundant wear protection measure. This decision would reduce production steps and overall costs. However, it should be remembered that the operating conditions of valves in ICEs are different from the laboratory material tests. Some variables like high temperatures or combustion gases are critical for the valve project.

### 6.3 FUTURE WORK SUGGESTIONS

From a *fundamental* point of view

To better understand the nature of the relationship between the nominal contact pressure and severe-to-mild transitions in metallic wear, several studies could be performed. The proposed steps consist in applying the methodology presented in this work for:

- 10 N tests.
- Pin-on-disc configuration in low (~10 MPa) and high (~1000 MPa) contact pressures.
- Testing other metallic materials and other surface hardening technologies.
- High temperature tests (e.g. 300 °C).

An increase the number of experimental points to the interrupted tests and to perform longer duration tests to verify the occurrence of a “steady-state” are additionally suggested.

From a *methodological* point of view:

Several specialized techniques (e.g. FIB, EBDS, TEM) can be used to investigate the evolution of the subsurface layer and its structure. In the SAE XEV-F valve steel, fracture in the NbC and its stress concentration effect on the subsurface region, and third-body formation, are both phenomena susceptible of been explored by such techniques.

From a *technological* point of view:

Other valve and valve seat materials can be tested under ball-on-disc dry sliding tests verify the extent of the validity of the methodology presented in this work, and to search for technological insights that could aid the project of the actual valve/valve-seat systems.

## 7 REFERENCES

Ajayi OO. Erck RA. "Variation of nominal contact pressure with time during sliding wear". Proceedings of the International Joint Tribology Conference. October 22-24 (2001). San Francisco (USA).

Available at: <https://digital.library.unt.edu/ark:/67531/metadc739200/metadata/>

Archard JF. "Contact and rubbing of flat surfaces" Journal of Applied Physics. 24. 981 (1953). <https://doi.org/10.1063/1.1721448>

Archard JF. Hirst W. "The wear of metals under unlubricated conditions". Proceedings of the Royal Society of London. A236 (1956).

DOI: [10.1098/rspa.1956.0144](https://doi.org/10.1098/rspa.1956.0144)

American Society for Testing and Materials. "ASTM G133-05: Standard test method for linearly reciprocating ball-on-flat sliding wear". ASTM (2005).

Bahadur S. "Wear research and development" Journal of Lubrication Technology, 100 (1978). pp. 449-454. [doi:10.1115/1.3453249](https://doi.org/10.1115/1.3453249)

Berthier Y. Vincent L. Godet M. "Velocity accommodation in fretting". Wear. 125 (1988) pp. 25-38. [https://doi.org/10.1016/0043-1648\(88\)90191-3](https://doi.org/10.1016/0043-1648(88)90191-3)

Bhushan B. "Introduction to tribology". John Wiley & Sons (2013).

ISBN [978-1-119-94453-9](https://www.isbn-international.org/product/9781119944539)

Blau P. "Running-in: art or engineering?". Journal of Materials Engineering (1991) 13: 47. <https://doi.org/10.1007/BF02834123>

Blau P. "Friction science and technology". Taylor & Francis (2009).

ISBN [9781420054040](https://www.isbn-international.org/product/9781420054040)

Blau P. "How common is the steady-state? The implications of wear transitions for materials selection and design". *Wear*, 332-333 (2015) pp. 1120-1128. <https://doi.org/10.1016/j.wear.2014.11.018>

Bowden FP. Ridler KEW. "Physical properties of surfaces - III—The surface temperature of sliding metals - The temperature of lubricated surfaces". *Proceedings of the Royal Society*. 154A (1936) pp. 640-656. DOI: [10.1098/rspa.1936.0074](https://doi.org/10.1098/rspa.1936.0074)

Bowden FP. Tabor D. "The area of contact between stationary and moving surfaces". *Proceedings of the Royal Society* 169A (1939) pp. 391-413. DOI: [10.1098/rspa.1939.0005](https://doi.org/10.1098/rspa.1939.0005)

Bowden FP. Moore AJW. Tabor D. "The Ploughing and Adhesion of Sliding Metals". *Journal of Applied Physics*. 14 (1943) pp. 80-91. <https://doi.org/10.1063/1.1714954>

Bowden FP. Tabor D. "The friction and lubrication of solids" Oxford University Press (1950). ISBN: [0198507771](https://www.isbn-international.org/number/0198507771)

Bryggman U. Soderberg S. "Contact conditions in fretting". *Wear*. 110 (1986) pp. 1-17. [https://doi.org/10.1016/0043-1648\(86\)90148-1](https://doi.org/10.1016/0043-1648(86)90148-1)

Czichos H. "A systems analysis data sheet for friction and wear tests and an outline for simulative testing". *Wear*. 41 (1977) pp. 45-55. [https://doi.org/10.1016/0043-1648\(77\)90190-9](https://doi.org/10.1016/0043-1648(77)90190-9)

Czichos H. "Tribology. A systems approach to the science and technology of friction, lubrication, and wear". Elsevier. Amsterdam (1978) pp.100. ISBN: [978-0-444-41676-6](https://www.isbn-international.org/number/978-0-444-41676-6)

Demkin NB. "Actual area of contact between solid surfaces (in Russian), 1962 (USSR Academy of Sciences Press, Moscow)

Dieter. GE. "Mechanical metallurgy" (SI Metric Ed.) McGraw-Hill (1988).

[ISBN 0-07-084187-X](#)

Dumbleton JH. Douthett JA. "The unlubricated adhesive wear resistance of metastable austenitic stainless steels containing silicon". *Wear*. 42 (1977) pp. 305-332.

[https://doi.org/10.1016/0043-1648\(77\)90060-6](https://doi.org/10.1016/0043-1648(77)90060-6)

Fargas G. Roa JJ. Mateo A. "Influence of pre-existing martensite on the wear resistance of metastable austenitic stainless steels" *Wear*. 364-365 (2016) pp. 40-47.

<https://doi.org/10.1016/j.wear.2016.06.018>

Farias MCM. Souza RM. Sinatora A. Tanaka DK. "The influence of applied load, sliding velocity and martensitic transformation on the unlubricated sliding wear of austenitic stainless steels". *Wear* 263. Issues 1–6. (2007) pp. 773-781.

<https://doi.org/10.1016/j.wear.2006.12.017>

Fink M. "Wear Oxidation—A new component of wear". *Transactions of the American Society for Steel Treating*. 18 (1930) pp. 1026-1034.

Fukuda K. Morita T. "Physical model of adhesive wear in early stage of sliding".

*Wear*. 376-377 (2017) pp. 1528 - 1533. <https://doi.org/10.1016/j.wear.2017.01.078>

Godet M. "The third body approach. A mechanical point of view of wear". *Wear*. 100 (1984) pp. 437-452. [https://doi.org/10.1016/0043-1648\(84\)90025-5](https://doi.org/10.1016/0043-1648(84)90025-5)

Goto H. Amamoto Y. "Effect of varying load on wear resistance of carbon steel under unlubricated conditions". *Wear*. 253 (2003) pp. 1256-1266.

[https://doi.org/10.1016/S0043-1648\(03\)00222-9](https://doi.org/10.1016/S0043-1648(03)00222-9)

Goto H. Amamoto Y. "Friction and wear of carbon steel near T<sub>1</sub>-transition under sliding". *Tribology International*. 39 (2006) pp. 756-762.

<https://doi.org/10.1016/j.triboint.2005.07.001>

Hashmi MSJ. "Comprehensive materials processing". Elsevier (2014) pp. 5474. ISBN: 978-0-08-096532-1.

Heilmann P. Don J. Sun TC. Rigney DA. "Sliding wear and transfer". Wear. 91 (1983) pp. 171-190. [https://doi.org/10.1016/0043-1648\(83\)90252-1](https://doi.org/10.1016/0043-1648(83)90252-1)

Hiratsuka K. Goto M. "The role of changes in hardness of subsurfaces, transfer particles and wear particles in initial-steady wear transition". Wear. 238 (2000) pp. 70-77. [https://doi.org/10.1016/S0043-1648\(99\)00342-7](https://doi.org/10.1016/S0043-1648(99)00342-7)

Hiratsuka K. Muramoto K. "Role of wear particles in severe-mild transition". Wear. 259 (2005) pp. 467-476. <https://doi.org/10.1016/j.wear.2005.02.102>

Hirst W. Lancaster JK. "Surface film formation and metallic wear". Journal of Applied Physics. 27 (1956) pp. 1057-1065. <https://doi.org/10.1063/1.1722541>

Hirst W. Lancaster JK. "The Influence of speed on metallic wear". Proceeding of the Royal Society of London. 259A (1960) pp. 228-241. DOI: 10.1098/rspa.1960.0220

Holm R. "Electric Contacts: Theory and Application". Gerbers. Stockholm. (1946).

Holmberg K. Andersson P. Erdemir A. "Global Energy Consumption due to Friction in Passenger Cars." Tribology International 47. (2012) pp. 221-34. doi:10.1016/j.triboint.2011.11.022

Hsu KL. Ahn TH. Rigney DA. "Friction, wear and microstructure of unlubricated austenitic stainless steels" Wear 60(1). (1980) pp. 13-37. DOI: 10.1016/0043-1648(80)90247-1

ISO 16610-21:2011 standard. "Geometrical product specifications (GPS) -- Filtration -- Part 21: Linear profile filters: Gaussian filters".

Iwabuchi A. Hori K. Kubosawa H. "The effect of oxide particles supplied at the interface before sliding on the severe-mild transition". *Wear*. 128 (1988) pp. 123-137.  
[https://doi.org/10.1016/0043-1648\(88\)90179-2](https://doi.org/10.1016/0043-1648(88)90179-2)

Jiang J. Stott FH. Stack MM. "The role of triboparticulates in dry sliding wear". *Tribology International*. 31 (1998) 245-256.  
[https://doi.org/10.1016/S0301-679X\(98\)00027-9](https://doi.org/10.1016/S0301-679X(98)00027-9)

Jimbert P. Iturrondobeitia M. Ibarretxe J. Fernandez-Martinez R. "Pin on disk against ball on disk for the evaluation of wear improvement on cryotreated metal cutting shears" 4th International Congress in Advances in Applied Physics and Materials Science (APMAS 2014) AIP Conf. Proc. 1653. 020048-1–020048-7. (2015).  
[doi: 10.1063/1.4914239](https://doi.org/10.1063/1.4914239)

Kayaba T. Kato K. "The analysis of adhesive wear mechanisms by successive observation of the wear process in SEM" ASME. Proceedings of the International Conference on Wear of Materials (1979) pp. 45-56.

Kato K. "Wear mode transitions". *Scripta Metallurgica et Materialia*. 24 (1990) pp. 815-820. [https://doi.org/10.1016/0956-716X\(90\)90118-Z](https://doi.org/10.1016/0956-716X(90)90118-Z)

Kato K. "Severe-mild wear transition by supply of oxide particles on sliding surface". *Wear*. 255 (2003) pp. 426-429.  
[https://doi.org/10.1016/S0043-1648\(03\)00077-2](https://doi.org/10.1016/S0043-1648(03)00077-2)

Kato K. "Effect of supply fine oxide particles onto rubbing steel surfaces on severe-mild wear transition and oxide film formation". *Tribology International*. 41 (2007) pp. 735-742. <https://doi.org/10.1016/j.triboint.2008.01.001>

Kato K. Eyre TS. Ralph B. "Wear mechanism map for nitrided steel". *Acta Metallurgica et Materialia*. 42 No. 5 (1994) pp. 1703-1713.  
[https://doi.org/10.1016/0956-7151\(94\)90380-8](https://doi.org/10.1016/0956-7151(94)90380-8)

Kato K. Komai K. "Tribofilm formation and mild wear by tribo-sintering of nanometer-sized oxide particles on rubbing steel surfaces". *Wear*. 262 (2007) pp. 36-41. <https://doi.org/10.1016/j.wear.2006.03.046>

Lancaster JK. "The influence of temperature on metallic wear". *Proceedings of the Physical society of London*. B70 (1957) pp. 112-118.  
<https://doi.org/10.1088/0370-1301/70/1/316>

Lim SC. Ashby MF. "Wear-mechanism maps". *Acta Metallurgica*, 35 (1987) pp. 1-24. [https://doi.org/10.1016/0001-6160\(87\)90209-4](https://doi.org/10.1016/0001-6160(87)90209-4)

Luo HS. Zhao C. "Low temperature salt bath hardening of AISI 201 austenitic stainless steel". *Physics Procedia* 50. (2013) pp. 38-42.  
<https://doi.org/10.1016/j.phpro.2013.11.008>

Mingolo N. Tschiptschin AP. Pinedo CE. "On the formation of expanded austenite during plasma nitriding of an AISI 316L austenitic stainless steel". *Surface and Coatings Technology* 7. (2006) pp.4215-4218.  
<https://doi.org/10.1016/j.surfcoat.2006.08.060>

Oketani H. Ishida M. Noda T. Ueta S. Kiriyaama M. "Trends in engine valve development for automobiles and motorcycles." *SAE Technical Paper* 2000-01-0907. (2000). [doi:10.4271/2000-01-0907](https://doi.org/10.4271/2000-01-0907).

Pharr GM. Herbert EG. Gao Y. "The indentation size effect: a critical examination of experimental observations and mechanistic interpretations". *Annual Review of Materials Research*. 40 (2010) pp. 271-292.  
<https://doi.org/10.1146/annurev-matsci-070909-104456>

Presidência da República Federativa do Brasil: LEI Nº 12.187. DE 29 DE DEZEMBRO DE 2009. "Institui a Política Nacional sobre Mudança do Clima - PNMC e dá outras providências". Casa Civil. Subchefia para Assuntos Jurídicos. Palácio do Planalto. Brasília (BR). Available at:

[http://www.planalto.gov.br/ccivil\\_03/\\_ato2007-2010/2009/lei/l12187.htm](http://www.planalto.gov.br/ccivil_03/_ato2007-2010/2009/lei/l12187.htm)

Presidência da República Federativa do Brasil: DECRETO Nº 7.390. DE 9 DE DEZEMBRO DE 2010. “Regulamenta os arts. 6o. 11 e 12 da Lei no 12.187. de 29 de dezembro de 2009. que institui a Política Nacional sobre Mudança do Clima - PNMC. e dá outras providências”.. Casa Civil. Subchefia para Assuntos Jurídicos. Palácio do Planalto. Brasília (BR). Available at:

[http://www.planalto.gov.br/ccivil\\_03/\\_ato2007-2010/2010/Decreto/D7390.htm](http://www.planalto.gov.br/ccivil_03/_ato2007-2010/2010/Decreto/D7390.htm)

Qian L. Li M. Zhou Z. Yang H. Shi X. “Comparison of nanoindentation hardness to microhardness”. Surface and Coatings Technology. 195 (2005) pp. 264– 271.

<https://doi.org/10.1016/j.surfcoat.2004.07.108>

Quinn TFJ. “Role of oxidation in the mild wear of steel”. British Journal of Applied Physics 13 (1962) 33. <https://doi.org/10.1088/0508-3443/13/1/308>

Quinn TFJ. Sullivan JL. Rowson DM. “Origins and development of oxidative wear at low ambient temperatures”. Wear. 94 (1984) pp. 175-191.

[https://doi.org/10.1016/0043-1648\(84\)90053-X](https://doi.org/10.1016/0043-1648(84)90053-X)

Rabinowicz E. “The wear coefficient - magnitude, scatter, uses.” Transactions of the ASME. 103 (1981) pp. 188-193. [doi:10.1115/1.3251624](https://doi.org/10.1115/1.3251624)

Rigney DA. “The roles of hardness in the sliding behavior of materials”. Wear. 175 (1994) pp. 63-69. [https://doi.org/10.1016/0043-1648\(94\)90169-4](https://doi.org/10.1016/0043-1648(94)90169-4)

Rigney DA. “Comments on the sliding wear of metals”. Tribology International v30 No. 5 (1997) pp.361 - 367. [https://doi.org/10.1016/S0301-679X\(96\)00065-5](https://doi.org/10.1016/S0301-679X(96)00065-5)

Rigney DA. “Transfer, mixing and associated chemical and mechanical processes during the sliding of ductile materials”. Wear. 245 (2000) pp. 1-9.

[https://doi.org/10.1016/S0043-1648\(00\)00460-9](https://doi.org/10.1016/S0043-1648(00)00460-9)

Rigney DA. Hirth JP. “Plastic deformation and sliding friction of metals”. Wear. 53 (1979) pp. 345-370. [https://doi.org/10.1016/0043-1648\(79\)90087-5](https://doi.org/10.1016/0043-1648(79)90087-5)

Rosenberg SJ. Jordan L. "Influence of oxide films on the wear of steels". Journal of research of the National Boureau of Standards. 13 (1934) pp. 267-279.

Ruff AW. "Comparison of Standard Ttest Methods for Non-lubricated Sliding Wear". Wear. 134 (1989) pp. 49-57. [https://doi.org/10.1016/0043-1648\(89\)90061-6](https://doi.org/10.1016/0043-1648(89)90061-6)

Sasada T. "Future direction of research in wear and wear resistant materials (status of understanding)" Tribology in the 80s. NASA conference publication 2300. 1 (1984) pp. 197-218.

Shih TS. Huang YS. Chen CF. "Constituted oxides/nitrides on nitriding 304. 430 and 17-4 PH stainless steel in salt baths over the temperature range 723 to 923 K" Applied Surface Science 258. (2011) pp. 81-88.  
<https://doi.org/10.1016/j.apsusc.2011.08.010>

Shirzadi A. Jackson S. "Structural alloys for power plants (operational challenges and high-temperature materials)". Elsevier. Cambridge (UK). 1st Edition. (2014) pp 516. ISBN: 978-0-85709-238-0.

Shvetzova. EM. "Anthology". Abrasion and wear (7). Academy of Sciences Press. USSR. 1953.

Schnurmann R. "Friction and wear". Wear. 5 (1962) pp. 31-42.  
[https://doi.org/10.1016/0043-1648\(62\)90178-3](https://doi.org/10.1016/0043-1648(62)90178-3)

Stachowiak G. Batchelor AW. "Engineering tribology" Elsevier. 3rd edition. (2005) pp. 832. ISBN: 9780750678360.

Stickels CA. "Carbide refining heat treatments for 52100 bearing steel". Metallurgical Transactions. 5 (1974) pp. 865-874. DOI: 10.1007/BF02643140

Suh NP. "The delamination theory of wear". Wear. 25 (1973) pp. 111-124.  
[https://doi.org/10.1016/0043-1648\(73\)90125-7](https://doi.org/10.1016/0043-1648(73)90125-7)

Suh NP. Jahanmir S. Abrahamson EP II. Turner APL. "Further investigation of the delamination theory of wear". ASME Journal of Lubrication Technology. 96 (1974) pp. 631-637. [doi:10.1115/1.3452511](https://doi.org/10.1115/1.3452511)

Suh NP. "An overview of the delamination theory of wear". Wear. 44 (1977) pp. 1-16. [https://doi.org/10.1016/0043-1648\(77\)90081-3](https://doi.org/10.1016/0043-1648(77)90081-3)

Sullivan JL. Hodgson SG. "A study of mild oxidative wear for conditions of low load and speed". Wear. 121 (1988) pp. 95-106. DOI: [10.1007/s11249-008-9361-y](https://doi.org/10.1007/s11249-008-9361-y)

Tylczak JH. Hawk JA. Wilson RD. "A Comparison of laboratory abrasion and field wear results" Wear 225–229 (1999) pp. 1059-1069. [https://doi.org/10.1016/S0043-1648\(99\)00043-5](https://doi.org/10.1016/S0043-1648(99)00043-5)

United Nations. 1992. "United Nations Framework Convention on Climate Change". FCCC/INFORMAL/84 GE.05-62220 (E) 200705. Available at: <https://unfccc.int/resource/docs/convkp/conveng.pdf>

Viáfara CC. Sinatora A. "Unlubricated sliding friction and wear of steels-An evaluation of the mechanism responsible for the T<sub>1</sub> wear regime transition". Wear. 271 (2011) pp. 1689-1700. <https://doi.org/10.1016/j.wear.2010.12.085>

Viáfara CC. Sinatora A. "The effect of hardness of sliding bodies on the wear regime transitions of steels". Lubrication Science. 25. (2012) pp. 126-138. DOI: [10.1002/ls.1198](https://doi.org/10.1002/ls.1198)

Wang Y. "Introduction to engine valvetrains". SAE International (2007). ISBN-10: [0768010799](https://doi.org/10.1002/ls.1198).

Waterhouse RB. "Fretting". Treatise on Materials Science and Technology. 13 (1979) pp. 259-286. [https://doi.org/10.1016/S0161-9160\(13\)70070-X](https://doi.org/10.1016/S0161-9160(13)70070-X)

Welsh NC. "Frictional heating and its influence on the wear of steels". Journal of Applied Physics. 28 (1957) pp. 960-968. <https://doi.org/10.1063/1.1722920>

Welsh NC. "The dry wear of steels: I and ii". Philosophical Transactions of the Royal Society of London. A257 (1965) pp. 31-72. DOI: [10.1098/rsta.1965.0002](https://doi.org/10.1098/rsta.1965.0002)

Whitenton EP. Blau PJ. "A comparison of methods for determining wear volumes and surface parameters of spherically tipped sliders". Wear 124 (3). (1988). pp. 291-309. [https://doi.org/10.1016/0043-1648\(88\)90219-0](https://doi.org/10.1016/0043-1648(88)90219-0)

Yang ZY. Naylor MGS. Rigney DA. "Sliding wear of 304 and 310 stainless steels" Wear 105. (1985) pp. 73-86. [https://doi.org/10.1016/0043-1648\(85\)90007-9](https://doi.org/10.1016/0043-1648(85)90007-9)

Yovanovich MM. "Micro and macro hardness measurements, correlations, and contact models" Collection of Technical Papers – 44th AIAA aerospace sciences meeting. Vol. 16 (2006) pp. 11702-11729.

Zuleta DA. "Influência da temperatura, velocidade e força no desgaste e no coeficiente de atrito de materiais para válvulas e sedes de válvulas de motores flex-fuel". (Ph.D. thesis) Polytechnic School of the University of São Paulo. São Paulo (Brazil). 2016.

Zum Gahr KH. "Wear by hard particles". Tribology International. 31 (1998) 587-596. doi:[10.1016/S0301-679X\(98\)00079-6](https://doi.org/10.1016/S0301-679X(98)00079-6).

Zum Gahr KH. "Microstructure and wear of materials". Elsevier (1987). ISBN. [0-444-42754-6](https://www.isbn-international.org/number/0-444-42754-6).